frontiers | Research Topics

Solubility phenomena in the context of nuclear waste disposal

Edited by
Xavier Gaona, Sarah Saslow, Hye-Ryun Cho,
Taishi Kobayashi and Bernd Grambow

Published in
Frontiers in Nuclear Engineering

FRONTIERS EBOOK COPYRIGHT STATEMENT

The copyright in the text of individual articles in this ebook is the property of their respective authors or their respective institutions or funders. The copyright in graphics and images within each article may be subject to copyright of other parties. In both cases this is subject to a license granted to Frontiers.

The compilation of articles constituting this ebook is the property of Frontiers.

Each article within this ebook, and the ebook itself, are published under the most recent version of the Creative Commons CC-BY licence. The version current at the date of publication of this ebook is CC-BY 4.0. If the CC-BY licence is updated, the licence granted by Frontiers is automatically updated to the new version.

When exercising any right under the CC-BY licence, Frontiers must be attributed as the original publisher of the article or ebook, as applicable.

Authors have the responsibility of ensuring that any graphics or other materials which are the property of others may be included in the CC-BY licence, but this should be checked before relying on the CC-BY licence to reproduce those materials. Any copyright notices relating to those materials must be complied with.

Copyright and source acknowledgement notices may not be removed and must be displayed in any copy, derivative work or partial copy which includes the elements in question.

All copyright, and all rights therein, are protected by national and international copyright laws. The above represents a summary only. For further information please read Frontiers' Conditions for Website Use and Copyright Statement, and the applicable CC-BY licence.

ISSN 1664-8714
ISBN 978-2-8325-4078-7
DOI 10.3389/978-2-8325-4078-7

About Frontiers

Frontiers is more than just an open access publisher of scholarly articles: it is a pioneering approach to the world of academia, radically improving the way scholarly research is managed. The grand vision of Frontiers is a world where all people have an equal opportunity to seek, share and generate knowledge. Frontiers provides immediate and permanent online open access to all its publications, but this alone is not enough to realize our grand goals.

Frontiers journal series

The Frontiers journal series is a multi-tier and interdisciplinary set of open-access, online journals, promising a paradigm shift from the current review, selection and dissemination processes in academic publishing. All Frontiers journals are driven by researchers for researchers; therefore, they constitute a service to the scholarly community. At the same time, the *Frontiers journal series* operates on a revolutionary invention, the tiered publishing system, initially addressing specific communities of scholars, and gradually climbing up to broader public understanding, thus serving the interests of the lay society, too.

Dedication to quality

Each Frontiers article is a landmark of the highest quality, thanks to genuinely collaborative interactions between authors and review editors, who include some of the world's best academicians. Research must be certified by peers before entering a stream of knowledge that may eventually reach the public - and shape society; therefore, Frontiers only applies the most rigorous and unbiased reviews. Frontiers revolutionizes research publishing by freely delivering the most outstanding research, evaluated with no bias from both the academic and social point of view. By applying the most advanced information technologies, Frontiers is catapulting scholarly publishing into a new generation.

What are Frontiers Research Topics?

Frontiers Research Topics are very popular trademarks of the *Frontiers journals series*: they are collections of at least ten articles, all centered on a particular subject. With their unique mix of varied contributions from Original Research to Review Articles, Frontiers Research Topics unify the most influential researchers, the latest key findings and historical advances in a hot research area.

Find out more on how to host your own Frontiers Research Topic or contribute to one as an author by contacting the Frontiers editorial office: frontiersin.org/about/contact

Solubility phenomena in the context of nuclear waste disposal

Topic editors
Xavier Gaona — Karlsruhe Institute of Technology (KIT), Germany
Sarah Saslow — Pacific Northwest National Laboratory (DOE), United States
Hye-Ryun Cho — Korea Atomic Energy Research Institute (KAERI), Republic of Korea
Taishi Kobayashi — Kyoto University, Japan
Bernd Grambow — UMR6457 Laboratoire de Physique Subatomique et des Technologies Associées (SUBATECH), France

Citation
Gaona, X., Saslow, S., Cho, H.-R., Kobayashi, T., Grambow, B., eds. (2023). *Solubility phenomena in the context of nuclear waste disposal*. Lausanne: Frontiers Media SA. doi: 10.3389/978-2-8325-4078-7

Table of contents

Frontiers in Nuclear Engineering

TYPE Editorial
PUBLISHED 21 November 2023
DOI 10.3389/fnuen.2023.1332806

EDITED AND REVIEWED BY
Sergei Dudarev,
United Kingdom Atomic Energy
Authority, United Kingdom

*CORRESPONDENCE
Xavier Gaona,
✉ xavier.gaona@kit.edu

RECEIVED 03 November 2023
ACCEPTED 10 November 2023
PUBLISHED 21 November 2023

CITATION
Gaona X, Grambow B, Kobayashi T, Cho H-R and Saslow SA (2023), Editorial: Solubility phenomena in the context of nuclear waste disposal.
Front. Nucl. Eng. 2:1332806.
doi: 10.3389/fnuen.2023.1332806

Editorial: Solubility phenomena in the context of nuclear waste disposal

Xavier Gaona[1]*, Bernd Grambow[2], Taishi Kobayashi[3], Hye-Ryun Cho[4] and Sarah A. Saslow[5]

[1]Institute for Nuclear Waste Disposal, Karlsruhe Institute of Technology, Karlsruhe, Germany, [2]SUBATECH (CNRS-IN2P3, Nantes University, IMT Atlantique), Nantes, France, [3]Department of Nuclear Engineering, Kyoto University, Kyoto, Japan, [4]Nuclear Chemistry Research Team, Korea Atomic Energy Research Institute, Daejeon, Republic of Korea, [5]Pacific Northwest National Laboratory, Richland, WA, United States

KEYWORDS

solubility, nuclear waste, radionuclides, engineered barriers, gas, thermodynamics

Editorial on the Research Topic
Solubility phenomena in the context of nuclear waste disposal

Safety concepts regarding the disposal of nuclear waste in underground repositories generally rely on a combination of engineered and geological barriers that minimize the potential release of radionuclides from the containment-providing rock zone and transport through the biosphere. The presence of water (e.g., groundwater and pore water of repository rocks), however, can alter the engineered barrier system, dissolve radionuclides, and facilitate radionuclide transport that, over millennia, may allow small fractions of water-soluble radionuclides to permeate to the biosphere. Thus, while barrier systems aim to prevent or hinder water from contacting the waste, the possible intrusion of aqueous solutions must be considered for several safety case scenarios impacted by the long-term evolution of a repository. Dissolution, precipitation, and solubility phenomena thus arise as important processes controlling the chemical behavior of radionuclides and other key materials relevant to such repositories and their safety assessment. The solubility and aqueous speciation of radionuclides are of particular interest as they provide upper limits on water-transportable radionuclide concentrations. For many radionuclides, solubility limits are reached only after release from the disposed waste products close to the disposal locations, where the expected maximal concentrations are highest. It is then often the solubility of a secondary phase, precipitated after the dissolution of a primary phase in the waste matrix, that controls the maximum transportable radionuclide concentration close to the disposal location.

Solubility phenomena of radioactive and other gases in water provide important constraints on gas transport and pressure build-up. Moreover, due to their thermodynamic foundation, solubility assessments offer insight into time-independent constraints (e.g., maximum concentrations of radionuclides or gases in a fluid phase) on the evolution of the disposal system. Particularly important in this regard is the geochemical modeling of radionuclide behavior in the engineered barrier system as well as in natural aquatic systems along the transport path of radionuclides to the biosphere. Despite its simplicity, the concept of solubility is difficult to apply in natural water systems as various water constituents will influence solubility, which may vary over the very long time considered in safety assessments of disposal. For instance, the interaction of natural waters with the components of the engineered barrier system surrounding the disposed waste products will influence solution pH, redox potentials, or ligand concentrations. Information obtained from studies evaluating radionuclide behavior provides valuable inputs that appropriately constrain safety analyses of nuclear waste disposal.

In this series of articles, solubility phenomena related to different domains and key components in the context of nuclear waste disposal are presented. Several of these contributions provide insight into the chemical, thermodynamic, and (SIT, Pitzer) activity models describing the investigated systems. This emphasizes the usefulness of solubility studies for the determination of thermodynamic properties, which can be implemented in thermodynamic databases (e.g., NEA-TDB, THEREDA, ThermoChimie, JAEA-TDB, or PSI-Nagra, among others) and further used in geochemical calculations of relevance for nuclear waste disposal.

Three contributions are dedicated to the solubility of key radionuclides, i.e., Pu, U, and ^{99}Tc. Cho et al. investigate the dissolution of PuO_2(cr) in natural waters under atmospheric conditions at T = 25°C and 60°C. By comparing experimental results with geochemical calculations, the authors explain the observed solubility behavior based on the oxidative dissolution of PuO_2(am, hyd), highlighting the key role of Pu(IV) colloids. Grambow et al. investigate the formation of UO_2(s) from aqueous solutions containing U(VI) and U(IV). Combining solubility experiments with thorough solid phase characterization and thermodynamic calculations, the authors conclude that their observations can be explained by three main effects: (i) oxidation of UO_2(s) to U_4O_9(s), (ii) the effect of particle size, and/or (iii) the presence of oxygen traces as low as $1{\cdot}10^{-8}$ atm. The mini-review by Singh et al. discusses some key contributions in the literature dealing with the solubility of ^{99}Tc and Re in different waste forms, i.e., glass, cement, ceramic, and geopolymers. The concluding remarks by the authors summarize future challenges that need to be addressed to minimize the solubilization of ^{99}Tc from the designed waste forms in different environments.

Sorel phases of the general formula xMg$(OH)_2{\cdot}y$MgCl$_2{\cdot}z$H$_2$O (x-y-z phases) are considered in the construction of geotechnical barriers in repositories in rock-salt geological formations. The comprehensive studies by Pannach et al. and Freyer et al. provide an extensive experimental basis (solubility data, solid phase characterization) to derive the thermodynamic and (Pitzer) activity models for the Sorel phases and $Mg(OH)_2$ in the Na-Mg-Cl-OH-H_2O system. The 3-1-8 Sorel phase and $Mg(OH)_2$ are identified as the stable solid phases, while the 5-1-8 Sorel phase is metastable. Bok et al. critically review the available solubility data of O_2 in water and saline solutions at temperatures up to 373 K. As a main outcome of this exercise, the authors provide a selection of thermodynamic data for dissolved oxygen O_2(aq), a temperature-dependent Henry's law constant, and Pitzer coefficients for the calculation of oxygen solubility in concentrated salt solutions of the system Na-K-H-Ca-Mg-Cl-SO_4-CO_3-PO_4-OH-H_2O(l), together with their validity range in terms of temperature (273–318 K), ionic strength (≤5 mol kg^{-1}) and O_2 partial pressure (≤101.325 kPa).

The last contribution to this Research Topic deals with beryllium as a chemotoxic element expected in specific waste streams of radioactive waste. Using a combination of solubility experiments, solid phase characterization, and molecular dynamics calculations, Cevirim-Papaioannou et al. derive thermodynamic and (SIT) activity models for the solubility and hydrolysis of Be(II) in dilute to concentrated $CaCl_2$ systems. These models are then used to predict the speciation of beryllium in cementitious environments, such as those considered in repository concepts for the disposal of low- and intermediate-level waste.

Author contributions

XG: Writing–original draft, Writing–review and editing. BG: Writing–original draft, Writing–review and editing. TK: Writing–original draft, Writing–review and editing. H-RC: Writing–original draft, Writing–review and editing. SAS: Writing–original draft, Writing–review and editing.

Conflict of interest

The authors declare that the research was conducted in the absence of any commercial or financial relationships that could be construed as a potential conflict of interest.

The author(s) declared that they were an editorial board member of Frontiers, at the time of submission. This had no impact on the peer review process and the final decision.

Publisher's note

Frontiers in Nuclear Engineering

TYPE Mini Review
PUBLISHED 04 January 2023
DOI 10.3389/fnuen.2022.1112080

EDITED BY
Taishi Kobayashi,
Kyoto University, Japan

REVIEWED BY
Shingo Kimuro,
Japan Atomic Energy Agency, Japan

*CORRESPONDENCE
Wooyong Um,
✉ wooyongum@postech.ac.kr

SPECIALTY SECTION
This article was submitted to Radioactive Waste Management, a section of the journal Frontiers in Nuclear Engineering

RECEIVED 30 November 2022
ACCEPTED 14 December 2022
PUBLISHED 04 January 2023

CITATION
Singh BK, Kim J, Pak D, Kim K and Um W (2023), Technetium (Tc)/Rhenium (Re) solubility and leaching behavior from waste forms: An overview.
Front. Nucl. Eng. 1:1112080.
doi: 10.3389/fnuen.2022.1112080

Technetium (Tc)/Rhenium (Re) solubility and leaching behavior from waste forms: An overview

Bhupendra Kumar Singh[1,2], Jueun Kim[1], Donghun Pak[1], Kyungwon Kim[1] and Wooyong Um[1,2,3]*

[1]Division of Advanced Nuclear Engineering (DANE), Pohang University of Science and Technology (POSTECH), Pohang, South Korea, [2]Nuclear Environmental Technology Institute (NETI), Pohang University of Science and Technology (POSTECH), Pohang, South Korea, [3]Division of Environmental Sciences and Engineering (DESE), Pohang University of Science and Technology (POSTECH), Pohang, South Korea

Technetium-99 (^{99}Tc), a radionuclide generated from nuclear industry is a great environmental concern because of its long half-life (2.13 × 10^5 years) and high mobility in environment. Therefore, apposite management of ^{99}Tc is imperative to control its hazardous radiological impact on humans and other livings. So far, the major strategy implementation has been the solidification and immobilization of ^{99}Tc radioactive waste in various matrices as waste forms and disposal in deep geological repository. However, by passing the time, ^{99}Tc may leach out/solubilize from the waste forms under different geochemical/environmental conditions. In this minireview, we discuss some key contributions towards the solubility of ^{99}Tc and rhenium (Re; a well-known surrogate of ^{99}Tc) from different waste forms. Specifically, we review the solubility of ^{99}Tc from glass, cement, ceramic, and geopolymer waste forms. The final section (conclusion) presents a short summary and future challenges need be addressed to impede the solubility of ^{99}Tc from the designed waste forms. We believe this minireview will be beneficial to provide a significant insight on the solubility of ^{99}Tc from aforementioned waste forms and in the design of robust matrices to minimize/prevent ^{99}Tc migration in various environments.

KEYWORDS

TC, solubility, leaching, waste form, Re

1 Introduction

Radioactive wastes generated from nuclear power plants' operation and decommissioning of nuclear reactors are serious environmental threat due to their long half-lives and impact of extremely hazardous radiations on geosphere as well as humans (Singh et al., 2021). The proper management of these radioactive wastes including high-level waste (HLW), low- and intermediate-level waste (LILW), and low-level waste (LLW)) is necessary to control their radiological effect on the environment. Among several radionuclides present in radioactive wastes, ^{99}Tc is one of the significant environmental risk contributors due to it long half-life and highly mobile behavior in oxic environment (Santikari et al., 2022). Therefore, it is essential to control/prevent the mobility of ^{99}Tc into the environment by immobilizing it in suitable and durable waste forms. In several studies, rhenium (Re) has been often used as a preferred non-radioactive surrogate for ^{99}Tc due to their close proximities in terms of speciation, ionic size, and hydration energy (Kim and Kruger, 2018; Duckworth et al., 2021). Since decades, various waste forms including glass, cements, geopolymer, and ceramics have been tested and used for solidification, immobilization, and retention of ^{99}Tc by disposing these waste forms in the deep geological repository (Um, 2018).

Over the time, ^{99}Tc immobilized in different waste forms (glass, cement, geopolymer, ceramics, etc.) under deep geological repository can be released/leached out from the solid matrices and migrate into environment under different environmental and geochemical conditions (Klein et al., 2021). Once released, ^{99}Tc can exist as Tc(VII) in oxic environment (pertechnetate (TcO_4^-); most common chemical species of Tc in the environment) or it can be reduced to Tc(IV) in the presence of electron donors (Meena et al., 2017). In order to prevent and control the solubility and leaching of ^{99}Tc from immobilized solid matrices and to design durable waste forms, it is necessary to understand the solubility behavior of ^{99}Tc from waste forms under different geochemical conditions. In this minireview, we summaries and discuss some of the key studies on solubility of ^{99}Tc and/or Re from the glass, cement, geopolymer, and ceramic waste forms. Additionally, we highlight the future challenges concerning the solubility of ^{99}Tc from waste forms and the design and formulation of durable waste form for efficient ^{99}Tc immobilization and retention capacity.

2 Solubility of Tc and Re from waste forms

The design and formulation of different solid matrices can significantly affect the retention capacity and solubility of ^{99}Tc in the immobilized waste forms. This section presents the selected studies on glass, cement, and other waste forms (geopolymer and ceramics) used for immobilization of ^{99}Tc and/or Re and their leaching/solubility behavior under different experimental conditions.

2.1 Solubility of Tc and Re from glass waste forms

Glass waste form has been preferably applied for immobilization of various radionuclides, including ^{99}Tc globally (Danilov et al., 2021; Donald et al., 1997; Jantzen, 2011). Therefore, the leaching behavior of Tc/Re from glass waste forms under various experimental conditions is necessary to address the durability of the designed glass matrices and long-term mobility of ^{99}Tc. Bibler and Jurgensen determined the effects of the redox conditions on the release of ^{99}Tc from borosilicate glass (Bibler and Jurgensen, 1987). The authors prepared two batches of glass waste forms under ambient oxidizing and reducing conditions. The leaching tests were performed according to the materials characterization center (MCC-1) test at 90°C and surface area to volume ratio (SA/V) 100 m^{-1}. The obtained leaching test results revealed that ^{99}Tc leached no faster than the glass-forming elements at ambient oxidizing conditions. Additionally, under high pH and reducing conditions, the normalized ^{99}Tc mass loss was observed as 0.02 g/m^2 only, even at significant dissolution of the glass.

A few studies performed the static leaching experiments to examine the leaching behavior of ^{99}Tc in ^{99}Tc doped borosilicate glass in disposal environment (Lemmens & Wang, 1992; Pirlet et al., 2002, 2004). A mixture of clay with synthetic pore water was used as the leachant to simulate the actual interstitial pore water. All tests were conducted in the glove box at SA/V 100 m^{-1}. The authors suggested that ^{99}Tc mass losses enhanced linearly with the time, and was observed to be faster at 90°C than at 40°C. Moreover, ^{99}Tc concentrations were higher in the oxidizing medium than in reducing medium at both 40 and 90°C.

Xu et al. evaluated Re retention and its stability in iron phosphate glass (Xu et al., 2013). The authors observed ~1.1 wt% retention of Re in iron phosphate glass. Moreover, when 2 wt% or more Re added, a white spherical inclusion (Na, K)ReO_4 was detected by XRD and EDX mapping. The chemical durability tests were performed according to American Society for Testing and Materials (ASTM) C 1285-02. In this method, 1.5 g of glass powder was mixed with 15 ml of deionized water (DIW) in a Teflon vessel and kept inside an oven at 90 °C. The normalized Re-released amount after 7-day Product Consistency Test (PCT) was found to be $< 10^{-2}$ g/m^2. Normalized Re- released along with other elements are shown in Figure 1.

Stefanovsky et al. developed sodium aluminum phosphate (SAP) glass and sodium aluminum iron phosphate (SAIP) glass and determined Re-released rate in both glasses (Stefanovsky et al., 2019). Re- released rate was evaluated *via* PCT test performed at 90°C for 7 days (d). The normalized Re leaching rates were calculated as 2.55×10^{-6} and 9.12×10^{-9} for SAP glass and 3.90×10^{-8} and 7.90×10^{-8} for SIAP glass in the oxidizing and reducing conditions, respectively. Both SAP and SAIP exhibited lower leach rates than the regulatory values (~10^{-5} g/cm^2d) specified for HLW glasses. Especially, a sharp decrease in the Re leach rate in SAP glass synthesized under reducing conditions as compared to the same glass produced under oxidizing conditions, was attributed to the enhanced fraction of Re in the reduced form as Re (0).

Pyo et al. developed a new alkali-alumino tellurite glass to incorporate highly volatile Tc/Re (Pyo et al., 2017) and tested leaching behavior of Re *via* PCT method for 7 d at 90°C. The developed tellurite glass incorporated 7 wt% of Re as Re(VII), in

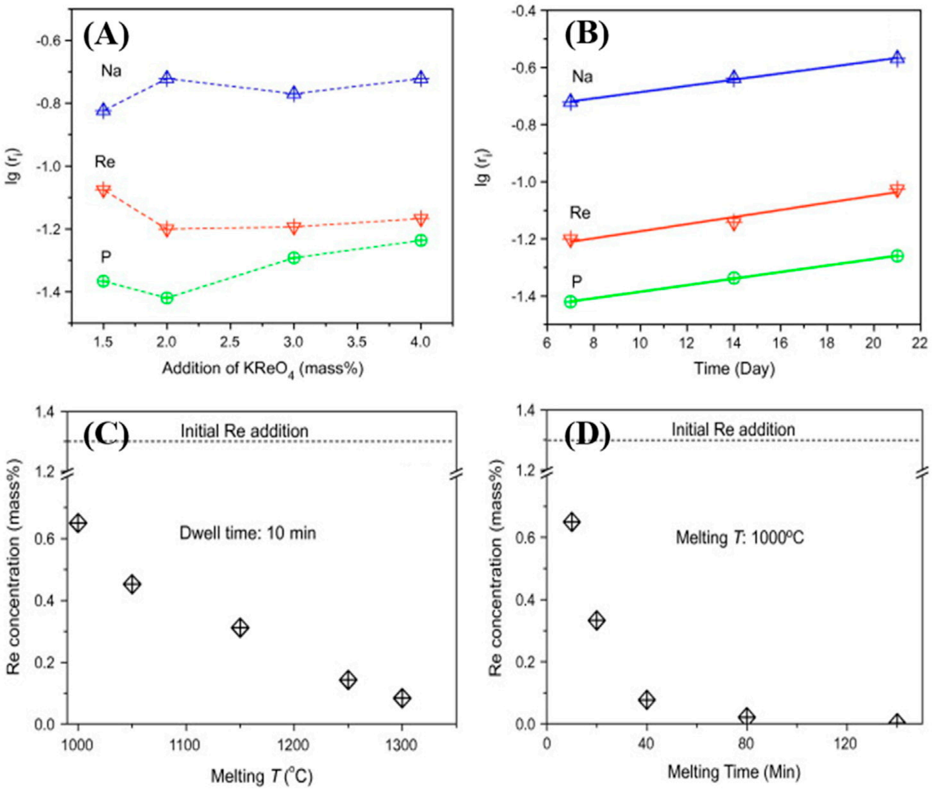

FIGURE 1
Normalized elemental release after 7 days product consistency test (PCT) at different mass% of $KReO_4$ **(A)**. Elemental release at 2-mass% of $KReO_4$ vs. PCT duration **(B)**. Concentrations of Re in 2-mass% of $KReO_4$ samples at different melting temperatures **(C)** and times **(D)**. Reproduced with permission from the reference Xu et al., 2013. Copyright from Elsevier 2013.

which ReO_4^- tetrahedra were linked to the glass network by bonding between non-bridging oxygens and Na^+ or Ca^{2+} ions (Figure 2A). The normalized elemental release data for Re and Te were observed as ~ 1 g/m^2 and 0.5 g/m^2, respectively, which is lower than the safety standard (<2 g/m^2) for the immobilized low activity waste requirement (Figure 2B).

2.2 Solubility of Tc and Re from cementitious waste forms

Cement is one of the known matrices used for efficient immobilization of various radioactive wastes due to its durable properties; chemical and thermal stability as well as corrosion resistivity (El-Kamash et al., 2006; Faiz et al., 2017; Goo et al., 2021). In this section, we discuss the solubility/leaching of Tc/Re from cementitious waste forms in different testing conditions. Simner et al. reported a Dynamic Leaching Method (DLM) to investigate ^{99}Tc leaching behavior from the saltstone monolith (cementitious material) samples at the Savannah River Site (SRS), in the United States of America (USA) (Simner et al., 2017). In order to simulate the transport of groundwater through saltstone, DLM applied a flexible-wall permeameter for ^{99}Tc leaching under the elevated hydraulic gradient. This method enabled a continuous flow of permeant through the monolith and analysis of the leachate to determine ^{99}Tc leaching as a function of pore volumes exchanged within the saltstone monolith. Approximately six pore volumes were passed through the monolith. ^{99}Tc concentrations in the leachate were found to be ~1×10^{-8} mol/L, which indicated that ^{99}Tc leaching in saltstone was controlled by the solubility of $TcO_2 . xH_2O$ compounds.

Santikari et al. investigated the leaching and transport of ^{99}Tc from cementitious waste forms in field lysimeters (Santikari et al., 2022). The authors tested two cementitious waste forms; a) slag-grout of 45%:45%:10% mixture of fly ash, blast furnace slag, and cement, respectively, and b) cement of 55%:45% mixture of cement and fly ash, respectively. The study used a duplicate source of each waste form buried in four lysimeters for approximately 10 months to compare the leaching behavior of ^{99}Tc under natural meteorological conditions in South Carolina, United States. Cumulative ^{99}Tc activity in the effluent was low

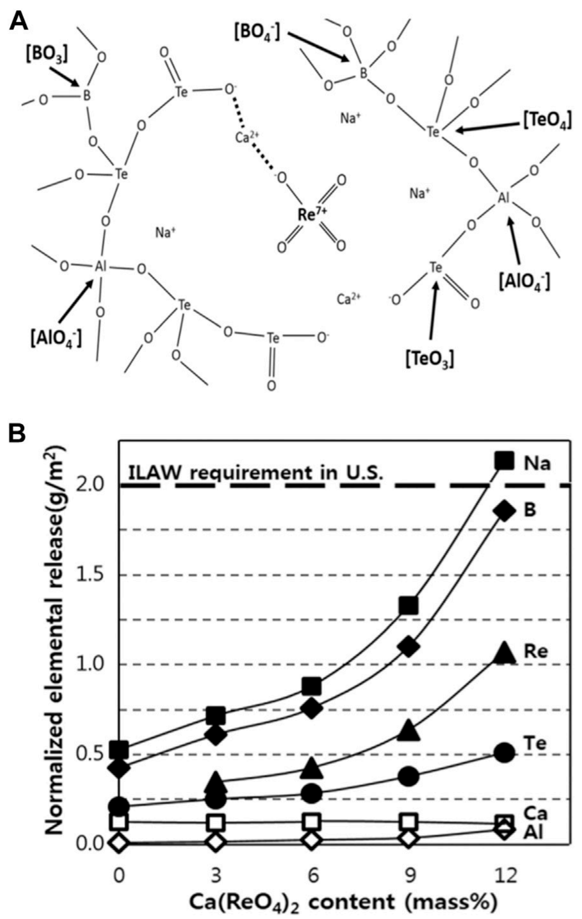

FIGURE 2
Illustration of the tellurite glass structure containing ReO_4^- ion units **(A)**. Normalized release of elements from glasses after 7-day PCT at different $Ca(ReO_4)_2$ contents **(B)**. Reproduced with permission from the reference Pyo et al., 2017. Copyright from Elsevier 2017.

(2×10^5 Bq) until ~300 ml of effluent produced from each lysimeter, and then it was enhanced at a rate of ~3,000 Bq/mL for all the lysimeters.

Cantrell et al. studied the solubility control of Tc from saltstone by $TcO_2?xH_2O$ and revealed that the Tc-release in water from saltstone under anoxic conditions can be considerably altered by the solubility of a $TcO_2?xH_2O$ phase (Cantrell et al., 2013). The authors prepared three reactors and a control with different saltstone sample compositions. All three reactors were composed of 45%, 45%, and 10% of blast furnace slag (BFS), fly ash (FA), and Portland cement (PC), respectively. However, ^{99}Tc content was altered in reactor first (0 µCi/kg), and kept similar in the reactors second and third (170 µCi/kg). The obtained data suggested that the solubility of $TcO_2.1.6H_2O$ acquired an equilibrium within 2 weeks with ~1.5×10^{-6} M^{99}Tc concentration. The starting redox potential (E_h) value was slightly below −100 mV, which lowered considerably between 0–14 d and almost stabilized below −400 mV by 20 d. The authors proposed that the concentrations of ^{99}Tc at equilibrium are expected to vary with $TcO_2.1.6H_2O$, as the saltstone pore fluid evolved over a time. Moreover, the solubility of $TcO_2 \cdot xH_2O$ can be dropped considerably due to lowered pH of the samples *via* carbonation over the times in an actual disposal scenario.

2.3 Solubility of Tc and Re from geopolymer and ceramic waste forms

Geopolymers and ceramic matrices have also been largely used for the incorporation and immobilization of various radionuclides. This section presents key contributions on the solubility/release of Tc and Re from geopolymer and ceramic waste forms. Pierce *et al.* reported an alkali alumino-silicate geopolymer, DuraLith geopolymer to encapsulate ^{99}Tc liquid radioactive waste (Pierce et al., 2010). The secondary waste simulant of the Hanford Tank Waste Treatment and Immobilization Plant was used to prepare the geopolymer monoliths and three methods developed for the U.S. Environmental Protection Agency (EPA) were applied to assess the stabilization of the DuraLith geopolymer. Diffusivity of ^{99}Tc was found to be as 3.76×10^{-12} cm^2/s and 9.93×10^{-9} cm^2/s, respectively, for 63 and 2 d cumulative leaching time in batch 1 batch 2 geopolymers. In addition, Xu et al. investigated the effect of blast furnace slag grades on fly ash based geopolymer waste forms (Xu et al., 2014). Ground granulated blast furnace slag (GGBFS) was used to improve the disadvantage of the fly ash based geopolymer and was classified into three grades, 80, 100, and 120. The authors prepared geopolymer mixed with different grades of GGBFSs using the Hanford secondary waste (HSW) simulants spiked by Re. The toxicity characteristic leaching procedure (TCLP) was also applied for the leaching test on fly ash geopolymer waste forms after 28 d of curing at room temperature. Based on the results, the authors suggested that all heavy metals and toxic elements present in the HSW simulant can be more efficiently immobilized by the geopolymer waste forms than Re.

Neeway et al. investigated ^{99}Tc (Re used as surrogate) and I solubility from a sodalite-bearing ceramic waste form using single-pass-flow-through (SPFT) tests (Neeway et al., 2016). The granular fluidized bed steam reforming (FBSR) materials were derived from non-radioactive Hanford low-activity waste (LAW) simulant, radioactive LAW simulant, and the actual radioactive Hanford waste from Tank SX-105. The release rate of Re was determined in the range between 16×10^{-4} g/m^{2}d and 24×10^{-4} g/m^{2}d, which is up to 3 times larger than that of the network-forming elements (Na, Al, and Si). Moreover, the release of Re, I, and ^{99}Tc from the FBSR samples exhibited similar behavior. Based on results, the authors presumed that the solubility of Re and ^{99}Tc was controlled by the mineral phase (sodalite), which was produced during the FBSR process and incorporated Re into the cage structure of the mineral.

Hartmann et al. investigated the crystallographic and hydrodynamic data of ^{99}Tc-based ceramic waste form (Hartmann et al., 2014). Pyrochlore ($Nd_2Tc_2O_7$), perovskite ($SrTcO_3$), and layered perovskite (Sr_2TcO_4) were synthesized using anhydrous crystalline TcO_2. Chemical durability of $Nd_2Tc_2O_7$ pyrochlore was measured and compared with ^{99}Tc containing borosilicate glass in close compliance with ASTM C1220. Pyrochlore was insufficiently sintered and did not produce ceramic, however, the specific weight loss of the porous $Nd_2Tc_2O_7$ was determined as 1.48×10^{-7} g/mm^{2}d; lower than that of the ^{99}Tc-containing borosilicate glass (6.43×10^{-7} g/mm^{2}d). Moreover, the relative ^{99}Tc-release was evaluated as 0.67% for $Nd_2Tc_2O_7$ pyrochlore, compared to 1.026 for the ^{99}Tc- containing borosilicate glass.

Alekseeva et al. reported the chemical stability (the leaching tests) of the phosphate-based ceramic ($NaRe_2(PO_4)_3$) produced by spark plasma sintering (Alekseeva et al., 2021). In this study, the authors used Re as a surrogate of ^{99}Tc. The leaching experiments were conducted for 28 d in distilled water at room temperature under the static mode. The Re-leaching rate was evaluated as 1.3×10^{-5} g/cm^{2}d after 28 d. In another approach, Singh et al. demonstrated the immobilization and leaching behavior of ^{99}Tc from magnesium potassium phosphate (MKP) ceramics using $SnCl_2$ as a reducing agent (Singh et al., 2006). The designed MKP ceramic waste forms were characterized by XRD and SEM-EDX. Based on results, the authors proposed that ^{99}Tc could be immobilized in a tetravalent state (Tc(IV)) in MKP ceramics because of reducing environment and microencapsulation in the ceramic matrix. The leaching tests were performed using PCT method for 36% elution-loaded waste forms. ^{99}Tc-leaching rate was evaluated between 1.1×10^{-3} g/m^{2}d and 8.5×10^{-3} g/m^{2}d at ambient temperature (25°C), in agreement with ASTM C 1285-94.

3 Conclusion and perspective

In summary, this mini review highlights and summarizes some of the key developments on solubility and release of ^{99}Tc and Re (surrogate of ^{99}Tc) from glass, cement, geopolymer, and ceramic waste forms using different leaching test methods and experimental conditions. In the section two (2) of this mini review, we emphasize on the leaching/release and retention capacity of ^{99}Tc and Re immobilized in these waste forms under various physicochemical testing parameters and geochemical conditions. In section 2.1, we presents solubility and leaching of Re and Tc from glass waste forms. Section 2.2. Discusses the solubility of Tc and Re from cementitious waste forms, whereas, section 2.3. Describes a few (key) contributions on solubility of Tc and Re from geopolymer and ceramic waste forms. In order to impede the solubility and release of immobilized ^{99}Tc from various waste forms disposed in underground repository and to minimize the mobility of ^{99}Tc in environment/geosphere, future studies and researches (both experimental and theoretical approaches) should be focused on to acquire a wide range of datasets (at different testing conditions) necessary for the design of robust and durable waste forms. This may include more fundamental structural information of candidate waste forms using a various advanced techniques, such as HRTEM, EXAFS, etc. By establishing a comprehensive database for relevant waste forms, it will be easier to design and select most suitable candidates for Re/Tc immobilization. We believe that this mini review will be beneficial to the readers to understand the solubility and release behavior of ^{99}Tc from aforementioned waste forms and to correlate its migration in environment under various geochemical conditions.

Author contributions

BKS, JK, DP, and KK contributed in writing and WU supervised this mini review. All authors discussed, finalized the contents to the article, and approved the submitted version.

Funding

This work was supported by the Institute for Korea Spent Nuclear Fuel (iKSNF) and National Research Foundation (NRF) of Korea grant funded by the Korea government (Ministry of Science and ICT, MSIT) (No. 2021M2E1A1085202).

Conflict of interest

The authors declare that the research was conducted in the absence of any commercial or financial relationships that could be construed as a potential conflict of interest.

Publisher's note

References

Alekseeva, L., Nokhrin, A., Orlova, A., Boldin, M., Lantcev, E., Murashov, A., et al. (2021). NaRe2(PO4)3 phosphate-based ceramic with kosnarite structure as a matrix for technetium immobilization. arXiv preprint arXiv:2111.12973 https://arxiv.org/abs/2111.12973 (Accessed November 25, 2021).doi:10.48550/arXiv.2111.12973

Bibler, N., and Jurgensen, A. (1987). Leaching Tc-99 from SRP glass in simulated tuff and salt groundwaters. *MRS Online Proc. Libr. Opl.* 112, 585. doi:10.1557/PROC-112-585

Cantrell, K. J., and Williams, B. D. (2013). Solubility control of technetium release from Saltstone by TcO2· xH2O. *J. Nucl. Mat.* 437 (1-3), 424–431. doi:10.1016/j.jnucmat.2013.02.049

Danilov, S. S., Frolova, A. V., Kulikova, S. A., Vinokurov, S. E., Maslakov, K. I., Teterin, A. Y., et al. (2021). Immobilization of rhenium as a technetium surrogate in aluminum iron phosphate glass. *Radiochemistry* 63 (1), 99–106. doi:10.1134/s106636222101015x

Donald, I., Metcalfe, B., and Taylor, R. (1997). The immobilization of high level radioactive wastes using ceramics and glasses. *J. Mat. Sci.* 32 (22), 5851–5887. doi:10.1023/A:1018646507438

Duckworth, S., Gaona, X., Castaño, D., Park, S., Altmaier, M., and Geckeis, H. (2021). Redox chemistry, solubility and hydrolysis of Re in reducing aquatic systems. Thermodynamic description and comparison with Tc. *Appl. Geochem.* 132, 105037. doi:10.1016/j.apgeochem.2021.105037

El-Kamash, A. M., El-Naggar, M. R., and El-Dessouky, M. I. (2006). Immobilization of cesium and strontium radionuclides in zeolite-cement blends. *J. Hazard. Mat.* 136, 310–316. doi:10.1016/j.jhazmat.2005.12.020

Faiz, Z., Fakhi, S., Bouih, A., Outayad, R., Benkdad, A., and Hannache, H. (2017). Leaching study of cesium from spent ion-exchange resins and Portland cement package. *Int. J. Environ. Sci. Technol.* 14, 1019–1026. doi:10.1007/s13762-016-1203-0

Goo, J. Y., Kim, B. J., Kang, M., Jeong, J., Jo, H. Y., and Kwon, J. S. (2021). Leaching behavior of cesium, strontium, cobalt, and europium from immobilized cement matrix. *Appl. Sci.* 11 (18), 8418. doi:10.3390/app11188418

Hartmann, T., and Alaniz-Ortez, I. J. (2014)., .Fabrication and chemical durability of ceramic technetium-based pyrochlores and perovskites as potential waste forms, *Adv. Sci. Technol.*, 94. Trans Tech Publications Ltd, 85–92. doi:10.4028/www.scientific.net/AST.94.85

Jantzen, C. (2011). “Development of glass matrices for high level radioactive wastes,” in *Handbook of advanced radioactive waste conditioning technologies* (Elsevier), 230–292. Chennai, Tamil Nadu. doi:10.1533/9780857090959.2.230

Kim, D., and Kruger, A. A. (2018). Volatile species of technetium and rhenium during waste vitrification. *J. Non-Cryst. Solids* 481, 41–50. doi:10.1016/j.jnoncrysol.2017.10.013

Klein, E., Hardie, S. M., Kickmaier, W., and McKinley, I. G. (2021). Testing repository safety assessment models for deep geological disposal using legacy contaminated sites. *Sci. Total Environ.* 776, 145949. doi:10.1016/j.scitotenv.2021.145949

Lemmens, K., and Wang, L. (1992). The leaching of Pu, Am, Np and Tc from high-level waste glasses in clay media. *MRS Online Proc. Libr. Opl.* 294, 147. doi:10.1557/PROC-294-147

Meena, A. H., and Arai, Y. (2017). Environmental geochemistry of technetium. *Environ. Chem. Lett.* 15 (2), 241–263. doi:10.1007/s10311-017-0605-7

Neeway, J. J., Qafoku, N. P., Williams, B. D., Snyder, M. M., Brown, C. F., and Pierce, E. M. (2016). Evidence of technetium and iodine release from a sodalite-bearing ceramic waste form. *Appl. Geochem.* 66, 210–218. doi:10.1016/j.apgeochem.2015.12.017

Pierce, E. M., Cantrell, K. J., Westsik, J. H., Parker, K. E., Um, W., Valenta, M. M., et al. (2010). *Secondary waste form screening test results—cast stone and alkali alumino-silicate geopolymer (No. PNNL-19505).* Richland, WA, US: Pacific Northwest National Lab.PNNL. doi:10.2172/989447

Pirlet, V., Lemmens, K., and Van Iseghem, P. (2004). Influence of the near-field conditions on the mobile concentrations of Np and Tc leached from vitrified HLW. *MRS Online Proc. Libr. Opl.* 824. doi:10.1557/PROC-824-CC7.5

Pirlet, V., Lemmens, K., and Van Iseghem, P. (2002). Leaching of Np and Tc from doped nuclear waste glasses in clay media: The effects of redox conditions. *MRS Online Proc. Libr. Opl.* 713, JJ13.6. doi:10.1557/PROC-713-JJ13.6

Pyo, J.-Y., Lee, C. W., Park, H.-S., Yang, J. H., Um, W., and Heo, J. (2017). Tellurite glasses for vitrification of technetium-99 from pyrochemical processing. *J. Nucl. Mat.* 493, 1–5. doi:10.1016/j.jnucmat.2017.05.052

Santikari, V. P., Witmer, M., Murdoch, L. C., Kaplan, D. I., and Powell, B. A. (2022). Leaching and transport of technetium from reducing cementitious waste forms in field lysimeters. *Sci. Total Environ.* 841 , 156596. doi:10.1016/j.scitotenv.2022.156596

Simner, S., Coutelot, F., Chang, H., and Seaman, J. (2017). Technetium leaching from cementitious materials. *MRS Adv.* 2 (13), 717–722. doi:10.1557/adv.2017.35

Singh, B. K., Hafeez, M. A., Kim, H., Hong, S., Kang, J., and Um, W. (2021). Inorganic waste forms for efficient immobilization of radionuclides. *ACS ES&T Eng.* 1 (8), 1149–1170. doi:10.1021/acsestengg.1c00184

Singh, D., Mandalika, V. R., Parulekar, S. J., and Wagh, A. S. (2006). Magnesium potassium phosphate ceramic for ^{99}Tc immobilization. *J. Nucl. Mat.* 348 (3), 272–282. doi:10.1016/j.jnucmat.2005.09.026

Stefanovsky, S. V., Prusakov, I. L., Stefanovsky, O. I., Kadyko, M. I., Averin, A. A., Makarenkov, V. I., et al. (2019). The structure of rhenium containing sodium alumino (iron) phosphate glasses. *Int. J. Appl. Glass Sci.* 10 (4), 479–487. doi:10.1111/ijag.13476

Um, W. (2018). “^{99}Tc immobilization in various waste forms,” in Proceedings of the 10th International Symposium on Technetium and Rhenium-Science and Utilization, 185–207.

Xu, H., Gong, W., Syltebo, L., Izzo, K., Lutze, W., and Pegg, I. L. (2014). Effect of blast furnace slag grades on fly ash based geopolymer waste forms. *Fuel* 133, 332–340. doi:10.1016/j.fuel.2014.05.018

Xu, K., Hrma, P., Um, W., and Heo, J. (2013). Iron phosphate glass for immobilization of ^{99}Tc. *J. Nucl. Mat.* 441 (1-3), 262–266. doi:10.1016/j.jnucmat.2013.06.008

frontiers | Frontiers in Nuclear Engineering

TYPE Original Research
PUBLISHED 04 April 2023
DOI 10.3389/fnuen.2023.1118594

Dissolution behaviors of PuO_2(cr) in natural waters

Hye-Ryun Cho[1,2]*, Sangki Cho[1,2], Jueun Kim[3], Sangsoo Han[3], Hee-Kyung Kim[1] and Wooyong Um[3]

[1]Nuclear Chemistry Research Team, Korea Atomic Energy Research Institute, Daejeon, Republic of Korea, [2]Radiochemistry in Nuclear Science and Technology, University of Science and Technology, Daejeon, Republic of Korea, [3]Division of Advanced Nuclear Engineering, Pohang University of Science and Technology, Pohang, Republic of Korea

Check for updates

OPEN ACCESS

EDITED BY
Michael Ojovan,
Imperial College London,
United Kingdom

REVIEWED BY
Tomo Suzuki-Muresan,
UMR6457 Laboratoire de Physique
Subatomique et des Technologies
Associées (SUBATECH), France
Anna Romanchuk,
Lomonosov Moscow State University,
Russia

*CORRESPONDENCE
Hye-Ryun Cho,
hrcho@kaeri.re.kr

SPECIALTY SECTION
This article was submitted to Radioactive Waste Management,
a section of the journal
Frontiers in Nuclear Engineering

RECEIVED 07 December 2022
ACCEPTED 24 March 2023
PUBLISHED 04 April 2023

CITATION
Cho H-R, Cho S, Kim J, Han S, Kim H-K and Um W (2023), Dissolution behaviors of PuO_2(cr) in natural waters.
Front. Nucl. Eng. 2:1118594.
doi: 10.3389/fnuen.2023.1118594

PuO_2(cr) dissolution in natural water was investigated at 25°C and 60°C under atmospheric conditions. The concentration of Pu in solutions [Pu], was monitored for 1 year of reaction time. PuO_2(cr) dissolution in natural water reached a steady state within 2 months at 25°C. The [Pu] in groundwater and seawater at pH 8 were in the range of [Pu] = 0.9–34 and 3.4–27 nM, respectively. The [Pu] in concrete porewater (rainwater equilibrated with concrete) at pH 8.1–10.9 was in the range of 0.1–3.2 nM. The [Pu] and pH values of groundwater were similar to those of seawater samples having a high ionic strength. The measured [Pu] at equilibrium in all samples was higher than the calculated solubility curves for PuO_2(am, hyd). Experimental evidence is insufficient to confirm the oxidation state of Pu in solution and solid phases. However, the results of geochemical modeling indicate that PuO_2(am, hyd) and aqueous Pu(IV) species are dominant in natural water samples of this work. The dissolution behavior of PuO_2(cr) in natural waters is comparable to the oxidative dissolution of PuO_2(am, hyd) in the presence of PuO_2(coll, hyd). The dissolution of PuO_2 in groundwater decreased at higher temperatures, whereas the influence of temperature in seawater and porewater was not significant under these experimental conditions.

KEYWORDS

PuO_2, solubility, dissolution, groundwater, seawater, concrete porewater

1 Introduction

The safety of radioactive waste disposal facilities can be guaranteed by strictly isolating radionuclides (RNs) until their toxicity is reduced to the level of natural radioactivity (IAEA, 2011). RNs can dissolve in natural water, react with various ligands, adsorb on engineering and natural barriers (clays and rocks), diffuse through barriers, and migrate along the flow of natural water (Kim, 2006). The disposal environment in each country and region differs by waste type, radioactive level, selected engineering and natural barriers, and natural water properties (Choi et al., 2013; Grambow, 2016; Zhang et al., 2020). The underground disposal environment is generally expected to be at high temperatures, anaerobic, and reducing and neutral or weakly basic pH conditions. In near-surface disposal facilities, aerobic conditions should be considered and depending on the location of the repository, the potential intrusion of seawater should also be considered. The migration behavior of RNs through natural water is estimated by geochemical modeling using thermodynamic data, such as solubility, formation constants, enthalpy and entropy of reaction, and sorption/diffusion properties of RNs. Several thermodynamic databases (TDB) have been developed by OECD NEA (Ragoussi and Brassinnes, 2015), ThermoChimie (Giffaut et al., 2014), NAGRA/PSI

TABLE 1 Isotopic inventory of PuO_2(s) (ORNL, USA) and its activities.

Isotope	$T_{1/2}$ (y)*	1990	2020 (p.w.)	
		Atom (%)	Atom (%)	Activity (α, %)
^{238}Pu	87.7	0.001	0.0008	0.20
^{239}Pu	2.41 $\times 10^4$	99.75	99.7477	92.54
^{240}Pu	6.56 $\times 10^3$	0.061	0.0609	0.21
^{241}Pu (β)	14.3	0.178	0.0418	-
^{241}Am	432.6	0	0.1363	7.05
^{242}Pu	3.75 $\times 10^5$	0.012	0.0120	0.00
^{244}Pu	8.13 $\times 10^7$	0.0005	0.0005	0.00
Total	-	100	100	100

*IAEA Chart of Nuclides (https://www-nds.iaea.org).

(Thoenen et al., 2014), and JAEA (Kitamura, 2020) to increase the reliability of geochemical modeling.

Plutonium chemistry in aqueous solutions is complex because of the redox sensitivity of Pu (Romanchuk et al., 2016) and reliable thermodynamic data on the dissolution, redox reaction, hydrolysis, complexation, *etc.*, of Pu are insufficient compared to other actinides. The thermodynamic constants recommended by the latest NEA-TDB (Grenthe et al., 2020) are related to only 9, 16, 6, and 18 reactions in aqueous solutions for Pu(III), Pu(IV), Pu(V), and Pu(VI), respectively, which are much lower than the 25 and 127 data for U(IV) and U(VI), respectively. Various essential data for the geochemical modeling of Pu in natural water, such as the reactions of Pu(III-VI) with OH^-, CO_3^{2-}, and Cl^-, are summarized in Supplementary Table S1. Data on the dissolution of various Pu solids are insufficient compared to those on the formation of aqueous Pu species. Reaction enthalpy and entropy are scarce and study for determination of the values has recently been encouraged for the reliable estimation of chemical behaviors of Pu at high temperatures (Cho et al., 2022). The geochemical modeling of Pu in repository environments contains a relatively large uncertainty; therefore, site-specific investigation of the chemical behavior of Pu is often required for the safety assessment of radioactive waste disposal facilities.

In this work, the dissolution of PuO_2(cr) in natural water contacted with air was investigated and compared to the calculated solubility curves of various Pu hydroxides. Groundwater, seawater, and rainwater were collected in the vicinity of Gyeongju, Korea, where the disposal site for low- and intermediate-level radioactive waste is located. The dissolution of PuO_2(cr) in various natural waters was observed for 1 year at 25°C and 60°C under atmospheric pressure to evaluate geochemical behaviors of Pu in near-surface disposal environments.

2 Materials and methods

2.1 PuO_2(s) powder

PuO_2(s) powder was purchased from Oak Ridge National Laboratory (ORNL) in 1990, with ^{239}Pu (99.75 atom %) and used as received. Table 1 shows the certified Pu isotope inventory (atom %) for 1990 and half-life. As a result of decay, the isotopic content and relative alpha activity changed in 2020 (over 30 years) and are shown in Table 1. ^{241}Am accumulated over time owing to the beta decay of ^{241}Pu. The alpha particles generated by ^{241}Am-decay were simultaneously counted with those generated by ^{239}Pu using a liquid scintillation counter (LSC) with an α/β discriminator.

2.2 Preparation of natural water samples

Three types of natural waters were used to investigate the solubility of PuO_2(s): groundwater (GW), seawater (SW), and concrete porewater (PW, rainwater (RW) equilibrated with concrete). The collection and preparation processes are as follows: GW samples were collected at two locations in the Gyeongju area every 3 months in a year (set A–D), considering the domestic seasonal change, and equilibrated with crushed granite or sedimentary rocks collected at the same site. Thus, 16 GW samples were prepared. SW and RW were collected at four different times (set A–D) and treated with seabed soil and concrete, respectively. All solid phases (composition, see the Supplementary Table S2) were crushed and sieved to prepare a powder with particle size in the range of 0.075–0.15 mm and added to natural water samples with a solid-liquid ratio of 10 g/L. Equilibrium was achieved while in contact with air. The sample reached a steady state after 1 month, which was confirmed by monitoring the pH. The solid phase was separated by filtration using a membrane filter with a pore size of 0.45 μm. The prepared natural water samples were stored in a refrigerator before use. The chemical compositions of the natural water samples were measured by inductively coupled plasma mass spectrometry (ICP-MS), inductively coupled plasma optical emission spectroscopy (ICP-OES), ion chromatography (IC), and a total organic carbon (TOC) analyzer in a creditable analytical laboratory.

2.3 Preparation of Pu samples

Pu samples were prepared by adding PuO_2(s) powder into natural water. A total of 30 mL of GW samples and 60 mL of SW and PW samples were prepared in plastic bottles (polyethylene). About 0.5–1.0 mg of PuO_2(s) powder was collected using a disposable pipette with a tip of ~1 mm (see Supplementary Figure S1A), and added to the natural water samples (see Supplementary Figure S1B). The end of the disposable pipette used for collecting PuO_2(s) powder was cut and placed in a sample bottle, which was not removed until the solubility measurement was completed. Black PuO_2(s) powder settled down to the bottom of the sample bottle containing natural water (see Supplementary Figure S1C). All samples were stored in a constant temperature chamber at 25°C, and the concentration of Pu ([Pu]) in natural water was periodically measured for 1 year. Then, four of the GW samples and one of the SW and PW samples (set A) were placed in a constant temperature chamber at 60°C to observe the dissolution of PuO_2(s) at higher temperatures. An aliquot of the supernatant was used for the determination of [Pu] which was quickly sampled outside the temperature-controlled chamber at 25°C and 60°C without phase separation. Phase separation by filtration could not be applied because of the small volume of the sample solution, which was limited by the amount of stocked $PuO_2(s)$ powder (~20 mg). While trying not to disturb the samples to prevent the floating of the settled $PuO_2(s)$, 0.5 mL of supernatant in GW samples and 1.0 mL in SW and PW samples were collected into LSC vials in triplicate.

2.4 pH, redox potential, and conductivity measurements

The pH of the natural water before and after equilibration with $PuO_2(s)$ was measured using a glass combination pH electrode (8103BNUWP Ross Ultra, Orion) calibrated using pH buffers (pH 4.01, 7.00, and 10.01, Orion) at room temperature (23°C ± 2°C). The redox potential values were measured using a combination ORP electrode (InLab® Redox, Mettler Toledo). The measured potential values were converted to E_h (*versus* the standard hydrogen electrode, SHE) by correcting the potential of the Ag/AgCl reference electrode. Conductivity (EC) was measured using a conductivity cell (TetraCon 925, WTW) calibrated with 0.001–1.0 M KCl solutions.

2.5 Liquid scintillation counter

A liquid scintillation counter (Tri-Carb4910TR, Packard) with an α/β discriminator was employed to determine the [Pu]. An aliquot of the natural water sample was mixed with 15 mL of LSC cocktail (Ultima Gold AB, PerkinElmer). The activity of ^{239}Pu was 92.54% of the total alpha activity (7.05% for ^{241}Am), based on the certified isotope inventory of Pu, as shown in Table 1. In considerations of the probable solubility difference between Pu and Am, the ratio of ^{239}Pu to total alpha activity in natural water samples were checked at the end of experiments by alpha spectrometry (Alpha analyst, CANBERRA). The ratio in 4 GW samples and a PW sample was 0.95 ± 0.01 and 0.92, respectively, which is comparable to the theoretical value (0.9254) in the PuO_2 solid state. Although, it was difficult to confirm the ratio in the SW samples due to the high salts contents that interfere the detection of the alpha emissions [Pu] in all the GW, PW, and SW samples were calculated using the theoretical ratio (0.9254) from the LSC measurement. The limit of detection (LOD) was calculated using the minimum detectable activity (MDA, Bq/mL), as in Eq. 1 (Currie, 1968),

$$\mathrm{MDA} = \frac{2.71 + 4.65 \times \sqrt{B \times t_B}}{T \times V} \tag{1}$$

where B (cps) is the count rate of the background material, t_B and T (s) are the measurement times for the background and sample, respectively, and V (mL) is the sample volume.

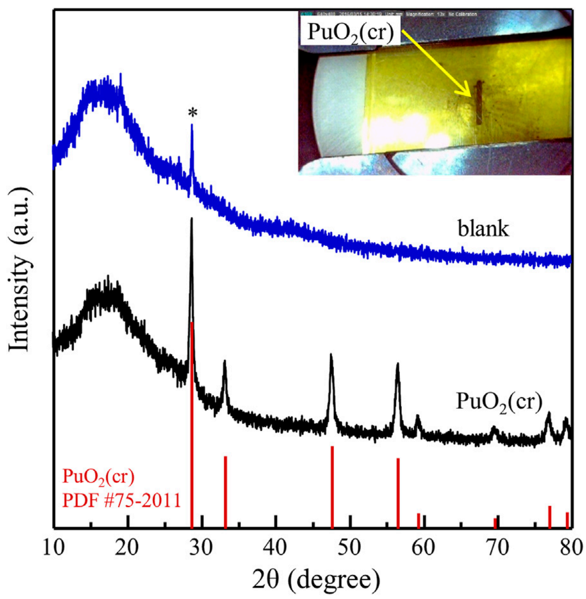

FIGURE 1
XRD spectrum of $PuO_2(cr)$ measured before solubility study. XRD spectrum of the blank sample without Pu is shown for comparison.

2.6 X-ray diffraction measurement

A shielded XRD system (D8 Advanced, Bruker AXS) with a modified microbeam was used to confirm the crystallinity of the $PuO_2(s)$ powder. The instrumentation has been described in detail elsewhere (Park et al., 2013). An appropriate amount of $PuO_2(s)$ powder was placed on an acrylic holder and covered with a polyimide film. The powder XRD spectra were obtained by step scanning in the range of 10°–80° (2θ) with a step interval of 0.02° (2θ) for 25 s per count; the total measurement time was approximately 24 h. The measured XRD spectrum of the $PuO_2(s)$ powder was compared with the reported powder diffraction file (PDF) (Gates-Rector and Blanton, 2019).

3 Results and discussion

3.1 $PuO_2(cr)$ characterization

Figure 1 shows the XRD data of the PuO_2 powder compared to that of a blank sample prepared with an acrylic holder covered with a polyimide film without Pu. Only one peak at approximately 28.7° (marked with an asterisk), corresponding to the applied film material, was observed. The picture in the inset of Figure 1 shows the upper side of the prepared sample, where the black PuO_2 powder is located in the center, with a size of 0.5 × 4 mm^2. The collected XRD pattern of PuO_2 was identical to the reported data for $PuO_2(cr)$ (PDF #75–2011) and no additional peaks were observed.

TABLE 2 Physical and chemical properties of representative natural water samples before and after equilibrated with the selected solid phase.

Set	Properties	Raw sample				Samples equilibrated with selected solid powders					
		GW1	GW2	SW	RW	GW1F	GW2F	GW1S	GW2S	SW	PW
A	pH	7.55	7.93	8.15	5.88	7.56	8.14	7.95	7.97	7.94	11.83
	E_h (mV)	220	213	134	303	134	140	147	148	135	48
	EC (μS/cm)	273.3	243.3	47,650	30.0	232.9	235.8	217.2	212.0	47,990	836.7
	Major (mg/L)										
	TOC	0.46	0.54	0.94	1.89	3.82	3.94	4.33	3.97	5.39	3.71
	Mg	6.04	5.91	1,189	0.59	6.35	6.15	6.13	5.65	1,208.5	0.07
	Na	19.90	21.25	10,103	5.09	21.71	22.19	22.11	22.46	10,084	8.22
	K	2.13	2.79	378.18	0.28	4.67	4.52	4.88	3.94	385.0	4.36
	Ca	11.03	13.96	361.63	0.33	13.49	16.62	10.19	10.97	401.5	54.77
	Si	19.79	24.93	n.d	n.d	17.02	13.20	3.29	4.5	n.d	4.52
	Cl	13.43	14.40	15,283	7.94	14.54	15.18	15.16	15.31	20,356	9.20
	SO_4	27.68	9.30	2,614	2.11	29.82	10.05	30.26	9.97	3,346	5.52
	HCO_3	42.9	52.3	67.3	3.2	47.2	59.4	37.7	50.5	70.3	97.5
	Minor (μg/L)										
	Al	10.69	7.15	0.53	4.28	3.54	2.60	4.83	1.92	7.70	1,136.7
	Li	4.96	6.78	141.78	0.09	8.36	7.67	12.46	7.10	134.36	4.75
	Sr	0.79	1.53	6,282.92	2.72	54.67	45.43	34.24	30.76	5,431.6	160.27

*n.d.: not detected.

3.2 Natural water characterization

Representative data (set A) for raw natural water samples are listed in Table 2, which include two groundwater samples (GW1 and GW2) collected at different locations, seawater (SW), and rainwater (RW). A pH of 8 was measured for both GW and SW, whereas that of RW was weakly acidic (pH 6). The redox potentials for all natural waters were confirmed to be weak oxidation conditions. A high conductivity of SW containing excessive amounts of salt, such as NaCl and $MgCl_2$ was found. GW and RW contained various ions of Mg, Na, K, Ca, Si, Cl, and SO_4^{2-} at the mg/L level, and Al, Li, and Sr at the μg/L level. The properties of natural water were changed by equilibrating it with the selected solid powder, as shown in Table 2. GW1 samples equilibrated with fractured granite (F) and sedimentary (S) rocks were named GW1F and GW1S, respectively. The pH of GW and SW remained at pH 8, whereas the pH of RW increased from 6 to 12 after equilibrating it with concrete (PW). An increase in the concentrations of Ca, Si, Al, *etc.*, in PW, was observed because of the leaching of components present in the concrete. Because GW and SW were already in equilibrium with the surrounding minerals and rocks at the time of collection, the change in the chemical composition due to the additional equilibrium step with the selected solids was not significant. The TOC was increased by the solid-liquid equilibrium in all natural waters.

The physicochemical properties of natural water samples do not critically depend on the domestic seasonal change (see data for set B–D in Supplementary Table S3). The pH of GW and SW was in the range of 7.6–8.2 and 7.8–7.9, respectively, whereas the pH of PW was in the range of 11.6–11.9. Although the E_h values were slightly reduced after the reaction with solids, they maintained oxidizing conditions. The conductivity of GW and SW did not change, whereas that of PW increased approximately 10 times after the reaction with the concrete. The TOC of GW, SW, and PW increased to 1.49–4.33, 1.95–5.39, and 3.71–16.08 mg/L, respectively, and the highest TOC was observed for the PW sample. The major cation concentrations in GW were in the order of Na > Ca > Si > K > Mg, and those in SW were in the order of Na > Mg > K ≈ Ca. Al, Ca, and Si, which are the major components of the concrete, were dominant in the PW samples. In the case of anion species, $HCO_3 > SO_4 \approx Cl$ are present in the GW and PW, and $Cl > SO_4 > HCO_3$ in the SW.

3.3 Dissolution behavior of PuO_2(cr) at 25°C

Figure 2 shows [Pu] as a function of reaction time at 25°C. Each data point is the average of the measurements in triplicate and error bar means standard deviation of triplicate (error bars (≤±0.05) were omitted when they are smaller than the symbol size). The measured data for the six samples (set A) listed in Table 2 are represented in Figure 2 (data for set B–D, see Supplementary Figure S2). The dashed lines in Figure 2 indicate the LOD of 1.3×10^{-10} M for 0.5 mL of GW samples in Figure 2A and 0.6×10^{-10} M for 1.0 mL of SW and PW samples

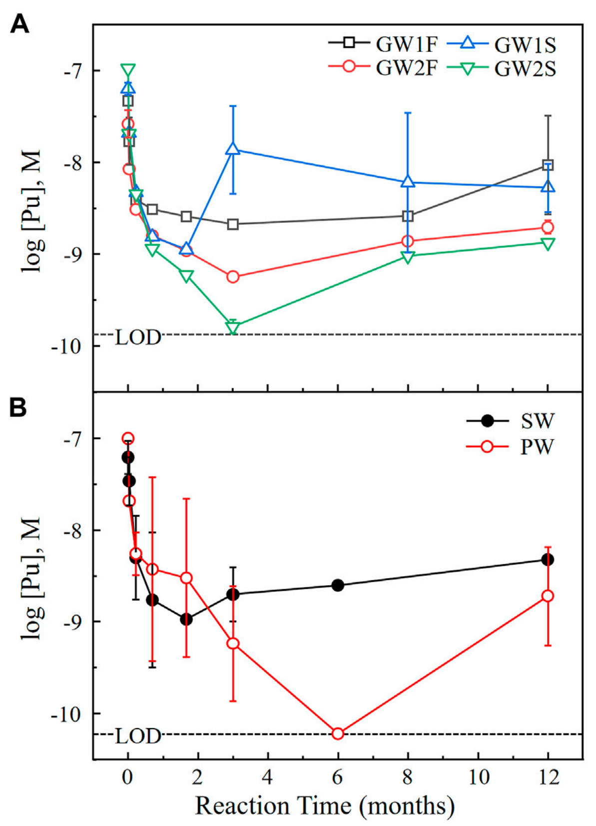

FIGURE 2
Dissolution behaviors of PuO_2(cr) at 25°C in **(A)** groundwater and **(B)** seawater and concrete porewater (set A) as a function of the reaction time. The dashed lines indicate the LOD by LSC under the given experimental conditions.

in Figure 2B. A rapid decrease of [Pu] was observed at the beginning of the experiments in all samples. This was caused by the highly reactive site on the surface of PuO_2(cr) powder made during manufacturing process that would dissolve very quickly in aqueous solutions. The high initial [Pu] decreased with the precipitation of Pu in a solubility-limited solid phase in equilibrium with the natural waters. All samples reached a steady state after 1–2 months of reaction time. After reaching equilibrium, the measured [Pu] was relatively high in a few samples. Such sudden change could be an experimental error caused by incomplete phase separation. Small PuO_2(cr) particles or colloids may have been included during the sampling of 0.5 or 1.0 mL of supernatant without filtration. Although the measured [Pu] at the same reaction time were significantly different in a few samples, all measured values had been averaged without excluding any data. These samples showed large errors as shown in Figure 2 for GW1S and PW samples.

As shown in Figure 2A, the dissolution of PuO_2(cr) in most GW samples reached equilibrium after 2 months. The characteristics of the GW samples did not differ depending on the sampling season, location, and type of equilibrium solid, as shown in Tables 2 and Supplementary Table S3, and no significant correlation was observed in the measured [Pu] in the various GW samples. The measured [Pu] after 3 months were in the range of 0.2–30 nM, and after 1 year of reaction time were 0.9–34 nM (see Figure 2A and Supplementary Figure S2A). The dissolution of PuO_2(cr) in the SW samples reached equilibrium after 2 months, and [Pu] at 1 year were 3.4–27 nM (see Figure 2B and Supplementary Figure S2B). As shown in Figure 2B (open circles), the lowest solubility of PuO_2(cr) was observed for PW, and some measured [Pu] were below the LOD at reaction times longer than 1 month. The measured [Pu] at 1 year in PW were 0.10–3.2 nM (LOD = 0.06 nM, see Figure 2B and Supplementary Figure S2C). All measured [Pu] at 1 year were listed in Table 3 (set A) and Supplementary Table S4 (set B–D).

To check whether the characteristics of natural water changed during the PuO_2(cr) dissolution study, the pH and conductivity of the samples were measured at the end of the experiments. GW samples in the pH range of 7.6–8.2 maintained a pH of 8 after the dissolution of PuO_2(cr). An initial conductivity of 163–390 μS/cm for the GW samples did not significantly change and was in the range of 217–338 μS/cm. The conductivity of SW was slightly changed from 45,900–59,500 to 46,900–50,700 μS/cm at constant pH. The pH and conductivity of the PW decreased from 12 to 8.1–10.9 and 484–1,000 to 120–370 μS/cm, respectively. For the six samples (set A), the measured pH and conductivity values after 1 year with PuO_2(cr) at 25°C are listed in Table 3 (pH of set B–D, see Supplementary Table S4). To understand the pH change of PW, the pH of the PW sample stored for the same period in a refrigerator without PuO_2(cr) was measured, which decreased from 11.6–11.9 to 9.4–10.7. As described in the experimental section, the concrete powder was removed from the equilibrated PW solution by filtration and stored in contact with air. CO_2 present in the ambient air continuously dissolves into the alkaline PW sample, the concentration of dissolved inorganic carbon increases, and therefore, the pH decreases over time (Beuvier et al., 2014). The decrease in conductivity of PW indicates a reduced concentration of dissolved ions, which could be induced by precipitation at lower alkalinity. The major leached components from the concrete in PW were Ca, Si, Al, and CO_3^{2-} ions at pH 12. The conductivity could be reduced owing to the formation of precipitates at neutral pH conditions; however, the change of dissolved ion concentration was not confirmed because the residual amount of the sample was not sufficient at the end of the experiments.

Figure 3 shows the measured [Pu] at 1 year in natural waters compared with the solubility curves of Pu hydroxide calculated based on the thermodynamic data listed in Supplementary Table S1. The measured pH and [Pu] were displayed for 16 GW (○), 4 SW (×), and 4 PW (□) samples. As mentioned above, the pH in PW samples was distributed in a relatively wide range of 8.1–10.9 and the [Pu] was 0.1–3.2 nM, which is lower than that of SW or GW samples. The pH value of most GW samples was maintained at approximately 8, and 4 GW samples (set C) were acidified to pH 7.1–7.4. The range of pH and [Pu] for GW and SW samples were similar.

The solid lines in Figure 3 were calculated using the reported solubility products of PuO_2(am, hyd), $Pu(OH)_3$(am), PuO_2OH(am), and $PuO_2(OH)_2$(am, hyd) and formation constants for aqueous Pu-OH species (I = 0 M, at 25°C) listed

TABLE 3 Representative [Pu], pH and conductivity of natural water samples with PuO_2 measured after 1 year of reaction time at 25°C and 60°C, respectively.

Sample	With PuO_2 after 1 year at 25°C			With PuO_2 after 1 year at 60°C	
	pH	EC (μS/cm)	[Pu] (mol/L)	pH	[Pu] (mol/L)
GW1F	8.02	289	1.4×10^{-8}	4.23	2.9×10^{-9}
GW2F	8.13	301	2.0×10^{-9}	5.00	1.9×10^{-10}
GW1S	7.88	275	5.9×10^{-9}	3.32	1.6×10^{-6}
GW2S	8.11	273	1.3×10^{-9}	3.59	5.5×10^{-10}
SW	7.57	46,900	4.7×10^{-9}	7.81	2.8×10^{-9}
PW	9.10	120	3.2×10^{-9}	6.70	1.8×10^{-9}

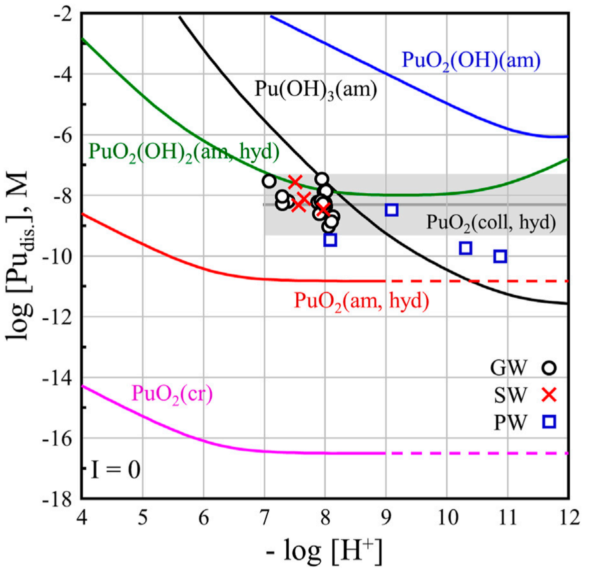

FIGURE 3
Solubility of PuO_2(cr) powder in natural water (GW, SW, and PW) were compared with the calculated solubility curves for hydroxide and oxide compounds of Pu(III-VI).

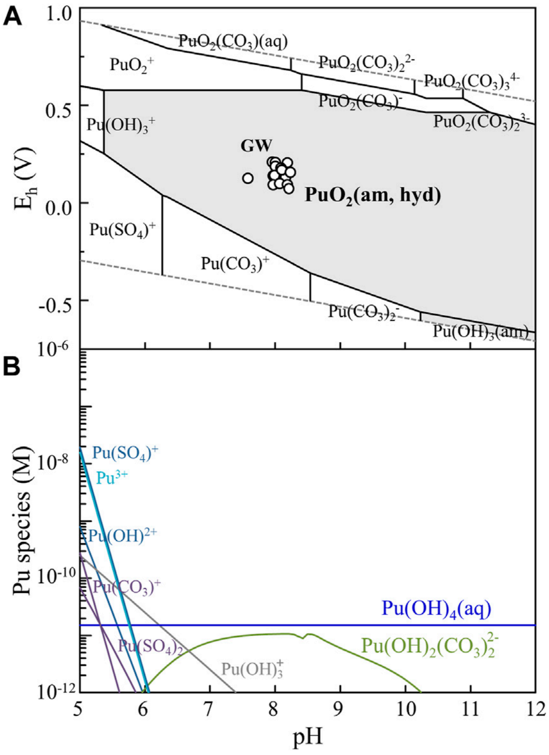

FIGURE 4
(A) Pourbaix diagram of Pu ([Pu] = 10^{-10} M) was a result of geochemical modeling at the GW1F condition (set A) and displayed with the measured E_h and pH values of GW (O) listed in Table 2 and Supplementary Table S3. The dashed lines indicate the boundaries of water stability: upper and lower limits for the oxidation and reduction of water, respectively. **(B)** Species distribution at [Pu] of 10^{-6} M in the GW1F sample shows that low concentrations of $Pu(OH)_4$(aq) and $Pu(OH)_2(CO_3)_2^{2-}$ species as dominant in this experimental condition. Geochemical modeling was carried out using Geochemist's workbench based on ThermoChimie v. 11a TDB.

in Supplementary Table S1. Because reliable logK values of $Pu(OH)_2^+$ and $Pu(OH)_3$ species have not been reported, −15.1 and −26.2 of $Am(OH)_2^+$ and $Am(OH)_3$ species were applied, respectively (Grenthe et al., 2020). The ionic strength of GW and PW samples was as low as a few millimoles, so it can be compared with the calculated solubility curve using thermodynamic data at the standard state (Grenthe et al., 2020). However, because the ionic strength of the SW samples was high (0.5 M), a direct comparison of the SW samples' results with the solubility curves shown in Figure 3 is not possible. The dissolution behaviors of PuO_2(cr) in SW could be related to the estimated solubility curves of Pu hydroxide at a 0.5 M ionic strength ([Cl^-] = 0.5 M) based on the specific ion interaction theory (SIT). However, the ion interaction coefficients for the Pu(III-VI) ions and Pu-OH species with Cl^- ions, such as ε(Pu^{4+}, Cl^-), ε($Pu(OH)^{3+}$, Cl^-), ε(PuO_2^{2+}, Cl^-), *etc.*, have not yet been reported (Grenthe et al., 2020). Generally, the solubility of actinide compounds increases at higher concentrations of [Cl^-] in NaCl, $MgCl_2$, and $CaCl_2$ solutions (Altmaier et al., 2013). The measured [Pu] in SW was comparable to the increased solubility curve of Pu solids at I = 0.5 M.

In this work, $PuO_2(cr)$ was applied to investigate dissolution in various natural waters. The solubility product of $PuO_2(cr)$, $\log K^{\circ}_{sp} = -64.0 \pm 0.5$, is included in ThermoChimie TDB v. 11a.[1] The calculated solubility curve for $PuO_2(cr)$ shown in Figure 3, which deviates significantly from the measured values. The solubility product of $PuO_2(cr)$ was calculated using Gibb's free energy of formation $\Delta_f G^{\circ}_m$ for the well-defined crystalline phase. As mentioned in the literature (Grenthe et al., 2020), the theoretical stability of $PuO_2(cr)$ can be evaluated using this value; however, it is difficult to interpret the dissolution behavior of $PuO_2(cr)$ in aqueous solutions. In our dissolution study of $PuO_2(cr)$ in natural water samples, a higher [Pu] than the solubility curve of PuO_2(am, hyd) was obtained for all the samples. This means that the crystallinity of $PuO_2(cr)$ was not maintained and probably converted to an amorphous solid phase. Amorphization by radiation effect has been reported for a few Pu solid phases such as Pu-oxalate and $PuF_4(cr)$ (McCoy et al., 2017; Corbey et al., 2021). Unfortunately, solid-phase characterization to confirm the transformation of solids could not be performed because of the limited amount of the remaining $PuO_2(s)$ in the samples after the solubility experiments.

Geochemical modeling was carried out in order to evaluate geochemical behaviors of Pu at the measured redox potentials under all the examined natural water conditions. A commercial software, Geochemist's Work Bench (GWB, standard, 17.0) was used for the modeling with ThermoChimie TDB v. 11a, which was updated with the latest NEA-TDB (Grenthe et al., 2020). Redox behavior, solubility limiting solid phase, and aqueous species distribution of Pu at natural water conditions were evaluated. For the modeling, the solubility product of $PuO_2(cr)$ was excluded, because it was too low to explain our experimental results. Under all natural water conditions, the solubility limiting solid phase was identified as PuO_2(am, hyd), and aqueous $Pu(OH)_4(aq)$, $Pu(OH)_2(CO_3)_2^{2-}$, and $Pu(OH)_3^{+}$ species was dominant in a pH of 7–12 (see Figure 4 for GW1F and Supplementary Figure S3 for SW and PW of sample set A, respectively). The pH and E_h of GW (○), SW (×), and PW (□) samples are shown in Figure 4A, Supplementary Figure S3A, S3C, respectively. Considering the thermodynamic data included in ThermoChimie TDB v. 11a, solid and aqueous species of Pu(IV) were dominant in the investigated natural water samples.

In all samples of GW, SW, and PW, the [Pu] was higher than the solubility curves of PuO_2(am, hyd) as shown in Figure 3. The initially settled black $PuO_2(s)$ remained until the end of experiments. The higher [Pu] at the present experimental condition where tetravalent Pu is dominant can be explained by the oxidative dissolution of PuO_2(am, hyd) in the presence of PuO_2(coll, hyd). The formation of PuO_{2+x}(am, hyd) during solubility measurement of PuO_2(am, hyd) in the presence of oxygen was reported by Neck *et al.* (Neck et al., 2007). They described that the (pe + pH) = 12.5 ± 1.2 at pH > 4 (Region C of the literature, see Supplementary Figure S4) can only be explained when considering the dominant colloidal PuO_2 in neutral and alkaline solution. The initial (pe + pH) value of natural water samples was in a range of 9.5–11.8 in this work, which is slightly lower than the Region C. Neck *et al.* (Neck et al., 2007) reported log[Pu] = −8.3 ± 1.0 in equilibrium with PuO_2(coll, hyd) in the neutral and basic pH ranges which is shown by the grey box in Figure 3. Dissolution behaviors of $PuO_2(cr)$ in various natural water are comparable to the solubility of the hydrated amorphous PuO_{2+x}(am, hyd) with the presence of hydrated PuO_2 colloids, PuO_2(coll, hyd). Due to the limited sample volumes, we were not able to perform phase separation to monitor the existence of colloidal Pu in our samples until the end of experiments. The GW samples (set B), SW and PW (set C) were stored at 25°C for 3-year, and the measured (pe + pH) values remained in a range of 12.9–13.4 at pH 7.7–8.1. The presence of colloidal Pu was confirmed by [Pu] analysis before and after ultrafiltration using a cellulose membrane filter (Amicon, Ultracel YM-10, 10 kD) which was rinsed with 6 mL of a sample solution. The results showed that most of Pu in the supernatant was colloidal Pu in GW and PW samples, and colloidal Pu was not found in SW (see Supplementary Table S5).

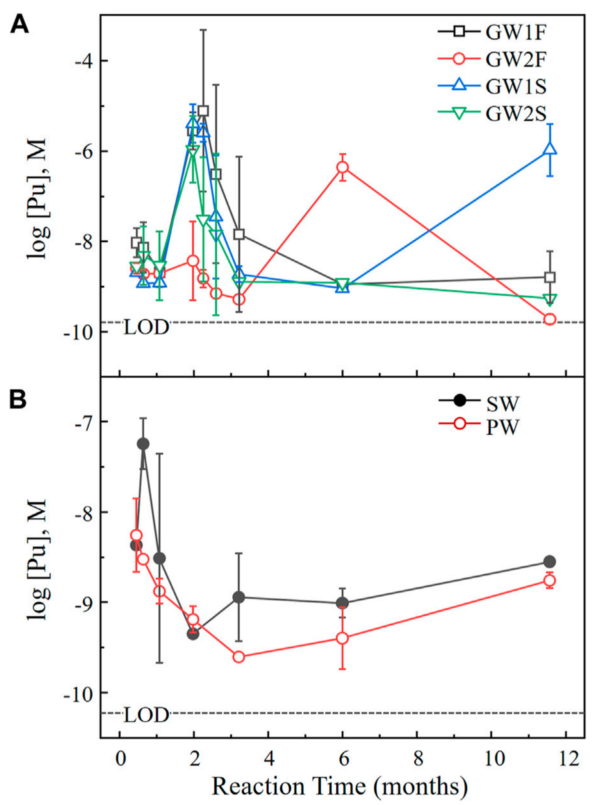

FIGURE 5
Dissolution behaviors of $PuO_2(cr)$ at 60°C in **(A)** groundwater and **(B)** seawater and concrete porewater (set A) as a function of the reaction time. The dashed lines indicate the LOD by LSC under the given experimental conditions.

3.4 Dissolution behavior of PuO_2 at 60°C

Among the natural water samples studied at 25°C, 4 GW, 1 SW, and 1 PW samples (set A) were selected to evaluate the dissolution behavior of PuO_2 at higher temperatures. Table 3 lists the pH and [Pu] of six samples measured before (at the end of the experiment at 25°C) and after 1 year of reaction time at 60°C. Figure 5 shows [Pu] as a function of reaction time at 60°C. Each data point is the average

---

[1] https://www.thermochimie-tdb.com

of the measurement for the 4 GW, 1 SW, and 1 PW samples in triplicate and error bar means standard deviation of triplicate (errors (≤±0.05) were omitted when smaller than symbol size). In the 4 GW samples [Pu] below 10^{-8} M observed at the initial time of reaction was dramatically increased to 10^{-5} M after 50 days, as shown in Figure 5A. Subsequently [Pu] gradually decreased over time. [Pu] in GW1F and GW2S reached a steady state after 6 months. At 1 year of the reaction time [Pu] was 2–10 times lower than the results at 25°C for GW1F, GW2F, and GW2S samples. The decrease of pH in GW samples was observed at 60°C. A significant change was observed in the GW1S sample, whose pH was 3.32 with a [Pu] of 1.6 μM. An increase in the [Pu] of the SW sample was observed at the beginning of the dissolution at 60°C, and then [Pu] gradually decreased. The reaction equilibrium was reached after 3 months, and [Pu] in the SW sample at higher temperatures was slightly decreased compared to the solubility of PuO_2 at 25°C. The pH 7.57 of the SW sample remained at pH 7.81 after 1 year at 60°C. In the PW sample, the measured [Pu] after 1 day at 60°C was 100 times higher than the last measured data at 25°C. The [Pu] continuously decreased over time and reached minimum after 3 months and then slowly increased until 1 year. The [Pu] in PW at 60°C was similar to or slightly lower than that measured at 25°C. The pH of the PW sample decreased from 9.10 to 6.70 during the 1-year experiment at 60°C.

The pH at 60°C significantly decreased in GW and PW, whereas no change in pH was observed in SW as shown in Table 3. Notably, the pH of GW samples at 60°C with a reaction time of 1 year dropped to 3.32–5.00, which was too low to consider because of equilibration with air. Actinide has been considered as a potential catalyst due to its electrical flexibility of 5 f-orbital and high reactivity in low oxidation states. The oxygen evolution reaction ($4OH^- \rightarrow O_2 + 2H_2O + 4e^-$) in alkaline solutions can occur by tetravalent actinides such as Th(IV) and U(IV), under mild conditions of the sample solution (Hu et al., 2019; Leduc et al., 2019). In this case, the reduction of Pu(IV) to Pu(III) would have occurred, but the change in the oxidation state in the liquid and solid phases of Pu could not be confirmed. The decrease in the pH of the PW samples is in the pH range, which can be interpreted as contact with air. No pH changes were observed in the SW samples. The biggest difference between the SW and GW/PW samples is the ionic strength (concentration of dissolved ions). It is considered that high concentrations of ions, such as Na^+, Mg^{2+}, Cl^-, and SO_4^{2-} caused different carbonate behaviors in the SW samples.

4 Conclusion

The dissolution behaviors of PuO_2(cr) in various natural waters were investigated, which is the basic parameter for the safety assessment of radioactive waste disposal facilities. The results were compared with geochemical modeling and estimated solubility curves of Pu hydroxides using a thermodynamic database. Groundwater, seawater, and concrete porewater were systematically prepared to consider various disposal environments. The concentration of dissolved Pu in three different natural waters that reached equilibrium with PuO_2(cr) was monitored at 25°C and 60°C in contact with air. The results at 25°C showed that the dissolution behaviors of PuO_2(cr) correspond to the oxidative dissolution of PuO_2(am, hyd) in the presence of PuO_2(coll, hyd). During the experimental period of 1 year, there was no significant change in the properties, such as pH, of the natural waters used in the experiments at 25°C. However, the results at 60°C are not conclusive, as the properties of the examined waters, in particular pH values, were considerably changed over time. To understand the dissolution behavior of Pu in natural waters at higher temperatures of the underground disposal environment, the influence of air contact should be excluded and high pressure should be considered.

Data availability statement

The original contributions presented in the study are included in the article/Supplementary Material, further inquiries can be directed to the corresponding author.

Author contributions

H-RC and WU defined the initial concept and experimental study. H-RC, H-KK, SC, SH, and JK performed experiments and evaluated the data. H-RC wrote the first draft of the manuscript, and all the authors wrote the sections and contributed to the revision and approval of the manuscript.

Funding

This study was supported by the Nuclear Research and Development Program of the National Research Foundation (NRF) of Korea (No. 2017M2A8A5014719) and the Institute for Korea Spent Nuclear Fuel and NRF of Korea (No. 2021M2E1A1085202).

Acknowledgments

The authors acknowledge the facility support from the KAERI Institutional Program (Project No. 521330-22).

Conflict of interest

The authors declare that the research was conducted in the absence of any commercial or financial relationships that could be construed as a potential conflict of interest.

Publisher's note

Supplementary material

The Supplementary Material for this article can be found online at: https://www.frontiersin.org/articles/10.3389/fnuen.2023.1118594/full#supplementary-material

References

Altmaier, M., Gaona, X., and Fanghänel, T. (2013). Recent advances in aqueous actinide chemistry and thermodynamics. *Chem. Rev.* 113, 901–943. doi:10.1021/cr300379w

Beuvier, T., Calvignac, B., Bardeau, J.-F., Bulou, A., Boury, F., and Gibaud, A. (2014). Quantification of the dissolved inorganic carbon species and of the pH of alkaline solutions exposed to CO_2 under pressure: A novel approach by Raman scattering. *Anal. Chem.* 86, 9895–9900. doi:10.1021/ac5025446

Cho, S., Kim, H.-K., Kim, T.-H., Cha, W., and Cho, H.-R. (2022). Thermodynamic studies on the hydrolysis of trivalent plutonium and solubility of $Pu(OH)_3$(am). *Inorg. Chem.* 61, 12643–12651. doi:10.1021/acs.inorgchem.2c01590

Choi, H.-J., Lee, J. Y., and Choi, J. (2013). Development of geological disposal systems for spent fuels and high-level radioactive wastes in Korea. *Nucl. Eng. Technol.* 45, 29–40. doi:10.5516/NET.06.2012.006

Corbey, J. F., Sweet, L. E., Sinkov, S. I., Reilly, D. D., Parker, C. M., Lonergan, J. M., et al. (2021). Quantitaitve microstructural characterization of plutonium oxalate auto-degradation and evidence for PuO_2 nanocrystal formation. *Eur. J. Inorg. Chem.* 2021, 3277–3291. doi:10.1002/ejic.202100511

Currie, L. A. (1968). Limits for qualitative detection and quantitative determination. Application to radiochemistry. *Anal. Chem.* 40, 586–593. doi:10.1021/ac60259a007

Gates-Rector, S., and Blanton, T. (2019). The powder diffraction file: A quality materials characterization database. *Powder Diffr.* 34, 352–360. doi:10.1017/S0885715619000812

Giffaut, E., Grivé, M., Blanc, P., Vieillard, P., Colàs, E., Gailhanou, H., et al. (2014). Andra thermodynamic database for performance assessment: ThermoChimie. *Appl. Geochem.* 49, 225–236. doi:10.1016/j.apgeochem.2014.05.007

Grambow, B. (2016). Geological disposal of radioactive waste in clay. *Elements* 12, 239–245. doi:10.2113/gselements.12.4.239

Grenthe, I., Gaona, X., Rao, L., Plyasunov, A., Runde, W., Grambow, B., et al. (2020). Second update on the chemical thermodynamics of uranium, neptunium, plutonium, americium and technetium. *Chem. Thermodyn.* 14. Boulogne-Billancourt France, OECD. doi:10.1787/20743300

Hu, C., Zhang, L., and Gong, J. (2019). Recent progress made in the mechanism comprehension and design of electrocatalysts for alkaline water splitting. *Energy and Environ. Sci.* 12, 2620–2645. doi:10.1039/C9EE01202H

IAEA (2011). *Disposal of radioactive waste. Specific safety requirements SSR-5.* Vienna, Austria: International Atomic Energy Agency.

Kim, J.-I. (2006). Significance of actinide chemistry for the long-term safety of waste disposal. *Nucl. Eng. Technol.* 38, 459–482.

Kitamura, A. (2020). *JAEA-TDB-RN in 2020: Update of JAEA's thermodynamic database for solubility and speciation of radionuclides for performance assessment of geological disposal of high-level and TRU wastes*. JAEA-Data/Code 20. Japan: JAEA. doi:10.11484/jaea-data-code-2020-020

Leduc, J., Frank, M., Jürgensen, L., Graf, D., Raauf, A., and Mathur, S. (2019). Chemistry of actinide centers in heterogeneous catalytic transformations of small molecules. *ACS Catal.* 9, 4719–4741. doi:10.1021/acscatal.8b04924

McCoy, K., Casella, A., Sinkov, S., Sweet, L., Mcnamara, B., Delegard, C., et al. (2017). Radiation damage and annealing in plutonium tetrafluoride. *J. Nucl. Mater.* 496, 379–387. doi:10.1016/j.jnucmat.2017.08.005

Neck, V., Altmaier, M., and Fanghänel, T. (2007). Solubility of plutonium hydroxides/hydrous oxides under reducing conditions and in the presence of oxygen. *C. R. Chim.* 10, 959–977. doi:10.1016/j.crci.2007.02.011

Park, Y.-S., Kim, J.-g., Seo, H.-S., Ha, Y.-k., and Song, K. (2013). Lattice parameter changes for spent UO_2 fuels with and without Gd. *Asian J. Chem.* 25, 7006–7008. doi:10.14233/ajchem.2013.04

Ragoussi, M.-E., and Brassinnes, S. (2015). The NEA thermochemical database project: 30 years of accomplishments. *Radiochim. Acta* 103, 679–685. doi:10.1515/ract-2015-2392

Romanchuk, A. Y., Kalmykov, S. N., Kersting, A. B., and Zavarin, M. (2016). Behavior of plutonium in the environment. *Russ. Chem. Rev.* 85, 995–1010. doi:10.1070/RCR4602

Thoenen, T., Hummel, W., Berner, U., and Curti, E. (2014). *The PSI/nagra chemical thermodynamic database 12/07.*

Zhang, Y., Zhang, Q.-Y., Duan, K., Yu, G.-Y., and Jiao, Y.-Y. (2020). Reliability analysis of deep underground research laboratory in Beishan for geological disposal of high-level radioactive waste. *Comput. Geotechnics* 118, 103328. doi:10.1016/j.compgeo.2019.103328

frontiers | Frontiers in Nuclear Engineering

TYPE Original Research
PUBLISHED 14 April 2023
DOI 10.3389/fnuen.2023.1158109

Check for updates

OPEN ACCESS

EDITED BY
Taishi Kobayashi,
Kyoto University, Japan

REVIEWED BY
Tiziana Missana,
Centro de Investigaciones Energéticas, Medioambientales y Tecnológicas, Spain
Hye-Ryun Cho,
Korea Atomic Energy Research Institute (KAERI), Republic of Korea

*CORRESPONDENCE
F. Bok,
f.bok@hzdr.de

SPECIALTY SECTION
This article was submitted to Radioactive Waste Management,
a section of the journal
Frontiers in Nuclear Engineering

RECEIVED 03 February 2023
ACCEPTED 10 March 2023
PUBLISHED 14 April 2023

CITATION
Bok F, Moog HC and Brendler V (2023), The solubility of oxygen in water and saline solutions.
Front. Nucl. Eng. 2:1158109.
doi: 10.3389/fnuen.2023.1158109

The solubility of oxygen in water and saline solutions

F. Bok[1]*, H. C. Moog[2] and V. Brendler[1]

[1]Actinide Thermodynamics Department, Institute of Resource Ecology, Helmholtz-Zentrum Dresden-Rossendorf e.V., Dresden, Germany, [2]Department Repository Research, Gesellschaft für Anlagen- und Reaktorsicherheit (GRS) gGmbH, Braunschweig, Germany

Oxygen is one of the key reaction partners for many redox reactions also in the context of nuclear waste disposal. Its solubility influences radionuclides' behavior, corrosion processes and even microbial activity. Therefore, a reliable calculation of the solubility of molecular oxygen in aqueous solutions is relevant for any safety assessment. Available geochemical speciation and reactive transport programs handle these data very differently. In some codes, the hypothetical equilibrium between dissolved oxygen and water is used to balance redox reactions. Equilibrium constants are given in "temperature grids" for up to 573.15 K. In other cases, temperature functions for the solubility of gaseous oxygen in water are given, without any reference to a valid temperature range. These settings become even more complicated when used in the context of modeling equilibria in high-saline solutions applying the Pitzer formalism. This raised the question about the experimental foundation of equilibrium constants given in such data files and their validity for the solubility of molecular oxygen in saline solutions. For this article, a thorough literature review was conducted with respect to the solubility of molecular oxygen in pure water and saline solutions. From these primary experimental O_2 solubility data a temperature-dependent Henry's law function as well as temperature-dependent binary and ternary Pitzer ion-interaction coefficients were derived. An internally consistent set of thermodynamic data for dissolved oxygen is presented, along with statements about its validity in terms of temperature and, as far as Pitzer interaction coefficients are concerned, of solution composition. This self-consistent activity-fugacity model containing thermodynamic data, Henry's law temperature equation, and Pitzer interaction coefficients is capable of providing a more accurate description of redox transformations, allowing a reduction of conservatism in safety assessment calculations, not only in the context of a nuclear repository. The model reproduces well the reliable experimental data available, and is capable to predict the oxygen solubility in complex solution media. The temperature functions used to describe Henry's constant and the Pitzer interaction coefficients are consistent with the implementation in commonly used geochemical computational programs, allowing direct use without further modification.

KEYWORDS

oxygen solubility, electrolyte solutions, water, Pitzer ion-interaction approach, E_H equation

1 Introduction

Redox reactions are important for the description of geochemical reactions in general (e.g., pyrite oxidation) and of solubility limitations of radioactive contaminants in particular. In a final deep geological repository (DGR) for radioactive waste, attainment of anoxic conditions is very likely in the post-closure phase of operation. In the event of any post-closure access of an aqueous solution to the waste, and assuming anoxic conditions, many radionuclides are immobile to a large extent through the formation of poorly soluble (hydro-)oxides in their reduced tetravalent form [e.g., TcO_2(am), $U(OH)_4$(am), $Np(OH)_4$(am), PuO_2(am/cr), etc.] (Grenthe et al., 2020). However, under strongly reducing conditions even their trivalent forms e.g., $Pu(OH)_3$(am/cr) might exist, showing a higher solubility and thus mobility than the tetravalent actinides (Grenthe et al., 2020). This holds also for higher redox states (penta-, hexa- or heptavalent), which are more soluble in water. Concerning all of these redox-triggered transformations, exact knowledge of the redox potential (E_H/pe) is essential, which in turn depends on the correct description of dissolved oxygen. For an assessment of the maximum likely mobilization of radionuclides from the near field of a DGR under the prerequisite of intrusion of water, the mass of available dissolved oxygen (being present, e.g., by diffusional transport or freshwater intrusion) is one key factor for the retardation of radionuclides in aqueous solution.

In geochemical speciation codes such as PHREEQC (Parkhurst and Appelo, 2013), Geochemist's Workbench (Bethke, 2022), or EQ3/6 (Wolery, 1992), redox reactions of any kind are linked for computational reasons to the hypothetical half-cell reaction

$$2\,H_2O\,(l) \rightleftharpoons O_2\,(g) + 4\,H^+ + 4\,e^- \tag{1}$$

Or, alternatively, to another form involving dissolved oxygen:

$$2H_2O\,(l) \rightleftharpoons O_2\,(aq) + 4H^+ + 4e^- \tag{2}$$

Adding the reaction

$$4H^+ + 4e^- \rightleftharpoons 2H_2\,(g) \tag{3}$$

for which, by definition, $\log_{10} K\,(3) = 0$ the half-cell reactions become

$$2H_2O\,(l) \rightleftharpoons O_2\,(g) + 2H_2\,(g) \tag{4}$$

$$2H_2O\,(l) \rightleftharpoons O_2\,(aq) + 2H_2\,(g) \tag{5}$$

Reactions (Eq. 4) and (Eq. 5) are sometimes referred to as "log*K*-E_H-reaction." In data files for the above-mentioned codes, equilibrium constants for these reactions are either given as functions of temperature or as "temperature grids," where pre-calculated values at defined temperatures (usually 0, 25, 60, 100, 150, 200, 250, and 300°C) are displayed. Unfortunately, this is usually done without any references to literature or a hint to the validity limits at all. The situation becomes even more obscure if the reaction (Eq. 5) containing O_2(aq) is used as half-cell reaction, because this reaction must in fact be considered as addition of reaction (Eq. 4) and

$$O_2\,(g) \rightleftharpoons O_2\,(aq). \tag{6}$$

This poses the question about the experimental foundations for the calculation of the solubility of molecular oxygen in water at temperatures up to 573.15 K. If applied in calculations for high-saline solutions the question arises concerning the impact of ionic strength in general or the presence of specific electrolytes on the solubility of molecular oxygen in particular. In such cases, the Pitzer ion-interaction approach provides a tool for calculating the activity coefficient in concentrated salt solutions (Pitzer, 1991). For this purpose, coefficients for a virial equation are used for binary and ternary interactions between ions as well as uncharged species in aqueous solution, reflecting the deviation from the behavior in pure water. In some data files, e.g., the "Yucca Mountain Pitzer file" (Mariner, 2004) delivered with the EQ3/6 code, Pitzer coefficients for O_2(aq) are included, some valid at 298.15 K only, others are given with a temperature function of unknown validity range. Compilations of data from different sources may cause inconsistencies, which, especially when using the interaction coefficients, may have a significant negative impact on the results of the models obtained.

Facing the task of extending a thermodynamic database based on traceable experimental data, simple adoption of precalculated equilibrium constants in temperature grids from parameter files in geochemical codes is not appropriate, particularly since they are provided in many databases without reference to the source of the primary data. Consequently, these data had to be comprehensibly and consistently recalculated from experimental data for the solubility of oxygen at various temperatures in both pure water and salt solutions and from standard formation data.

For this purpose, solubility data of O_2 in pure water as well as in a wide variety of electrolyte solutions were critically evaluated and combined with well-established thermodynamic data for liquid water H_2O(l), H_2(g), and O_2(g) to create an internally consistent set of equilibrium constants for reactions (Eqs 4–6). With respect to O_2(g) solubility data, the focus was on the system of oceanic salts (including carbonates), which are relevant as potential host rocks implying solutions of high ionic strengths. The alkali ((di-)hydrogen) phosphates were included for inorganic phosphate ions that can form in nuclear waste repositories when phosphate glasses or lanthanide phosphate monazites ($LnPO_4$), as waste forms of highly active waste streams, undergo dissolution processes in contact with water. The acids of the anions contained in the system were included in the data set to represent the case of acid-forming oxidation of minerals (acid mine drainage). Hydroxides were included to allow calculation for alkaline solutions from cement pore waters.

2 Theory and methods

Henry's law constant ($K_{O_2(aq)}$) using the partial pressure of O_2 in the gas phase describes the equilibrium condition for dissolution reaction of O_2 in water (Eq. 6) with $\gamma_{O_2(aq)}$ being the O_2 activity coefficient, $m_{O_2(aq)}$ the molal O_2 concentration in solution and $f_{O_2(aq)}$ the O_2 fugacity in the gas phase.

$$K_{O_2\,(aq)} = \frac{[O_2\,(aq)]}{[O_2\,(g)]} = \frac{\gamma_{O_2\,(aq)} \cdot m_{O_2\,(aq)}}{f_{O_2\,(g)}} \tag{7}$$

Geochemical codes treat the temperature dependence of equilibrium constants as polynomial functions with several temperature-dependent terms (Eq. 8) or mathematically equivalent transformations thereof.

$$\log_{10} K\,(T) = A_1 + A_2 T + \frac{A_3}{T} + A_4 \ln T + \frac{A_5}{T^2} + A_6 T^2 \tag{8}$$

The *Pitzer formalism* is widely used to account for the deviation from ideality of aqueous solutions of high ionic strength. It has proven capable of calculating solubilities in saturated solutions in the system of oceanic salts: Na^+, K^+, Mg^{2+}, Ca^{2+} – Cl^-, $SO_4{}^{2-}$, $HCO_3{}^-$ – CO_2(g) – H_2O(l). The probably most cited paper in this respect is the one by Harvie, Møller and Weare (Harvie et al., 1984), whose results are often referred to as "HMW-database." The usability of their database was demonstrated for a huge amount of application cases. One example especially relevant for nuclear waste disposal is by Herbert, who successfully modeled dissolution and precipitation processes in complex, saturated salt solutions in German rock salt formations (Herbert et al., 2000). Later, the HMW-database was extended to higher temperatures (Christov and Møller, 2004). Its popularity, as well as that of the Pitzer formalism in general, was promoted by the fact that it got implemented in various geochemical codes, such as PHREEQC, EQ3/6, Geochemist's Workbench, but also in CHEMAPP (Eriksson and Spencer, 1995; Eriksson et al., 1997), GEMS (Wagner et al., 2012; Kulik et al., 2013), or recently TOUGHREACT (Zhang et al., 2006). In parallel, the HMW-database was further developed and extended in response to the necessities of national programs for the disposal of radioactive waste in salt rock formations with the potential to contain high-saline solutions, e.g., the Yucca Mountain project (United States) (Mariner, 2004), the Waste Isolation Pilot Plant project (United States) (Domski and Nielsen, 2019), or the Oceanic Salt System from Voigt (2020) (Voigt, 2020a; Voigt, 2020b) with the alkali phosphate data from Scharge et al. (2013), Scharge et al. (2015) and the carbonate data from Harvie et al. (1984) as compiled in the THEREDA project in Germany (Moog et al., 2015; THEREDA, 2023). The Pitzer formalism was also applied to marine chemistry. Millero and co-workers over many years worked on a database specifically suited for seawater, e.g., (Pierrot and Millero, 2017). Recently, the Scientific Committee on Ocean Research of the International Council for Science (SCOR) created working group 145 to establish a reference seawater chemical speciation model, which is based on the Pitzer model (Turner et al., 2016).

The Pitzer formalism extends the Debye-Hückel equation with a virial expansion to account for binary and ternary ionic-strength-dependent specific interactions between ions of likewise and opposite charge (Pitzer, 1991). Explicit formulations for binary and ternary solutions of cations and anions are given by Scharge et al. (2012). In the present work, non-ideal interactions between a neutral component O_2(aq) and cations or anions are investigated. More specifically, the focus is set on binary λ-interactions (between a neutral and a charged solute) and ternary ζ-interactions (one uncharged and two oppositely charged solutes), η-interactions (one uncharged and two similar charged solutes) and μ-interactions (two different uncharged and one charged solutes). The activity coefficient for a neutral species according to Pitzer (Pitzer, 1991) is:

$$\begin{aligned}\ln\gamma_N = {} & 2\left(\sum_c m_c\lambda_{Nc} + \sum_a m_a\lambda_{Na} + \sum_n m_n\lambda_{Nn}\right) + \sum_c\sum_a m_c m_a\zeta_{Nca} \\ & + \sum_c\sum_{c'} m_c m_{c'}\eta_{Ncc'} + \sum_a\sum_{a'} m_a m_{a'}\eta_{Naa'} + \sum_c\sum_n m_c m_n\mu_{Nnc} \\ & + \sum_a\sum_n m_a m_n\mu_{Nna}\end{aligned} \tag{9}$$

Note, that in Eq. 9 $\eta_{Ncc'}$, $\eta_{Naa'}$, $\mu_{Nn'c}$ and $\mu_{Nn'a}$ refer to interactions between a neutral solute and to two different non-neutral solutes with likewise charge. These interactions are mathematically identical to a ternary ζ-interaction. It is perhaps for this reason, that sometimes they are not properly distinguished in data files and instead referred to as ζ- or even ψ-interactions altogether.

A few publications are available in the literature providing Pitzer interaction coefficients for molecular oxygen in electrolyte solutions. Namely, the works of Clegg and Brimblecombe (1990), Millero et al. (2002a), Millero et al. (2002b), Millero et al. (2003), Millero and Huang (2003), Geng and Duan (2010), and Zheng and Mao (2019) are worth mentioning here. However, combining these data sets with the only existing Pitzer data set valid for higher temperatures and including the whole Oceanic Salt System (THEREDA) leads to inconsistencies. Such inconsistent databases will produce incorrect modeling results. This is demonstrated in Figure 1 by recalculating experimental data of O_2 solubility in NaCl solution from literature (Millero et al., 2002a; Millero et al., 2002b; Millero et al., 2003). This does not mean that the various available Pitzer datasets for oxygen are of poor quality. However, it illustrates the importance of consistent data sets.

2.1 Data treatment

This work focusses on primary experimental results. Respective literature on the solubility of molecular oxygen in pure water as well as in electrolyte solutions was collected, critically assessed, and used to recalibrate the temperature-dependent Henry's law constant as well as the Pitzer interaction coefficients.

In many publications, the O_2 solubility data are given in figures only. In these cases, the data were re-digitized using the software package "Engauge Digitizer" from Mitchell et al. (2020). The uncertainty resulting from this digitization step depends on the quality of the graphics, but in most cases can be neglected compared to the experimental uncertainty.

Experimentally obtained O_2 solubility data are published using various different formats and units. Here, all datasets were recalculated to a micromolal scale (μmoles O_2 per kg of water) as a function of salt concentration in molal scale (moles salt per kg of water). If the concentration data were available in a volume-related concentration unit, e.g., molar (moles per liter solution), they were converted using the density functions according to Söhnel and Novotný (1985). All solubility data on molecular oxygen in both, pure water and electrolyte solutions are provided in the supporting information.

2.2 Parameter optimization

All parameters for temperature dependency equations—for Henry's law temperature equation as well as for the Pitzer interaction coefficients—were determined using the geochemical speciation software PHREEQC (batch version 3.7) (Parkhurst and Appelo, 2013) coupled with the parameter estimation software UCODE_2014 (Poeter et al., 2014) that uses a minimization of sum of squared residuals approach.

To determine the numerical values for the parameters of the temperature dependent Henry's law Eq. 8, data for the oxygen solubility in pure water were collected from the literature. These solubility datasets were used to fit the simplified temperature function equation using parameters A_1, A_3, and A_4 only. The common geochemical codes (e.g., ChemApp, Geochemist's Workbench, PHREEQC, ToughReact) use six temperature parameters (Eq. 8 or mathematically equivalent transformations thereof) for the temperature-dependent description of reaction constants. Since a complete set of these temperature parameters must be specified in the code-specific parameter files, the other parameters (A_2, A_5 and A_6) are set to zero. Older codes like EQ3/6 use a temperature-dependend grif of up to eight log*K* values; these can be easily calculated from the parameterized equation.

Most geochemical programs treat the Pitzer coefficients and their temperature parameter in a different way. There, polythermal equations use terms where the temperature is given relative to a reference temperature (mostly T = 298.15 K, sometimes referred to as "25°-centered"), see Eq. 10 or mathematically equivalent transformations thereof.

$$P = X_0 + X_1\left(\frac{1}{T} - \frac{1}{T_r}\right) + X_2 \ln\left(\frac{T}{T_r}\right) + X_3 (T - T_r) + X_4 (T^2 - T_r^{\,2}) + X_5\left(\frac{1}{T^2} - \frac{1}{T_r^{\,2}}\right) \tag{10}$$

P is a Pitzer coefficient (here λ, ζ or η), *T* is the temperature in Kelvin, and T_r is the reference temperature (298.15 K) and ln the natural logarithm.

It was numerically impossible to fit all necessary temperature function parameters for all relevant Pitzer coefficients simultaneously. Therefore, a step-by-step approach was chosen: By definition, the coefficient $\lambda(O_2\text{-}Cl^-)$ and therefore all temperature parameters for (X_0–X_5) were set to 0. First, the Pitzer coefficients at T = 298.15 K were fitted using the experimental O_2 solubility data for the chemical subsystem H^+, Na^+, K^+ - Cl^-, OH^- - $H_2O(l)$ only. The resulting values of the coefficients were then used in the successive fitting of the chemical subsystems H^+, Na^+, K^+ - SO_4^{2-} - $H_2O(l)$, Na^+, K^+ - CO_3^{2-} - $H_2O(l)$ and H^+, Na^+, K^+ - PO_4^{3-} - $H_2O(l)$. All obtained interaction coefficients were then used as boundary conditions to fit interaction coefficients within the chemical subsystems of the Earth alkaline chlorides and Earth alkaline sulfates, respectively: Mg^{2+}, Ca^{2+} - Cl^-, OH^- - $H_2O(l)$ as well as Mg^{2+} - SO_4^{2-}, OH^- - $H_2O(l)$. Finally, the interaction coefficients $\eta(Cl^-\text{-}SO_4^{2-})$ and $\eta(Na^+\text{-}Mg^{2+})$ for ternary salt solutions (NaCl + Na_2SO_4, NaCl + $MgCl_2$) were fitted.

During the parameter determination, first all possible combinations of binary (λ) and ternary (ζ/η/μ) Pitzer coefficients should be determined. It became apparent that not all such coefficients were needed to describe the system, or that some combinations of binary and ternary coefficients were strongly cross-correlated. By reducing the number of adjustable coefficients, it was possible to create a data set that was sufficient to describe the system while using a minimum number of coefficients.

The coefficient for the ternary interaction $\zeta(O_2\text{-}Na^+\text{-}OH^-)$ is not needed for the description of the system at 298.15 K. However, for the polythermal description of the system, this interaction cannot be neglected. Therefore, the coefficient was set to zero at 298.15 K.

The values of the Pitzer coefficients at T = 298.15 K correspond to the X_0 parameters in Eq. 10. Thus, in the following steps, the Pitzer coefficients valid at T = 298.15 K were used as boundary parameters for the fits of the temperature dependency parameters X_1 to X_5. It was found that only the first two parameters (X_1 and X_2) had to be adjusted to fully describe the temperature dependency of the $O_2(aq)$ Pitzer coefficients. Thus, all other parameters (X_3, X_4 and X_5) are set to zero.

A simultaneous fit of the temperature equations parameters including all chemical systems was not possible. Therefore, temperature parameters for the systems of solutions of binary electrolytes were iteratively fitted individually and sequentially until none of the parameters changed. Figure 2 shows the fitting scheme for the generation of the Pitzer interaction coefficients temperature parameters. Thus, a consistent set of parameterized temperature equations of the Pitzer interaction coefficients could be deduced.

The coefficient for the ternary interaction $\zeta(O_2\text{-}K^+\text{-}HSO_4^-)$ could not be retrieved at 298.15 K as there are no experimental data for this temperature. The only O_2 solubility data available for the alkali hydrosulfate ($NaHSO_4$ and $KHSO_4$) system were acquired at 310.2 K (Lang and Zander, 1986). The experimental data of the chemical system O_2-Na_2SO_4-H_2O could be described without a ternary interaction coefficient. For the description of the experimental data of the chemical system O_2-K_2SO_4-H_2O, however, a ternary interaction coefficient $\zeta(O_2\text{-}K^+\text{-}HSO_4^-)$ had to be introduced. To do so, the value for the $\zeta(O_2\text{-}K^+\text{-}HSO_4^-)$ coefficient was determined only in the context of the fits of the temperature parameters but had to be used as temperature independent one, since only experimental measured values for a single temperature are available. Verifying calculations including this coefficient in the fits of the 298.15 K data (X_0 parameter) showed that this coefficient has no influence on the previously determined systems—namely, O_2-K_2SO_4-H_2O.

For the chemical systems for which no O_2 solubility data are available at temperatures different from T = 298.15 K (carbonate system, phosphate system, ternary salt mixtures) no temperature parameters of the Pitzer coefficients could be obtained. Consequently, these Pitzer coefficients are valid at T = 298.15 K only and not included in Figure 2.

3 Data assessment

3.1 Literature review and data selection

The aim of this work was to create a thermodynamic data set to calculate the oxygen solubility in pure water as well as in solutions containing ions ubiquitous in nature: Na^+, K^+, Mg^{2+}, Ca^{2+}, Cl^-, HSO_4^-/SO_4^{2-}, HCO_3^-/CO_3^{2-}, $H_2PO_4^-/HPO_4^{2-}/PO_4^{3-}$.

IUPAC published two reviews by Battino et al. (1981) and Clever et al. (2014) on available solubility data of molecular oxygen in pure water as part of the Solubility Data Series. This data collection was used here as a basis to create a temperature function for the solubility of O_2. From these reviews, only solubility data within the temperature range from 273.15 up to 373.15 K with an oxygen partial pressure of 101.325 kPa were used. Solubility data at temperatures above 373.15 K were omitted as they are not the focus of the intended future usage of this data set. Moreover, due to the large scattering of

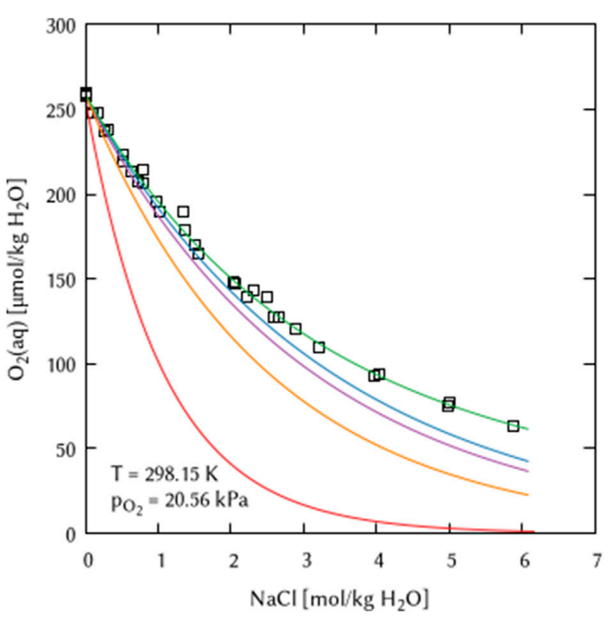

FIGURE 1
Effect of combining inconsistent Pitzer datasets on the example of O_2 solubility in NaCl solution. □ Experimental data from Millero et al. (2002a), Millero et al. (2002b), Millero et al. (2003), lines: Calculation using the THEREDA Pitzer dataset (Moog et al., 2015; Voigt, 2020a; Voigt, 2020b; THEREDA, 2023) in combination with: blue) Millero et al. (2003), purple) Clegg and Brimblecombe (1990), orange) Geng and Duan (2010), red) Zheng and Mao (2019), green) this work.

the experimental data, using them significantly impaired the quality of the fitting results of the Henry's law constant's temperature equation at lower temperatures—specifically below 298.15 K.

For the O_2 solubility in salt solutions, the number of publications containing experimental data is quite limited. A critical data evaluation was performed using the following criteria:

- Completeness of experimental conditions given,
- For datasets of electrolyte solutions: Agreement of the O_2 solubility in the peripheral system (pure water at the given temperature) with accepted experimental values of the review workers of IUPAC or the calculated values from the temperature function of this work,
- Consistency in the order of magnitude and progression of the O_2 solubility decrease with increasing salt concentration between datasets from different sources,
- Total gas pressure up to 101.325 kPa (1 atm): experimental datasets derived at higher pressures were discarded,
- Temperature range: References with experimental O_2 solubility were ranked higher when they 1) provide data at T = 298.15 K and 2) provide data over a broader temperature range. This was done in order to create a data set with the highest possible applicability while maintaining consistency with the interaction coefficients valid at T = 298.15 K that were created in the first fitting step.

The literature review and data assessment on O_2 solubility in salt solutions is given in Table 1.

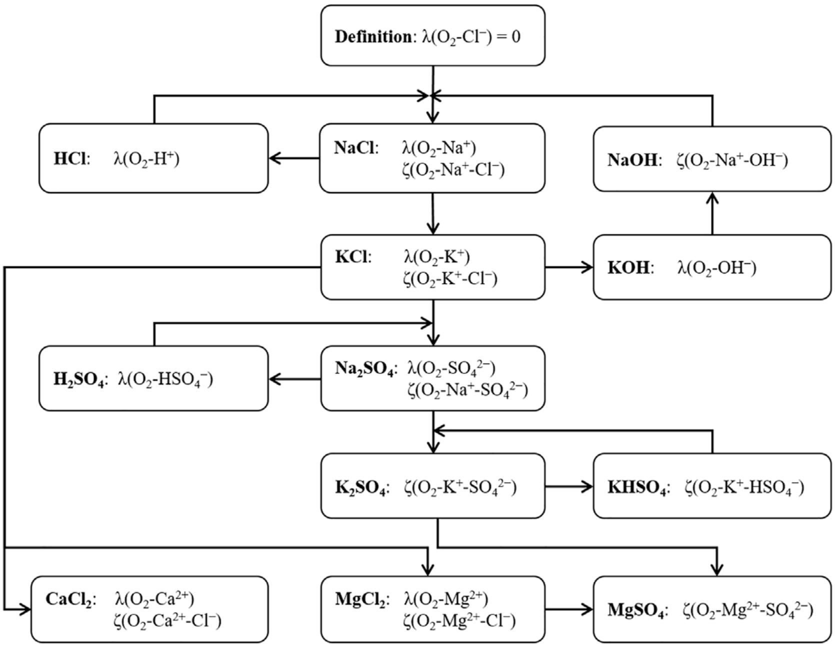

FIGURE 2
Fitting scheme for the generation of the Pitzer interaction coefficients temperature parameters.

TABLE 1 Literature review and data assessment on O_2 solubility in salt solutions.

References	Electrolyte	O_2 partial pressure	Temperature	Comments	Selected for fitting
		[kPa]	[K]		
Armenante and Karlsson (1982)	NaCl	20.9	293.15	Dataset shows a significantly stronger O_2 solubility decrease with increasing electrolyte concentration compared with other references dealing with NaCl.	No
Baykut and Aroguz (1989)	NaCl, $MgCl_2$, Na_2SO_4, Na_3PO_4,	102.26	293.15–308.15	A pressure of 767 mm Hg is given but no information on the O_2 partial pressure. The given O_2 concentrations suggest that air and not pure oxygen was used. The O_2 solubility value in pure water is significantly lower (−10%) from data recommended by IUPAC (Battino et al., 1981; Clever et al., 2014), the O_2 concentration calculated with the Henry's law function from this work. The O_2 solubility is only given for NaCl and Na_2SO_4 solutions as tabulated values. For other salt solutions only graphs are available, their quality is too poor to extract the solubility data.	No
Bikov (1937)	KCl	9,810	273.15–513.15	O_2 solubility in air and pure oxygen at p_{tot} = 9.81 MPa is given. These O_2 partial pressures were considered to be outside the validity range of the Henry's law temperature function generated in this work.	No
Bohr (1910)	H_2SO_4	101.325	294.15	The O_2 solubility value in pure water is significantly lower (−24%) from data recommended by IUPAC (Battino et al., 1981; Clever et al., 2014), the O_2 concentration calculated with the Henry's law function from this work.	No
Broden and Simonson (1978)	$NaHCO_3$	1,000–5,000	333.15–433.15	The high-pressure datasets are out of the validity range of the Henry's law constant function obtained in this work. So, these datasets had to be rejected and no binary or ternary Pitzer interaction coefficients for O_2(aq) and HCO_3^- could be obtained.	No
Broden and Simonson (1979)	$NaHCO_3$	1,000–5,000	333.15–433.15	The high-pressure datasets are out of the validity range of the Henry's law constant function obtained in this work. So, these datasets had to be rejected and no binary or ternary Pitzer interaction coefficients for O_2(aq) and HCO_3^- could be obtained.	No
Bruhn et al. (1965)	NaOH, H_2SO_4	101.325	323.15–523.15	Only the experimental data at T = 323.15 K were used in this paper. H_2SO_4 dataset shows a much smaller decrease of the O_2 concentration with increasing acid concentration.	NaOH: Yes, H_2SO_4: No
Chatenet et al. (2000)	NaOH	98–99	298.15	No shortcoming	Yes
Cramer (1980)	NaCl	4,300–5,200	276.15–562.15	The O_2 partial pressures used were considered to be outside the validity range of the Henry's law temperature function generated in this work.	No

(Continued on following page)

TABLE 1 (*Continued*) **Literature review and data assessment on O_2 solubility in salt solutions.**

References	Electrolyte	O_2 partial pressure	Temperature	Comments	Selected for fitting
		[kPa]	[K]		
Cramer (1984)	NaCl	21.21	273.15–298.15	The O_2 solubility in pure water does not match with values recommended by IUPAC (Battino et al., 1981; Clever et al., 2014) nor the O_2 concentration calculated with the Henry's law function from this work.	No
Das (2005)	H_2SO_4	101.325	298.15	No shortcoming	Yes
Davis et al. (1967)	KOH	101.325	273.15–333.15	O_2 solubility deviates significantly (−1.5% to −6.8%) from data recommended by IUPAC (Battino et al., 1981; Clever et al., 2014) and the O_2 concentration calculated with the Henry's law function from this work.	T = 298.15 K: Yes, other temperatures: No
Eucken and Hertzberg (1950)	NaCl, KCl, $MgCl_2$	101.325	273.15–298.15	O_2 solubility deviates significantly (up to +7.6%) from data recommended by IUPAC (Battino et al., 1981; Clever et al., 2014) and the O_2 concentration calculated with the Henry's law function from this work.	No
Geffcken (1904)	NaCl, HCl, NaOH, KOH, K_2SO_4, H_2SO_4	101.325	288.15 and 298.15	In the alkaline chloride and alkaline sulfate datasets, the O_2 solubility decrease with electrolyte concentration strongly differs from the trend of the decrease in other references using these electrolytes. Furthermore, the available data exceed the solubility limit of K_2SO_4. The dataset was used in the systems where only few to no data are available.	HCl, NaOH, KOH, H_2SO_4: Yes, NaCl KCl, K_2SO_4: No
Glazunov et al. (1997)	NaOH	100	358.15	Observed O_2 solubility data are too low by a factor of ten.	No
Gubbins and Walker (1965)	KOH, H_2SO_4, H_3SO_4	101.325	298.15	Dataset shows a significantly lower O_2 solubility in the lower H_2SO_4 concentration range than the data from all other references dealing with H_2SO_4.	H_2SO_4: No, KOH, H_3PO_4: Yes
Hayduk (1991)	H_2SO_4	101.325–1013.2	298.15–458.15	Experimental data outside the validity range of the Henry's law temperature function used in this work.	No
Iwai et al. (1993)	NaCl, K_2HPO_4, KH_2PO_4	101.325	NaCl: 303.15 and 310.15, K_2HPO_4, KH_2PO_4: 298.15	As this is the only dataset available for the K_2HPO_4 and the KH_2PO_4 system, it is difficult to assess whether the data are reliable; the information in the reference does not contradict the use of this dataset. In the NaCl subsystem, the O_2 solubility decreases stronger with electrolyte concentration than in other datasets [e.g., (Millero et al., 2002a; Millero et al., 2002b; Millero et al., 2003)].	K_2HPO_4, KH_2PO_4: Yes, NaCl: No
Iwai et al. (1990)	NaCl	15	298.15	O_2 partial pressure of 15 kPa is given but does not match with the O_2 solubility in pure water which seems to be close to 101.325 kPa.	No
Kaskiala (2002)	H_2SO_4	100	298.15–328.15	In comparison with other experimental datasets, this one shows a much smaller decrease of the O_2 concentration with increasing acid concentration.	No

(Continued on following page)

TABLE 1 (*Continued*) Literature review and data assessment on O_2 solubility in salt solutions.

References	Electrolyte	O_2 partial pressure [kPa]	Temperature [K]	Comments	Selected for fitting
Khomutov and Konnik (1974)	NaCl, KCl, NaOH, Na_2SO_4, K_2SO_4, Na_2CO_3, K_2CO_3, Na_3PO_4, K_3PO_4	21.278	298.15	Dataset shows a significantly stronger decrease of O_2 solubility with increasing electrolyte concentration than data from Millero et al. (2003) [28, 29]. However, since there are no other experimental O_2 solubility datasets for some chemical systems (Na_2CO_3, K_2CO_3, Na_3PO_4, K_3PO_4), these raw data are used in the fit.	Na_2CO_3, K_2CO_3, Na_3PO_4, K_3PO_4: Yes, NaCl, KCl, NaOH, Na_2SO_4, K_2SO_4: No
Knaster and Apelbaum (1964)	KOH	101.325	294.15–348.15	Datasets show a stronger decrease in O_2 solubility in the range of 2–5 m KOH than all datasets from other KOH references.	No
Lang and Zander (1986)	NaCl, KCl, $MgCl_2$, $CaCl_2$, NaOH, KOH, Na_2SO_4, $NaHSO_4$, K_2SO_4, $KHSO_4$, $MgSO_4$, H_2SO_4	101.325	310.2	Significantly stronger decrease in O_2 solubility with NaCl, KCl concentration than the Millero et al. (2003) data. As this is the only dataset available for the systems $NaHSO_4$ and $KHSO_4$, it is difficult to assess whether the data are reliable; the information in the reference does not contradict the use of this dataset.	$KHSO_4$: Yes, all others: No
Li (1994)	H_2SO_4	101.325	298.15–353.15	O_2 solubility deviates significantly (up to +5%) from data recommended by IUPAC (Battino et al., 1981; Clever et al., 2014) and the O_2 concentration calculated with the Henry's law function from this work.	No
MacArthur (1916)	NaCl, KCl, $MgCl_2$, $CaCl_2$, Na_2SO_4, K_2SO_4	21.2	298.15	O_2 solubility deviates significantly (−3 to −5%) from data recommended by IUPAC (Battino et al., 1981; Clever et al., 2014) and the O_2 concentration calculated with the Henry's law function from this work. Also, the K_2SO_4 dataset shows a significantly stronger decrease of O_2 solubility with increasing electrolyte concentration than data from Millero et al. (2003), Millero and Huang (2003). In NaCl system, the measured O_2 solubility at 6 mol/kg H_2O NaCl is too high (comparable values were reached at ~3 mol/kg H_2O in other papers).	No
Millero et al. (2002a)	NaCl, $MgCl_2$, Na_2SO_4, $MgSO_4$	20.56	298.15	No principle shortcoming. The dataset of the mixed electrolyte solution $MgCl_2$ + $MgSO_4$ was rejected because the authors mentioned the usage of two different stock solutions and inconsistent O_2 solubility in this subsystem.	NaCl + Na_2SO_4, Na_2SO_4+$MgSO_4$, NaCl + $MgCl_2$: Yes, $MgCl_2$+$MgSO_4$: No
Millero et al. (2002b)	NaCl, $MgCl_2$, Na_2SO_4, $MgSO_4$	20.56	273.15–318.15	No shortcoming	Yes
Millero et al. (2003)	NaCl, KCl, $CaCl_2$, K_2SO_4	20.56	298.15	No shortcoming	Yes
Millero and Huang (2003)	KCl, $CaCl_2$, K_2SO_4	20.56	278.15–318.15	No shortcoming	Yes
Narita et al. (1983)	H_2SO_4	101.325	298.15	No shortcoming	Yes
Ohkubo (2000)	NaCl	?	298.15–363.15	O_2 partial pressure unclear, O_2 solubility relative to solubility in pure water given	No

(Continued on following page)

TABLE 1 (*Continued*) Literature review and data assessment on O_2 solubility in salt solutions.

References	Electrolyte	O_2 partial pressure	Temperature	Comments	Selected for fitting
		[kPa]	[K]		
Pospíšol and Lužný (1960)	KOH	101.325	293.15	Dataset shows a much smaller decrease of the O_2 concentration with increasing KOH concentration (up to 2.5 times higher O_2 concentration than the other datasets).	No
Reynafarje et al. (1985)	KCl	20.2	278.15–313.15	No pure electrolyte solution: K-HEPES buffered KCl solutions	No
Shoor et al. (1968)	KOH	101.325	298.15–373.15	No shortcoming	Yes
Tan et al. (2001)	Na_2CO_3	1,000–10,000	308.15	Dataset was obtained using pressures above 101.325 kPa, which is out of scope of this work.	No
Yasunishi (1977)	Na_2SO_4	101.325	288.15–308.15	O_2 solubility deviates significantly (+4.8 to +10.0%) from data recommended by IUPAC (Battino et al., 1981; Clever et al., 2014) and the O_2 concentration calculated with the Henry's law function from this work.	No
Yasunishi (1978)	KCl, $MgCl_2$, $CaCl_2$, NaOH, $MgSO_4$, Na_2CO_3	101.325	288.15–308.15	O_2 solubility deviates significantly (up to +11%) from data recommended by IUPAC (Battino et al., 1981; Clever et al., 2014) and the O_2 concentration calculated with the Henry's law function from this work.	No
Zhang et al. (2009)	NaOH	101.325	296	No shortcoming	Yes

TABLE 2 Temperature parameters of the logarithmic Henry's law constant ($\log K_{H,cp}$) for the O_2 solubility in pure water, Eq. 8.

Parameter	Value	Standard error
A_1	−71.95	0.35
A_3	3,625	34
A_4	9.984	0.056

4 Modelling results and discussion

4.1 Solubility of oxygen in pure water

The obtained temperature parameters for the $\log K_{H,cp}$ of the O_2 solubility in pure water are given in Table 2. The resulting temperature dependency equation describes the oxygen solubility in pure water very well (see Figure 3) while using only three of the six possible temperature terms.

Comparing the value at T = 298.15 K calculated with the obtained temperature function of Henry's constant with values found in other thermodynamic databases shows very good agreement, see Table 3.

4.2 Thermodynamic data for $O_2(aq)$

To create an internally consistent set of equilibrium constants for reactions (Eqs 4, 5) it is necessary to select thermodynamic data for $H_2O(l)$, $O_2(g)$ and $H_2(g)$. The temperature function for the standard molar Gibbs enthalpy of formation is calculated with

$$\Delta_f G_m^0(T) = \Delta_f G^0_{i,T=T_0} - S^0_m(T - T_0) + \int_{T_0}^{T} C^0_{p,m}(T)\mathrm{d}T - T\int_{T_0}^{T}\frac{C^0_{p,m}(T)}{T}\mathrm{d}T \quad (11)$$

Within the frame of this chapter, we adopt the following general temperature function as extension of Eq. 8:

$$f(T) = A_1 + A_2 T + \frac{A_3}{T} + A_4 \ln T + \frac{A_5}{T^2} + A_6 T^2 + A_7 T^3 + A_8 T \ln T \quad (12)$$

Application of this temperature function for $C^0_{p,m}(T)$, integration and rearrangement of Eq. 12 yields a general expression for the standard Gibbs energy of formation:

$$\Delta_f G_m^0(T) = B_1 + B_2 T + \frac{B_3}{T} + B_4 \ln T + \frac{B_5}{T^2} + B_6 T^2 + B_7 T^3 + B_8 T \ln T \quad (13)$$

with

$$B_1 = \Delta_f G^0_{i,T=T_0} + S^0_m T_0 - A_1 T_0 - \frac{A_2}{2}T_0^2 - \frac{A_6}{3}T_0^3 - A_3(\ln T_0 - 1) + \frac{A_5}{T_0} \quad (14)$$

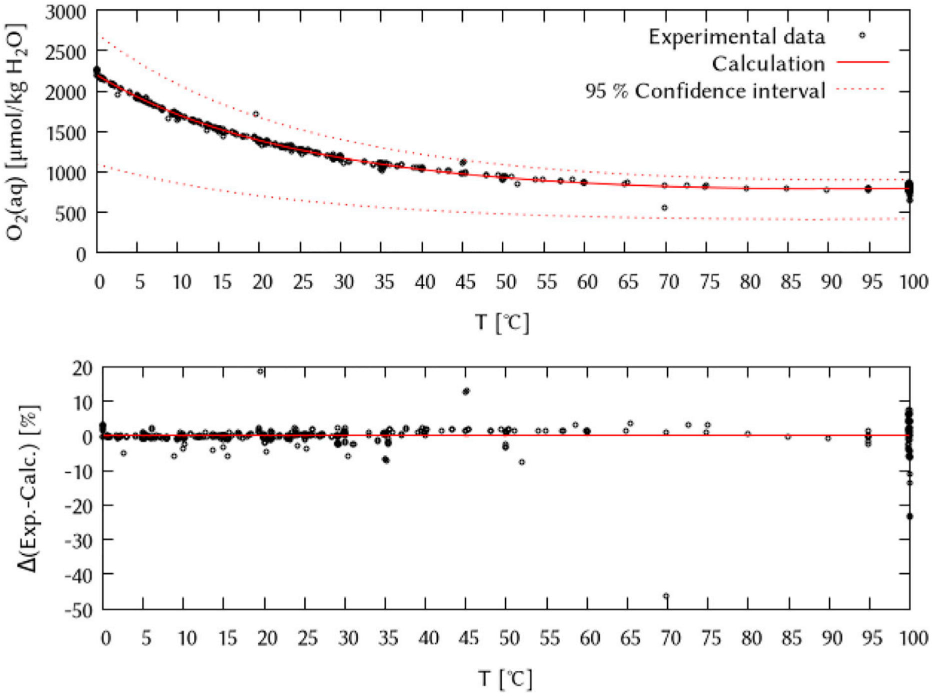

FIGURE 3
Temperature dependency of the logarithmic Henry's law constant of the O_2 solubility in pure water (expressed in µmol/kg H_2O·101.325 kPa). Points: experimental data from literature references given by IUPAC (Battino et al., 1981; Clever et al., 2014), solid line: calculation (this work), dashed line: 95% confidence interval.

TABLE 3 Comparison of the logarithmic Henry's law constant ($\log K_{H,cp}$) for the O_2 solubility in pure water at T = 298.15 K used in different thermodynamic database projects and other sources.

Database	$\log K_{H,cp}$	Data references
OECD/NEA Thermochemical Database (TDB) Project Ragoussi and Costa (2019)	−2.90	Calculated from Cox et al. (1989)
ThermoChimie V11a Giffaut et al. (2014)	−2.90	Calculated from Cox et al. (1989)
PSI/Nagra Chemical Thermodynamic Database (12/07) Thoenen et al. (2014)	−2.8944	Calculated from Pearson and Berner (1991)
THERMODDEM Blanc et al. (2012)	−2.90	Calculated from Cox et al., (1989)
LLNL Delany and Lundeen (1991)	−2.8983	Calculated from Cox (1978)
JAEA Kitamura (2020)	−2.8983	Calculated from data in Kelley (1960) and Cox (1978)
JESS May and Muray (1991)	−2.96	Read and Broyd (1991)
JESS May and Muray (1991)	−2.90	Lumsdon and Evans (1995)
JESS May and Muray (1991)	−3.066	Carpenter (1966)
JESS May and Muray (1991)	−2.81	Phillips et al. (1985)
Mean of the above	−2.92	
This work	−2.904	

$$B_2 = -S^0_{i,T=T_0} + A_1\left(1 + \ln T_0\right) + A_2 T_0 + \frac{A_6}{2}T_0^2 - \frac{A_3}{T_0} - \frac{A_5}{2T_0^2} \quad (15)$$

$$B_3 = -\frac{A_5}{2} \quad (16)$$

$$B_4 = A_3 \quad (17)$$

$$B_5 = 0 \quad (18)$$

$$B_6 = -\frac{A_2}{2} \quad (19)$$

$$B_7 = -\frac{A_6}{6} \quad (20)$$

$$B_8 = -A_1 \quad (21)$$

For the corresonding temperature function for O_2(aq) the compiled solubility data for oxygen in pure water (Table 2) were used. The equilibrium constant for reaction (Eq. 6) can be expressed as [index numbers of coefficients refer to the general function (Eq. 12)]

$$\Delta_r G^0(T)(6) = -RT\ln(10)\log_{10}K(T)(6) = A_1 + A_2 T + A_8 T\ln T \quad (22)$$

Using the corresponding parameters for O_2(g) the temperature function for the standard molar Gibbs enthalpy of formation is then calculated with

$$\Delta_f G^0_{O_2\,(aq)}(T) = \Delta_r G^0(T)(6) + \Delta_f G^0_{O_2\,(g)}(T) \quad (23)$$

For the next step, we use the following relations, where all temperature parameters A_i refer to the temperature function for $\Delta_r G^0(T)(6)$ in the form of the general function (Eq. 12). For this specific case only A_1, A_2, and A_8 are unlike zero.

$$\begin{aligned}\Delta_r H^0(T)(6) &= -T^2\frac{\partial}{\partial T}\left(\frac{\Delta_r G^0(T)(5)}{T}\right)_p \\ &= A_1 + \frac{2A_3}{T} - A_4(1-\ln T) + \frac{3A_5}{T^2} - A_6 T^2 \\ &\quad - 2A_7 T^3 - A_8 T\end{aligned} \quad (24)$$

$$\begin{aligned}\Delta_r S(T)(6) &= -\frac{\partial}{\partial T}\left(\Delta_r G^0(T)(6)\right)_p \\ &= -A_2 + \frac{A_3}{T^2} - \frac{A_4}{T} + \frac{2A_5}{T^3} - 2A_6 T - 3A_7 T^2 - A_8(1+\ln T)\end{aligned} \quad (25)$$

$$\begin{aligned}\Delta_r C^0_p(T)(6) &= \frac{\partial}{\partial T}\left(\Delta_r H^0(T)(6)\right)_p \\ &= -\frac{2A_3}{T^2} + \frac{A_4}{T} - \frac{6A_5}{T^3} - 2A_6 T - 6A_7 T^2 - A_8\end{aligned} \quad (26)$$

One notes that the T^{-3}-term in Eq. 26 is not present in the standard T-function, Eq. 12. However, it is unequal to zero only if there is a T^{-2}-term in $\log K(T)$. This happens to be not the case in our proposal for $\log K(T)(6)$.

After evaluation for $T = T_0$ standard molar enthalpy of formation, standard entropy, and standard partial molal heat capacity of O_2(aq) is calculated using the relations:

$$\Delta_f H^0_{O_2\,(aq),T=T_0} = \Delta_r H^0_{T=T_0}(6) \quad (27)$$

$$S^0_{O_2\,(aq),T=T_0} = \Delta_r S^0_{T=T_0}(6) + S^0_{O_2\,(g),T=T_0} \quad (28)$$

$$C^0_{p,O_2\,(aq)}(T) = \Delta_r C^0_p(T)(6) + C^0_{p,O_2\,(g)}(T) \quad (29)$$

with $\Delta_f H^0_{O_2\,(g),T=T_0} = 0$.

Selected and calculated thermodynamic data are summarized in Tables 4–6. Standard formation data were adopted from Cox et al. (1989); heat capacities between 280 and 500 K were adopted from Chase (1998). For liquid water $\Delta_f H^0_{H_2O\,(l),T=T_0}$ and $S^0_{H_2O\,(l),T=T_0}$ are identical in both sources. Applying the temperature function for $C^0_{p,H_2O\,(l)}(T)$ as indicated in Table 5, a value of $C^0_{p,H_2O\,(l),T=T_0} = 75.418$ J/mol·K could be obtained, which is in good agreement with $C^0_{p,H_2O\,(l),T=T_0} = 75.351 \pm 0.080$ J/mol·K from Cox et al. (1989) and Chase (1998). For gaseous oxygen Cox et al. (1989) lists $S^0_{O_2\,(g),T=T_0} = 205.152 \pm 0.005$ J/mol·K which covers $S^0_{O_2\,(g),T=T_0} = 205.147$ J/mol·K given by Chase (1998). For gaseous oxygen, a value of $C^0_{p,O_2\,(g),T=T_0} = 29.376$ J/K mol could be obtained, which exactly matches the value given by Chase (1998) and is in close agreement with $C^0_{p,O_2\,(g),T=T_0} = 29.378 \pm 0.003$ J/mol·K given in (Cox et al., 1989). For gaseous hydrogen Cox et al. (1989) and Chase (1998) list identical values for $S^0_{H_2\,(g),T=T_0}$ and $C^0_{p,H_2\,(g),T=T_0}$.

Uncertainties for standard formation data for O_2(g), H_2(g), and H_2O(l) were adopted from Cox et al. (1989). Uncertainties for standard reaction and standard formation data for O_2(aq) were calculated from the error of the temperature parameters for reaction (Eq. 6) in Table 2.

The obtained values are in good agreement with $\Delta_f H^0_{O_2\,(aq),T=T_0} = -12{,}134$ J/mol and $S^0_{O_2\,(aq),T=T_0} = 109$ J/mol·K as given by Shock et al. (1989). A significant difference remains for the standard partial molal heat capacity for O_2(aq) at 298.15 K which is given in the same source as $C^0_{p,T=T_0} = 234$ J/mol·K. A reason for this is probably that Shock et al. in their work evaluated experimental data by Benson et al. (1979) and Stephan et al. (1956) only. Finally, with

$$\Delta_r G^0_m(T) = \sum_i \upsilon_i \Delta_f G^0_i(T) \quad (30)$$

$$\Delta_r G^0_m(T) = -RT\ln(10)\log_{10}K(T) \quad (31)$$

it was possible to calculate the temperature functions for $\log K(T)$ for reaction (Eqs 4, 5) by rearrangement of Eq. 31 and summation of corresponding temperature parameters for $\Delta_f G^0_i(T)$. Table 6 summarizes the results.

The valid range of temperature for reaction (Eq. 4) [formation of O_2(g)] is determined by the available heat capacity data for H_2O(l). For reaction (Eq. 5) [formation of O_2(aq)] it is limited by the availability of solubility data. Note, that for the latter reaction the given validity range is valid for low saline solutions only. In saline solutions where Pitzer coefficients are applied and the geochemical code works with a half-cell reaction involving O_2(aq), the valid temperature range can be lower and depends on the particular system, see Section 4.5.

TABLE 4 Standard reaction data for O_2(aq).

Data type	Unit	Value
$\Delta_r H^0_{i,T=T_0}$	J/mol	−12,411 ± 971
$\Delta_r S^0_{i,T=T_0}$	J/mol K	−97 ± 14
$\Delta_r G^0_{i,T=T_0}$	J/mol	16,593 ± 3,168
$\Delta_r C^0_{p,T=T_0}$	J/mol K	191 ± 1

TABLE 5 Standard formation data for $H_2O(l)$, $O_2(g)$, $H_2(g)$, and $O_2(aq)$. Temperature parameters for $C_p^0(T)$ with regard to the general function (Eq. 12) were fitted to values from Chase (1998).

Species	$\Delta_f H^0_{i,T=T_0}$	References	$S^0_{i,T=T_0}$	References	$\Delta_f G^0_{i,T=T_0}$	References	$C_p^0(T)$ (J/mol K)				T_{min}/T_{max}	$C^0_{p,T=T_0}$ (1)	References
	(J/mol)		(J/mol K)		(J/mol)		A_1	A_2	A_5	A_6	(K)	(J/ mol K)	
$H_2O(l)$	−285,830 ± 40 (2)	Cox et al. (1989)/ Chase (1998)	69.95 ± 0.03 (2)	Cox et al. (1989)/ Chase (1998)	−237,140 ± 41	(1)	149 ± 11	−0.33 ± 0.04	−1,056,714 ± 250,728	0.00042 ± 0.00004	280/500	75.418	Chase (1998)
$O_2(g)$	0	(By definition)	205.152 ± 0.005 (2)	Cox et al. (1989)	0	(By definition)	24.64 ± 0.03	0.0121 ± 0.0001	100,230 ± 1,433	0	298.15/500	29.376	Chase (1998)
$O_2(aq)$	−12,411 ± 971	(This work)	108 ± 14	(This work)	16,593 ± 3,168	(This work)	(3)	(3)	(3)	(3)	(3)	249.90 ± 0.07	(This work)
$H_2(g)$	0	(By definition)	130.68 ± 0.003 (2)	Cox et al. (1989)/ Chase (1998)	0	(By definition)	33.6 ± 0.2	−0.012 ± 0.001	−174,946 ± 3,652	1.01 ± 0.05×10^{-5}	298.15/500	28.836	Chase (1998)

(1) Internally calculated. (2) Data uncertainty adopted from Cox et al. (1989). (3) With our selection for the temperature dependence of Henry's law constant (Eq. 8 and Table 2) no temperature function for the standard molar heat capacity of reaction $\Delta_r C^0_{p,m}(T)$(6) can be derived. Hence, no temperature dependence for the standard molar heat capacity for $O_2(aq)$ can be given.

Using the temperature parameters in Table 6 the so-called "temperature grid" for "logK for E_H-reaction" for codes like EQ3/6 was re-calculated. The results are given in Table 7. The range of temperature for which our parameters should be used is in fact narrower than is suggested in some data files for EQ3/6 or Geochemist's Workbench.

Not surprisingly, equilibrium constants given in Table 7 are similar to those currently available in data files for geochemical codes. The values given in this work, however, can be traced back to published standard formation and solubility data.

4.3 Solubility of oxygen in electrolyte solutions at T = 298.15 K

4.3.1 The system Na^+, K^+, H^+/Cl^-, OH^- - $H_2O(l)$

All binary mixtures of the chemical systems Na^+, K^+, H^+/Cl^-, OH^- - $H_2O(l)$ were fitted simultaneously to obtain the Pitzer coefficients. As an initial coefficient $\lambda(O_2(aq)\text{-}Cl^-)$ was set to zero. Binary interaction coefficients (λ) for all cations and anions in the system could be obtained. During parameter reduction, it was found that only the ternary interaction coefficients $\zeta(O_2(aq)\text{-}Na^+\text{-}Cl^-)$ and $\zeta(O_2(aq)\text{-}K^+\text{-}Cl^-)$ are necessary to describe the system (Figure 4). Later fits of the temperature dependence parameters showed that a ternary $\zeta(O_2(aq)\text{-}Na^+\text{-}OH^-)$ coefficient becomes necessary at higher temperatures. At T = 298.15 K this coefficient was set to 0.

4.3.2 The system Na^+, K^+, H^+/HSO_4^-, SO_4^{2-} - $H_2O(l)$

The obtained binary interaction coefficients (λ) were used as initial values for the simultaneous fitting of the binary mixtures of the system Na^+, K^+, H^+/HSO_4^-, SO_4^{2-} - $H_2O(l)$. The full set of binary [$\lambda(O_2(aq)\text{-}HSO_4^-)$ and $\lambda(O_2(aq)\text{-}SO_4^{2-})$] and ternary interaction coefficients [$\zeta(O_2(aq)\text{-}Na^+\text{-} SO_4^{2-})$ and $\zeta(O_2(aq)\text{-}K^+\text{-}SO_4^{2-})$] was found do be necessary for a full description of the system (Figure 5).

For the solubility of oxygen in $NaHSO_4$ or $KHSO_4$ solutions, there are no data at T = 298.15 K available in literature. Thus, the $\zeta(O_2(aq)\text{-}K^+\text{-}HSO_4^-)$ value was not fitted from data at 298.15 K but from the only available data at 310.2 K from Lang and Zander (1986). The value was derived from a fitting using the polythermal data set (see Section 4.4). Since no temperature dependency could be retrieved, the $\zeta(O_2(aq)\text{-}K^+\text{-}HSO_4^-)$ value was set temperature independent. Therefore, the obtained value must be set to the 298.15 K term (A_0) in Eq. 10. The implementation of the $\zeta(O_2(aq)\text{-}K^+\text{-}HSO_4^-)$ coefficient had no influence of the fitting of the $\zeta(O_2(aq)\text{-}K^+\text{-}SO_4^-)$ coefficient, which was counterchecked. No value had to be fitted for $\zeta(O_2(aq)\text{-}Na^+\text{-}HSO_4^-)$ in $NaHSO_4$ solutions because the dataset derived in this work was already sufficient to describe the oxygen solubility in this solution without another ternary interaction coefficient (see Section 4.4.2).

4.3.3 The system Na^+, K^+/CO_3^{2-} - $H_2O(l)$

The previously obtained binary interaction coefficients (λ) were used as boundary conditions for the simultaneously fitting of the binary mixtures of the system Na^+,K^+/CO_3^{2-} - $H_2O(l)$. A binary [$\lambda(O_2\text{-}CO_3^{2-})$] as well as two ternary interaction coefficients [$\zeta(O_2(aq)\text{-}Na^+\text{-}CO_3^{2-})$ and $\zeta(O_2(aq)\text{-}K^+\text{-}CO_3^{2-})$] are required to describe the two systems (Figure 6).

TABLE 6 Temperature parameters for logK(T) for E_H reaction (Eqs 4, 5) according to Eq. 8.

Reaction	A_1	A_2	A_3	A_4	A_5	A_6	T_{min}/T_{max}
$2\,H_2O\,(l) \rightleftharpoons O_2\,(aq) + 2H_2\,(g)$	9.54885	0.01699	−28,638.33637	−0.78510	48,675.35491	−0.00001	273.15/373.15
$2\,H_2O\,(l) \rightleftharpoons O_2\,(g) + 2H_2\,(g)$	81.49885	0.01699	−32,263.33637	−10.76910	48,675.35491	−0.00001	298.15/473.15

TABLE 7 Calculated equilibrium constants for E_H reactions (Eqs 4, 5) as a function of temperature. Values in brackets are beyond the recommended range of validity.

T	$2\ H_2O(l) \rightarrow O_2(aq) + 2H_2(g)$	$2\ H_2O(l) \rightarrow O_2(g) + 2H_2(g)$
273.15	−94.9376	−92.2692
298.15	−85.9967	−83.0898
333.15	−75.6640	−72.5880
373.15	−66.1484	−63.0380
433.15	(−55.0488)	−52.0814
473.15	(−49.1486)	−46.3556
533.15	(−41.8864)	(−39.4232)
573.15	(−37.8522)	(−35.6368)

TABLE 8 Binary and ternary ion-neutral species interaction coefficients (λ, ζ, η) for the solubility of O_2 in salt solutions at T = 298.15 K. The uncertainty information refers to one standard deviation.

λ (species 1-2)	Value	ζ/η (species 1-2-3)	Value
$O_2(aq)$-Cl^-	0 (by definition)	$O_2(aq)$-H^+-HSO_4^-	−0.002472 ± 0.000302
$O_2(aq)$-H^+	0.02598 ± 0.00171	$O_2(aq)$-Na^+-Cl^-	−0.003767 ± 0.00579
$O_2(aq)$-Na^+	0.1315 ± 0.0093	$O_2(aq)$-Na^+-CO_3^{2-}	0.007437 ± 0.0224
$O_2(aq)$-K^+	0.135 ± 0.010	$O_2(aq)$-Na^+-SO_4^{2-}	−0.0381 ± 0.0073
$O_2(aq)$-Mg^{2+}	0.2293 ± 0.0032	$O_2(aq)$-Na^+-PO_4^{3-}	−0.0594 ± 0.0564
$O_2(aq)$-Ca^{2+}	0.2519 ± 0.0063	$O_2(aq)$-K^+-Cl^-	−0.01711 ± 0.00647
$O_2(aq)$-OH^-	0.06785 ± 0.00965	$O_2(aq)$-K^+-CO_3^{2-}	−0.09697 ± 0.017
$O_2(aq)$-SO_4^{2-}	0.1334 ± 0.0082	$O_2(aq)$-K^+-HPO_4^{2-}	−0.09593 ± 0.0286
$O_2(aq)$-HSO_4^-	0.03842 ± 0.00201	$O_2(aq)$-K^+-$H_2PO_4^-$	−0.1678 ± 0.0547
$O_2(aq)$-CO_3^{2-}	0.3234 ± 0.015	$O_2(aq)$-K^+-HSO_4^-	0.07411 ± 0.00741
$O_2(aq)$-PO_4^{3-}	0.2946 ± 0.0496	$O_2(aq)$-K^+-SO_4^{2-}	−0.1618 ± 0.078
$O_2(aq)$-HPO_4^{2-}	0.2512 ± 0.0241	$O_2(aq)$-Mg^{2+}-Cl^-	−0.006612 ± 0.00101
$O_2(aq)$-$H_2PO_4^-$	0.3718 ± 0.0233	$O_2(aq)$-Mg^{2+}-SO_4^{2-}	−0.05115 ± 0.00586
$O_2(aq)$-$H_3PO_4(aq)$	0.04841 ± 0.00241	$O_2(aq)$-Ca^{2+}-Cl^-	−0.01269 ± 0.00291
		$O_2(aq)$-Na^+-Mg^{2+}	−0.01753 ± 0.00601
		$O_2(aq)$-Cl-SO_4^{2-}	−0.01445 ± 0.00811

4.3.4 The system Na^+, K^+, H^+/H_3PO_4, $H_2PO_4^-$, HPO_4^{2-}, PO_4^{3-} - $H_2O(l)$

The O_2 solubility in solutions of Na_3PO_4, K_3PO_4, K_2HPO_4, KH_2PO_4, and H_3PO_4 were fitted simultaneously to obtain the interaction coefficients. For the System O_2-K_3PO_4 it was found that no ternary interaction coefficient $\zeta(O_2(aq)\text{-}K^+\text{-}PO_4^{3-})$ is necessary to describe the experimental data while a $\zeta(O_2(aq)\text{-}Na^+\text{-}PO_4^{3-})$ was required for the System O_2-Na_3PO_4. Also for

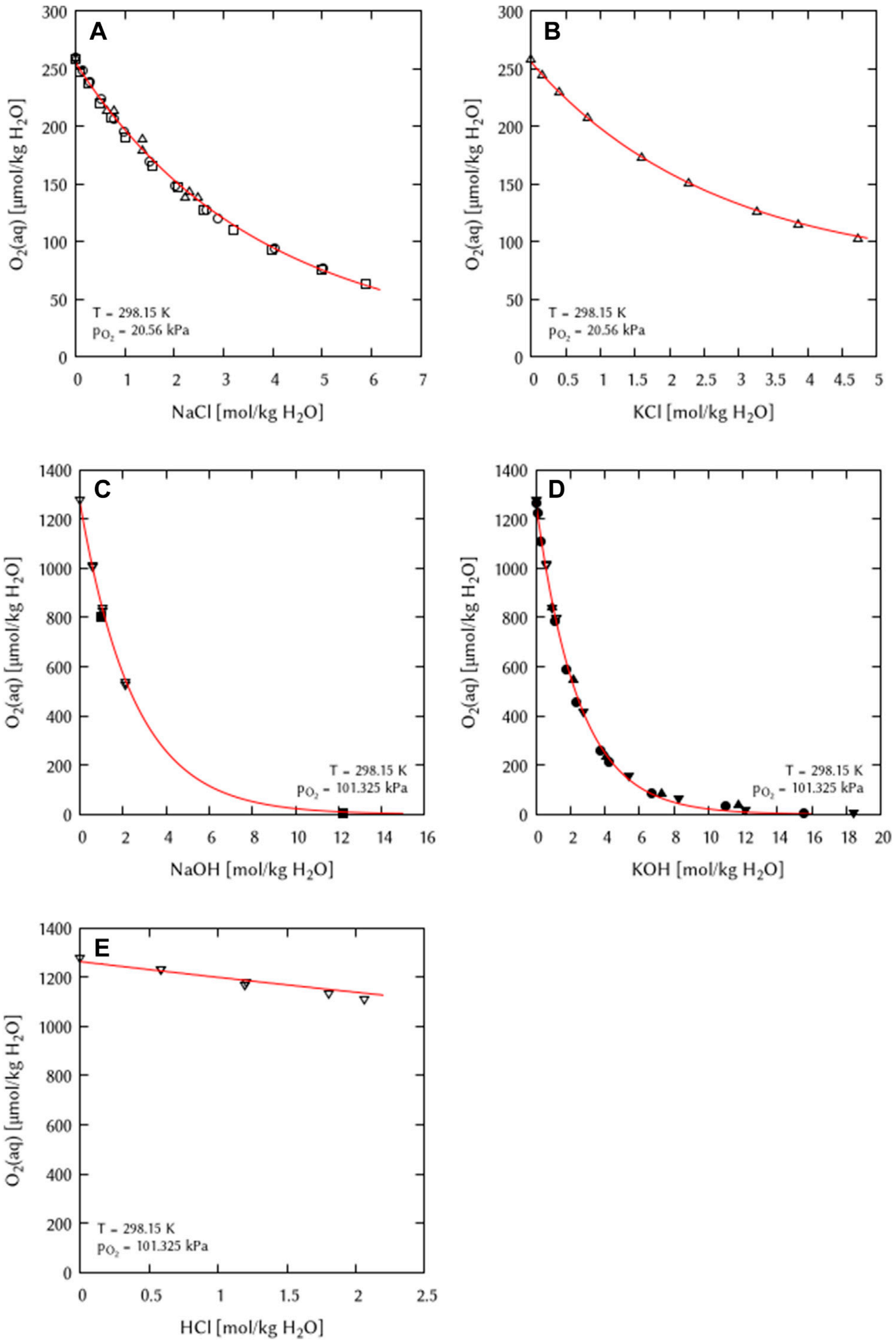

FIGURE 4
Modelling of the O_2 solubility in binary solutions of **(A)** NaCl, **(B)** KCl, **(C)** NaOH, **(D)** KOH, and **(E)** HCl as a function of the electrolyte concentration at T = 298.15 K (Points: Experimental data from: □ Millero et al. (2002a), ○ Millero et al. (2002b), △ Millero et al. (2003), ▽ Geffcken (1904), ■ Chatenet et al. (2000), ● Davis et al. (1967), ▲ Gubbins and Walker (1965), ▼ Shoor et al. (1968), Lines: this work).

the acidic potassium phosphate solutions (KH_2PO_4 and K_2HPO_4) as well as for phosphoric acid solutions, ternary interaction coefficients were found to be indispensable to fully describe these systems (Figure 7). No experimental O_2 solubility data were available for the acidic sodium phosphate solutions (NaH_2PO_4 and Na_2HPO_4). Therefore, it cannot be specified whether or not ternary interaction coefficients are necessary in these subsystems.

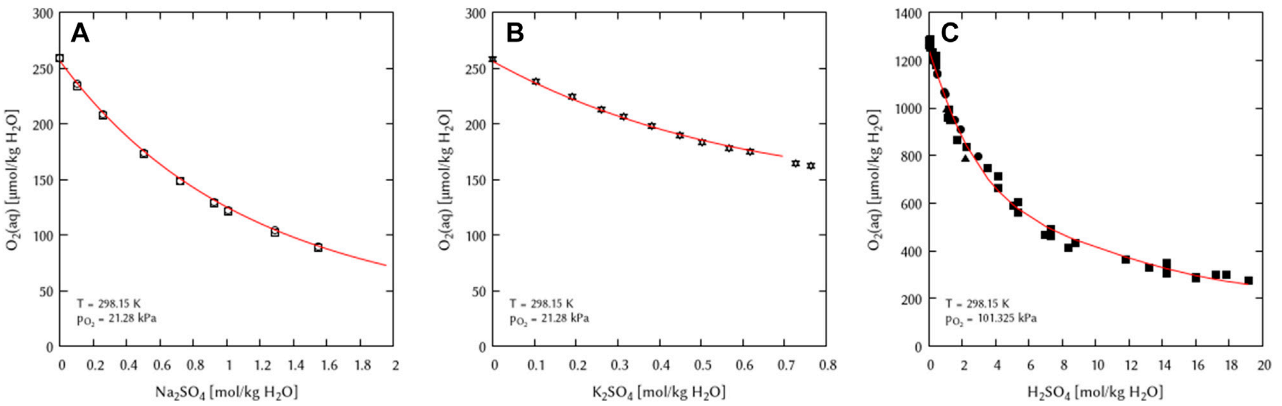

FIGURE 5
Modelling of the O_2 solubility in binary solutions of **(A)** Na_2SO_4, **(B)** K_2SO_4, and **(C)** H_2SO_4 as a function of the electrolyte concentration at T = 298.15 K (Points: Experimental data from: □ Millero et al. (2002a), ○ Millero et al. (2002b), △ Millero et al. (2003), ▽ Millero and Huang (2003), ■ Das (2005), ● Geffcken (1904), ▲ Narita et al. (1983), Lines: this work).

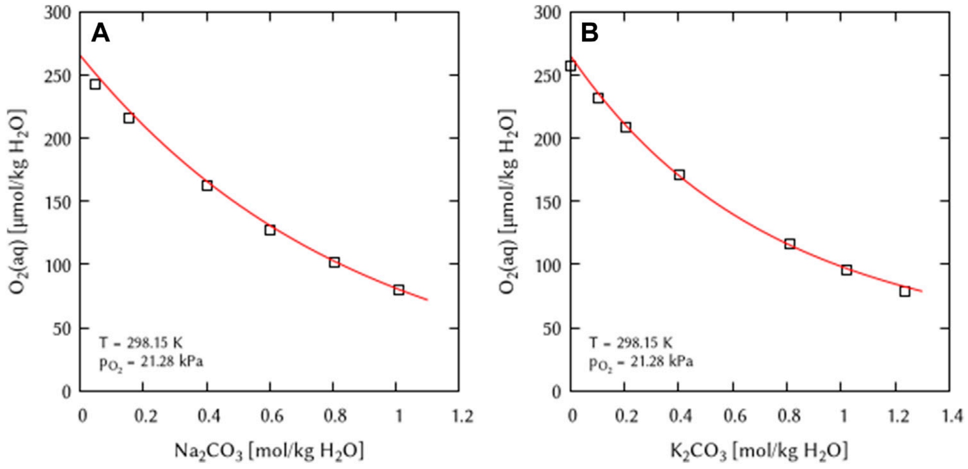

FIGURE 6
Modelling of the O_2 solubility in binary solutions of **(A)** Na_2CO_3, and **(B)** K_2CO_3 as a function of the electrolyte concentration at T = 298.15 K (Points: Experimental data from □ Khomutov and Konnik (1974), Lines: this work).

4.3.5 Earth alkaline salt solutions ($CaCl_2$, $MgCl_2$, $MgSO_4$)

Using the previously determined Pitzer coefficients as boundary conditions, the interaction coefficients for Earth alkaline salts and mixtures of salt solutions were deduced. For all three systems, a binary as well as a ternary interaction coefficient was necessary for a complete description (Figure 8).

4.3.6 Interaction coefficients for ternary salt solutions

The O_2 solubility data in ternary solutions of NaCl + $MgCl_2$ and NaCl + Na_2SO_4 was used to deduce the coefficients $\eta(O_2(aq)\text{-}Na^+\text{-}Mg^{2+})$ and $\eta(O_2(aq)\text{-}Cl^-\text{-}SO_4^{2-})$. The O_2 solubility data in the ternary solution of Na_2SO_4 + $MgSO_4$ was not used in the fitting procedure but to verify the obtained η coefficient (Figure 9). The obtained calculation results are in good agreement with the experimental data. The O_2 solubility data in the ternary solution of $MgCl_2$ + $MgSO_4$ was also not used in the fitting, the authors claimed the usage of two different stock solutions within the experiment (Millero et al., 2002a). Only one data point matches with the calculation suggesting that—in agreement with the primary source—this point belonged to one charge of stock solutions while the other points belong to the experiments with other stock solutions.

Millero et al. (2002a) also experimentally studied O_2 solubility in the quaternary-reciprocal systems Na^+, Mg^{2+}/Cl^-, SO_4^{2-} - H_2O were given. Interaction coefficients for these kind of systems could not be deduced because the Pitzer ion-interaction approach is limited to coefficients for ternary interactions while in this case a coefficient would be necessary for an interaction between four different species (O_2-c-a-a'/O_2-c-c'-a) in solution.

The obtained Pitzer interaction coefficients—ion-neutral species pairs, λ and ion-neutral species triplets, ζ and η—are given in Table 8.

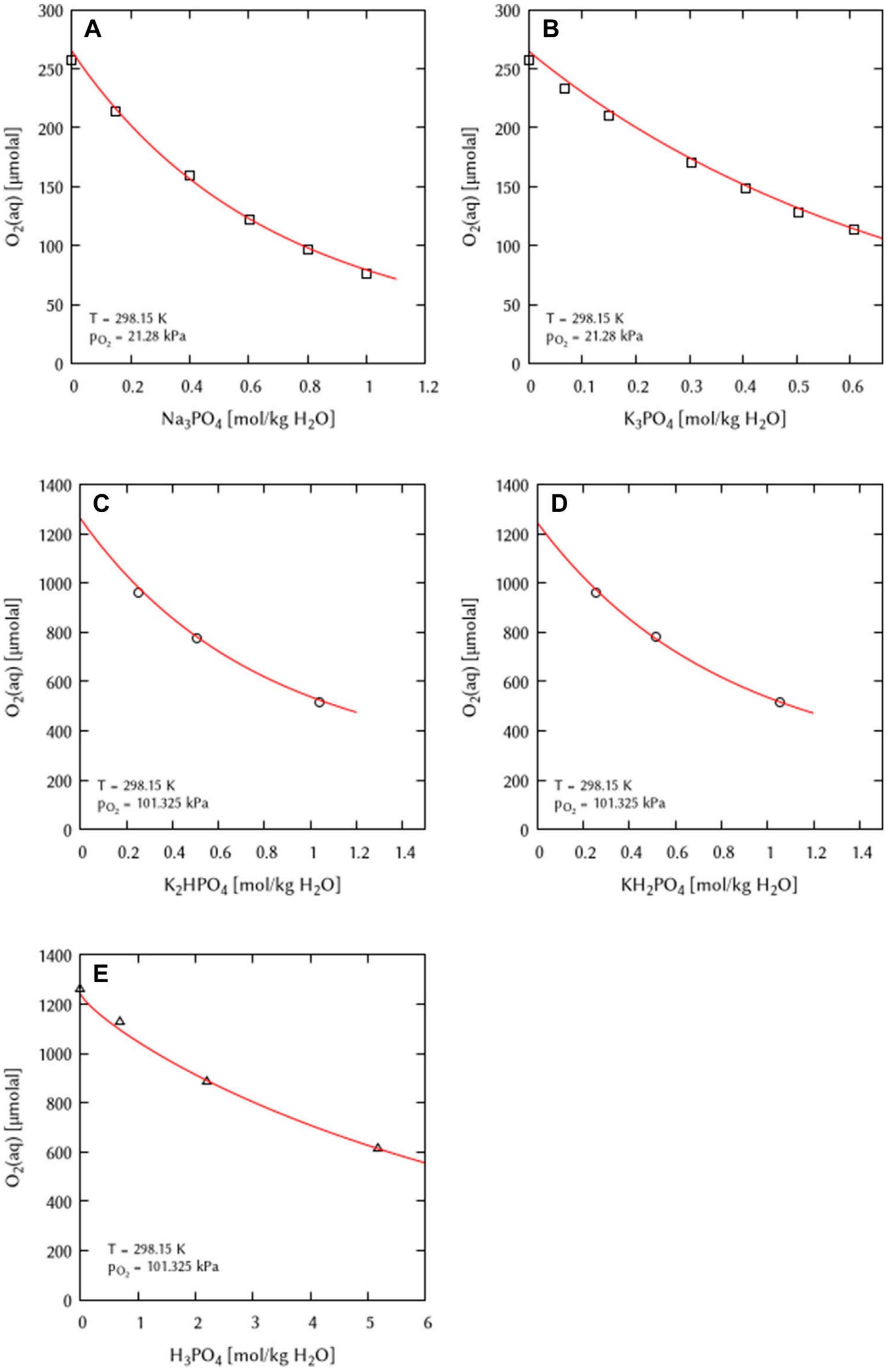

FIGURE 7
Modelling of the O_2 solubility in binary solutions of **(A)** Na_3PO_4, **(B)** K_3PO_4, **(C)** K_2HPO_4, **(D)** KH_2PO_4, and **(E)** H_3PO_4 as a function of electrolyte concentration at T = 298.15 K (Points: Experimental data from □ Khomutov and Konnik (1974), ○ Iwai et al. (1993), △ Gubbins and Walker (1965), Lines: this work).

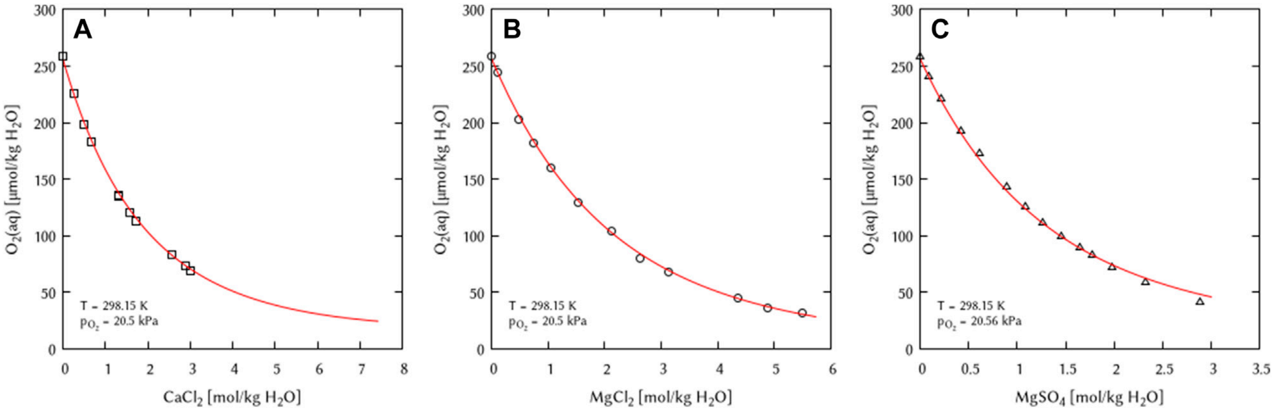

FIGURE 8
Modelling of the O_2 solubility in binary solutions of **(A)** $CaCl_2$, **(B)** $MgCl_2$, and **(C)** $MgSO_4$ as a function of electrolyte concentration at T = 298.15 K (Points: Experimental data from □ Millero et al. (2003), ○ Millero et al. (2002a), △ Millero et al. (2002b) Lines: this work).

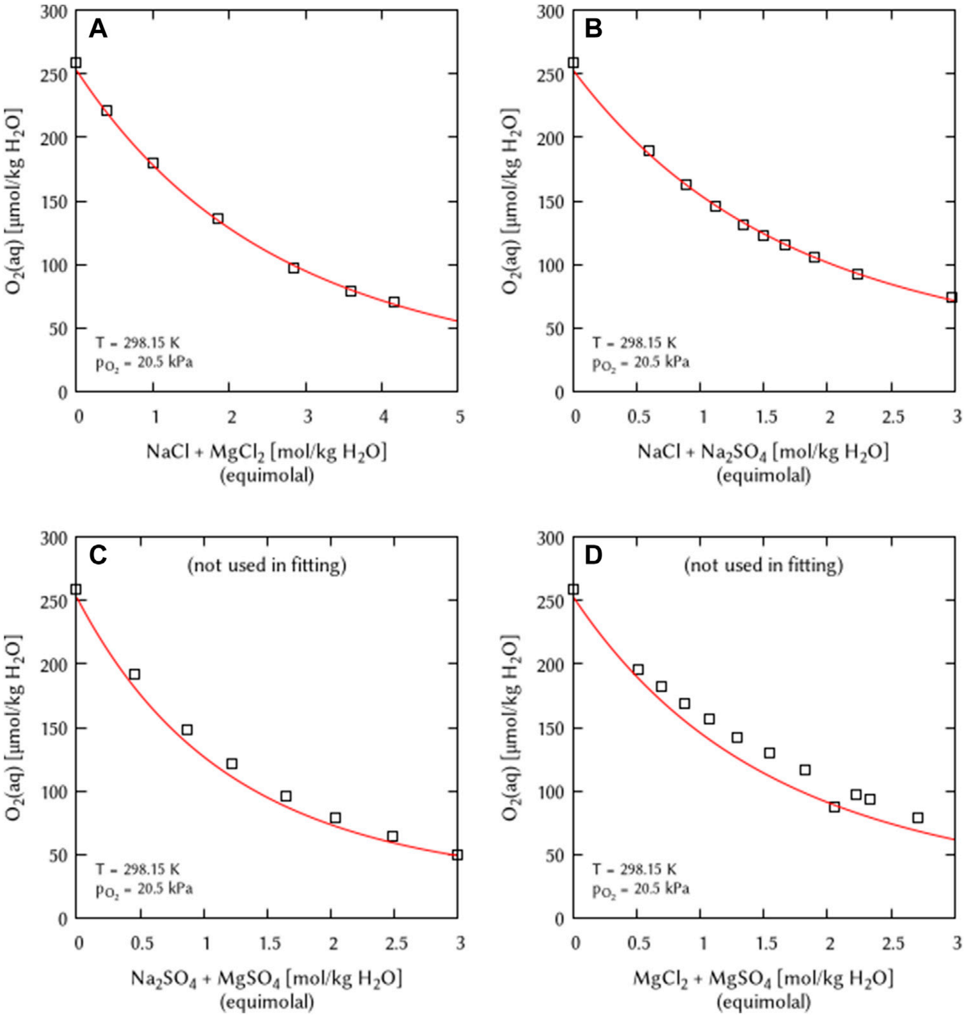

FIGURE 9
Modelling of the O_2 solubility in equimolal solutions of **(A)** NaCl + $MgCl_2$, **(B)** NaCl + Na_2SO_4, **(C)** Na_2SO_4+$MgSO_4$, and **(D)** $MgCl_2$ + $MgSO_4$ as a function of electrolyte concentration at T = 298.15 K (Points: Experimental data from □ Millero et al. (2002a), Lines: this work).

TABLE 9 Parameters for the temperature dependency function of the binary and ternary interaction coefficients (λ, ζ). The uncertainty information refers to one standard deviation.

λ/ζ (Species: 1-2-3)	X_0	X_1	X_2
$O_2(aq)$-Cl^-	0 (by definition)	0 (by definition)	0 (by definition)
$O_2(aq)$-H^+	0.02598 ± 0.00171	4,941 ± 533	16.4 ± 1.8
$O_2(aq)$-Na^+	0.1315 ± 0.0093	2,897 ± 274	9.614 ± 0.947
$O_2(aq)$-K^+	0.135 ± 0.010	−1,004 ± 527	−3.513 ± 1.79
$O_2(aq)$-Mg^{2+}	0.2293 ± 0.0032	2,981 ± 860	9.9 ± 2.9
$O_2(aq)$-Ca^{2+}	0.2519 ± 0.0063	2,821 ± 651	9.449 ± 2.26
$O_2(aq)$-OH^-	0.06785 ± 0.00965	1,230 ± 280	3.934 ± 0.882
$O_2(aq)$-SO_4^{2-}	0.1334 ± 0.0082	−6,654 ± 1,150	−22.01 ± 3.38
$O_2(aq)$-HSO_4^-	0.03842 ± 0.00201	−45.38 ± 27.7	0 (fixed)
$O_2(aq)$-H^+-HSO_4^-	−0.002472 ± 0.000302	0 (fixed)	0 (fixed)
$O_2(aq)$-Na^+-Cl^-	−0.003767 ± 0.00579	−1,075 ± 128	−3.663 ± 0.442
$O_2(aq)$-Na^+-OH^-	0 (fixed)	−40.7 ± 17.9	0 (fixed)
$O_2(aq)$-Na^+-SO_4^{2-}	−0.0381 ± 0.0073	4,216 ± 1,820	13.49 ± 5.92
$O_2(aq)$-K^+-Cl^-	−0.01711 ± 0.00647	747.7 ± 319	2.464 ± 1.07
$O_2(aq)$-K^+-SO_4^{2-}	−0.1618 ± 0.078	164.7 ± 102	0 (fixed)
$O_2(aq)$-Mg^{2+}-Cl^-	−0.006612 ± 0.00101	−875.5 ± 351	−2.974 ± 1.18
$O_2(aq)$-Mg^{2+}-SO_4^{2-}	−0.05115 ± 0.00586	5,181 ± 550	16.86 ± 1.86
$O_2(aq)$-Ca^{2+}-Cl^-	−0.01269 ± 0.00291	24.49 ± 1.81	0 (fixed)

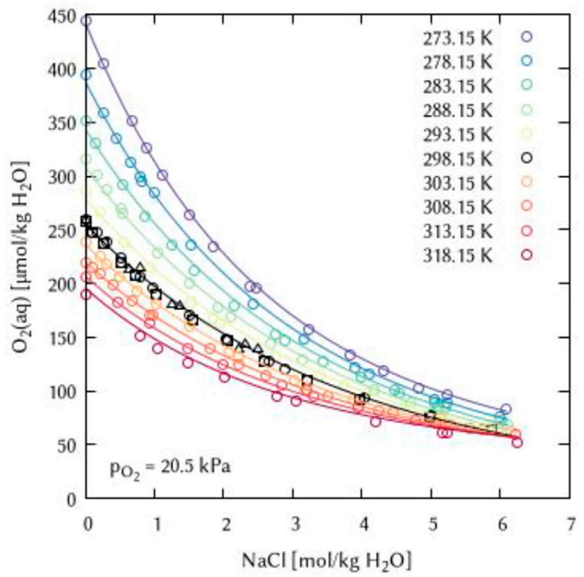

FIGURE 10
Modelling of the O_2 solubility in sodium chloride solution as a function of temperature and NaCl concentration. (Points: Experimental data from □ Millero et al. (2002a), ○ Millero et al. (2002b), △ Millero et al. (2003), Lines: this work).

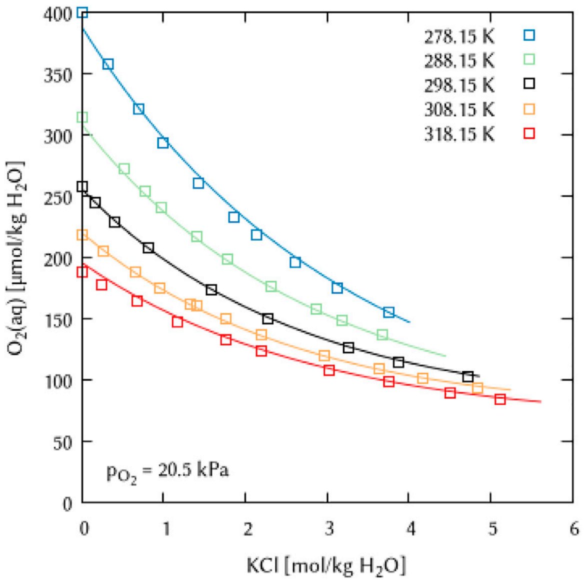

FIGURE 11
Modelling of the O_2 solubility in potassium chloride solution as a function of temperature and KCl concentration. (Points: Experimental data from □ Millero et al. (2003), Lines: this work).

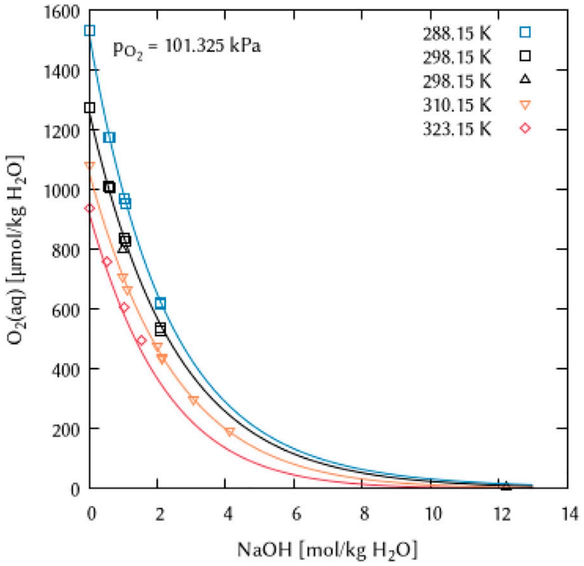

FIGURE 12
Modelling of the O_2 solubility in sodium hydroxide solution as a function of temperature and NaOH concentration. (Points: Experimental data from □ Geffcken (1904), △ Chatenet et al. (2000), ▽ Lang and Zander (1986) and ☐ Bruhn et al. (1965), Lines: this work).

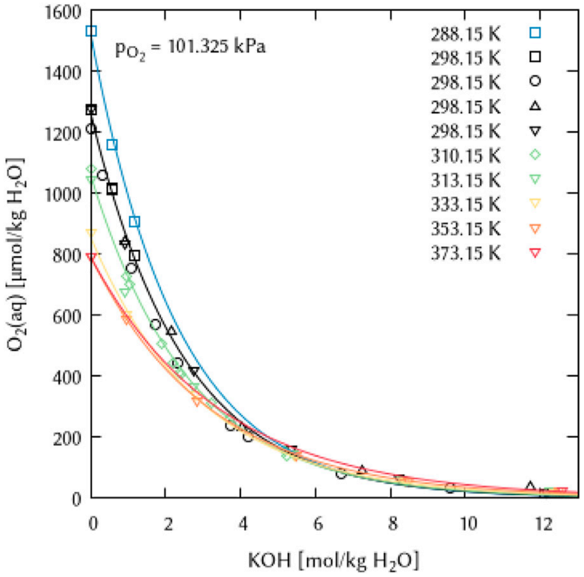

FIGURE 13
Modelling of the O_2 solubility in potassium hydroxide solution as a function of temperature and KOH concentration. (Points: Experimental data from □ Geffcken (1904), ○ Davis et al. (1967), △ Gubbins and Walker (1965), ▽ Shoor et al. (1968) and ☐ Lang and Zander (1986), Lines: this work).

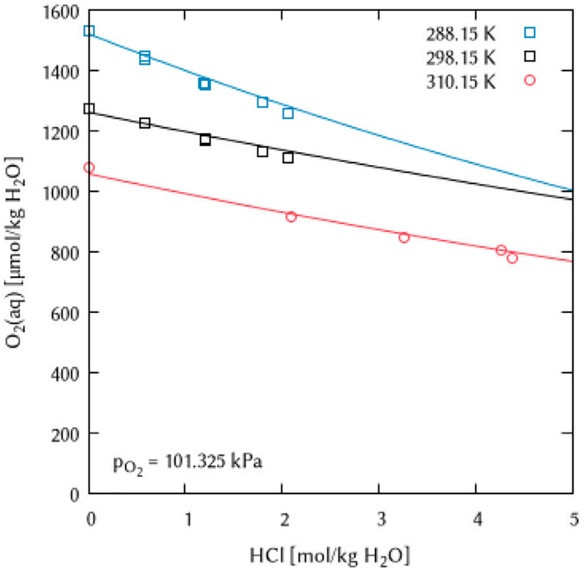

FIGURE 14
Modelling of the O_2 solubility in hydrochloric acid solution as a function of temperature and HCl concentration. (Points: Experimental data from □ Geffcken (1904) and ○ Lang and Zander (1986), Lines: this work).

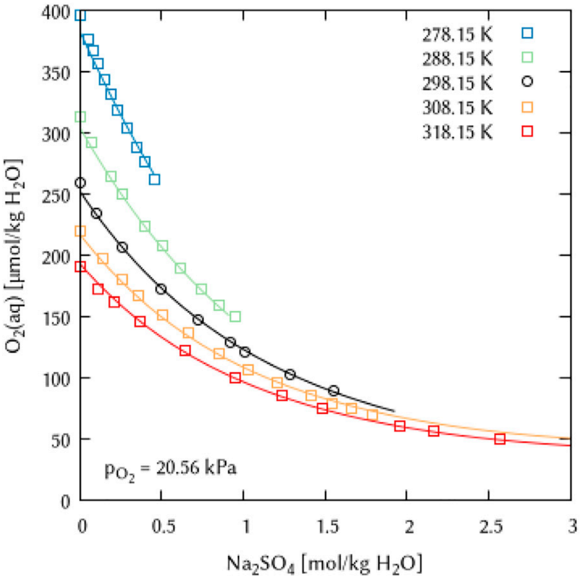

FIGURE 15
Modelling of the O_2 solubility in sodium sulfate solution as a function of temperature and Na_2SO_4 concentration. (Points: Experimental data from ○ Millero et al. (2002a) and □ Millero et al. (2002b), Lines: this work).

4.4 Temperature dependency of O_2 solubility in salt solutions

For the polythermal description of O_2 solubility in electrolyte solutions, the Pitzer interaction coefficients valid for 298.15 K were used as a boundary condition for fitting of the temperature parameters for Eq. 10 on top of them. These parameter fittings were run individually for each electrolyte and then iterated until no changes were observed anymore.

4.4.1 The system Na^+, K^+, H^+/Cl^-, OH^- - $H_2O(l)$

The binary systems of the alkali metal chlorides, alkali metal hydroxides and hydrochloric acid allowed to determine the temperature dependency for two binary interaction coefficients: $\lambda(O_2(aq)\text{-}Na^+)$, $\lambda(O_2(aq)\text{-}K^+)$, and $\lambda(O_2(aq)\text{-}H^+)$ as well as for two ternary coefficients $\zeta(O_2(aq)\text{-}Na^+\text{-}Cl^-)$ and $\zeta(O_2(aq)\text{-}K^+\text{-}Cl^-)$ (see Figures 10, 11). For each coefficient, the temperature dependency can be described using only two of the six parameters of Eq. 10, which are the $X_1\,(1/T - 1/T_r)$ and the $X_2 \ln(T/T_r)$ terms.

For the ternary coefficient $\zeta(O_2(aq)\text{-}Na^+\text{-}OH^-)$ with a value of 0 at T = 298.15 K, only the first parameter of the temperature dependency equation was found to be necessary to adequately describe the experimental points available (Figure 12).

Even though the few available experimental points on O_2 solubility at higher KOH concentrations and raised temperatures (T = 353.15–373.15 K) are not well reproduced in terms of the expected trend of temperature dependence (Figure 13), the introduction of another ternary coefficient $\zeta(O_2(aq)\text{-}K^+\text{-}OH^-)$ or temperature dependence parameters thereof did not lead to any improvement. Furthermore, it can be assumed that the deviation of the calculation from the expected trend (lowering the O_2 solubility with increasing temperature) in this concentration and temperature range is lower than the experimental uncertainty to be expected.

For solutions of hydrochloric acid, even in the polythermal system, no ternary interaction coefficient and thus no temperature parameters were necessary to describe the very few points on O_2 solubility as a function of temperature and electrolyte concentration (Figure 14).

4.4.2 The system Na^+, K^+, H^+/HSO_4^-, SO_4^{2-} - $H_2O(l)$

In the systems of alkali metal sulfate and sulfuric acid solutions, it was possible to obtain parameters describing the temperature dependence of the Pitzer interaction coefficients. Again, the fitting of a maximum of two terms was sufficient to describe the available data points for the Na_2SO_4 and H_2SO_4 systems (Figures 15, 16).

In the K_2SO_4 solutions, O_2 solubility is poorly described at both very low (278.15 K) and very high (318.15 K) temperatures, yielding too high values with increasing electrolyte concentration (Figure 17) in both cases. Since the temperature dependence equation of the Pitzer interaction coefficients in the geochemical codes centers around the value of 298.15 K (see Eq. 10), these effects cannot be compensated, as a fit improvement in the temperature range above 298.15 K causes a corresponding deterioration below 298.15 K and *vice versa*.

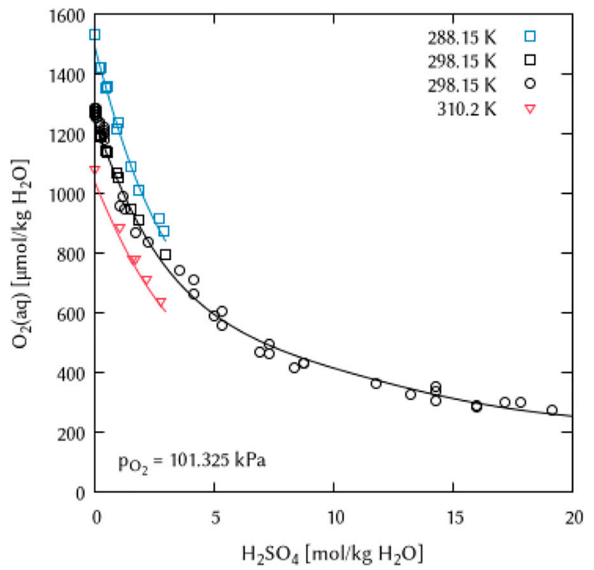

FIGURE 16
Modelling of the O_2 solubility in sulfuric acid solution as a function of temperature and H_2SO_4 concentration. (Points: Experimental data from □ Geffcken (1904), ○ Das (2005) and ▽ Lang and Zander (1986), Lines: this work).

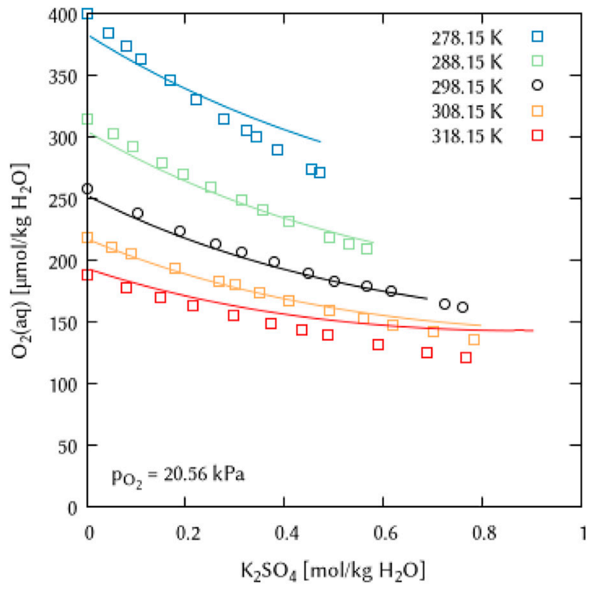

FIGURE 17
Modelling of the O_2 solubility in potassium sulfate solution as a function of temperature and K_2SO_4 concentration. (Points: Experimental data from ○ Millero et al. (2003) and □ Millero and Huang (2003), Lines: this work).

The systems Na^+/HSO_4^- - $H_2O(l)$ and K^+/HSO_4^- - $H_2O(l)$ could not be used for the estimation of the ternary interaction coefficients $\zeta(O_2(aq)\text{-}Na^+\text{-}HSO_4^-)$ or $\zeta(O_2(aq)\text{-}K^+\text{-}HSO_4^-)$ because of the lack of O_2 solubility data at 298.15 K. The only available experimental datasets are at 310.2 K generated by Lang and Zander (1986). Thus, it is not possible to obtain a ζ coefficient at 298.15 K that is necessary for the fitting with the temperature dependency equation used in this study. The systems Na^+/HSO_4^- - $H_2O(l)$ and K^+/HSO_4^- - $H_2O(l)$ were

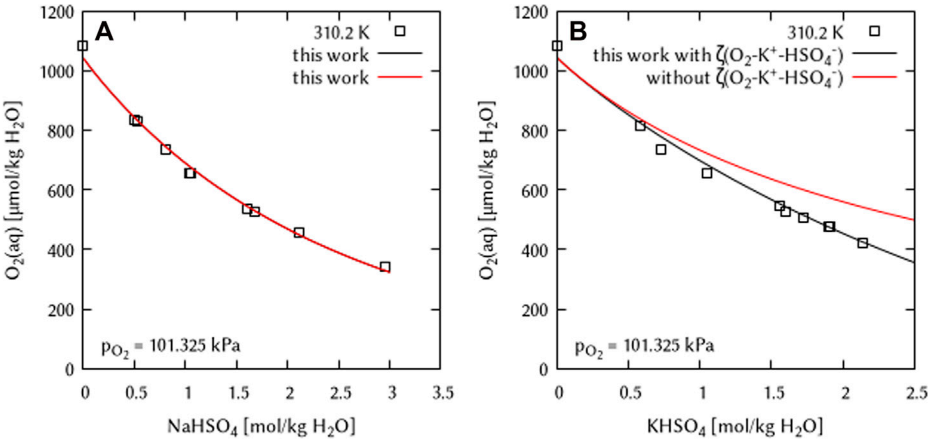

FIGURE 18
Modelling of the O_2 solubility in binary solutions of **(A)** $NaHSO_4$, and **(B)** $KHSO_4$ as a function of electrolyte concentration at 310.2 K using the Pitzer coefficient set of this work. [Points: Experimental data from □ Lang and Zander (1986), Lines: this work].

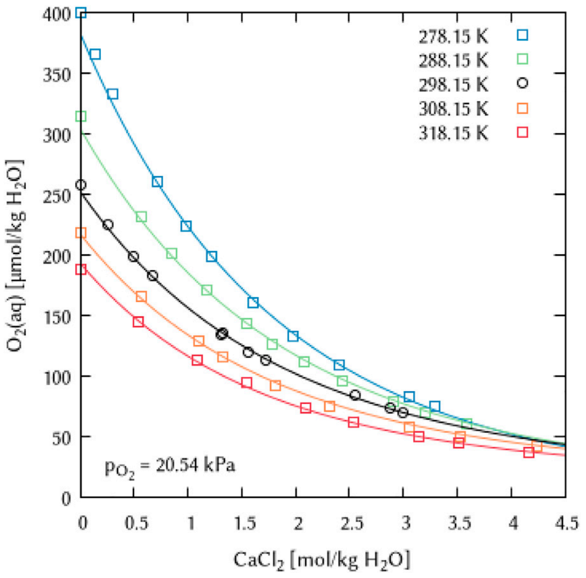

FIGURE 19
Modelling of the O_2 solubility in calcium chloride solution as a function of temperature and $CaCl_2$ concentration. [Points: Experimental data from ○ Millero et al. (2003) and □ Millero and Huang (2003), Lines: this work].

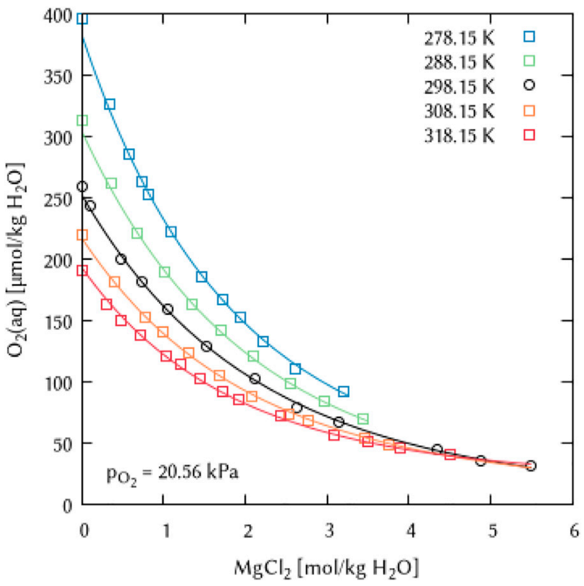

FIGURE 20
Modelling of the O_2 solubility in magnesium chloride solution as a function of temperature and $MgCl_2$ concentration. [Points: Experimental data from ○ Millero et al. (2002a) and □ Millero et al. (2002b), Lines: this work].

modelled using the obtained dataset. Results indicate that no ternary interaction coefficient $\zeta(O_2(aq)\text{-}Na^+\text{-}HSO_4^-)$ is necessary to describe the O_2 solubility data in the system Na^+/HSO_4^- - $H_2O(l)$ (see Figure 18).

Modelling results for the chemical system K^+/HSO_4^- - $H_2O(l)$ without an ternary interaction coefficient show a discrepancy between the experimental results from Lang and Zander (1986) and the modelling. Thus, a ternary interaction coefficient $\zeta(O_2(aq)\text{-}K^+\text{-}HSO_4^-)$ was fitted at T = 310.2 K. Due to the lack of solubility data at other temperatures, no parameters for the temperature function could be derived. Therefore, this ternary coefficient was assumed to be temperature independent.

4.4.3 Earth alkaline salt solutions ($CaCl_2$, $MgCl_2$, $MgSO_4$)

The binary systems of the alkaline Earth metal salts $CaCl_2$, $MgCl_2$ and $MgSO_4$ were used to derive the temperature

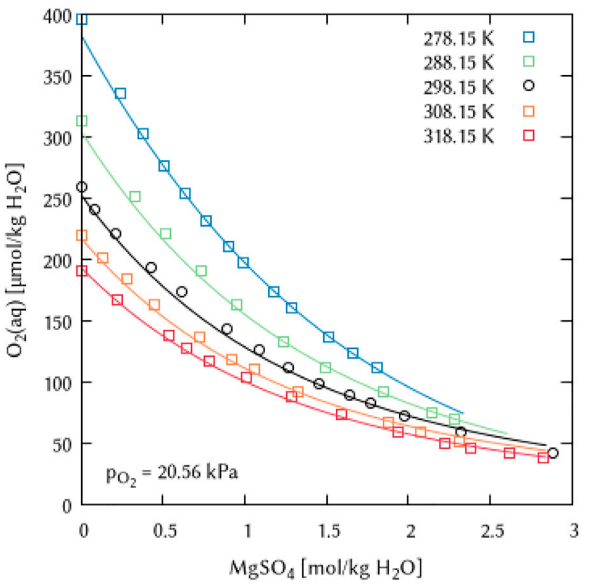

FIGURE 21
Modelling of the O_2 solubility in magnesium sulfate solution as a function of temperature and $MgSO_4$ concentration. [Points: Experimental data from ○ Millero et al. (2002a) and □ Millero et al. (2002b), Lines: this work].

dependency parameters for the binary interaction coefficients $\lambda(O_2(aq)\text{-}Ca^{2+})$ and $\lambda(O_2(aq)\text{-}Mg^{2+})$ as well as for the ternary coefficients $\zeta(O_2(aq)\text{-}Ca^{2+}\text{-}Cl^-)$, $\zeta(O_2(aq)\text{-}Mg^{2+}\text{-}Cl^-)$ and $\zeta(O_2(aq)\text{-}Mg^{2+}\text{-}SO_4{}^{2-})$, see Figures 19–21. For the magnesium salt solutions, the temperature dependency of the interaction coefficients requires two parameters $[X_1(1/T - 1/T_r)$ and $X_2 \ln(T/T_r)]$ while for the calcium chloride solution, the $X_1(1/T - 1/T_r)$ temperature parameter alone was sufficient for the complete description of the system.

The full list of obtained temperature parameters for the polythermal Pitzer interaction coefficients is given in Table 9.

For the carbonate, the phosphate, and ternary systems in the oceanic salt system, no temperature dependency parameters of the interaction coefficients could be deduced so far due to the very limited data available. Therefore, for polythermal datasets, the temperature function parameters X_1–X_5 for the Pitzer interaction coefficients are set to zero.

4.5 Validity ranges

The conservative validity range for this dataset is given as follows:

- Temperature: T = 273–318 K,

TABLE 10 Validity ranges (T, I, p) according to the experimental conditions used for the parameter fitting.

Electrolyte	Temperature [K]	Electrolyte concentration [mol/kg H_2O]	O_2 partial pressure [kPa]	Total pressure [kPa]
Pure water	273.15–373.15	0	101.325	101.325
NaCl	273.15–318.15	0–6.5	20.56	101.325
KCl	278.15–318.15	0–5.5	20.56	101.325
$MgCl_2$	278.15–318.15	0–5.5	20.56	101.325
$CaCl_2$	278.15–318.15	0–4.5	20.54	101.325
HCl	288.15–310.2	0–5	101.325	101.325
H_2SO_4	288.15–310.2	0–20	101.325	101.325
Na_2SO_4	278.15–318.15	0–2.7	20.56	101.325
K_2SO_4	278.15–318.15	0–0.8	20.56	101.325
$MgSO_4$	278.15–318.15	0–3	20.56	101.325
NaOH	288.15–323.15	0–13	101.325	101.325
KOH	288.15–373.15	0–19	101.325	101.325
Na_2CO_3	298.15	0–2.2	21.28	101.325
K_2CO_3	298.15	0–1.3	21.28	101.325
H_3PO_4	298.15	0–6	101.325	101.325
KH_2PO_4	298.15	0–1.2	101.325	101.325
K_2HPO_4	298.15	0–1.2	101.325	101.325
K_3PO_4	298.15	0–0.6	21.28	101.325
Na_3PO_4	298.15	0–1	21.28	101.325

- Ionic strength: I ≤ 5 mol/kg H_2O,
- O_2 partial pressure: $p(O_2) \leq 101.325$ kPa.

This generalized specification is not valid for all chemical subsystems. The validity ranges of temperature and ionic strength of the individual background electrolyte are given in Table 10 according to the experimental data sets used for the parameter fitting.

4.6 Known deficiencies

4.6.1 Missing interactions coefficient for binary solutions

For the O_2 solubility in binary solutions of bicarbonates only one experimental dataset (O_2 in $NaHCO_3$ solutions with T = 323–423 K and p = 1–5 MPa) is available in literature (Broden and Simonson, 1978) and (Broden and Simonson, 1979). It was not possible to extrapolate to 298.15 K and 101.325 kPa using the temperature and pressure dependency functions given in the articles or other extrapolation methods. Therefore, neither this binary interaction coefficient $\lambda(O_2(aq)\text{-}HCO_3^-)$ nor its temperature function parameters could be deduced so far.

4.6.2 Missing interaction coefficients for ternary solutions

There are no O_2 solubility data for other ternary mixtures of salt solutions published in literature beside the work of Millero et al. (2002a) (system Na^+, Mg^{2+}/Cl^-, SO_4^{2-} - $H_2O(l)$ at 298.15 K). Therefore only the interaction coefficients $\zeta(O_2(aq)\text{-}Na^+\text{-}Mg^{2+})$ and $\zeta(O_2(aq)\text{-}Cl^-\text{-}SO_4^{2-})$ for these ternary systems could be deduced. Here, especially the ternary interaction coefficients with hydroxide [$\zeta(O_2(aq)\text{-}OH^-\text{-}Cl^-)$ and $\zeta(O_2(aq)\text{-}OH^-\text{-}SO_4^{2-})$] would be of interest, since the O_2 solubility decreases significantly more in alkaline solutions than in neutral or acidic electrolyte solutions. For all other ternary (or higher) mixtures, no interaction coefficients could be obtained. The same applies to the temperature dependence of the O_2 interaction parameters in ternary electrolyte solutions.

Ternary interactions coefficients for systems with alkaline Earth ions (Mg^{2+}, Ca^{2+}) and bivalent or trivalent anions (CO_3^{2-}, SO_4^{2-}, PO_4^{3-})—except $\zeta(O_2(aq)\text{-}Mg^{2+}\text{-}SO_4^{2-})$—are assumed to be unnecessary because of the low solubility of the formed solid phases, e.g., calcite, dolomite, gypsum or apatite. The contributions of these ions in such solutions are sufficiently covered by the binary interaction coefficients.

5 Conclusion

In this paper, a set of thermodynamic formation data for dissolved oxygen $O_2(aq)$ consistent with standard formation data for $O_2(g)$, $H_2(g)$, $H_2O(l)$, and a temperature-dependent Henry's law constant is presented. In combination with binary and ternary Pitzer coefficients they allow the calculation of oxygen solubility in concentrated salt solutions of the system Na^+, K^+, H^+, Ca^{2+}, Mg^{2+}/Cl^-, SO_4^{2-}, CO_3^{2-}, PO_4^{3-}, OH^- - $H_2O(l)$, including also the associated acids and bases. By combining a very large number of experimental papers, which have been subjected to critical evaluation, the data set is based on a wide range of data, which in turn ensures robustness.

Contrary to values for the so-called log$K$-E_H-grid circulating among geochemical modelers, values given herein can be traced back to experimental solubility data and standard formation data. Moreover, their validity in terms of temperature and solution composition is clearly stated.

The use of the dataset allows a more accurate description of the redox state of saline solutions. This does not only improve the description of the solubility of redox-sensitive radionuclides, but is also applicable to a variety of other processes—from material corrosion to microbial activity. The presented dataset allows modeling with a broader application range than the data compilations previously available in the literature, both in terms of the number of chemical subsystems and the temperature range. With a more precise description of redox conditions, it is possible to further reduce conservatism in safety assessment calculations, not only in the context of a nuclear repository.

Data availability statement

The original contributions presented in the study are included in the article/Supplementary Material, further inquiries can be directed to the corresponding author.

Author contributions

FB: conceptualization, methodology, data analysis, software, fitting (Henry's law constant and Pitzer ion-interaction coefficients), writing; HM: methodology and data review (thermodynamics), writing; VB: review and editing, supervision, funding acquisition.

Funding

This work was funded by BGE—the federal company for radioactive waste disposal, with the contract number 45181017.

Conflict of interest

The authors declare that the research was conducted in the absence of any commercial or financial relationships that could be construed as a potential conflict of interest.

Publisher's note

Supplementary material

The Supplementary Material for this article can be found online at: https://www.frontiersin.org/articles/10.3389/fnuen.2023.1158109/full#supplementary-material

References

Armenante, P. M., and Karlsson, H. T. (1982). Salting-out parameters for organic acids. *J. Chem. Eng. Data* 27, 155–156. doi:10.1021/je00028a016

Battino, R., Cargill, R. W., Chen, C. T. A., Clever, H. L., Roth, J. A., Cramer, A. L., et al. (1981). *IUPAC solubility data Series vol. 7: Oxygen and ozone*. Oxford: Pergamon Press, 533.

Baykut, S., and Aroguz, A. Z. (1989). The effect of different electrolytes on the solubility of gases in water. *Chim. Acta Turc.* 17, 365–375.

Benson, B. B., Krause, D., Jr., and Peterson, M. A. (1979). The solubility and isotopic fractionation of gases in dilute aqueous solution. I. Oxygen. *J. Solut. Chem.* 8, 655–690. doi:10.1007/BF01033696

Bethke, C. M. (2022). *Geochemical and biogeochemical reaction modeling*. 3rd Edition. Cambridge: Cambridge University Press. ISBN-13: 978-1-108-79086-4.

Bikov, M. M. (1937). The solubility of gases in solutions of salts under pressure at high temperature. *Tr. Voronezhsk. Gos. Univ.* 9, 29–57.

Blanc, P., Lassin, A., Piantone, P., Azaroual, M., Jacquemet, N., Fabbri, A., et al. (2012). Thermoddem: A geochemical database focused on low temperature water/rock interactions and waste materials. *Appl. Geochem.* 27 (10), 2107–2116. doi:10.1016/j.apgeochem.2012.06.002

Bohr, C. (1910). Über die Löslichkeit von Gasen in konzentrierter Schwefelsäure und in Mischungen von Schwefelsäure und Wasser. *Z. Phys. Chem.* 71, 47–50. doi:10.1515/zpch-1910-7104

Broden, A., and Simonson, R. (1978). Solubility of oxygen Part 1. Solubility of oxygen in water at temperatures ≤150°C and pressures ≤5MPa. *Sven. Papperstidn.* 81, 541–544.

Broden, A., and Simonson, R. (1979). Solubility of oxygen Part 2. Solubility of oxygen in sodium hydrogen carbonate and sodium hydroxide solutions at temperatures ≤150°C and pressures ≤5MPa. *Sven. Papperstidn.* 82, 487–491.

Bruhn, G., Gerlach, J., and Pawlek, F. (1965). Untersuchungen über die Löslichkeit von Salzen und Gasen in Wasser und wässrigen Lösungen bei Temperaturen oberhalb von 100 °C (Studies on the solubility of salts and gases in water and aqueous solutions at temperatures above 100 °C). *Z. Anorg. Allg. Chem.* 337 (1-2), 68–79. doi:10.1002/zaac.19653370111

Carpenter, J. H. (1966). New measurements of oxygen solubility in pure and natural Water. *Limnol. Ocean.* 11, 264–277. doi:10.4319/lo.1966.11.2.0264

M. W. Chase, Jr. (Editor) (1998). "Journal of physical and chemical reference data, monograph No. 9, NIST-JANAF thermochemical Tables," *Published by the American chemical society and the American institutes of physics for the national Institute of standards and technology*. Fourth Edition (Gaithersburg, Maryland: National Institute of Standards and Technology), 20899.

Chatenet, M., Aurousseau, M., and Durand, R. (2000). Electrochemical measurement of the oxygen diffusivity and solubility in concentrated alkaline media on rotating ring-disk and disk electrodes—Application to industrial chlorine-soda electrolyte. *Electrochim. Acta* 45, 2823–2827. doi:10.1016/S0013-4686(00)00325-X

Christov, C., and Møller, N. (2004). A chemical equilibrium model of solution behavior and solubility in the H-Na-K-Ca-OH-Cl-HSO_4-SO_4-H_2O system to high concentration and temperature. *Geochim. Cosmochim. Acta* 68 (18), 3717–3739. doi:10.1016/j.gca.2004.03.006

Clegg, S., and Brimblecombe, P. (1990). The solubility and activity coefficient of oxygen in salt solutions and brines. *Geochim. Cosmochim. Acta* 54, 3315–3328. doi:10.1016/0016-7037(90)90287-U

Clever, H. L., Battino, R., Miyamoto, H., Yampolski, Y., and Young, C. L. (2014). IUPAC-NIST solubility data Series. 103. Oxygen and ozone in water, aqueous solutions, and organic liquids (supplement to solubility data Series volume 7). *J. Phys. Chem. Ref. Data* 43, 033102-1–033102-209. doi:10.1063/1.4883876

Cox, J. D. (1978). CODATA recommended key values for thermodynamics, 1977 Report of the CODATA Task Group on key values for thermodynamics, 1977. *J. Chem. Thermodyn.* 10 (10), 903–906. doi:10.1016/0021-9614(78)90050-2

Cox, J. D., Wagman, D. D., and Medvedev, V. A. (1989). *CODATA key values for thermodynamics*. New York: Hemisphere Publishing Corp.

Cramer, S. D. (1984). Oxygen solubility in brines. *Ind. Eng. Chem. Process. Des. Dev.* 23 (3), 618–620. doi:10.1021/i200026a035

Cramer, S. D. (1980). The solubility of oxygen in brines from 0 to 300 °C. *Ind. Eng. Chem. Process. Des. Dev.* 19 (2), 300–305. doi:10.1021/i260074a018

Das, T. N. (2005). Saturation concentration of dissolved O_2 in highly acidic aqueous solutions of H_2SO_4. *Ind. Eng. Chem. Res.* 44, 1660–1664. doi:10.1021/ie049539m

Davis, R. E., Horvath, G. L., and Tobias, C. W. (1967). The solubility and diffusion coefficient of oxygen in potassium hydroxide solutions. *Electrochim. Acta* 12, 287–297. doi:10.1016/0013-4686(67)80007-0

Delany, J. M., and Lundeen, S. R. (1991). *The LLNL thermochemical data base - revised data and file format for the EQ3/6 package (No. UCID-21658)*. Livermore, CA, United States: Lawrence Livermore National Lab (LLNL.

Domski, P., and Nielsen, S. R. (2019). *WASTE ISOLATION PILOT PLANT AP-183 Revision 1 analysis plan to update the WIPP geochemical thermodynamic database (DATA0. FM1) to Data0. FM4 for CRA-2019*.

Eriksson, G., Hack, K., and Petersen, S. (1997). Chemapp—A programmable thermodynamic calculation interface. *Werkst. Woche* 96, 47–51.

Eriksson, G., and Spencer, P. (1995). "A general thermodynamic software interface," in *Proceedings 2nd colloquium on process simulation* (Otaniemi: Helsinki University of Technology), 113. (Report TKK-V-B104).

Eucken, A., and Hertzberg, G. (1950). Aussalzeffekt und Ionenhydratation. *Z. Phys. Chem.* 195, 1–23. doi:10.1515/zpch-1950-19502

Geffcken, G. (1904). Beiträge zur Kenntnis der Löslichkeitsbeeinflussung. *Z. Phys. Chem.* 49, 257–302. doi:10.1515/zpch-1904-4925

Geng, M., and Duan, Z. (2010). Prediction of oxygen solubility in pure water and brines up to high temperatures and pressures. *Geochim. Cosmochim. Acta* 74, 5631–5640. doi:10.1016/j.gca.2010.06.034

Giffaut, E., Grivé, M., Blanc, P., Vieillard, P., Colàs, E., Gailhanou, H., et al. (2014). Andra thermodynamic database for performance assessment: ThermoChimie. *Appl. Geochem.* 49, 225–236. doi:10.1016/j.apgeochem.2014.05.007

Glazunov, A. I., Kryazhev, A. M., and Musinsky, S. V. (1997). Растворимость кислорода в растворач Гидроокиси натрия (Oxygen solubility in sodium hydroxide solutions). *Celljuloza, Bum. karton* 7-8, 17–19.

Grenthe, I., Gaona, X., Plyasunov, A. V., Rao, L., Runde, W. H., Grambow, B., et al. (2020). *Second update on the chemical thermodynamics of uranium, neptunium, plutonium, americium and technetium*. Boulogne-Billancourt, France: OECD Nuclear Energy Agency, Data Bank, 1572.

Gubbins, K. E., and Walker, R. D., Jr. (1965). The solubility and diffusivity of oxygen in electrolytic solutions. *J. Electrochem. Soc.* 112, 469–471. doi:10.1149/1.2423575

Harvie, C. E., Møller, N., and Weare, J. H. (1984). The prediction of mineral solubilities in natural waters: The Na-K-Mg-Ca-H-Cl-SO_4-OH-HCO_3-CO_3-CO_2-H_2O system to high ionic strengths at 25°C. *Geochim. Cosmochim. Acta* 48 (4), 723–751. doi:10.1016/0016-7037(84)90098-X

Hayduk, W. (1991). *Final Report concerning the solubility of oxygen in sulfuric acid-zinc pressure leaching solutions*. Ottawa, Canada: University of Ottawa, Chemical Engineering, 40.

Herbert, H. J. (2000). "Zur Geochemie und geochemischen Modellierung hochsalinarer Lösungen," in *Hannover Bundesanstalt für Geowissenschaften und Rohstoffe (BGR)*. Editors J. Geologisches and R. D. Sonderhefte (Stuttgart, Germany: Schweizerbart Science Publishers). ISBN 978-3-510-95845-0.

Iwai, Y., Eya, H., Itoh, Y., Arai, Y., and Takeuchi, K. (1993). Measurement and correlation of solubilities of oxygen in aqueous solutions containing salts and sucrose. *Fluid Phase Equilib.* 83, 271–278. doi:10.1016/0378-3812(93)87030-5

Iwai, Y., Kohashi, K., Eya, H., Honda, K., and Arai, Y. (1990). Measurement and correlation of oxygen solubilities in aqueous solutions containing salts and sugar. *Kagaku Kogaku Ronbun* 16, 1247–1251. doi:10.1252/kakoronbunshu.16.1247

Kaskiala, T. (2002). Determination of oxygen solubility in aqueous sulphuric acid media. *Min. Eng.* 15, 853–857. doi:10.1016/S0892-6875(02)00089-4

Kelley, K. K. (1960). High-temperature heat-content, heat-capacity, and entropy data for the elements and inorganic compounds. *U. S. Bureau Mines Bull.* 584, 232.

Khomutov, N. E., and Konnik, E. I. (1974). Solubility of oxygen in aqueous electrolyte solutions. *Russ. J. Phys. Chem.* 48, 21–362. or *Zh. Fiz. Khim*, 48, (1974), 620–37.

Kitamura, A. (2020). *JAEA-TDB-RN in 2020: Update of JAEA's thermodynamic database for solubility and speciation of radionuclides for performance assessment of geological disposal of high-level and TRU wastes*. JAEA-Data/Code, 2020–020. doi:10.11484/jaea-data-code-2020-020

Knaster, M. B., and Apelbaum, L. A. (1964). Растворимость водорода и кислорода в концентрированныч растворач едкоГо кали (Solubility of hydrogen and oxygen in concentrated solutions of potassium hydroxide). *Zh. Fiz. Khim.* 38 (1), 223–225.

Kulik, D. A., Wanger, T., Dmytrieva, S. V., Kosakowski, G., Hingerl, F. F., Chudneno, K. V., et al. (2013). GEM-selektor geochemical modeling package: Revised algorithm and GEMS3K numerical kernel for coupled simulation codes. *Comput. Geosci.* 17 (1), 1–24. doi:10.1007/s10596-012-9310-6

Lang, W., and Zander, R. (1986). Salting-out of oxygen from aqueous electrolyte solutions: Prediction and measurement. *Ind. Eng. Chem. Fundam.* 25, 775–782. doi:10.1021/i100024a050

Li, H. (1994). *The solubilities of oxygen in sulphuric acid solutions containing copper and/or nickel sulphates at atmospheric and high pressure*. Master thesis (Ottawa, Canada: University of Ottawa), 110.

Lumsdon, D. G., and Evans, L. J. (1995). "Predicting chemical speciation and computer simulation," in *Chemical speciation in the environment* (Berlin, Germany: Springer), 86–134.

MacArthur, D. G. (1916). Solubility of oxygen in salt solutions and the hydrates of these salts. *J. Phys. Chem.* 20, 495–502. doi:10.1021/j150168a003

Mariner, P. (2004). *In-drift precipitates/salts model*. No. ANL-EBS-MD-000045, REV 02. Las Vegas, Nevada, USA: Yucca Mountain Project.

May, P. M., and Muray, K. (1991). Jess, a joint expert speciation system—II. The thermodynamic database. *Talanta* 38 (12), 1419–1426. doi:10.1016/0039-9140(91)80290-G

Millero, F. J., Huang, F., and Graham, T. B. (2003). Solubility of oxygen in some 1-1, 2-1, 1-2, and 2-2 electrolytes as a function of concentration at 25°C. *J. Solut. Chem.* 32, 473–487. doi:10.1023/A:1025301314462

Millero, F. J., Huang, F., and Laferiere, A. L. (2002). Solubility of oxygen in the major sea salts as a function of concentration and temperature. *Mar. Chem.* 78, 217–230. doi:10.1016/S0304-4203(02)00034-8

Millero, F. J., Huang, F., and Laferiere, A. L. (2002). The solubility of oxygen in the major sea salts and their mixtures at 25°C. *Geochim. Cosmochim. Acta* 66, 2349–2359. doi:10.1016/S0016-7037(02)00838-4

Millero, F. J., and Huang, F. (2003). Solubility of oxygen in aqueous solutions of KCl, K_2SO_4, and $CaCl_2$ as a function of concentration and temperature. *J. Chem. Eng. Data* 48, 1050–1054. doi:10.1021/je034031w

Mitchell, M., Muftakhidinov, B., Winchen, T., van Schaik, B., Wilms, A., Kylesower, et al. (2020). Engauge digitizer software. Available at: http://markummitchell.github.io/engauge-digitizer (Accessed February 19, 2020). doi:10.5281/zenodo.3558440

Moog, H. C., Bok, F., Marquardt, C. M., and Brendler, V. (2015). Disposal of nuclear waste in host rock formations featuring high-saline solutions - implementation of a thermodynamic reference database (THEREDA). *Appl. Geochem.* 55, 72–84. doi:10.1016/j.apgeochem.2014.12.016

Narita, E., Lawson, F., and Han, K. H. (1983). Solubility of oxygen in aqueous electrolyte solutions. *Hydrometallurgy* 10, 21–37. doi:10.1016/0304-386X(83)90074-9

Ohkubo, M. (2000). 製塩工程における高濃度電解質水溶液の溶存酸素濃度測定 (Measurement of solubility of oxygen in electrolyte solution used in salt manufacturing process). *Bull. Soc. Sea Water Sci. Jpn.* 54 (2), 111–116. doi:10.11457/swsj1965.54.111

Parkhurst, D. L., and Appelo, C. A. J. (2013). *Description of input and examples for PHREEQC version 3—a computer program for speciation, batch-reaction, one-dimensional transport, and inverse geochemical calculations*. U.S. Geological Survey, Book 6, Chapter 43, Section A of Techniques and Methods, 497.

Pearson, F. J., Jr., and Berner, U. R. (1991). *Nagra thermochemical data base I. Code data*, 80. Nagra, Technical Report 91–17.

Phillips, S. L., Phillips, C. A., and Skeen, J. (1985). *Hydrolysis, formation and ionization constants at 25° C, and at high temperature-high ionic strength*. Berkeley, CA, USA: Lawrence Berkeley Laboratory, 411. Lawrence Berkeley Laboratory Report No. LBL-14996.

Pierrot, D., and Millero, F. J. (2017). The speciation of metals in natural waters. *Aquat. Geochem.* 23, 1–20. doi:10.1007/s10498-016-9292-4

Pitzer, K. S. (1991). "Ion interaction approach: Theory and data correlation," in *Activity coefficients in electrolyte solutions*. Editor K. S. Pitzer (Boca Raton, Florida: CRC Press), 75–153.

Poeter, E. P., Hill, M. C., Lu, D., Tiedeman, C. R., and Mehl, S. (2014). *UCODE_2014, with new capabilities to define parameters unique to predictions, calculate weights using simulated values, estimate parameters with SVD, evaluate uncertainty with MCMC, and More*. Report Number: GWMI 2014-02. Indianapolis, Indiana, USA: Integrated Groundwater Modeling Center, 189.

Pospíšol, J., and Lužný, Z. (1960). Absorptionskoeffizienten des Sauerstoffes in Lösungen von Kaliumhydroxyd. *Collect. Czech. Chem. Commun.* 25, 589–592. doi:10.1135/cccc19600589

Ragoussi, M. E., and Costa, D. (2019). Fundamentals of the NEA Thermochemical Database and its influence over national nuclear programs on the performance assessment of deep geological repositories. *J. Environ. Radioact.* 196, 225–231. doi:10.1016/j.jenvrad.2017.02.019

Read, D., and Broyd, T. W. (1991). Recent progress in testing chemical equilibrium models: The CHEMVAL project. *Radiochim. Acta* 52 (2), 453–456. doi:10.1524/ract.1991.5253.2.453

Reynafarje, B., Costa, L. E., and Lehninger, A. L. (1985). O_2 solubility in aqueous media determined by a kinetic method. *Anal. Biochem.* 145, 406–418. doi:10.1016/0003-2697(85)90381-1

Scharge, T., Muñoz, A. G., and Moog, H. C. (2012). Activity coefficients of fission products in highly salinary solutions of Na^+, K^+, Mg^{2+}, Ca^{2+}, Cl^-, and SO_4^{2-}: Cs^+. *J. Chem. Eng. Data* 57 (6), 1637–1647. doi:10.1021/je200970v

Scharge, T., Munoz, A. G., and Moog, H. C. (2015). Thermodynamic modeling of high salinary phosphate solutions. II. Ternary and higher systems. *J. Chem. Thermodyn.* 80, 172–183. doi:10.1016/j.jct.2013.12.017

Scharge, T., Munoz, A. G., and Moog, H. C. (2013). Thermodynamic modelling of high salinary phosphate solutions. I. Binary systems. *J. Chem. Thermodyn.* 64, 249–256. doi:10.1016/j.jct.2013.05.013

Shock, E. L., Helgeson, H. C., and und Sverjensky, D. A. (1989). Calculation of the thermodynamic and transport properties of aqueous species at high pressures and temperatures: Standard partial molal properties of inorganic neutral species. *Geochim. Cosmochim. Acta* 53, 2157–2183. doi:10.1016/0016-7037(89)90341-4

Shoor, S. K., Walker, R. D., and Gubbins, K. E. (1968). Salting out of nonpolar gases in aqueous potassium hydroxide solutions. *J. Phys. Chem.* 73 (2), 312–317. doi:10.1021/j100722a006

Söhnel, O., and Novotný, P. (1985). *Densities of aqueous solutions of inorganic substances*. Amsterdam, Netherlands: Elsevier Publishing Company, 336.

Stephan, E. F., Hatfield, N. S., Peoples, R. S., and Pray, H. A. H. (1956). *The solubility of gases in water and in aqueous uranyl salt solutions at elevated temperatures and pressures*. Columbus, Ohio: Battelle Memorial Institute. Battelle Memorial Institute Report, BMI-1067.

Tan, Z. Q., Gao, G. H., Yu, Y. X., and Gu, G. (2001). Solubility of oxygen in aqueous sodium carbonate solution at pressures up to 10 MPa. *Fluid Phase Equilibria* 180, 375–382. doi:10.1016/S0378-3812(01)00371-5

THEREDA (2023). THEREDA – thermodynamic reference database. Available at: https://www.thereda.de/.

Thoenen, T., Hummel, W., Berner, U. R., and Curti, E. (2014). *The PSI/nagra chemical thermodynamic database 12/07*. PSI Report No. 14-04. ISSN 1019-0643.

Turner, D. R., Achterberg, E. P., Chen, C.-T. A., Clegg, S. L., Hatje, V., Maldonado, M. T., et al. (2016). Toward a quality-controlled and accessible pitzer model for seawater and related systems. *Front. Mari. Sci.* 3, 1–12. doi:10.3389/fmars.2016.00139

Voigt, W. (2020). Hexary system of oceanic salts – polythermal pitzer dataset (numerical supplement). *THEREDA J.* 1 (1), 1–9. URN: urn:nbn:de:bsz:105-qucosa2-782361.

Voigt, W. (2020). Temperature extension of NaCl Pitzer coefficients and $\Delta_R G^\circ$(NaCl). *THEREDA J.* 1 (2), 1–6. URN: urn:nbn:de:bsz:105-qucosa2-782374.

Wagner, T., Kulik, D. A., Hingerl, F. F., and Dmytrieva, S. V. (2012). GEM-selektor geochemical modeling package: TSolMod library and data interface for multicomponent phase models. *Can. Mineral.* 50 (5), 1173–1195. doi:10.3749/canmin.50.5.1173

Wolery, T. (1992). *EQ3/6, A software package for the geochemical modelling of aqueous systems*. UCRL MA 110662 Part I. Livermore, CA, USA: Lawrence Livermore National Laboratory.

Yasunishi, A. (1977). Solubilities of sparingly soluble gases in aqueous sodium sulfate and sulfite solutions. *J. Chem. Eng. Jpn.* 10 (2), 89–94. doi:10.1252/jcej.10.89

Yasunishi, A. (1978). Solubility of oxygen in aqueous electrolyte solutions. *Kagaku Kogaku Rombunshu* 4, 185–189. doi:10.1252/kakoronbunshu.4.185

Zhang, C., Fan, F.-R., and Bard, A. J. (2009). Electrochemistry of oxygen in concentrated NaOH solutions: Solubility, diffusion coefficients, and superoxide formation. *J. Am. Chem. Soc.* 131, 177–181. doi:10.1021/ja8064254

Zhang, G., Spycher, N., Sonnenthal, E., and Steefel, C. I. (2006). *Implementation of a Pitzer activity model into TOUGHREACT for modeling concentrated solutions*. TOUGH Symposium 2006, Technical Program and Abstracts, Berkley, May 15–17.

Zheng, J., and Mao, S. (2019). A thermodynamic model for the solubility of N_2, O_2 and Ar in pure water and aqueous electrolyte solutions and its applications. *Appl. Geochem.* 107, 58–79. doi:10.1016/j.apgeochem.2019.05.012

frontiers | Frontiers in Nuclear Engineering

TYPE Correction
PUBLISHED 17 October 2023
DOI 10.3389/fnuen.2023.1292254

OPEN ACCESS

EDITED AND REVIEWED BY
Taishi Kobayashi,
Kyoto University, Japan

*CORRESPONDENCE
F. Bok,
✉ f.bok@hzdr.de

RECEIVED 11 September 2023
ACCEPTED 02 October 2023
PUBLISHED 17 October 2023

CITATION
Bok F, Moog HC and Brendler V (2023), Corrigendum: The solubility of oxygen in water and saline solutions.
Front. Nucl. Eng. 2:1292254.
doi: 10.3389/fnuen.2023.1292254

Corrigendum: The solubility of oxygen in water and saline solutions

F. Bok[1]*, H. C. Moog[2] and V. Brendler[1]

[1]Actinide Thermodynamics Department, Institute of Resource Ecology, Helmholtz-Zentrum Dresden-Rossendorf e.V., Dresden, Germany, [2]Department Repository Research, Gesellschaft für Anlagen- und Reaktorsicherheit (GRS) gGmbH, Braunschweig, Germany

KEYWORDS

oxygen solubility, electrolyte solutions, water, Pitzer ion-interaction approach, E_H equation

A Corrigendum on
The solubility of oxygen in water and saline solutions

by Bok F, Moog HC and Brendler V (2023). Front. Nucl. Eng. 2:1158109. doi: 10.3389/fnuen.2023.1158109

In the published article, there was an error in Table 5. In line 3 [without table head, O_2(aq)] in the T_{min}/T_{max} column the stated temperature range is wrong. Since no temperature coefficients for $C_p^0(T)$ of O_2(aq) can be given, this field must stay empty. The table's footnote has been adjusted accordingly. The corrected Table 5 and it's caption *Standard formation data for H_2O(l), O_2(g), H_2(g), and O_2(aq). Temperature parameters for $C_p^0(T)$ with regard to the general function (**Eq. 12**) were fitted to values from **Chase (1998)**.* appears below.

In the published article, there was an error in Table 9. In line 7 [without table head, O_2(aq)-OH^-] in the last column (X_2) it has to be 3.934 ± 0.882, not 3.6934 ± 0.882. In line 15 [without table head, O_2(aq)-K^+-SO_4^{2-}] in the second column (X_0) it has to be −0.1618 ± 0.078 not −0.1575 ± 0.0688 and in the third column (X_1) it has to be 164.7 ± 102 not 183.5 ± 70.3. The corrected Table 9 and its caption *Parameters for the temperature dependency function of the binary and ternary interaction coefficients (λ, ζ). The uncertainty information refers to one standard deviation.* appears below.

The authors apologize for these errors and state that this does not change the scientific conclusions of the article in any way. The original article has been updated.

TABLE 5 Standard formation data for H_2O(l), O_2(g), H_2(g), and O_2(aq). Temperature parameters for $C_p^0(T)$ with regard to the general function (Eq. 12) were fitted to values from **Chase (1998)**.

Species	$\Delta_f H^0_{i,T=T_0}$	References	$S^0_{i,T=T_0}$	References	$\Delta_f G^0_{i,T=T_0}$	References	$C_p^0(T)$ (J/mol K)				T_{min}/T_{max}	$C^0_{p,T=T_0}$ (1)	References
	(J/mol)		(J/mol K)		(J/mol)		A_1	A_2	A_5	A_6	(K)	(J/mol K)	
H_2O(l)	−285,830 ± 40 (2)	Cox et al. (1989)/ Chase (1998)	69.95 ± 0.03 (2)	Cox et al. (1989)/ Chase (1998)	−237,140 ± 41	(1)	149 ± 11	−0.33 ± 0.04	−1,056,714 ± 250,728	0.00042 ± 0.00004	280/500	75.418	Chase (1998)
O_2(g)	0	(By definition)	205.152 ± 0.005 (2)	Cox et al. (1989)	0	(By definition)	24.64 ± 0.03	0.0121 ± 0.0001	100,230 ± 1,433	0	298.15/500	29.376	Chase (1998)
O_2(aq)	−12,411 ± 971	(This work)	108 ± 14	(This work)	16,593 ± 3,168	(This work)	(3)	(3)	(3)	(3)	(3)	249.90 ± 0.07	(This work)
H_2(g)	0	(By definition)	130.68 ± 0.003 (2)	Cox et al. (1989)/ Chase (1998)	0	(By definition)	33.6 ± 0.2	−0.012 ± 0.001	−174,946 ± 3,652	1.01 ± 0.05 × 10^{-5}	298.15/500	28.836	Chase (1998)

(1) Internally calculated. (2) Data uncertainty adopted from **Cox et al. (1989)**. (3) With our selection for the temperature dependence of Henry's law constant (**Eq. 8** and **Table 2**) no temperature function for the standard molar heat capacity of reaction $\Delta_r C^0_{p,m}(T)$(6) can be derived. Hence, no temperature dependence for the standard molar heat capacity for O_2(aq) can be given.

TABLE 9 Parameters for the temperature dependency function of the binary and ternary interaction coefficients (λ, ζ). The uncertainty information refers to one standard deviation.

λ/ζ (Species: 1-2-3)	X_0	X_1	X_2
O_2(aq)-Cl^-	0 (by definition)	0 (by definition)	0 (by definition)
O_2(aq)-H^+	0.02598 ± 0.00171	4,941 ± 533	16.4 ± 1.8
O_2(aq)-Na^+	0.1315 ± 0.0093	2,897 ± 274	9.614 ± 0.947
O_2(aq)-K^+	0.135 ± 0.010	−1,004 ± 527	−3.513 ± 1.79
O_2(aq)-Mg^{2+}	0.2293 ± 0.0032	2,981 ± 860	9.9 ± 2.9
O_2(aq)-Ca^{2+}	0.2519 ± 0.0063	2,821 ± 651	9.449 ± 2.26
O_2(aq)-OH^-	0.06785 ± 0.00965	1,230 ± 280	3.934 ± 0.882
O_2(aq)-SO_4^{2-}	0.1334 ± 0.0082	−6,654 ± 1,150	−22.01 ± 3.38
O_2(aq)-HSO_4^-	0.03842 ± 0.00201	−45.38 ± 27.7	0 (fixed)
O_2(aq)-H^+-HSO_4^-	−0.002472 ± 0.000302	0 (fixed)	0 (fixed)
O_2(aq)-Na^+-Cl^-	−0.003767 ± 0.00579	−1,075 ± 128	−3.663 ± 0.442
O_2(aq)-Na^+-OH^-	0 (fixed)	−40.7 ± 17.9	0 (fixed)
O_2(aq)-Na^+-SO_4^{2-}	−0.0381 ± 0.0073	4,216 ± 1,820	13.49 ± 5.92
O_2(aq)-K^+-Cl^-	−0.01711 ± 0.00647	747.7 ± 319	2.464 ± 1.07
O_2(aq)-K^+-SO_4^{2-}	−0.1618 ± 0.078	164.7 ± 102	0 (fixed)
O_2(aq)-Mg^{2+}-Cl^-	−0.006612 ± 0.00101	−875.5 ± 351	−2.974 ± 1.18
O_2(aq)-Mg^{2+}-SO_4^{2-}	−0.05115 ± 0.00586	5,181 ± 550	16.86 ± 1.86
O_2(aq)-Ca^{2+}-Cl^-	−0.01269 ± 0.00291	24.49 ± 1.81	0 (fixed)

Publisher's note

Frontiers in Nuclear Engineering

TYPE Original Research
PUBLISHED 30 May 2023
DOI 10.3389/fnuen.2023.1188789

Solid-liquid equilibria of Sorel phases and Mg $(OH)_2$ in the system Na-Mg-Cl-OH-H_2O. Part I: experimental determination of OH^- and H^+ equilibrium concentrations and solubility constants at 25°C, 40°C, and 60°C

Melanie Pannach[1], Iris Paschke[1], Volker Metz[2], Marcus Altmaier[2], Wolfgang Voigt[1] and Daniela Freyer[1]*

[1]TU Bergakademie Freiberg, Institut für Anorganische Chemie (TU BAF), Freiberg, Germany, [2]Karlsruher Institut für Technologie, Institut für Nukleare Entsorgung (KIT-INE), Karlsruhe, Germany

OPEN ACCESS

EDITED BY
Taishi Kobayashi,
Kyoto University, Japan

REVIEWED BY
Kenso Fujiwra,
Japan Atomic Energy Agency, Japan
Jun-Yeop Lee,
Pusan National University, Republic of Korea

*CORRESPONDENCE
Daniela Freyer,
Daniela.freyer@chemie.tu-freiberg.de

RECEIVED 17 March 2023
ACCEPTED 24 April 2023
PUBLISHED 30 May 2023

CITATION
Pannach M, Paschke I, Metz V, Altmaier M, Voigt W and Freyer D (2023), Solid-liquid equilibria of Sorel phases and Mg $(OH)_2$ in the system Na-Mg-Cl-OH-H_2O. Part I: experimental determination of OH^- and H^+ equilibrium concentrations and solubility constants at 25°C, 40°C, and 60°C.
Front. Nucl. Eng. 2:1188789.
doi: 10.3389/fnuen.2023.1188789

Sorel phases are the binder phases of the magnesia building material (Sorel cement/concrete) and of special concern for the construction of long-term stable geotechnical barriers in repositories for radioactive waste in rock salt, as potentially occurring brines are expected to contain $MgCl_2$. Sorel phases, in addition to $Mg(OH)_2$, are equally important as pH buffers to minimize solubility and potential mobilization of radionuclides in brine systems. In order to obtain a detailed database of the relevant solid-liquid equilibria and the related pH_m values of the equilibrium solutions, extensive experimental investigations were carried out. Solid phase formation was studied by suspending MgO and $Mg(OH)_2$ in NaCl saturated $MgCl_2$-solutions at 25°C. $Mg(OH)_2$ and the 3-1-8 Sorel phase were identified as the stable solid phases, while the 5-1-8 Sorel phase is metastable. Equilibration at 40°C did not lead to any solid phase changes. Both OH^- and H^+ equilibrium concentrations were analyzed as a function of $MgCl_2$ concentration at 25°C and 40°C. In addition to our already published solid-liquid equilibria for the ternary system Mg-Cl-OH-H_2O (25°C–120°C), the equilibrium H^+ concentrations (pH_m) determined at 25°C, 40°C and 60°C are now reported. Analyzing these data together with known ion-interaction Pitzer coefficients, the solubility constants for $Mg(OH)_2$ and the 3-1-8 phase at these three temperatures, for the metastable 5-1-8 phase at 25°C and for the 2-1-4 phase at 60°C have been consistently calculated.

KEYWORDS

solubility equilibrium, system Na-Mg-Cl-OH-H_2O, system Mg-Cl-OH-H_2O, magnesium oxychloride, Sorel phases, $Mg(OH)_2$, solubility constant

1 Introduction

Sorel phases are of particular importance for the construction of geotechnical barriers (plugs and sealing systems) in the host rock salt and the establishment of a favorable geochemical environment (i.e., by buffering of pH_m and limiting carbonate concentrations) to minimize radionuclide transport processes via potential aqueous solutions.

Sorel phases [named after Stanislas Sorel, who was the first to describe the formation of a hardening material by the reaction of caustic magnesium oxide with magnesium chloride solution (Sorel & Dumas, 1867)] are the binder phases of the magnesia building material (Sorel cement or concrete) with the general composition $xMg(OH)_2 \cdot yMgCl_2 \cdot zH_2O$ (x-y-z phases). It has been empirically known for more than 100 years that Sorel cement does not corrode in salt (Unknown author, 1902). However, within the safety assessment of a repository, the long-term stability of the geotechnical barrier must be proven. This can be evidenced by analyzing the existing solubility equilibria between Sorel phases and salt solutions of the host rock. Depending on the ratio of MgO and the $MgCl_2$ solution (and their concentration) in the building material formulation and the developing setting temperature, the 3-1-8, 5-1-8 and/or also 9-1-4 phase may be present when the setting reaction is complete. However, sufficient solubility equilibrium data of Sorel phases in NaCl-saturated solutions are not yet available in the literature.

In addition to the binder phase function, both Sorel phases and $Mg(OH)_2$ can act as pH buffers of salt solutions (Bodine, 1976) as is realized in the Waste Isolation Pilot Plant (WIPP) in New Mexico with MgO as additive of backfill materials (Monastra & Grandstaff, 1999). In case of a brine access a weakly alkaline milieu is generated, providing favorable geochemical conditions for radionuclide retention. Therefore, in addition to the usual data describing solubility equilibria [Na^+, Mg^{2+}, Cl^-, OH^- solution concentrations in the presence of $Mg(OH)_2$ and Sorel phases], the H^+ concentrations are of particular interest.

In recent decades, the Sorel phases occurring in the basic ternary system $Mg\text{-}Cl\text{-}OH\text{-}H_2O$- the 3-1-8, 5-1-8, 9-1-4, 2-1-4, 2-1-2, and 3-1-0 phases - have been extensively characterized (de Wolff & Walter-Lévy, 1949; Bianco, 1951; Walter-Lévy & Bianco, 1951; de Wolff & Walter-Lévy, 1953; de Wolff & Kortlandt, 1954; Cole & Demediuk, 1955; Demediuk et al., 1955; Bianco, 1958; Sugimoto et al., 2007; Dinnebier et al., 2010; Dinnebier et al., 2012; Bette et al., 2015). Solubility data are available in terms of OH^- or H^+ concentrations in $MgCl_2$-containing solutions (ternary system $Mg\text{-}Cl\text{-}OH\text{-}H_2O$) or in $NaCl\text{-}MgCl_2$-containing mixed solutions (system $Na\text{-}Mg\text{-}Cl\text{-}OH\text{-}H_2O$). For a conversion between concentration of free OH^- and H^+ the ionic product of water, K_W^0 (Eq. 1), must be known for $MgCl_2$ and $NaCl\text{-}MgCl_2$ solutions at concentrations of interest.

$$K_W^0 = \frac{[H^+] \cdot [OH^-] \cdot \gamma_\pm^2}{a_W} = \frac{K_W \cdot \gamma_\pm^2}{a_W} \tag{1}$$

In addition to the free OH^-, which is related to H^+ via the Kw, in basic systems other hydroxide solution species [e.g., $MgOH^+$ (Palmer & Wesolowski, 1997)] exist, which yield together with the free OH^- the total OH^- concentration.

A comprehensive data set is available for the ternary system $Mg\text{-}Cl\text{-}OH\text{-}H_2O$ from 25°C to 120°C by specifying the OH^- solution concentrations (Pannach et al., 2017), including the evaluation of earlier data (20°C: D'Ans & Katz, 1941, 25°C; Robinson & Waggaman, 1909, 50°C; Nakayama, 1960, 100°C; Nakayama, 1959, 120°C; Dinnebier et al., 2010). Accordingly, in addition to $Mg(OH)_2$, the four basic magnesium chloride hydrates (Sorel phases) 3-1-8, 9-1-4, 2-1-4, and 2-1-2 occur as thermodynamically stable solid phases depending on temperature and solution concentration (Figure 1). The 3-1-8 phase exists between 25°C and 80°C and was found to be metastable at 100°C. The 9-1-4, 2-1-4, and 2-1-2 phases occur at the higher temperatures or higher $MgCl_2$ concentrations. In general, the hydroxide solution concentration in the system increases with temperature. For the 5-1-8 phase, only a temporary occurrence was observed during the solubility studies. It is therefore a metastable phase of the system (Feitknecht, 1926; Feitknecht & Held, 1944; Bianco, 1951; Cole & Demediuk, 1955; Newman, 1955; Bianco, 1958; Pannach et al., 2017).

For the NaCl-containing system $Na\text{-}Mg\text{-}Cl\text{-}OH\text{-}H_2O$, a data set exists only for 20°C at not specified NaCl solution concentrations (D'Ans et al., 1955). Analogous to the ternary system, the stable solids are $Mg(OH)_2$ in solutions with low $MgCl_2$ concentrations, and the 3-1-8 phase at higher $MgCl_2$ concentrations. The invariant point $Mg(OH)_2(s)$ + 3-1-8 phase was given by D'Ans et al., 1955 with 0.555 $MgCl_2$ molal and 0.53 $Mg(OH)_2$ mmolal. Metastable data points for $Mg(OH)_2$ are also given. A comparison of these 20°C data from D'Ans et al., 1955 with those of the ternary system $Mg\text{-}Cl\text{-}OH\text{-}H_2O$ at 25°C from Pannach et al. (2017) in Figure 2 shows that in the presence of NaCl the stability range of the 3-1-8 phase extends towards lower $MgCl_2$ concentrations.

Molal H^+ concentrations (pH_m) were determined in the ternary system at 22°C ± 2°C by Altmaier et al. (2003) in the presence of $Mg(OH)_2$ and the 3-1-8 phase; in the quaternary system $Na\text{-}Mg\text{-}Cl\text{-}OH\text{-}H_2O$ for $Mg(OH)_2$ in solutions with very low NaCl concentration by Altmaier et al. (2003); Xiong (2008) and in almost NaCl-saturated solutions for the 5-1-8 phase (Xiong et al., 2010). Comparison of these data in Figure 3 shows that the pH_m in the presence of $Mg(OH)_2$ decreases more with increasing $MgCl_2$ concentration (from about 10.7 to 8.9) than in the region of the 3-1-8 phase (from about 8.9 to 8.7) as shown in the comprehensive data set for the ternary system $Mg\text{-}Cl\text{-}OH\text{-}H_2O$. In agreement with the "OH^- based data set" (Figures 1, 2), the invariant point of $Mg(OH)_2$ and the 3-1-8 phase is inferred to exist

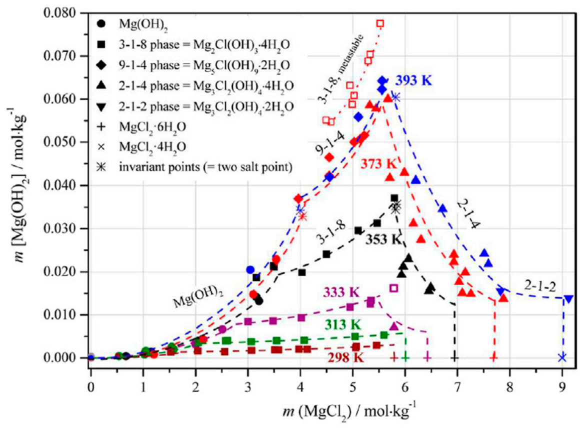

FIGURE 1
Solubility data of the ternary system $Mg\text{-}Cl\text{-}OH\text{-}H_2O$ from 25°C to 120°C (Pannach et al., 2017).

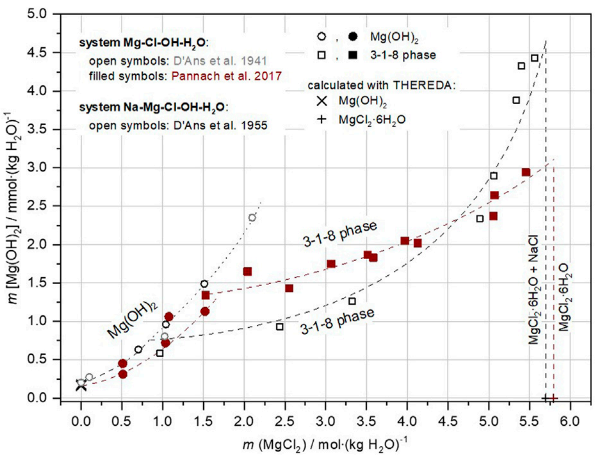

FIGURE 2
Comparison of solubility data in the quaternary system Na-Mg-Cl-OH-H_2O at 20°C (D'Ans et al., 1955) and the ternary system Mg-Cl-OH-H_2O at 25°C (Pannach et al., 2017).

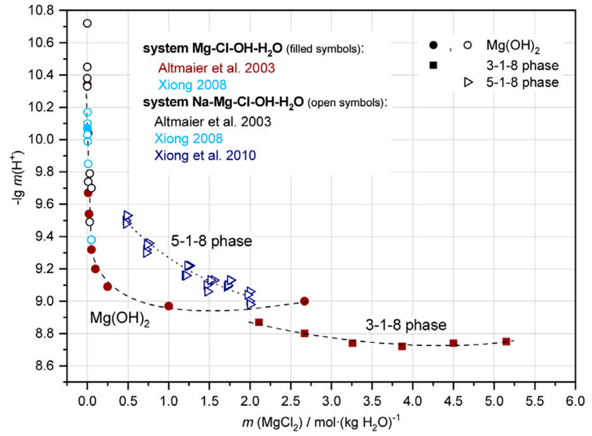

FIGURE 3
Molal H^+ concentrations (as -lg m (H^+) = pH_m) of the ternary Mg-Cl-OH-H_2O and the quaternary Na-Mg-Cl-OH-H_2O system at 25°C from literature. In the solutions containing very low $MgCl_2$ of Altmaier et al. (2003), the NaCl concentrations vary from 0.01 to 5.0 molal. In the measurements of Xiong et al., 2010, an approximated saturation concentration of NaCl was adjusted.

between 1.5 and 2.0 $MgCl_2$ molal in the ternary system. In the presence of NaCl there are no data for > 0.1 $MgCl_2$ molal for neither $Mg(OH)_2$ nor the 3-1-8 phase available. The pH_m values determined by Xiong et al. (2010) in the presence of the 5-1-8 phase in the $MgCl_2$ concentration range from 0.5 to 2.0 molal in nearly NaCl-saturated solutions roughly compare to the trend of the 3-1-8 phase for the ternary system, but are shifted to a higher basicity.

With the determination of the H^+ molalities, solubility constants were calculated by Altmaier and Xiong using an activity coefficient model for 25 °C corresponding to the reactions (2), (3) and (4) (see also chapter 3.3):

$Mg(OH)_2$:

$$Mg(OH)_{2\,(s)} + 2H^+ \rightleftharpoons Mg^{2+} + 2\,H_2O \tag{2}$$

$$\begin{aligned} \lg K_{S,25^\circ C,Mg(OH)2} &= 17.16 \pm 0.1 \text{ from Mg-Cl-OH-H}_2\text{O system Altmaier et al. (2003)} \\ &= 17.01 \pm 0.1 \text{ from Na-Mg-Cl-OH-H}_2\text{O system Altmaier et al. (2003)} \\ &= 17.05 \pm 0.2 \text{ from Na-Mg-Cl-OH-H}_2\text{O system Xiong (2008)} \end{aligned}$$

$$\textbf{3-1-8 phase} = 3Mg(OH)_2 \cdot MgCl_2 \cdot 8H_2O$$

$$= Mg_2Cl(OH)_3 \cdot 4H_2O\text{: } Mg_2Cl(OH)_3 \cdot 4\,H_2O_{(s)} + 3\,H^+ \rightleftharpoons 2\,Mg^{2+} + Cl^- + 7\,H_2O \tag{3}$$

$$\lg K_{S,25^\circ C,3\text{-}1\text{-}8} = 26.15 \pm 0.16 \quad \text{from Mg-Cl-OH-H}_2\text{O system} \quad \text{Altmaier et al. (2003)}$$

$$\textbf{5-1-8 phase} = 5Mg(OH)_2 \cdot MgCl_2 \cdot 8H_2O$$

$$= Mg_3Cl(OH)_5 \cdot 4H_2O\text{: } Mg_3Cl(OH)_5 \cdot 4\,H_2O_{(s)} + 5\,H^+ \rightleftharpoons 3\,Mg^{2+} + Cl^- + 9\,H_2O \tag{4}$$

$$\lg K_{S,25^\circ C,5\text{-}1\text{-}8} = 43.21 \pm 0.33 \quad \text{from Na-Mg-Cl-OH-H}_2\text{O system} \quad \text{Xiong et al. (2010)}$$

The solubility constant determined for $Mg(OH)_2$ in both the Mg-Cl-OH-H_2O and Na-Mg-Cl-OH-H_2O system agree very well within the given error limits.

In this work, the studies on the solubility equilibria of the Sorel phases and $Mg(OH)_2$ (brucite as mineral) were extended with the determination of the OH^- and H^+ solution concentrations in the system Na-Mg-Cl-OH-H_2O (NaCl-saturated) at 25°C and 40°C. In addition to the already known H^+ equilibrium concentrations in the ternary system Mg-Cl-OH-H_2O at 25°C, measurements at 40°C and 60°C beside 25°C were presented together with the calculation of solubility constants for $Mg(OH)_2$ and the Sorel phases at 25°C, 40°C, and 60°C.

Part II of the paper present the geochemical model developing on the basis of the experimental data.

2 Materials and methods

2.1 Starting materials

$MgCl_2 \cdot 6H_2O$, CAS No. 7791–18–6, (Fluka, purity > 99%, and Merck, ACS reagent, > 99%), $Mg(OH)_2$, CAS No. 1309–42–8 (BioUltra, > 99%, from Fluka and M725 from Magnesia, 99%), MgO, CAS No. 1309–48–4 (M2923 from Magnesia, > 97%) and NaCl, CAS No. 7647–14–5 (from Merck, ACS reagent, ≥ 99.0%) were used for the investigations. The phase purity of all substances was checked by X-ray powder diffraction.

The magnesium chloride solutions were prepared by appropriate weighing of deionized water (CO_2-free by boiling or flowing through with argon for 1 h) and $MgCl_2 \cdot 6H_2O$. A suspension of NaCl ensured saturation in the respective $MgCl_2$ solutions.

All solution concentrations are given in molal (molality m) with the unit mol·(kg $H_2O)^{-1}$ or mmolal = mmol·(kg $H_2O)^{-1}$.

2.2 Preparation of the solid-liquid mixtures for equilibrations in the quaternary system Na-Mg-Cl-OH-H_2O (NaCl-saturated) at 25°C and 40°C

For the preparation of the mixtures of solutions with solids in the quaternary system Na-Mg-Cl-OH-H_2O at 25°C (sample Series 1 of TUBAF, Table 1), 1 g MgO was weighed into 250 mL PP wide-neck bottles with 200 g NaCl-saturated, n molal in $MgCl_2$ each. The suspensions were annealed at 25°C ± 1°C and regularly shaken by hand every 1–3 days over a period of about 1 year.

Another sample series (sample Series 2 of KIT-INE, Table 3) was prepared by weighing 300 mg of $Mg(OH)_2$ (Fluka, BioUltra) into approximately 200 mL (240–270 g solution) of NaCl-saturated n molal $MgCl_2$ solutions. The suspensions were stored in sealed vessels at 24°C ± 2°C in a glove box under argon atmosphere and also shaken regularly by hand. Over a period of 6 years, the development of the H^+ solution concentrations were followed with a glass electrode (see chapter 2.4) and finally the solid phase was determined by X-ray.

The solids obtained after 1 year in sample series 1 [these were $Mg(OH)_2$ and the 3-1-8 phase] were filtered off and re-suspended in new solutions of 200 g NaCl-saturated n molal $MgCl_2$ solutions (partly in double approach) in 250 mL PP wide-neck bottles and equilibrated at 25°C for 131–144 days (sample Series 3a of TUBAF) and at 40°C for 32–84 days (sample Series 3b of TUBAF), see Table 4. In the case of the 40°C samples, the 2-1-4 Sorel phase (obtained in our previous studies on the ternary system Mg-Cl-OH-H_2O (Pannach et al., 2017)) was also added. The temperature of the suspensions was controlled at 25°C ± 0.2°C and at 40°C ± 0.2°C in a water bath with continuous stirring using a Teflon magnetic stirrer. Subsequently, the solution and solid phases were separated using a micro glass fibre filter (Munktell, grade MGF = 0.7 μm).

2.3 Solid-liquid mixtures in the ternary system Mg-Cl-OH-H_2O at 25°C, 40°C, and 60°C

In Pannach et al. (2017) we published our results on the determination of solubility equilibria in the ternary system Mg-Cl-OH-H_2O at 25°C–120°C. In addition to the reported OH^- solubility concentrations as a function of $MgCl_2$ concentration, we also finally measured the H^+ concentrations in the equilibrated suspensions at 25, 40°C and 60°C. These results are presented here as sample Series 4 (a-c) of TUBAF. The weights of the initial solution and solid components are given in Table 5 together with the equilibrium data. All suspensions were tempered in sealed 250 mL wide-necked PP bottles in water baths (25°C ± 0.2°C and 40°C ± 0.2°C, thermostat type EB, Julabo Labortechnik GmbH or 60°C ± 0.2 °C shaking water bath, company GFL, model 1,083) and shaken regularly by hand (25°C, 40°C) or automatically (60°C). Further experimental details can be found in Pannach et al. (2017).

2.4 Analytics

Solutions: The Mg^{2+} concentration was analyzed by complexometric titration in NH_3/NH_4Cl buffered solutions (pH 9–10) with Erio T as indicator and 0.05 M Na-EDTA solution (Biedermann & Schwarzenbach, 1948) (relative analytical error ± 0.3%). The Cl^- concentration was determined according to the method of Mohr (Schulze & Simon, 2009) in a $Na_2CO_3/NaHCO_3$ buffered solution (pH 8–9) with K_2CrO_4 as indicator and 0.1 M $AgNO_3$ solution (relative analytical error ± 0.2%). The total OH^- concentrations were determined volumetrically by acid-base back titration (0.01 M HCl and 0.01 M NaOH solution) with potentiometric endpoint determination and a pH glass electrode (combination electrode, type ROSS, Thermo-Orion 8103BN, filling solution 3 M KCl). Reported results are the mean of double or triple titrations, where for each the sample solution of 10–20 g was directly weighed (relative analytical error ± 0.3%). The analyzed OH^- concentrations are given as $Mg(OH)_2$ concentrations in the following figures and tables. The Na^+ concentration was determined with the flame photometer (type BWB-XP, BWB-XP Technologies) and from sample No. 26 (Table 3, sample series 3) by ion chromatography due to equipment failure of the flame photometer.

The H^+ concentrations were determined potentiometrically according to the method of Altmaier et al. (2003) using glass electrodes calibrated to m (H^+) at 25°C, 40°C and 60°C. At 25°C the potential measurements were carried out with a ROSS type pH glass electrode, Thermo-Orion 8103BN (combination electrode, filling solution 3 M KCl) - same for sample Series 2 (KIT-INE laboratory) and 3a and 4a (TUBAF laboratory). For the measurements at 40°C and 60°C (TUBAF sample Series 3b and 4b, 4c), a combination electrode with a temperature sensor of the type SenTix82 (company WTW, filling solution 3 M KCl solution) was used. Both pH electrodes were calibrated against standard pH buffer solutions (pH = 4–10, Riedel de Haën, Fisher Brand and Merck) at the corresponding temperatures. The pH value is defined in dilute aqueous solutions of ionic strength $I <$ 0.1 molal by the activity of the H^+ concentration. Measurements in aqueous solutions of higher ionic strength give to an operative pH value (pH_{exp}), from which the H^+ solution concentration is calculated using an empirical correction factor A_m (Altmaier et al., 2003):

$$-\lg m\left(H^+\right) = pH_m = pH_{exp} + A_m \tag{5}$$

The correction factor A_m depends on the solution composition, absolute concentration and temperature. This empirical relationship between A and a n molal salt solution of $I > 0.1$ molal is described by the following quadratic equations (in molal concentration units m_i):

$$A_i = B_0 + B_1 \cdot \sum_i m_i + B_2 \cdot \left(\sum_i m_i\right)^2$$

Na-Mg-Cl-OH-H_2O system:
25°C (for sample Series 2 and 3a with NaCl and $MgCl_2$ calibration solutions):

$$A_{NaCl/MgCl2} = A_{NaCl} + A_{MgCl2} \tag{6}$$

$$\text{with} \quad A_{NaCl} = -0.0988 + 0.1715 \cdot m_{NaCl} + 0.0013 \cdot \left(m_{NaCl}\right)^2$$

$$A_{MgCl2} = -0.0887 + 0.2275 \cdot m_{MgCl2} + 0.0043 \cdot \left(m_{MgCl2}\right)^2$$

40°C (for sample Series 3b with NaCl/$MgCl_2$ mixing solutions):

$$A_{NaCl/MgCl2} = 0.04853 + 0.13377 \cdot m_{NaCl/MgCl} + 0.00188 \cdot \left(m_{NaCl/MgCl}\right)^2 \tag{7}$$

Mg-Cl-OH-H_2O system (for sample Series 4):
25°C (for Series 4a):

$$A_{MgCl2} = -0.0887 + 0.2275 \cdot m_{MgCl2} + 0.0043 \cdot \left(m_{MgCl2}\right)^2 \tag{8}$$

40°C (for Series 4b):

$$A_{MgCl2} = -0.0968 + 0.4474 \cdot m_{MgCl2} + 0.0141 \cdot \left(m_{MgCl2}\right)^2 \tag{9}$$

60°C (for Series 4c):

$$A_{MgCl2} = -0.1926 + 0.4025 \cdot m_{MgCl2} + 0.0126 \cdot \left(m_{MgCl2}\right)^2 \tag{10}$$

Using the correction factor A_m and the measured pH_{exp} values, the molal H^+ concentrations of the solutions were determined with an accuracy of ± 0.05 pH units.

Solids: The solid phases (after filtration from the solution washed with cold ($T < 5$°C) deionized water and subsequently with cold ($T < 5$°C) ethanol to remove adhering wash water; finally dried at room temperature in an exsiccator) were identified by X-ray powder diffraction (Bruker D8 Discover with linear detector Vantec-1 at TUBAF or Bruker AXS D8 Advance at KIT-INE; each with Cu-Kα radiation). The samples were prepared as flat plates after grinding.

SEM images (exemplarily from the appropriately washed solids) were taken by TUBAF on gold-coated samples using a TESCAN Vega 5130 SB scanning electron microscope with a cathode voltage of 20 kV.

3 Results and discussions

3.1 Solid phase development in the quaternary system Na-Mg-Cl-OH-H_2O at 25°C

The development of the solid phase composition in the system Na-Mg-Cl-OH-H_2O was followed at 25°C in NaCl saturated n molal $MgCl_2$ solutions by suspending caustic MgO (sample Series 1 of TUBAF) as well as $Mg(OH)_2$ (sample Series 2 of KIT-INE) with ≤ 1 g solid in 200 g solution.

MgO suspension in dilute $MgCl_2$ solutions (0.2 molal) resulted in the formation of $Mg(OH)_2(s)$ beside the present NaCl. $Mg(OH)_2(s)$ was also formed in 0.5 m_{MgCl2} solution. Finally, after 349 days, a mixture of $Mg(OH)_2(s)$ and 3-1-8 phase was detected. The $MgCl_2$ concentration was slightly increased to 0.56 molal (Table 1). In a 1.0 m_{MgCl2} solution, $Mg(OH)_2(s)$ was also identified within the first weeks and transformed into the 3-1-8 phase over months (see powder diffractograms taken within 1 year in Figure 4A). The SEM image (Figure 4C) shows the typical long needles of the 3-1-8 phase, between which particles of $Mg(OH)_2(s)$ are still visible in the "212-day sample" (Figure 4B).

In 2 or 3 m_{MgCl2} solutions, the formation of the 5-1-8 phase in addition to $Mg(OH)_2$ and/or the 3-1-8 phase was observed within the first few days (Figure 5). After a few weeks, only the 3-1-8 phase was present in addition to NaCl(s). In the concentrated $MgCl_2$ solutions (4 and 5.5 m_{MgCl2}, NaCl-saturated), the 3-1-8 phase could be identified as a solid phase after 3 days already. This time-dependent change of the solid phase composition in the differently concentrated $MgCl_2$ solutions (NaCl-saturated) at 25°C ± 1°C is schematically summarized in Figure 6. All values of the initial solid-solution samples as well as the analyzed solution are given in Table 1.

In the case of the $Mg(OH)_2(s)$ suspension (sample Series 2), the development of the pH_m was monitored over an even longer period of 2,394 days (6.5 years) (Figure 7). At the beginning of the measurements, three samples (the 0.5, 2.0 and 4.0 m_{MgCl2} suspensions, all NaCl-saturated) were selected, from which a few milligrams of solid phase were taken after 16 days to determine their composition. At this time, only the 3-1-8 phase was identified in the 4.0 m_{MgCl2} solution, whereas a mixture of $Mg(OH)_2(s)$ and 3-1-8 phase was found in the 2.0 m_{MgCl2} solution. In this solution, the $Mg(OH)_2(s)$ continued to transform into the 3-1-8 phase with time, as shown in the final diffractograms recorded after 2,394 days (6.5 years) in Figure 8. Only in the 0.5 m_{MgCl2} solution $Mg(OH)_2$ could be detected as the remaining solid.

The measured pH_m show values (of the otherwise weakly acidic NaCl-$MgCl_2$ solutions) that are buffered in the weakly basic range within the first 400 days. After a maximum value is reached, a decrease to a constant value is observed, indicating that the equilibrium state has been established. The difference between the intermediate maximum value and the equilibrium value was up to 0.2 pH_m units in the solutions with lower $MgCl_2$ concentrations, in the more concentrated $MgCl_2$ solutions (3, 4 m_{MgCl2}) it was significantly smaller. Within the analytical error of ± 0.05 pH_m units, it can be assumed that equilibrium was reached in all suspensions after approximately 500 days. In general,

TABLE 1 Set of samples used in Series 1. Sample compositions and analytical results after 349 days of equilibration at 25°C.

No.	initial solid—liquid system				solid—liquid system			
					after suspension of 349 days			
	solid phases		$MgCl_2$ solution		$MgCl_2$	NaCl	$Mg(OH)_2$	solid + $NaCl_{(s)}$
	MgO	NaCl						
	[g]		[g]	[molal]	[molal]		[mmolal]	
1	1.0007	70.73	199.99	0.2	0.20	5.57	0.34	$Mg(OH)_2$
2	1.0004	60.60	200.00	0.5	0.56	4.86	0.78	$Mg(OH)_2$ + 3-1-8
3	1.0013	47.17	200.00	1.0	1.00	4.19	1.71	3-1-8
4	1.0026	29.57	200.01	2.0	1.97	2.35	2.22	3-1-8
5	1.0006	15.51	200.01	3.0	3.01	0.98	2.88	3-1-8
6	1.0005	8.55	200.01	4.0	3.94	0.29	3.21	3-1-8
7	1.0051	4.05	199.99	5.5	5.51	0.04	3.89	3-1-8

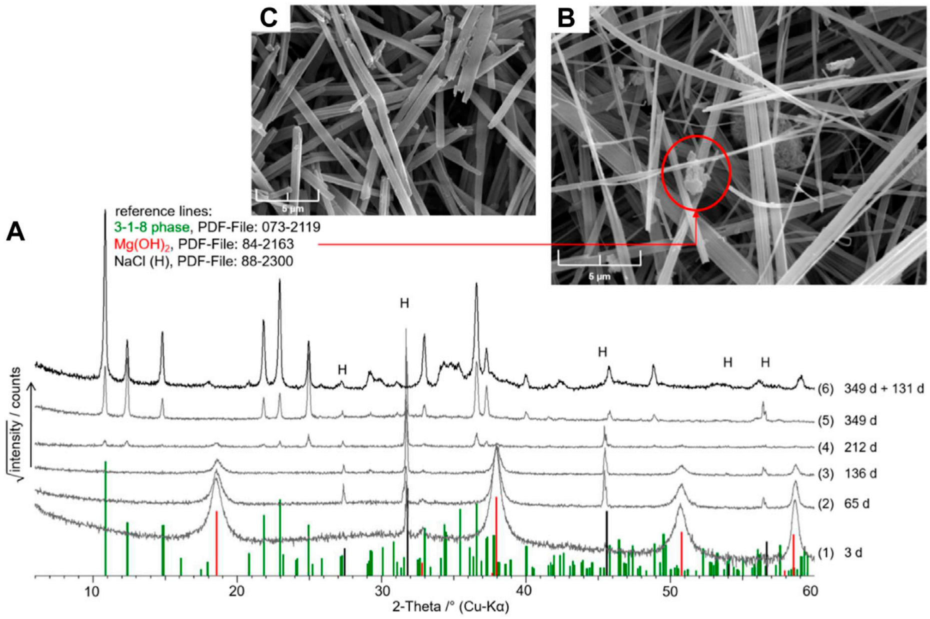

FIGURE 4
(A) X-ray powder diffractograms of the solids obtained after different times of MgO suspension in NaCl-saturated 1.0 m_{MgCl2} solution (diff. No. 1–5); diff. No. 6: solid after re-suspension of the "349-day solid" (diff. No. 5) in new NaCl-saturated 1.0 m_{MgCl2} solution and further 131 days of suspension (= sample No. 18 of Series 3, Table 4); **(B)** SEM images of the solid after 212 days (diff. No. 4) and **(C)** after 349 days (diff. No. 5).

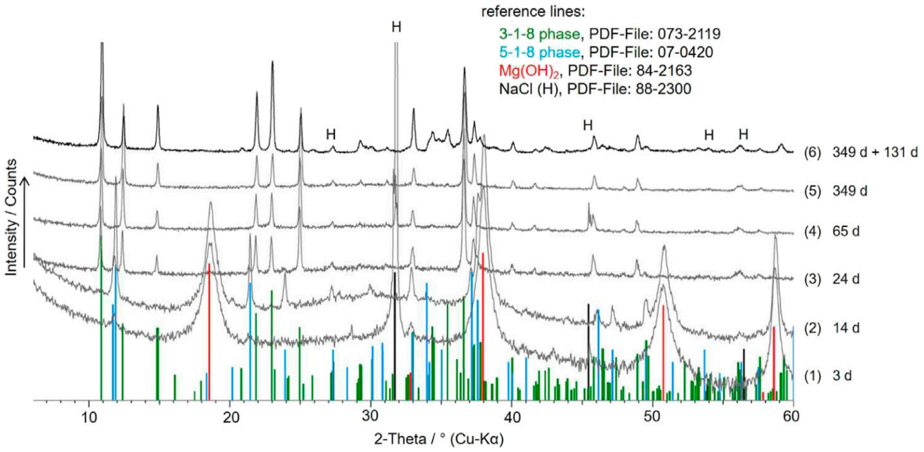

FIGURE 5
X-ray powder diffractograms of the solids obtained after different times of MgO suspension in NaCl-saturated 2.0 m_{MgCl2} solution (diff. No. 1–5); diff. No. 6: solid after re-suspension of the "349-day solid" (diff. No. 5) in new NaCl-saturated 2.0 m_{MgCl2} solution and further 131 days of suspension (= sample No. 20 of Series 3, Table 4).

higher pH_m values can be observed in solutions of lower $MgCl_2$ concentration (Figure 7). All analytical results obtained at the end of the measurements, after 2,394 days, are shown in Table 3 together with the initial data of this sample Series 2.

The results of the sample Series 1 and 2 show unanimously that, starting from MgO or $Mg(OH)_2(s)$ in $MgCl_2$ solutions of medium concentration ($0.5< m_{MgCl2} < 4$), the approach to equilibrium needs longer periods of time (months—about 1 year), but is relatively quickly (hours - days) in 4 m_{MgCl2}, where the equilibrium phase is 3-1-8 phase. Up to 0.5 m_{MgCl2}, $Mg(OH)_2(s)$ is identified as the stable solid phase. In the case of sample Series 1, the intermediate occurrence of the 5-1-8 phase was also observed.

3.2 Solid-liquid equilibria

3.2.1 Na-Mg-Cl-OH-H_2O system: OH^- and H^+ equilibrium concentrations at 25°C und 40°C

The stable solids, $Mg(OH)_2(s)$ and 3-1-8 phase, as well as their mixture (all being obtained from sample Series 1, where respective

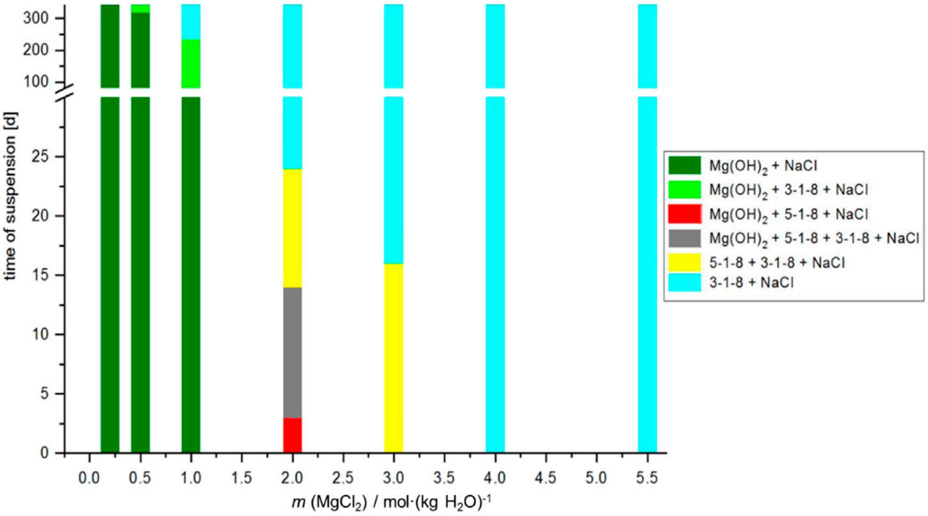

FIGURE 6
Time-dependent solid phase formation at 25°C starting from MgO suspension in the NaCl-saturated $MgCl_2$ solutions (sample Series 1, Table 1). The solution concentrations subsequently analyzed are shown in Figure 9 (blue symbols).

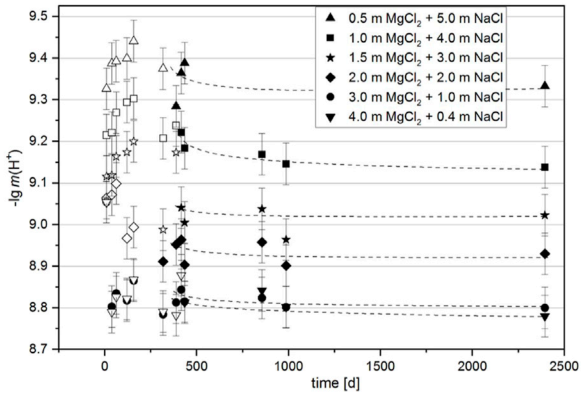

FIGURE 7
Time-dependent development of pH_m in samples with initial $Mg(OH)_2(s)$ suspended in NaCl-saturated $MgCl_2$ solutions (sample Series 2). Filled symbols indicate measured values with deviations from each other smaller than the analytical error of $pH_m = \pm 0.05$ (the beginning of gradually stabilizing values).

solids were filtered off), were again suspended as a new sample Series 3a in corresponding NaCl-$MgCl_2$ solutions at 25°C and analyzed after 131–140 days. No further changes in the composition of the solid phases were observed. The analyzed OH^- solution concentrations (for Series 1 in Table 1 and Series 3 in Table 4) are shown in Figure 9 as a function of $MgCl_2$ concentration. The comparison in Figure 9 shows that the OH^- solution concentrations of sample Series 1 are significantly higher than those of sample Series 3, despite their long-term suspension of almost 1 year (349 days). We have already observed such a behavior (remaining in the OH^- supersaturated region) in our investigations on the solid-solution equilibria in the ternary system Mg-Cl-OH-H_2O at 25°C (not at higher temperatures), using caustic MgO as the initial phase (Pannach et al., 2017). The causes seem to be structural defects (stacking faults in the H_2O-Mg-OH polyhedral layer sequences) and amorphous fractions, especially of the 3-1-8 phase, which arise during its formation from highly OH^- supersaturated solutions. These stacking fault (domains) cause a higher inner energy of the 3-1-8 lattice and are the reason for the slightly higher solubility. On contact or suspension in appropriate OH^- free solution, they dissolve with recrystallisation (defect-free) until equilibrium is reached at low OH^- solution concentrations according to sample Series 3. Still further, i.e., multiple recrystallisation tests did not lead to any further lowering of the OH^- solution concentration. Therefore, in the following, only the OH^- concentrations determined by means of sample Series 3 will be considered as equilibrium concentrations. They agree well with those of D'Ans et al., 1955 at unknown NaCl concentration (open black squares in Figure 9 (cf; Figure 2) up to ≤ 5 m_{MgCl2}. A clear deviation to higher values can be seen in 5.0–5.5 m_{MgCl2} solution, suggesting still supersaturated states. The reported invariant point between $Mg(OH)_2(s)$ and 3-1-8 phase at a $MgCl_2$ concentration of 0.555 molal and 0.53 $Mg(OH)_2$ mmolal agrees very well with our values of 0.56 $MgCl_2$ molal and 0.55 ± 0.03 $Mg(OH)_2$ mmolal. Furthermore, D'Ans et al., 1955 still give metastable data points for $Mg(OH)_2(s)$ at higher $MgCl_2$ concentrations (open circles in Figure 9).

In addition to the samples equilibrated at 25°C, $Mg(OH)_2(s)$ and the 3-1-8 phase as well as the 2-1-4 phase were also suspended at 40°C in corresponding NaCl-saturated $MgCl_2$ solutions for 32–84 days (sample Series 3b). Again, only $Mg(OH)_2(s)$ and the 3-1-8 phase remained as the stable solids at this temperature, the 2-1-4 phase converted either into $Mg(OH)_2(s)$ or the 3-1-8 phase as shown in Table 4. Compared to the 25°C data, higher OH^- concentrations are analyzed at 40°C with a consistent trend towards increasing OH^- concentrations with increasing m_{MgCl2}. The highest values are reached at $MgCl_2$ saturation. At 40°C its value is twice the one at 25°C. The invariant point between $Mg(OH)_2(s)$ and 3-1-8 phase

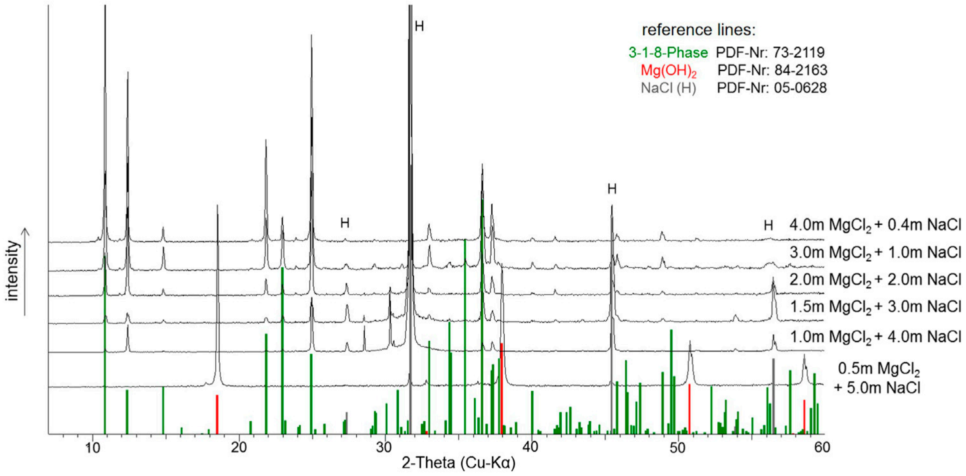

FIGURE 8
X-ray powder diffractograms of the solid phases after 2,394 days of suspension of $Mg(OH)_2(s)$ in NaCl-saturated $MgCl_2$ solutions (sample Series 2, see Table 3).

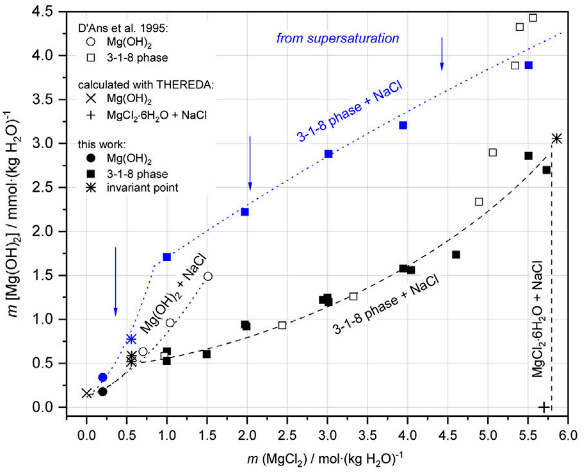

FIGURE 9
$Mg(OH)_2$ solution concentrations in the Na-Mg-Cl-OH-H_2O system at 25°C, obtained with sample Series 1 after 349 days, blue symbols (suspension of caustic MgO as initial solid, supersaturation approach) and sample Series 3a after 131–144 days, full black symbols [equilibration of $Mg(OH)_2(s)$ and 3-1-8 phase as initial solids].

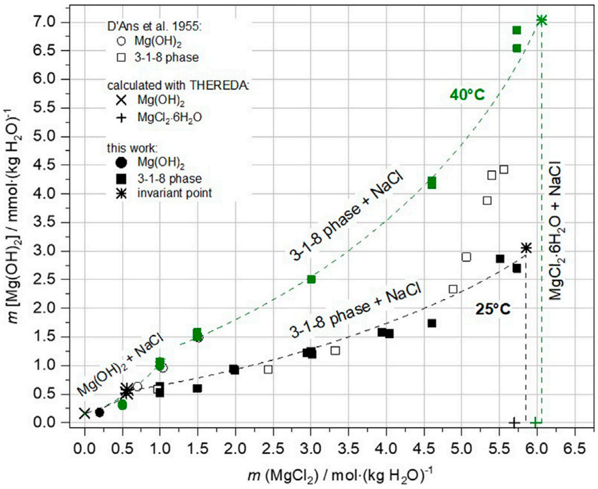

FIGURE 10
$Mg(OH)_2$ equilibrium concentrations in presence of the stable solids $Mg(OH)_2(s)$ and 3-1-8 phase (and $MgCl_2{\cdot}6H_2O$ at $MgCl_2$-saturation) at NaCl saturation in the Na-Mg-Cl-OH-H_2O system at 25°C and 40°C.

(+NaCl) has shifted from 0.56 m_{MgCl2} at 25°C to about 1.1–1.3 m_{MgCl2} at 40 °C in the NaCl-saturated solutions (Figure 10). The corresponding OH^- concentration has approximately tripled from about 0.0005 m $Mg(OH)_2$ to 0.0013–0.0015 m.

The pH_m analyzed in sample Series 2 at 25°C and sample Series 3a and 3b at 25°C and 40°C respectively (Tables 3, 4) are presented in Figure 11. The 25°C values of Series 2 form a common isotherm with those determined for Series 3a. Obviously, equilibrium with respect to H^+ solution concentrations had been reached with both sample series in the different laboratories. As no OH^- concentrations were analyzed for sample Series 2 (KIT-INE), it is not possible to say whether equilibrium has also been reached for the OH^- solution concentration in these suspensions over the long monitoring period of 6.5 years in comparison with sample Series 3a.

The pH_m measured at 25°C are highest (H^+ concentrations lowest) in the solutions with lowest $MgCl_2$ concentrations in equilibrium with $Mg(OH)_2(s)$ (pH_m = 9.57 in 0.2 m_{MgCl2} NaCl saturated solution, see all values in Tables 3, 4). In $MgCl_2$-free NaCl-saturated solution, pH_m still increases to 10.72, as shown by the data point from Altmaier et al. (2003) in Figure 11. At the invariant point of $Mg(OH)_2(s)$ + 3-1-8-phase + NaCl in 0.56 m_{MgCl2} solution, the pH_m was determined to be 9.32. As the $MgCl_2$ concentration increases, the pH_m in the presence of 3-1-8 phase + NaCl(s) decreases only gradually over the wide concentration range to pH_m = 8.7 in 5.5 m_{MgCl2} solution. Compared

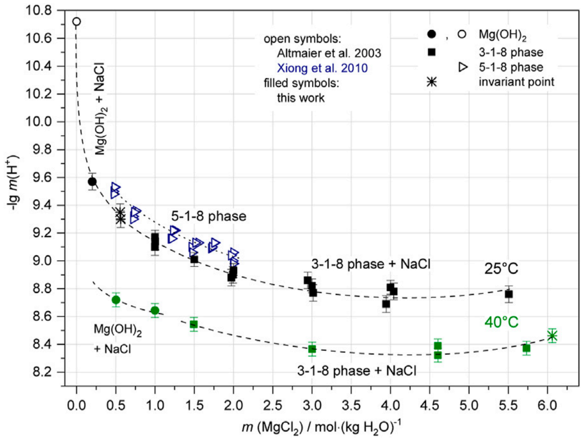

FIGURE 11
pH_m in the system Na-Mg-Cl-OH-H_2O at NaCl saturation and 25°C (filled black symbols: sample Series 2 and sample Series 3a) in comparison with literature values (open circle: Altmaier et al., 2003, blue; Xiong et al., 2010, cf; Figure 3) and 40°C (green symbols: sample Series 3b).

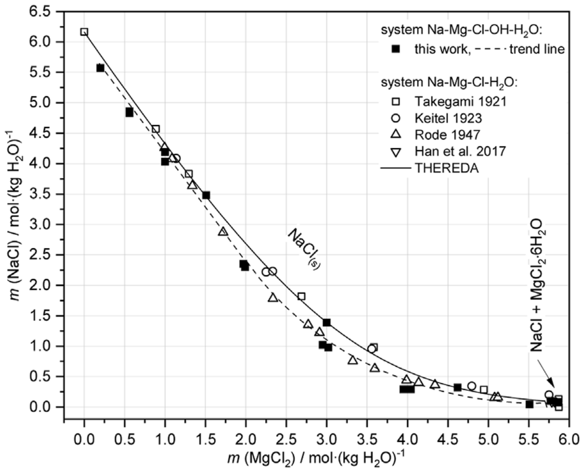

FIGURE 12
Analyzed NaCl saturation concentrations in the system Na-Mg-Cl-OH-H_2O in presence of $Mg(OH)_2(s)$ resp. 3-1-8 phase (see Table 4, Series 3a) in compare to the OH^- free, ternary Na-Mg-Cl-H_2O system (literature data) at 25°C (Takegami, 1921, Keitel, 1923, Rode, 1947, Han et al., 2017).

to the 25°C data of Xiong et al. (2010) for the 5-1-8 phase in the investigated range of $0.5 \geq m_{MgCl2} \leq 2$ (NaCl saturated), the pH_m are at higher values compared to both $Mg(OH)_2(s)$ and the 3-1-8 phase. This indicates a metastable occurrence of the 5-1-8 phase, which is consistent with our observations of solid phase formation in the system (see Section 3.1), showing the intermediate occurrence of the 5-1-8 phase.

The data curve shown in Figure 11 for the samples at 40°C runs nearly parallel to the respective curve for 25°C, shifted to lower pH_m by about 0.6 units in the presence of $Mg(OH)_2(s)$ and about 0.4 units in the presence of the 3-1-8 phase (see also Table 4). With $Mg(OH)_2(s)$ as solid phase in 0.5 and 1 m_{MgCl2} solution, the pH_m was measured as 8.72 and 8.64 respectively. In the presence of the 3-1-8 phase, the values again decrease only slightly with increasing m_{MgCl2}. Between $4 < m_{MgCl2} < 5$ a flat minimum occurs at $pH_m \sim 8.3$. At the invariant point of 3-1-8 phase + $MgCl_2{\cdot}6H_2O(s)$ + NaCl(s) the pH_m is 8.4–8.5.

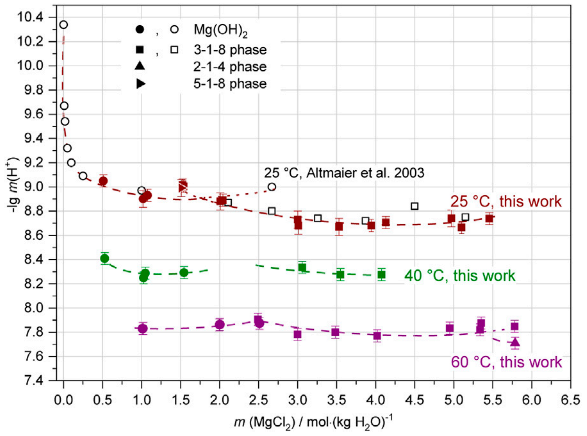

FIGURE 13
pH_m in the Mg-Cl-OH-H_2O system at 25°C (after 1,172 or 1,417 days of equilibration), 40°C (after 1,885–2,148 days) and 60°C (after 1,081–1,830 days) in comparison with the literature (open black symbols: Altmaier et al., 2003).

Beside the analyzed OH^- and H^+ solution concentration, also the NaCl concentrations of saturation determined in sample Series 3a are plotted for 25°C in Figure 12. As the data show, at least approximate NaCl saturation is approached with the initial compositions of sample Series 2 (Table 3) after equilibration in the Na-Mg-Cl-OH-H_2O system. Compared to the OH^- free, ternary Na-Mg-Cl-H_2O system, the adjustment of the very low OH^- saturation concentration causes within the scatter of the experimental data only a very slight decrease of the NaCl saturation concentration in the Na-Mg-Cl-OH-H_2O system.

3.2.2 Mg-Cl-OH-H_2O system: H^+ equilibrium concentrations at 25°C, 40°C and 60°C

In the study on the solubility equilibria in the ternary system Mg-Cl-OH-H_2O from 25°C to 120°C (Pannach et al., 2017), the pH_m in the samples equilibrated at 25°C, 40°C and 60°C were measured but not yet published. The results are given now in Table 4 (as sample Series 4a, b and c) together with all initial components. Figure 13 shows the pH_m as a function of $MgCl_2$ concentration for all three temperatures. The values for 40°C and 60°C are shifted to lower pH_m by about 0.6–0.4 units. The intersection of the branches for $Mg(OH)_2(s)$ and 3-1-8 phase data indicate the invariant points, which shift from 1.7–1.8 m_{MgCl2} at 25°C to about 2 at 40°C and 2.5 at 60°C (as already observed by Pannach et al. (2017) on the basis of the "OH^- isotherms"). At 60°C a further Sorel phase, the 2-1-4 phase, increases relative to the 3-1-8 phase near the $MgCl_2$ saturation. Thus, we could measure also a pH_m value in presence of this phase in 5.8 m_{MgCl2} solution.

3.2.3 Comparison of NaCl-free and NaCl saturated system at 25°C

Comparing the two systems at 25°C shows that the stability field of the 3-1-8 phase in NaCl-saturated solutions expands towards lower $MgCl_2$ concentrations, as can be seen by the shift of the invariant point with $Mg(OH)_2(s)$ from m_{MgCl2} of 1.7–1.8 in NaCl-free to 0.56 in NaCl-saturated solution (Figures 14, 15).

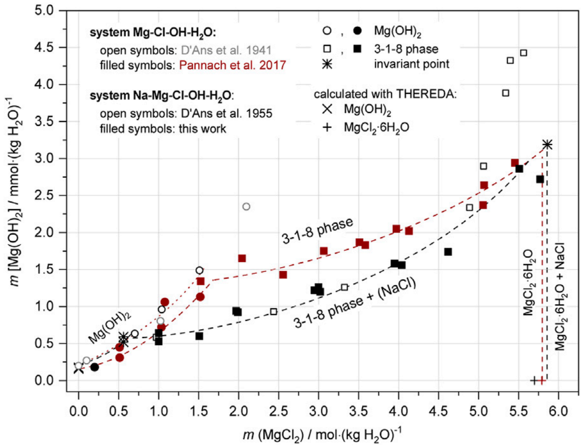

FIGURE 14
Comparison of OH⁻ solution concentrations in the systems Na-Mg-Cl-OH-H$_2$O (black symbols) and Mg-Cl-OH-H$_2$O (Pannach et al., 2017) (brown symbols) at 25°C.

The OH⁻ concentrations and thus the solubility of the 3-1-8 phase are lower in NaCl-saturated than in NaCl-free solutions. However, the OH⁻ concentrations approach each other when reaching saturation concentration of MgCl$_2$ (Figure 14).

With the invariant point at 0.56 m_{MgCl2}, a MgO-based concrete geotechnical barrier consisting of 3-1-8 binder phase (besides inert aggregates) will be in equilibrium with NaCl-saturated solutions as soon as concentrations of MgCl$_2$ as low as 0.56 m_{MgCl2} are present. For solutions not saturated with NaCl higher concentrations are needed to ensure stability of the binder phase against the solution. In NaCl-free solutions a minimum of 1.7–1.8 m_{MgCl2} is required.

As can be seen in Figure 15, Mg(OH)$_2$(s) buffers a pH$_m$ range from 9.3 to 9.6 in NaCl-saturated solutions, and if they are free of MgCl$_2$ up to 10.7. From 0.56 m_{MgCl2}, a pH$_m$ of about 9.3 is established by the 3-1-8 phase, decreasing to pH$_m$ = 8.7 with further increase in MgCl$_2$ concentration. This pH$_m$ range also is found in NaCl-free solutions in the presence of the 3-1-8 phase. An analogous situation would be found when comparing the 40°C data of both systems, however, shifted by 0.6–0.4 units to lower pH$_m$ values.

3.3 Solubility constants for Mg(OH)$_2$(s) and the Sorel phases 3-1-8, 2-1-4 and 5-1-8 at 25°C, 40°C und 60°C

The solubility constants, lg K_S, for Mg(OH)$_2$(s) and the Sorel phases 3-1-8 and 2-1-4 were calculated from the molal equilibrium H⁺ concentrations in the NaCl-saturated MgCl$_2$ solutions at 25°C and 40°C (Tables 3, 4) and in the MgCl$_2$ solutions free of NaCl at 25°C, 40°C and 60°C (Table 5) according to Eqs 11–18. The calculation of lg K_S was also possible for the metastable 5-1-8 phase by measuring the H⁺ concentration during its intermediate appearance in a 25 °C suspension (sample No. 46 in Table 5). The activity coefficients γ_i of Mg^{2+}, H⁺ und Cl⁻ and the water activity a_W were calculated using the Pitzer data set of THEREDA for the hexary system of oceanic salts including acids and bases [THEREDA, Voigt (2020)].

Mg(OH)$_2$:

$$Mg^{2+} + 2\,H_2O \rightleftharpoons Mg(OH)_{2\,(s)} + 2H^{+} \tag{11}$$

$$lgK^{\circ}_{S,Mg(OH)_2} = \lg\left(\frac{m^2_{H^+}}{m_{Mg^{2+}}}\cdot\frac{\gamma^2_{H^+}}{\gamma_{Mg^{2+}}}\cdot\frac{1}{a^2_W}\right) \tag{12}$$

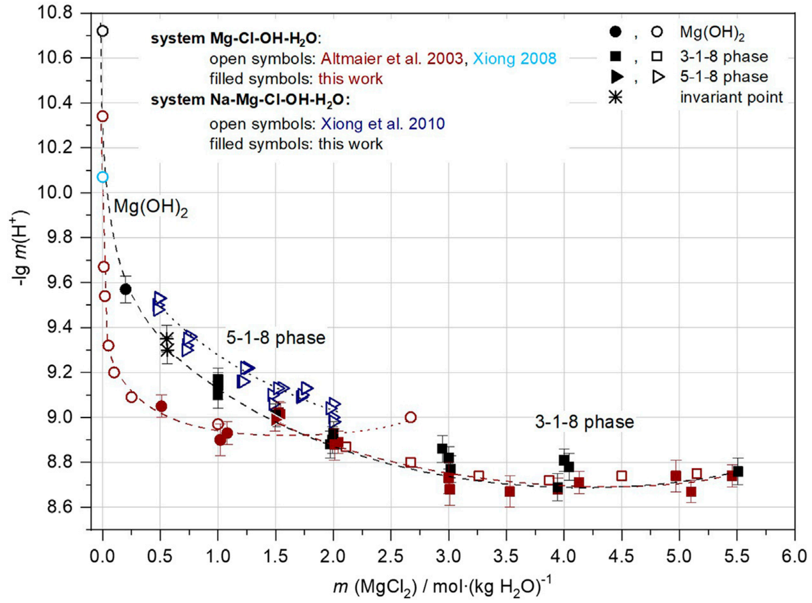

FIGURE 15
Comparison of pH$_m$ in the Na-Mg-Cl-OH-H$_2$O system (black symbols) and the Mg-Cl-OH-H$_2$O system (brown symbols) at 25°C.

TABLE 2 Solubility constants (lg K_S) for $Mg(OH)_2$(s), and the Sorel phases 3-1-8, 5-1-8 und 2-1-4 in compare to available data from literature.

Solid	T [°C]	System Mg-Cl-OH-H_2O		System Na-Mg-Cl-OH-H_2O		Overall mean value, lg K_S
		lg K_S ± σ	Reference	lg K_S ± σ	Reference	
$Mg(OH)_2$	25	−17.16 ± 0.10 −17.16 ± 0.08	Altmaier et al. (2003) this work	−17.05 ± 0.20 −17.01 ± 0.10 −17.17 ± 0.03	Xiong (2008) Altmaier et al. (2003) this work	−17.1 ± 0.2
	40	−15.86 ± 0.09	this work	−16.00 ± 0.06	this work	−15.9 ± 0.1
	60	−14.92 ± 0.02	this work	-		
3-1-8 phase	25	−26.15 ± 0.16 −26.10 ± 0.13	Altmaier et al. (2003) this work	−26.16 ± 0.13	this work	−26.1 ± 0.2
	40	−24.72 ± 0.04	this work	−24.88 ± 0.16	this work	−24.8 ± 0.2
	60	−23.04 ± 0.11	this work	-		
5-1-8 phase	25	−43.39 ± 0.25*	this work	−43.21 ± 0.33	Xiong et al. (2010)	−43.3 ± 0.3
2-1-4 phase	60	−32.95 ± 0.20*	this work	-		

*as only one sample was available, the deviation was calculated from the H^+ concentration determination uncertainty of ± 0.05 pH units.

TABLE 3 Initial components and sample composition for sample Series 2 (KIT-INE). Solution composition after equilibration (6.5 years) and calculated solubility constants for the stable solids $Mg(OH)_2$ and 3-1-8 phase in the Na-Mg-Cl-OH-H_2O (NaCl-saturated) system at 25°C.

No.	Initial solid-liquid system				Equilibrated solid-liquid system				
	Solid $Mg(OH)_2$	NaCl-saturated $MgCl_2$ solution			$MgCl_2$	NaCl	-lg *m* (H^+)	Solid + $NaCl_{(s)}$	-lg K_S
		$MgCl_2 \cdot 6H_2O$	NaCl	H_2O					
	[g]				[molal]^a				
8	0.3	20.330	58.440	189.191	0.50	5.00	9.34	$Mg(OH)_2$	17.14
9	0.3	40.660	46.752	178.382	1.00	4.00	9.17	3-1-8	26.19
10	0.3	60.990	35.064	167.573	1.50	3.00	9.01	3-1-8	26.11
11	0.3	81.320	23.376	156.764	2.00	2.00	8.93	3-1-8	26.16
12	0.3	121.980	11.688	135.147	3.00	1.00	8.82	3-1-8	26.18
13	0.3	162.640	4.675	113.529	4.00	0.40	8.81	3-1-8	26.40

^{a}Calculated from initial solution compounds (not analyzed).

3-1-8 phase:

$$2\,Mg^{2+} + Cl^- + 7\,H_2O \rightleftharpoons Mg_2Cl(OH)_3 \cdot 4H_2O_{(s)} + 3\,H^+ \tag{13}$$

$$lgK^{\circ}_{S,3-1-8} = lg\left(\frac{m^3_{H^+}}{m^2_{Mg^{2+}} \cdot m_{Cl^-}} \cdot \frac{\gamma^3_{H^+}}{\gamma^2_{Mg^{2+}} \cdot \gamma_{Cl^-}} \cdot \frac{1}{a^7_W}\right) \tag{14}$$

2-1-4 phase:

$$3\,Mg^{2+} + 2\,Cl^- + 8\,H_2O \rightleftharpoons Mg_3Cl_2\,(OH)_4 \cdot 4H_2O_{(s)} + 4\,H^+ \tag{15}$$

$$lgK^{\circ}_{S,2-1-4} = lg\left(\frac{m^4_{H^+}}{m^3_{Mg^{2+}} \cdot m^2_{Cl^-}} \cdot \frac{\gamma^4_{H^+}}{\gamma^3_{Mg^{2+}} \cdot \gamma^2_{Cl^-}} \cdot \frac{1}{a^8_W}\right) \tag{16}$$

5-1-8 phase:

$$3\,Mg^{2+} + Cl^- + 9\,H_2O \rightleftharpoons Mg_3Cl(OH)_5 \cdot 4H_2O_{(s)} + 5\,H^+ \tag{17}$$

$$lgK^{\circ}_{S,5-1-8} = lg\left(\frac{m^5_{H^+}}{m^3_{Mg^{2+}} \cdot m_{Cl^-}} \cdot \frac{\gamma^5_{H^+}}{\gamma^3_{Mg^{2+}} \cdot \gamma_{Cl^-}} \cdot \frac{1}{a^9_W}\right) \tag{18}$$

All calculated lg K_S values are given as mean values in Table 2 for each system and temperature (single values in Tables 3–5) compared with literature data where available. For $Mg(OH)_2$(s) a mean value at 25°C of lg K_S = −17.17 ± 0.03 is obtained for NaCl-saturated solutions (Tables 3, 4) and lg K_S = −17.16 ± 0.08 for NaCl-free solutions (Table 5). The values are in a very good agreement with those of Altmaier et al. (2003) and Xiong (2008) within the given error range as can be seen in Table 2. There are some more studies on solubility constants for $Mg(OH)_2$(s) discussed and evaluated by Altmaier et al. (2003), which agree within an overall mean value of lg $K_{S,Mg(OH)2,25°C}$ = −17.1 ± 0.2. For 40°C we determined lg $K_{S,Mg(OH)2,40°C}$ = −15.9 ± 0.2 from the two mean values, lg K_S = −16.00 ± 0.06 from NaCl-saturated solutions (Table 4) and lg K_S = −15.86 ± 0.09 from the NaCl-free solutions (Table 5). At 60°C a value of lg $K_{S,Mg(OH)2,60°C}$ = −14.92 ± 0.02 was calculated from the NaCl-free $MgCl_2$ solutions (Table 5).

For the 3-1-8 phase the obtained value of lg $K_{S,3\text{-}1\text{-}8,25°C}$ = −26.10 ± 0.13 agrees very well with Altmaier et al. (2003) (−26.15 ± 0.16) from

TABLE 4 Initial components and sample composition for sample Series 3 (TUBAF). Analyzed solution composition after equilibration at 25°C (131–144 days), at 40°C (32–84 days) and calculated solubility constants for the stable solids $Mg(OH)_2$ and 3-1-8 phase in the Na-Mg-Cl-OH-H_2O (NaCl-saturated) system.

No.	Initial solid-liquid system					Equilibrated solid-liquid system					
	Solids			$MgCl_2$ solution		$MgCl_2$	NaCl	$Mg(OH)_2$	-lg $m(H^+)$	Solid + $NaCl_{(s)}$	-lg K_S
			NaCl	[g]	[mmolal]	[mmolal]		[mmolal]			
	[g]										
T = 25°C (sample Series 3a)											
14	$Mg(OH)_2$	<2	70.07	199.99	0.2	0.20	5.57	0.18	9.57	$Mg(OH)_2$	17.20
15	$Mg(OH)_2$ + 3-1-8	<2	60.20	200.00	0.5	0.56	4.86	0.59	9.30	$Mg(OH)_2$	
16	$Mg(OH)_2$ + 3-1-8	<2	60.21	200.01	0.5	0.56	4.83	0.52	9.35	$Mg(OH)_2$ + 3-1-8	
17	$Mg(OH)_2$ + 3-1-8	<2	47.15	201.02	1.0	1.00	4.03	0.53	9.10	3-1-8	25.98
18	3-1-8	<2	47.15	200.01	1.0	1.00	4.19	0.64	9.14	3-1-8	26.08
19	3-1-8	<2	29.59	199.98	2.0	1.97	2.35	0.94	8.88	3-1-8	25.99
20	3-1-8	<2	29.56	200.03	2.0	1.99	2.30	0.92	8.90	3-1-8	26.04
21	3-1-8	<2	15.58	200.01	3.0	2.95	1.02	1.22	8.86	3-1-8	26.33
22	3-1-8	<2	15.56	200.05	3.0	3.02	0.98	1.20	8.77	3-1-8	26.07
23	3-1-8	<2	8.95	200.01	4.0	3.95	0.29	1.58	8.69	3-1-8	26.06
24	3-1-8	<2	8.58	200.99	4.0	4.04	0.29	1.56	8.78	3-1-8	26.32
25	3-1-8	<2	4.05	200.01	5.5	5.51	0.04	2.86	8.76	3-1-8	26.32
26	3-1-8	2.0	0.96	98.67	1.5	1.51	3.48	0.60	n. d.	3-1-8	
27	3-1-8	2.0	0.99	100.04	3.0	3.00	1.39	1.26	n. d.	3-1-8	
28	3-1-8	2.0	1.05	99.95	4.5	4.62	0.32	1.74	n. d.	3-1-8	
29	3-1-8	2.1	0.98	101.77	5.75	5.77	0.10	2.72	n. d.	3-1-8	
30	3-1-8 + $MgCl_2 \cdot 6H_2O$	2.0	1.00	95.31	5.9	5.86	0.08	3.19	n. d.	3-1-8 + $MgCl_2 \cdot 6H_2O$	
T = 40°C (sample Series 3b)											
31	$Mg(OH)_2$	2.0	0.98	100.70	0.5	0.50	4.98	0.29	n. d.	$Mg(OH)_2$	
32	2-1-4	3.0	1.00	100.68	0.5	0.50	4.98	0.33	8.72	$Mg(OH)_2$	15.93
33	$Mg(OH)_2$	2.0	1.00	99.78	1.0	1.0	4.04	0.99	n. d.	$Mg(OH)_2$	
34	2-1-4	2.0	1.01	101.17	1.0	1.0	4.04	1.06	8.64	$Mg(OH)_2$	16.06
35	3-1-8	2.0	1.02	100.98	1.5	1.49	3.25	1.50	n. d.	3-1-8	
36	2-1-4	3.0	1.00	100.70	1.5	1.49	3.25	1.58	8.54	3-1-8	24.65
37	2-1-4	3.0	1.02	99.81	3.0	3.00	1.22	2.50	8.37	3-1-8	24.75
38	3-1-8	3.0	1.01	100.03	4.5	4.60	0.30	4.23	8.32	3-1-8	24.89
39	2-1-4	3.1	1.01	100.30	4.5	4.60	0.30	4.16	8.39	3-1-8	25.09
40	3-1-8	3.0	1.01	99.45	5.75	5.73	0.03	6.86	n. d.	3-1-8	
41	2-1-4	3.1	0.99	100.16	5.75	5.73	0.03	6.54	8.37	3-1-8	25.02
42	3-1-8 + $MgCl_2 \cdot 6H_2O$	2.1	1.01	98.36	6.06	6.01	0.10	7.04	8.46	3-1-8 + $MgCl_2 \cdot 6H_2O$	

n. d.: not determined.

TABLE 5 Initial components and sample composition for sample Series 4 (TUBAF). Analyzed solution composition after equilibration at 25°C (3 years), at 40°C (3 years) and 60°C (205–318 days) in the system Mg-Cl-OH-H_2O. Calculated solubility constants for the stable solids $Mg(OH)_2$, 3-1-8 and 2-1-4 phase and the metastable 5-1-8 phase.

No.	Initial solid-liquid system				Equilibrated solid-liquid system				
	Solid		$MgCl_2$ solution		$MgCl_2$	$Mg(OH)_2$	-lg $m(H^+)$	Solid	-lg K_S
	[g]		[g]	[molal]	[molal]	[mmolal]			
T = 25°C (sample Series 4a)									
43	(MgO	1.0013)[a]	199.99	0.5	0.51	0.45	9.05	$Mg(OH)_2$	17.27
44	(MgO	1.0019)[a]	200.00	1.0	1.02	n. d.	8.90	$Mg(OH)_2$	17.08
45	(MgO	1.0000)[a]	200.00	1.0	1.08	1.06	8.93	$Mg(OH)_2$	17.14
46	(MgO	1.0313)[a]	201.42	1.5	1.51	2.84	8.99	5-1–8[b]	43.39
47	(MgO	1.0015)[a]	200.01	1.5	1.54	2.31	9.01	3-1–8[b]	26.19
48	(MgO	0.0948)[a]	200.01	2.0	2.01	n. d.	8.88	3-1-8	26.06
49	(MgO	1.0003)[a]	200.00	3.0	3.00	n. d.	8.73	3-1-8	25.99
50	(MgO	0.0949)[a]	200.03	3.0	3.01	n. d.	8.68	3-1-8	25.84
51	(MgO	1.0087)[a]	200.97	3.5	3.53	n. d.	8.67	3-1-8	25.94
52	(MgO	0.9293)[a]	185.81	4.0	3.95	2.74	8.68	3-1-8	26.04
53	(MgO	0.0947)[a]	200.02	5.0	4.97	n. d.	8.74	3-1-8	26.29
54	(MgO	1.0011)[a]	200.00	5.0	5.10	3.41	8.67	3-1-8	26.08
55	3-1-8	0.1018	157.25	1.5	1.53	1.34	9.02	3-1-8	26.21
56	3-1-8	0.1010	150.00	2.0	2.04	1.65	8.89	3-1-8	26.11
57	3-1-8	0.1080	149.99	4.0	4.13	2.02	8.71	3-1-8	26.15
58	3-1-8	0.1104	150.09	5.5	5.46	2.94	8.74	3-1-8	26.27
T = 40°C (sample Series 4b)									
59	(MgO	1.0011)[a]	200.00	0.5	0.53	1.25	8.41	$Mg(OH)_2$	15.99
60	(MgO	1.0009)[a]	200.00	1.0	1.05	1.63	8.28	$Mg(OH)_2$	15.83
61	(MgO	1.0035)[a]	200.00	1.0	1.03	0.83	8.24	$Mg(OH)_2$	15.75
62	(MgO	1.0003)[a]	200.00	1.5	1.55	2.58	8.29	$Mg(OH)_2$	15.86
63	3-1-8	0.1514	150.01	3.0	3.06	3.76	8.34	3-1-8	24.74
64	3-1-8	0.1513	150.01	3.5	3.55	3.99	8.28	3-1-8	24.67
65	3-1-8	0.1546	150.00	4.0	4.08	4.10	8.28	3-1-8	24.75
T = 60°C (sample Series 4c)									
66	(MgO	0.9999)[a]	199.99	1.0	1.01	1.26	7.83	$Mg(OH)_2$	14.90
67	(MgO	1.0004)[a]	200.37	2.5	2.49	8.57	7.87	3-1–8[b]	23.00
68	(MgO	1.0006)[a]	200.01	5.5	5.34	12.53	7.82	3-1-8	23.06
69	$Mg(OH)_2$	0.1004	199.95	1.0	1.02	0.96	7.83	$Mg(OH)_2$	14.90
70	$Mg(OH)_2$	0.1110	200.06	2.0	1.99	3.39	7.86	$Mg(OH)_2$	14.94
71	3-1-8	0.2307	200.01	2.0	2.00	3.11	7.86	$Mg(OH)_2$	14.95
72	3-1-8	0.2551	200.02	2.5	2.51	6.63	7.87	$Mg(OH)_2$	14.93
73	3-1-8	0.2679	200.01	3.0	2.99	8.41	7.78	3-1-8	22.86

(Continued on following page)

TABLE 5 (*Continued*) **Initial components and sample composition for sample Series 4 (TUBAF). Analyzed solution composition after equilibration at 25°C (3 years), at 40°C (3 years) and 60°C (205–318 days) in the system Mg-Cl-OH-H_2O. Calculated solubility constants for the stable solids $Mg(OH)_2$, 3-1-8 and 2-1-4 phase and the metastable 5-1-8 phase.**

No.	Initial solid-liquid system				Equilibrated solid-liquid system				
	Solid		$MgCl_2$ solution		$MgCl_2$	$Mg(OH)_2$	-lg $m(H^+)$	Solid	-lg K_S
	[g]		[g]	[molal]	[molal]	[mmolal]			
				T = 60°C (sample Series 4c)					
74	3-1-8	0.2893	200.00	3.5	3.48	8.59	7.80	3-1-8	22.99
75	3-1-8	0.2730	200.02	4.0	4.02	9.29	7.77	3-1-8	22.95
76	3-1-8	0.3378	200.02	5.0	4.95	11.77	7.83	3-1-8	23.13
77	3-1-8	0.1984	200.00	5.5	5.35	13.36	7.88	3-1-8	23.24
78	3-1-8	0.6237	200.04	6.0	5.78	16.24	7.85	3-1–8[b]	23.10
79	2-1-4	0.4122	200.07	6.3	5.79	7.13	7.71	2-1-4	32.95

No's in italics: already listed in Pannach et al. (2017). All other No's are additional equilibrated samples.

[a] clear OH^--supersaturated $MgCl_2$-solution after filtration of the remaining MgO [see exp. part in Pannach et al. (2017)].

[b] metastabile.

n. d. not determined.

measurements in $MgCl_2$ solutions at 25°C. Our measurements in NaCl-saturated $MgCl_2$ solutions (Tables 3, 4) yield a consistent value of lg $K_{S,3\text{-}1\text{-}8,25°C} = -26.16 \pm 0.13$. At 40°C, equally consistent values with lg $K_{S,3\text{-}1\text{-}8,40°C} = -24.88 \pm 0.16$ and -24.72 ± 0.04 were calculated from the NaCl-saturated (Table 4) and NaCl-free solutions (Table 5). From the measurements at 60°C in $MgCl_2$ solutions a lg $K_{S,3\text{-}1\text{-}8,60°C} = -23.04 \pm 0.11$ results accordingly. For the 2-1-4 phase occurring at and above 60°C in concentrated $MgCl_2$ solution, the solubility constant could only be determined from one sample (in 5.79 molal $MgCl_2$-solution, Table 5) with lg $K_{S,2\text{-}1\text{-}4,60°C} = -32.95 \pm 0.2$.

4 Conclusion

Sorel phases are binder phases of the magnesia building material (Sorel cement/concrete) highly suitable for construction of geotechnical barriers in rock salt formations. Compared with classical concrete, materials based on Sorel phases possess the principal property of being stable against saline $MgCl_2$ containing solutions. This specific feature represents a crucial prerequisite for the construction of geotechnical barriers in repositories for radioactive waste in rock salt, as potentially occurring brines are expected to contain $MgCl_2$. In addition, to minimize solubility and possible mobilization of actinides in brines systems, the pH should preferably be buffered in the weakly alkaline range. Detailed understanding of relevant solid-liquid equilibria and related pH_m data for the equilibrium solutions provide the scientific basis and information in the context of safety analysis.

In this work, the solid-liquid equilibria of the Sorel phases and $Mg(OH)_2$(s) in the system Na-Mg-Cl-OH-H_2O at saturation of NaCl were determined at 25°C and 40°C. Starting from the suspension of MgO (sample Series 1, ss 1) and $Mg(OH)_2$(s) (sample Series 2, ss 2), the solid phase formation was followed at 25°C over a period of one (ss 1) and 6 years, respectively, including the determination of H^+ solution concentrations, pH_m, (ss 2) as a function of $MgCl_2$ molality.

$Mg(OH)_2$(s) and the 3-1-8 phase were identified as the stable solids in the system. Following their further equilibration at 25°C and 40°C (ss 3), the equilibrium OH^- and H^+ concentrations (pH_m) were determined. $Mg(OH)_2$(s) is the stable phase in the presence of NaCl-saturated solutions with low $MgCl_2$ content (up to about 0.56 m_{MgCl2}) and the 3-1-8 phase in the more concentrated $MgCl_2$ solutions at 25°C. At 40°C, the invariant point shifts to 1–1.5 m_{MgCl2}. The 5-1-8 Sorel phase was found to occur only intermediately during the study period of ss1 and is therefore only a metastable phase in the solid-solution system.

In addition to the already published solid-liquid equilibria for the ternary system Mg-Cl-OH-H_2O (25°C–120°C) in Pannach et al. (2017), the pH_m determined at 25°C, 40°C and 60°C are reported here. Using these and with known ion-interaction Pitzer coefficients, the solubility constants for $Mg(OH)_2$(s) and the 3-1-8 phase could be calculated for 25°C, 40°C and 60°C. From the measurements in the ternary system it was also possible to calculate the solubility constant for the metastable 5-1-8 phase at 25°C and for the 2-1-4 phase at 60°C, which was found only at higher temperature in the ternary system at high $MgCl_2$ concentrations.

On the basis of the solid-liquid equilibria determined in this work, it is now possible to predict the long-term stability of magnesia building material in contact with solutions in a saline environment on a significantly improved scientific level and with high robustness. The pH_m values developing in equilibrium with the respective Sorel phases or $Mg(OH)_2$(s) are identified as a function of the solution composition for the system Na-Mg-Cl-OH-H_2O at NaCl saturation.

The data also allow an extension of the Pitzer dataset in THEREDA to calculate the solubility equilibria of Sorel phases and $Mg(OH)_2(s)$ in complex salt solutions of the hexary system of oceanic salts, which is presented in Part II of this work.

Data availability statement

The original contributions presented in the study are included in the article/supplementary material, further inquiries can be directed to the corresponding author.

Author contributions

DF: initiator of the investigation, head of the research area, data evaluation and writer of the paper. MP: experimentator, analysis and data evaluation, preparation of figures and tables. IP: experimentator, analysis. VM: experimentator and data evaluation. MA: experimentator, analysis, date evaluation, and co-writer of the paper. WV: initiator of some measurements, advisor, and co-writer of the paper.

Funding

Open Access Funding by the Publication Fund of the TU Bergakademie Freiberg.

Acknowledgments

We would like to thank the former German Federal Ministry for Economic Affairs and Energy (BMWi) for financial support within the R&D project 02E10880 “Relationship between chemism and mechanical properties of the MgO building material” (2010–2014), and the Federal Company for the Disposal of Radioactive Waste (BGE) with the current research project TEKFuE-21-02-js “Sorel phases equilibria”.

Conflict of interest

Publisher’s note

References

Altmaier, M., Metz, V., Neck, V., Müller, R., and Fanghänel, T. (2003). Solid-liquid equilibria of $Mg(OH)_2(cr)$ and $Mg_2(OH)_3Cl{\cdot}4H_2O(cr)$ in the system Mg-Na-H-OH-Cl-H_2O at 25°C. *Geochim. Cosmochim. Acta* 67 (19), 3595–3601. doi:10.1016/s0016-7037(03)00165-0

Bette, S., Dinnebier, R. E., Röder, C., and und Freyer, D. (2015). A solid solution series of atacamite type $Ni_{2x}Mg_{2\text{-}2x}Cl(OH)_3$. *J. Solid State Chem.* 228, 131–140. doi:10.1016/j.jssc.2015.04.015

Bianco, Y. (1958). The basic chlorides and bromides of magnesium. *Ann. Chim.* 13, 370–404.

Bianco, Y. (1951). The formation of basic magnesium chlorides at 50-175°C by aqueous methods. *C. R. Acad. Sci.* 232, 1108–1110.

Biedermann, T. W., and Schwarzenbach, G. (1948). The “complexometric” titration of alkaline earths and some other metals with Eriochromschwarz. *Chimia* 2, 56–59.

Bodine, M. W. (1976). Magnesium hydroxychloride: A possible pH buffer in marine evaporite. *Geology* 4, 76–80. doi:10.1130/0091-7613(1976)4<76:mhappb>2.0.co;2

Cole, W. F., and Demediuk, T. (1955). X-ray, thermal and dehydration studies on magnesium oxychlorides. *Austr. J. Chem.* 8 (2), 234–251. doi:10.1071/ch9550234

D’Ans, J., Busse, W., and Freud, H. E. (1955). Über basische Magnesiumchloride. *Kali Steinsalz* 8, 3–7.

D’Ans, J., and Katz, W. (1941). Magnesiumhydroxyd-Löslichkeiten, p_H-Zahlen und Pufferung im System H_2O-$MgCl_2$-$Mg(OH)_2$. *Kali Steinsalz* 35, 37–41.

de Wolff, P. M., and Kortlandt, D. (1954). Crystal structure determination from an x-ray powder diffraction pattern of β-$Mg_2(OH)_3Cl$. *Appl. Sci. Res. B3*, 3, 400–408. doi:10.1007/bf02123918

de Wolff, P. M., and Walter-Lévy, L. (1949). Structures and formulas of some constituents of Sorel cement. *C. R. Acad. Sci.* 229, 1232–1234.

de Wolff, P. M., and Walter-Lévy, L. (1953). The crystal structure of $Mg_2(OH)_3(Cl,Br){\cdot}4H_2O$. *Acta Cryst.* 6, 40–44. doi:10.1107/s0365110x53000089

Demediuk, T., Cole, W. F., and Hueber, V. H. (1955). Studies on magnesium and calcium oxychlorides. *Austr. J. Chem.* 8 (2), 215–233. doi:10.1071/ch9550215

Dinnebier, R. E., Freyer, D., Bette, S., and Oestreich, M. (2010). $9Mg(OH)_2{\cdot}MgCl_2{\cdot}4H_2O$, a high temperature phase of the magnesia binder system. *Inorg. Chem.* 49 (21), 9770–9776. doi:10.1021/ic1004566

Dinnebier, R. E., Oestreich, M., Bette, S., and Freyer, D. (2012). $2Mg(OH)_2{\cdot}MgCl_2{\cdot}2H_2O$ and $2Mg(OH)_2{\cdot}MgCl_2{\cdot}4H_2O$, two high temperature phases of the magnesia cement system. *Z. Anorg. Allg. Chem.* 638 (3-4), 628–633. doi:10.1002/zaac.201100497

Feitknecht, W., and Held, F. (1944). Über die Hydroxychloride des Magnesiums. *Helv. Chim. Acta* 27, 1480–1495. doi:10.1002/hlca.194402701189

Feitknecht, W. (1926). Über das Verhalten von schwer löslichen Metalloxyden in den Lösungen ihrer Salze. Zur Kenntnis der Magnesiumoxyd-Zemente I. *Helv. Chim. Acta* 9, 1018–1049. doi:10.1002/hlca.192600901137

Han, H., Dong, O., Li, D., and Zeng, D. (2017). Phase diagram of the NaCl-$MgCl_2$-H_2O system at 25-75°C and its application for $MgCl_2{\cdot}6H_2O$ purification. *Russ. J. Phys. Chem.* 91 (7), 1255–1259. doi:10.1134/s0036024417070147

Keitel, H. (1923). Die Systeme KCl-$MgCl_2$-H_2O und NaCl-$MgCl_2$-H_2O. *Kali* 17, 261–265.

Monastra, V., and Grandstaff, D. E. (1999). Kinetics of MgO dissolution and buffering of fluids in the waste isolation Pilot plant (WIPP) repository. *Mat. Res. Soc. Symp. Proc.* 556, 625–632. doi:10.1557/proc-556-625

Nakayama, M. (1959). A new basic triple salt containing magnesium hydroxide Part II. The quaternary system KCl-$MgCl_2$-$Mg(OH)_2$-H_2O at 100°. *Bull. Agr. Chem. Soc. Jpn.* 23(1), 46–48. doi:10.1271/bbb1924.23.46

Nakayama, M. (1960). A new basic triple salt containing magnesium hydroxide Part IV. The quinary system KCl-K_2SO_4-$MgCl_2$-$MgSO_4$-$Mg(OH)_2$-H_2O at 50°. *Bull. Agr. Soc. Jpn.* 24(4), 362–371. doi:10.1271/bbb1924.24.362

Newman, E. S. (1955). A study of the system magnesium oxide-magnesium chloride-water and the heat of formation of magnesium oxychloride. *J. Res. Natl. Bur. Stand.* 54 (6), 347–355. doi:10.6028/jres.054.039

Palmer, D. A., and Wesolowski, D. J. (1997). Potentiometric measurements of the first hydrolysis quotient of magnesium (II) to 250°C and 5 molal ionic strength (NaCl). *J. Solut. Chem.* 26 (2), 217–232. doi:10.1007/bf02767923

Pannach, M., Bette, S., and Freyer, D. (2017). Solubility equilibria in the system $Mg(OH)_2$-$MgCl_2$-H_2O from 298 to 393 K. *J. Chem. Ing. Data* 62, 1384–1396. doi:10.1021/acs.jced.6b00928

Robinson, W. O., and Waggaman, W. H. (1909). Basic magnesium chlorides. *J. Phys. Chem.* 13, 673–678. doi:10.1021/j150108a002

Rode, T. (1947). Vapor pressure and solubility of the aqueous reversible system 2 NaCl + $MgSO_4$ ↔ Na_2SO_4 + $MgCl_2$, stable and metastable diagram. *Izv. Sek. Fiz. Khim. Anal. Akad. Nauk. SSSR* 15, 234–265.

Schulze, G., and Simon, J. (2009). *Jander/jahr maßanalyse*. Berlin: de Gruyter.

Sorel, S., and Dumas, M. (1867). Sur un nouveau ciment magnésien. *C. R. Acad. Sci.* 65, 102–104.

Sugimoto, K., Dinnebier, R. E., and Schlecht, T. (2007). Structure determination of $Mg_3(OH)_5Cl{\cdot}4H_2O$ (F5 phase) from laboratory powder diffraction data and its impact on the analysis of problematic magnesia floors. *Acta Cryst.* B63, 805–811. doi:10.1107/s0108768107046654

Takegami, S. (1921). A study of the reciprocal salt pairs: $Na_2Cl_2+MgSO_4 \leftrightarrow Na_2SO_4+MgCl_2$ at 25°C. *Mem. Coll. Sci. Kyoto Imp. Univ.* 4, 317–342.

THEREDA. *Thermodynamic reference database*. Release (2021). Available at: www.thereda.de.

Unknown author (1902). Wasserdichte Verdämmung im Steinsalzgebirge. *Glückauf* 38 (14), 307–309.

Voigt, W. (2020). Hexary system of oceanic salts – polythermal pitzer dataset (numerical supplement). *THEREDA-J* 01 (02), 1–9.

Walter-Lévy, L., and Bianco, Y. (1951). Action of magnesia on magnesium chloride solutions at 100°. *C. R. Acad. Sci.* 232, 730 – 732.

Xiong, Y., Deng, H., Nemer, M., and Johnsen, S. (2010). Experimental determination of the solubility constant for magnesium chloride hydroxide hydrate ($Mg_3Cl(OH)_5{\cdot}4H_2O$, phase 5) at room temperature, and its importance to nuclear waste isolation in geological repositories in salt formations. *Geochim. Cosmochim. Acta* 74, 4605–4611. doi:10.1016/j.gca.2010.05.029

Xiong, Y. (2008). Thermodynamic properties of brucite determined by solubility studies and their significance to nuclear waste isolation. *Aquat. Geochem.* 14, 223–238. doi:10.1007/s10498-008-9034-3

frontiers | Frontiers in Nuclear Engineering

TYPE Review
PUBLISHED 21 September 2023
DOI 10.3389/fnuen.2023.1208582

OPEN ACCESS

EDITED BY
Bernd Grambow,
UMR6457 Laboratoire de Physique Subatomique et des Technologies Associées (SUBATECH), France

REVIEWED BY
Axel Liebscher,
Federal Company for Radioactive Waste Disposal, Germany
George Dan Miron,
Paul Scherrer Institut (PSI), Switzerland

*CORRESPONDENCE
Wolfgang Voigt,
✉ wolfgang.voigt@chemie.tu-freiberg.de

RECEIVED 19 April 2023
ACCEPTED 04 September 2023
PUBLISHED 21 September 2023

CITATION
Voigt W and Freyer D (2023), Solubility of anhydrite and gypsum at temperatures below 100°C and the gypsum-anhydrite transition temperature in aqueous solutions: a re-assessment.
Front. Nucl. Eng. 2:1208582.
doi: 10.3389/fnuen.2023.1208582

Solubility of anhydrite and gypsum at temperatures below 100°C and the gypsum-anhydrite transition temperature in aqueous solutions: a re-assessment

Wolfgang Voigt* and Daniela Freyer

Institut für Anorganische Chemie, TU Bergakademie Freiberg, Freiberg, Germany

Anhydrite and gypsum are omnipresent in sedimentary rocks of all types. They occur as massive layers or are distributed within other geological formations as in clays. Understanding the conditions of formation and the stability of the hydrated and anhydrous form of calcium sulfate is crucial in an elucidation of the genesis of the geological formations envisaged as potential host rock for radioactive waste disposal. Estimations of the temperature, where gypsum is dehydrated to anhydrite in water vary between 30°C and 60°C. The extremely slow crystallization kinetics of anhydrite at $T < 90°C$ prevents a direct determination of this transition temperature. In the present work the different approaches to fix this temperature are discussed. It is shown that careful assessment of solubility data and calorimetric measurements yields a transition temperature of 42°C ± 1°C. For results essentially deviating from this value methodic deficiencies are revealed and discussed. Thus, a long-standing discussion about the thermodynamic aspect of the gypsum-anhydrite conversion can be closed, not the kinetic part.

KEYWORDS

solubility equilibrium, gypsum, anhydrite, transition temperature, thermodynamics

1 Introduction

Calcium sulfate occurs in several forms: as dihydrate (mineral: gypsum), as hemi-hydrate (mineral: bassanite) and anhydrous (mineral: anhydrite). Anhydrite occurs for instance in the important Zechstein formation as “Hauptanhydrit” within evaporitic geological formations and is omnipresent in other sedimentary rocks like clays. The occurrence of the different forms of calcium sulfate in various environments can be an indication for certain processes in the genesis of the geological formation. Geochemists have to answer various questions as: are these minerals of primary or secondary origin? At which temperature they have been formed? Which remineralization reactions could form the mineral assembly found in the geological zone. Naturally, answers to these questions will be part of the safety assessment for a potential nuclear disposal in a geological host in rock salt or in clay.

The answer, how anhydrite could be formed at $T < 50°C$ or 60°C is still open, since in the lab in time scales of years no primary precipitation has been observed. When saturating an aqueous solution with $CaSO_4$ at ambient temperatures gypsum ($CaSO_4·2H_2O$) represents the thermodynamically stable phase. Enhancing the temperature at a certain point the anhydrous phase, anhydrite, becomes the stable phase and gypsum the metastable phase.

The temperature, where both phases can co-exist represents the transition temperature. For this point the solubility of both phases is equal. The experimental difficulty to fix the transition temperature more accurate is caused by the very slow kinetics of crystallization and dissolution of anhydrite in water at T < 100°C.

In our review on crystallization and stability of $CaSO_4$-containing phases (Freyer and Voigt, 2003) we summarized the various opinions on the transition temperature gypsum-anhydrite without critical assessing solubility and other data. Thus, a broad interval of 42°C–60°C was left for discussion.

In the mean-time a series of papers appeared related to the transition temperature gypsum-anhydrite. Krumgalz published a collection of solubility data of gypsum, anhydrite and hemi-hydrate of $CaSO_4$ in water and performed empirical fits of the temperature dependence (Krumgalz, 2018). According to these equations the crossing-point of the gypsum and anhydrite solubility curve is at 45.6°C and $m(CaSO_4) = 0.01545$ mol/kgw. Shen et al. (2019) assessed solubility data in the system $CaSO_4$-H_2O to establish a Pitzer model. Their solubility-based model gives the gypsum-anhydrite transition at 42.8°C. An electrolyte—NRTL model to describe the solubilities in the system $CaSO_4$–H^+-PO_4^{3-}-SO_4^{2-}-H_2O was developed by Messnaoui and Bounahmidi (2006). Their model (adapted thermodynamic data of the $CaSO_4$ phases) yield a transition temperature near 28°C (read off from their Figure 5). Berdugo et al. gave an extensive review of the phase diagram $CaSO_4$–H_2O covering most of the available literature without a conclusion to a preferred transition temperature gypsum-anhydrite (Berdugo et al., 2008). Van Driessche et al. (2011) while analyzing the possible growth rates of the giant gypsum crystals in the Naica mine (Mexico) assume a transition temperature of 58°C. Zeng et al. established thermodynamic models of the systems $CaSO_4$–H_2O and $CaSO_4$-H_2SO_4–MSO_4–H_2O (M = Cu, Zn, Ni. Mn) within a temperature range of 25°C–90°C (Zeng and Wang, 2011; Wang et al., 2012; Wang et al., 2013). For the system $CaSO_4$-H_2SO_4-H_2O solubility data were determined for gypsum and anhydrite (Wang et al., 2013). According to their model the transition temperature is 41.8°C. A paper entitled "the gypsum—anhydrite paradox revisited" appeared in year 2014 (Ossorio et al., 2014). In this work kinetic experiments and arguments are discussed for finding primary anhydrite crystallized below 60°C in geological time scales.

The purpose of the following work is to fix the transition temperature gypsum-anhydrite as accurate as possible by re-assessing published solubility data in water and electrolyte solutions as well as calorimetric data.

2 Methodology

2.1 Thermodynamic relationships

The general Eq. 1 connects reaction quantities as the standard Gibbs energy $\Delta_R G^\varnothing$, enthalpy $\Delta_R H^\varnothing$, entropy $\Delta_R S^\varnothing$ with the equilibrium constant $K^\varnothing$ of that reaction.

$$\Delta_R G^\varnothing = \Delta_R H^\varnothing - T\Delta_R S^\varnothing = -RT \cdot \ln K^\varnothing \tag{1}$$

For the gypsum-anhydrite conversion reactions (I–III) are of interest.

$$CaSO_{4(s)} + 2\,H_2O_{(l)} \rightarrow CaSO_4 \cdot 2H_2O_{(s)} \tag{I}$$

$$CaSO_{4(s)} \rightarrow Ca^{2+}_{(aq)} + SO^{2-}_{4(aq)} \tag{II}$$

$$CaSO_4 \cdot 2H_2O_{(s)} \rightarrow Ca^{2+}_{(aq)} + SO^{2-}_{4(aq)} + 2H_2O_{(l)} \tag{III}$$

Reactions (II) and (III) represent the solubility constants of anhydrite (Eq. 2) and gypsum (Eq. 3).

$$K_{II}^\varnothing = m_{Ca2+} m_{SO4(2-)} \gamma^2_{\pm\,CaSO4} \tag{2}$$

$$K_{III}^\varnothing = m_{Ca2+} m_{SO4(2-)} \gamma^2_{\pm\,CaSO4} \cdot a_w^2 \tag{3}$$

with m_i and $\gamma_\pm$ the corresponding molalities and mean activity coefficients. Combining Eqs 2, 3 yields the equilibrium constant $K_I^\varnothing$ (Eq. 4) for reaction (I).

$$\begin{aligned} -\Delta_R G_I^\varnothing &= RT \cdot \ln K_I^\varnothing = RT \cdot \ln K_{II}^\varnothing - RT \cdot \ln K_{III}^\varnothing = RT \cdot \ln \frac{K_{II}^\varnothing}{K_{III}^\varnothing} \\ &= -2RT \cdot \ln a_w \end{aligned} \tag{4}$$

Applying these equations several strategies can be derived to determine the conditions (T, solution composition) for the simultaneous solubility equilibrium of gypsum and anhydrite (I).

2.1.1 Solubility determinations in water

The most widely applied method represents the determination of the solubility of anhydrite and gypsum in dependence on temperature in pure water within the stable and metastable region. At the temperature, where the two solubility curves cross each other the constants $K_{II}^\varnothing\,and\,K_{III}^\varnothing$ are equal and thus this temperature represents the conversion or transition temperature between gypsum and anhydrite. Note that right-hand side of Eq. 4 becomes zero in pure water ($a_w = 1$) or dilute solutions, for which $a_w = 1$ might be assumed.

2.1.2 Solubility determinations in electrolyte solutions

In electrolyte solutions the transition temperature will decrease, since $a_w < 1$. This is easily shown by combining Eqs 1, 4 and solving for T (Eq. 4a). The standard data $\Delta_R H^\varnothing$ and $\Delta_R S^\varnothing$

$$\frac{\Delta_R H^\varnothing}{(\Delta_R S^\varnothing - 2Rln_{aw})} = T \tag{4a}$$

are independent on electrolyte composition and $ln(a_w)$ becomes negative. Thus, a positive value is added in the denominator, which requires a reduced T to maintain equality in Eq. 4a. The crossing-point of the solubility curves of gypsum and anhydrite as a function of electrolyte concentration at T < T (transition, water) yields the electrolyte concentration, where at the chosen temperature both solids are in equilibrium. If the water activity is known at the given electrolyte concentration and solution temperature then through Eq. 4a a relation between water activity and transition temperature can be established. The relation is independent on the type of electrolyte.

2.1.3 Calorimetric determination of the transition temperature

At the transition temperature in pure water or dilute solutions the water a_w can be set to 1.0, which according to Eq. 4 gives

TABLE 1 Methods applied in estimation of the transition temperature gypsum-anhydrite.

References	Transition Temperature/ °C	Method
van't Hoff (1912)	63.5	ΔV, ΔP of reaction
Partridge and White (1929)	38–39	Solubility in water
Hill (1937)	42 ± 1	Solubility in water
Posnjak (1938)	42 ± 1	Solubility in water
Kelley et al. (1941)	40	Calorimetric
Bock (1961)	42	Solubility in water
Zen (1965)	46 ± 25	Re-analysis calorimetric data
Power et al. (1964)	41 ± 1	Solubility in water
Marshall, W. L. et al. (1964), Marshall and Slusher (1966)	42	Thermodyn. model $CaSO_4$-NaCl-H_2O
Hardie (1967)	58 ± 2	Conversion reaction in electrolyte solutions
D'Ans (1968)	About 40	Solubility in water and model
Blount, C. W. and Dickson, F. W. (1973)	56 ± 3	Solubility in water
GRIGOR'EV and SHAMAEVP (1976)	About 40	Emf concentration cell
Knacke and Gans (1977)	55.5 ± 1.5	Gypsum growth detection in solution, when anhydrite is metastable
Innorta et al. (1980)	49.5 ± 2.5	Solubility in water
Corti and Fernandez-Prini (1984)	42.6 ± 0.4	Thermodyn. model $CaSO_4$-H_2O
Möller (1988b)	49	Thermodyn. model $CaSO_4$-NaCl-Na_2SO_4-$CaCl_2$-H_2O
Raju and Atkinson (1990)	59.9	Thermodyn. model $CaSO_4$-H_2O
Messnaoui and Bounahmidi (2006)	28–30	Thermodyn. model $CaSO_4$-H_2SO_4-H_3PO_4-H_2O
Azimi et al. (2007)	40 ± 2	Thermodyn. model $CaSO_4$-H_2O
Kontrec et al. (2002)	40	Transformation kinetics[a]
Altmaier et al. (2011)	43.0	Thermodyn. model (THEREDA) Na^+, K^+, Mg^{2+}, Ca^{2+}//Cl^-, SO_4^{2-}-H_2O
Wang et al. (2013)	41.8	Thermodyn. model $CaSO_4$-H_2SO_4-H_2O
Krumgalz (2018)	45.6	Solubility, statistical analysis
Li et al. (2018)	41.1	Thermodyn. model $CaSO_4$-H_2O
Shen et al. (2019)	42.8	Thermodyn. model $CaSO_4$-H_2O

[a]Kontrec et al. cited in the table of transition temperatures of Krumgalz (2018) did not determine the transition temperature in his kinetic experiments.

$$\Delta_R G_I^{\varnothing} = 0 = \Delta_R H_I^{\varnothing} - T_{trans}\,\Delta_R S_I^{\varnothing} \tag{5}$$

The right-hand side contains only quantities, which can be determined calorimetrically and thus are independent on kinetics of crystallization. When the reaction enthalpy and entropy of reaction (I) are determined as function of T, then through Eq. 5 the T_{trans} can be calculated.

2.1.4 Thermodynamic modeling of data of different types and systems

A diversity of thermodynamic and equilibrium data can be combined using an activity model within a framework of Eqs 1–4. The success depends on an appropriate data assessment and a compromise between number of adjustable parameters and accuracy of data description.

In Table 1 references are listed in which the transition temperature was predicted using the different methods.

2.2 Solubility determination

2.2.1 Anhydrite and gypsum in water

The most direct way to determine the transition temperature is to determine experimentally the solubility of gypsum and anhydrite in dependence on temperature. Due to the slow kinetics of anhydrite crystallization gypsum can exist metastable for long time in aqueous suspension considerable above the transition temperature. Vice versa anhydrite can exist metastable below the transition temperature due to low rates of gypsum nucleation under conditions of not too high supersaturation (Lancia et al., 1999;

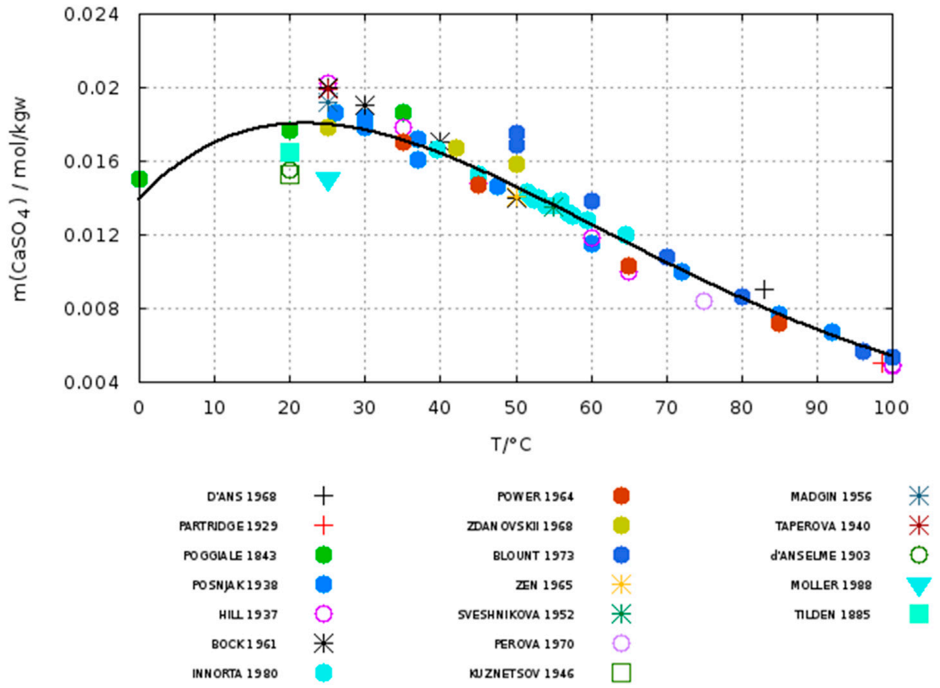

FIGURE 1
Solubility of anhydrite. Symbols: data of different authors as listed and accepted by Krumgalz (2018) line: fit by Krumgalz (2018). Citations see Krumgalz.

Fu et al., 2012; Otalora and Garcia-Ruiz, 2014). Thus, the determination of the crossing point is experimentally feasible. The more difficult part in such an investigation represents the solubility curve of anhydrite. In water below 80°C it is practically not possible to achieve saturation by crystallizing anhydrite from a supersaturated solution. Saturating water by dissolving anhydrite is also a slow process. Thus, the experimenter is not sure whether saturation was reached or not after a certain time. Other factors are also important for the observed solubility values of anhydrite, these are:

- Purity of natural anhydrite
- Preparation method of anhydrous calcium sulfate from gypsum (particularly temperature/time profile of dewatering)
- Crystal size and the surface energy
- Purity of substances for gypsum preparation (soluble impurities)
- Analytical and sampling technique
- Mechanical attrition due to stirring

These factors are more important for anhydrite than for gypsum, since for instance tiny anhydrite crystals will have a higher solubility and because crystallization does not occur the dissolved part from these crystals remains in solution and causes a higher solubility. On the other side, using samples with large crystals separated from fines, the dissolution kinetics becomes extremely slow.

In order to eliminate effects of fines in solubility experiments with anhydrite D'Ans (1968) applied a 3-week boiling for aging natural, grinded anhydrite samples. Hill prepared anhydrite by boiling gypsum in 20% sulfuric acid for 3 days (Hill, 1934; Hill, 1937).

2.2.1.1 Solubility of anhydrite

Krumgalz (2018) collected data of solubility of calcium sulfate in water from 110 papers. From these he extracted 190 data points for anhydrite up to 408°C. 83 data points of anhydrite solubility were at T ≤ 100°C, from which he accepted 64. As outliers he treated points located outside of an 80% confidence (corresponds approx. 1.3 σ) interval without giving the interval for his functions. For the interval 0°C–200°C he gave the fitting function Eq. 6

$$m_{sat,CaSO4} = 7.737E-13\cdot T^5 - 5.106E-10\cdot T^4 + 1.254E-7\cdot T^3 - 1.330E-5\cdot T^2 + 4.239E-4\cdot T + 0.01395 \qquad (6)$$

T in °C, m in mol/kgw, kgw = kg H_2O N = 125 σ = 8.48E-4

Using Eq. 6 and the data set data set of N points (Tmax = 200°C) accepted by Krumgalz we calculated a std. deviation given above as σ. In Figure 1 the data for anhydrite accepted by Krumgalz are plotted up to 100°C with an identification of the authors. His fitted curve (Eq. 6) turns down below 25°C, which is a consequence particularly of the data from Poggiale (1843). Inspection of the original papers revealed that some data had been misinterpreted by Krumgalz, for example, Poggiale determined the solubility of gypsum, not of anhydrite. Table 2 lists the data, which were identified as wrong or outliers in this work for the temperature range up to 100°C.

Figure 2 shows a plot of the corrected data list (changed data list Table 2) with a fit as a quadratic function (Eq. 7) and the original

TABLE 2 Changes made in this work in respect to the data list (Krumgalz, 2018).

T/°C	$CaSO_4$/mol/kgw	References	Change
0.0	0.01506	Poggiale (1843)	Deleted
20.0	0.01770	Poggiale (1843)	Deleted
20.0	0.0155	d'Anselme (1903)	Deleted
20.0	0.0153	Kuznetsov (1946)	Deleted
20.0	0.0205	D'Ans et al. (1955)	Added
25.0	0.015	Möller (1988b)	Deleted[a]
35.0	0.01866	Poggiale (1843)	Deleted
50.0	0.0175	Blount, C. W. and Dickson, F. W. (1973)	Deleted
50.0	0.0169	Dickson, F. W. et al. (1963)	Deleted
50.0	0.0136	D'Ans (1968)	Added
50.0	0.0139	D'Ans (1968)	Added
50.0	0.0144	D'Ans (1968)	Added

[a]No exp. data in this work.

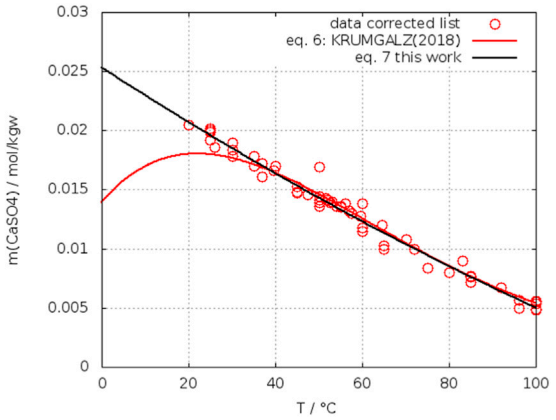

FIGURE 2
Solubility of anhydrite in water: comparison of the fit in this work with Krumgalz (2018).

curve from Krumgalz. The difference within the range 40°C–60°C is small, but is significant in respect to the temperature of crossing the solubility curve of gypsum as will be shown later. The behavior below 25°C seems to be more realistic with the new function.

$$m_{CaSO4} = 0.02532 - 2.37528E - 4 \cdot T + 3.44419 \cdot T^2 \qquad (7)$$

T in °C N = 59 $\sigma = 6.63E\text{-}4$

A third set of data was considered from the authors (Hill, 1937; Posnjak, 1938; Bock, 1961; Power et al., 1964), who particularly investigated the solubility of anhydrite in parallel to the one of gypsum to fix the temperature of crossing of the solubility curves. The fit of their anhydrite data yields Eq. 8—plot in comparison to all others see below in Section 2.2.2.

$$m_{CaSO4} = 0.026985 - 3.10225E - 4 \cdot T + 9.19957E - 7 \cdot T^2 \qquad (8)$$

T in °C N = 24 $\sigma = 4.8E\text{-}4$

It is remarkable that Eq. 8 shows the lowest std. deviation in comparison with the previous fits.

2.2.1.2 Solubility of gypsum

Due to the large amount of data for gypsum, initially we assumed, that it is unnecessary to select or unselect certain points. However, the data reported by 62 different authors or author groups contain a large number of single point determinations in water, while the authors interest was focused to systems with the presence of other electrolytes. The data accepted by Krumgalz for gypsum are plotted in Figure 3. All the data accepted by Krumgalz are represented by stars. To distinguish several authors other symbols are overlayed. The red curve represents the fit of Krumgalz (2018) (Eq. 9). Using his Eq. 9 and the data of his accepted list we calculated a std. deviation as given below.

$$m_{CaSO4} = 0.01281 + 1.641E - 4 \cdot T - 2.868E - 6 \cdot T^2 + 1.179E - 8 \cdot T^3 \qquad (9)$$

T in °C N = 206 $\sigma = 3.07E\text{-}4$

For most of the data the scatter is smaller than in case of anhydrite. The data of Innorta et al. (1980) are highlighted as red closed circles in Figure 3. These data are significant lower than the majority of data of other authors, when T ≥ 40°C. A reason for this deviation can be found in a notice in the text of their paper, where it was stated, in case they detected gypsum in the suspension (quantitatively by calibrated XRD) the solubility datum was considered as belonging to the gypsum equilibrium due to its faster crystallization kinetics.

Unfortunately, although a calibration curve for solid mixtures anhydrite/gypsum was shown, no quantitative statement was made about the portion of gypsum if present in the suspension. Because Innorta et al. emphasize to had been able to check the presence of each of the solid phases down to 0.05%, one can assume that the gypsum content was quite low in these cases. Thus, it becomes

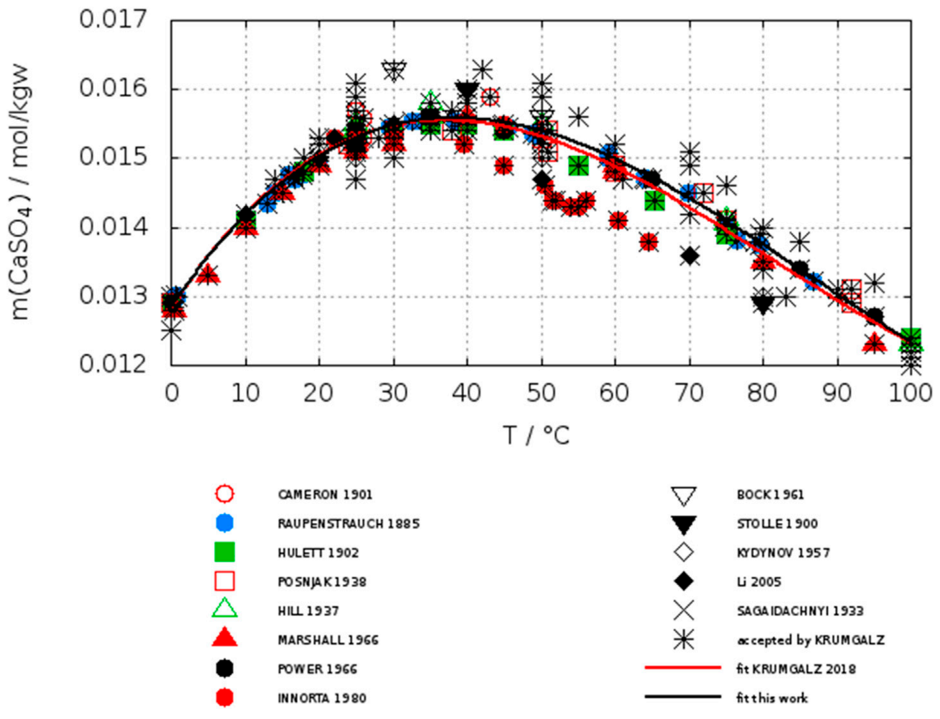

FIGURE 3
Solubility data of gypsum in water as accepted by Krumgalz (2018), his fit (red line), our fit (black line) with reduced data set (see Table 3).

TABLE 3 Deleted data from the gypsum data set of Krumgalz (2018).

T/°C	m_{CaSO4}/mol/kgw	References
25.0	0.0147	Nakayama and Rasnik (1967)
25.0	0.0159	Zieler 1927[a]
25.0	0.0161	Block and Waters, O. B. (1968)
30.0	0.0163	Bock (1961)
42.0	0.0163	Zdanovskii, A. B. and Vlasov, G. A. (1968)
50.0	0.0161	Bell and Taber (1906)
70.0	0.0136	Li and Demopoulos (2005)
80.0	0.0129	Stolle (1900)
80.0	0.0130	Kydynov and Druzhinin 1957[a]
100.0	0.0120	Sagaidachnyi and Mordberg (1933)

[a]Author given in table of Krumgalz (2018), but not cited in his reference list.

understandable that in the region, where anhydrite is expected to present the stable phase (T > 40°C), gypsum was present in an amount not large enough to reach its higher metastable saturation concentration. There are a few low-lying points of Stolle (1900), Kydynov (1957) and Li and Demopoulos, (2005) for which no particular reason can be found in the original paper. However, these points are also considered as outliers (see Table 3). Even in the large data set of Krumgalz for gypsum the effect of low-lying data of Innorta et al. is evident. A fit (Eq. 10) with a reduced set of data (see Table 3) shifts the curve significantly as can be seen comparing the red (Krumgalz) and black (this work) curves and decreases the std. deviation.

$$m_{CaSO4} = 0.012826 + 1.58843E - 4 \cdot T - 2.65673E - 6 \cdot T^2 + 1.01943E - 8 \cdot T^3 \qquad (10)$$

T in °C N = 182 $\sigma = 2.05E\text{-}4$

Analogous to anhydrite a separate fit of the data given by the authors (Hill, 1937; Posnjak, 1938; Bock, 1961; Power et al., 1964) was performed (Eq. 11), which yielded a std. deviation nearly identical to our reduced data set (Eq. 10).

$$m_{CaSO4} = 0.01294 + 1.59165E - 4 \cdot T - 2.74714E - 6 \cdot T^2 + 1.10437E - 8 \cdot T^3 \qquad (11)$$

T in °C N = 37 $\sigma = 2.02E\text{-}4$.

2.2.2 Transition temperature gypsum-anhydrite in water

The purely statistically fitted curves of the data by Krumgalz (Eqs 6, 9) yield a crossing point of the gypsum-anhydrite solubility curve at 45.6°C (Figure 4). This value looks like a compromise between the low and high valued estimations. However, considering the std. deviation of the functions the limits are between 40.4°C and 51.1°C. Considering our fits with the corrected data sets for gypsum and anhydrite (Eqs 7, 10) gives a temperature of 43.9°C (Figure 4) with lower and upper limits of 40.4°C and 48.6°C. The numerical values are listed in Table 4.

Figure 5 shows a plot of the Eqs 8, 11 from the fit of the data sets of authors, who investigated particularly both gypsum and anhydrite to

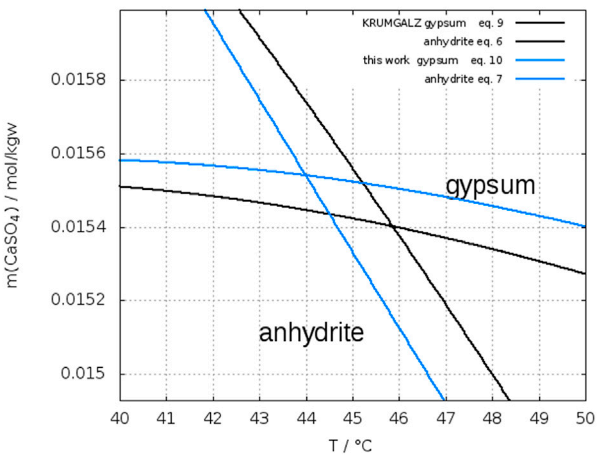

FIGURE 4
Crossing-points of fitted curves of the gypsum and anhydrite solubility according to Krumgalz (2018) black lines and this work blue lines.

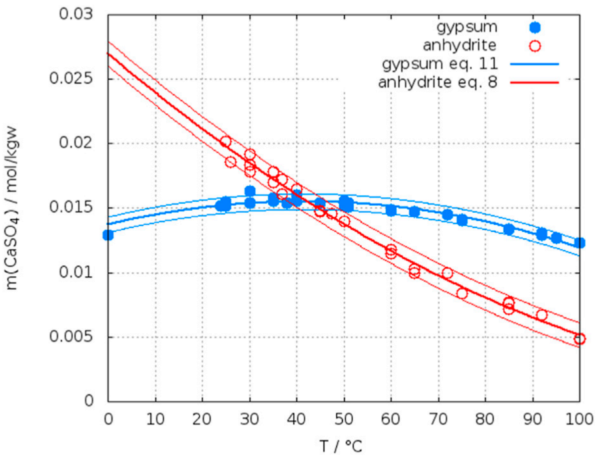

FIGURE 5
Crossing-point of solubility curve of gypsum and anhydrite from data of Hill (1937), Posnjak (1938), Bock (1961), and Power et al. (1964); symbols: exp. data; lines: fit of their data, red anhydrite (Eq. 8) blue gypsum (Eq. 11); thin lines: fit $\pm\ \sigma$.

determine the crossing point. In this case a transition temperature of 41.9°C is obtained with narrower error limits between 38.9°C and 45.1°C.

As one can see from Figure 4, the transition temperature shifts to lower values, when correcting the data set of Krumgalz and even lower (Figure 5), if one selects and combines the data of the authors (Hill, 1937; Posnjak, 1938; Bock, 1961; Power et al., 1964), who had been dealing with the subject particularly. The same is valid for the uncertainty, which is lowest in the last row of Table 4. The results of the authors mentioned above, are plotted separately in Figure 6. Locating the crossing points in enlarged plots yields

(Hill, 1937) 42.4°C
(Bock, 1961) 42.4°C
(Power et al., 1964) 41.6°C
(Posnjak, 1938) 42.0°C, 44.5°C (this point was from a non-aged anhydrite)

The variation is very much smaller than from the statistical fits of the individual solubility curves of gypsum and anhydrite from different authors, who have investigated the solubility of either gypsum or anhydrite. The two values from Posnjak originate from two qualities of anhydrite he had used. The higher temperature results from the solubility of an anhydrite prepared by heating gypsum for a few hours at 500°C without aging, the lower is from a natural sample, which Posnjak himself assigns as the more reliable datum. The conclusion from all these considerations is that pure statistical treatment of assumed reliable data yield a transition temperature between 42°C and 45°C with a broad confidence interval of ±8°C. The particular designed experiments to determine the transition temperature by solubility determinations of both solid phases by the respective authors gave 42°C with a scatter of only ±1°C. Separate fitting of their results for gypsum and anhydrite gave the same transition temperature, but a wider scatter (±3°C). These facts hint on methodic differences (errors), which are compensated, when investigating both phases with the same (analytical, sampling) technique. From our personal experience we know, that beside other factors, sampling techniques have a large effect on the results of solubility determinations. They are quite individual and a detailed description would be too lengthy for a publication in scientific journal. In conclusion, 42°C ± 1°C should be considered as the correct transition temperature in water.

By the way, a thorough discussion, why the high value of the transition temperature of van't Hoff (1912) is wrong can be found by Posnjak (1938). In brief, the conclusions of van't Hoff are based on misinterpretations of tedious dilatometric and tensiometric measurements of hydration/dehydration reactions of gypsum into hemi-hydrate and anhydrite in water and electrolyte solutions.

2.2.3 Solubility of gypsum and anhydrite in electrolyte solutions

Several authors supposed that equilibration times to reach the solubility equilibrium with anhydrite are shorter in electrolyte solutions than in pure water, particularly in solutions of sulfuric acid. To the knowledge of the present authors no quantitative examination of this effect was published until now. However, about 20 years ago, occasionally we made an observation, which underlines this kinetic effect. A company producing electrolytic copper from baths of $CuSO_4$ in solutions of sulfuric acid at about 40°C asked us to identify the type of scale on the electrodes forming regularly after about one to 2 weeks. This scale was pure anhydrite (determined by means of XRD patterns) deposited from impurities in the electrolytic baths. In pure water gypsum would form at these temperatures. Unfortunately, that time we did not further examine the phenomenon. The preferred preparation method of Hill (1937) to obtain well-crystallized anhydrite was boiling in 20% sulfuric acid. He reported crystal sizes of 20–30 µm (Hill, 1934). Doubtless, this points also to an improved crystallization kinetics of anhydrite in electrolyte solutions.

TABLE 4 Transition temperatures gypsum-anhydrite according to fits of different data selections.

Equation anhy and gyps	Ttrans °C	low limit °C	High limit °C	ΔT K	References
6 and 9	**45.6**	40.6	51.1	10.5	Krumgalz (2018)
7 and 10	**43.9**	40.4	48.6	8.2	This work, corrected data list of Krumgalz
8 and 11	**41.9**	38.9	45.1	6.2	(Hill, 1937; Posnjak, 1938; Bock, 1961; Power et al., 1964) summarized

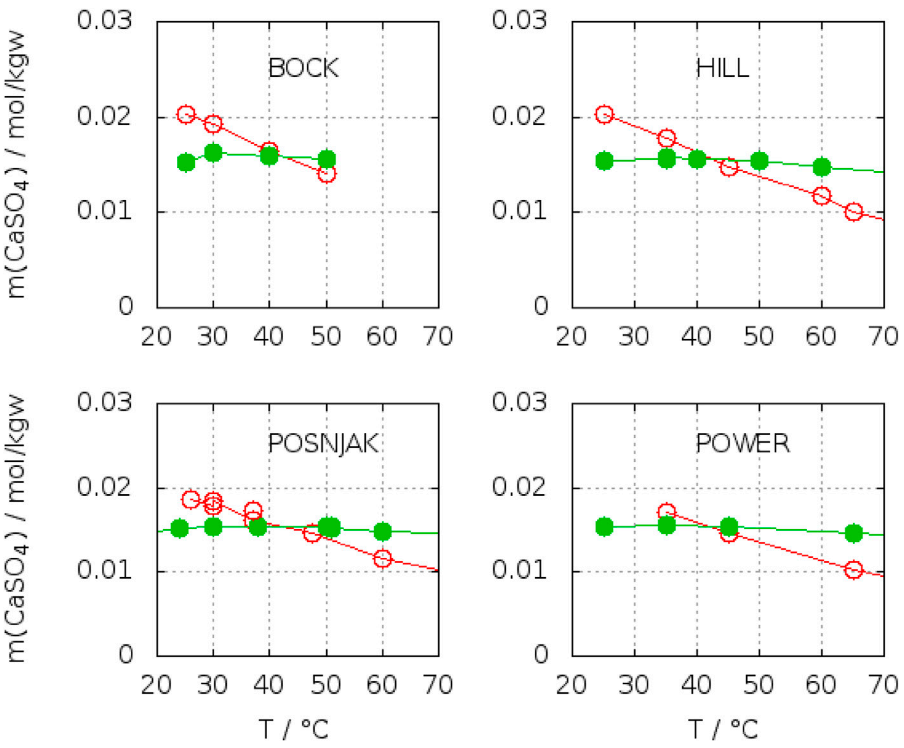

FIGURE 6
Experimentally determined crossing points of gypsum and anhydrite solubility curves in water according to Hill (1937), Posnjak (1938), Bock (1961), and Power et al. (1964).

Bearing in mind these observations one could expect more precise determinations of the crossing-points of the anhydrite and gypsum solubility curves in electrolyte solutions. On the other side, accurate analytical determination of low concentrations of calcium and sulfate is more difficult in presence of a large excess electrolytes. Whereas the gypsum solubility was investigated in a large number of electrolyte solutions, this is not true for anhydrite. Zdanovskii, A. B. and Vlasov, G. A. (1968) determined the solubility of both phases in solutions of H_2SO_4 at T = 10°C, 25°C, 35°C, 42°C, and 50°C. Wang et al. (2013) reported such investigations for T = 25°C, 50°C, 75°C, and 90°C. The results for 25°C are shown in Figure 7. The black curves represent the data of Zdanovskii, A. B. and Vlasov, G. A. (1968). They cross each between 2.4–2.6 mol/kgw H_2SO_4. The data for anhydrite of Wang et al. (2013) are considerably higher, whereas both authors data agree for gypsum at $m_{H2SO4} \leq 1.5$ mol/kgw. At higher concentration of H_2SO_4 the data of Wang et al. fall below the curve of Zdanovskii and Vlasov. Unfortunately, Wang et al. did not continue the investigation of gypsum up to the crossing point with anhydrite. Extrapolating their gypsum curve crosses that of anhydrite at approx. 4 mol/kgw H_2SO_4. The data of Zdanovskii and Vlasov at 35°C are plotted in Figure 8. The solubility of anhydrite and gypsum equals at $m_{(H2SO4)}$ = 1.4 mol/kgw. Figure 9 shows the analogous plot for 42°C. Here the crossing point is located at about 0.35 mol/kgw. Figure 10 shows the results for T = 10°C, the only data available below 25°C. In this case the crossing-point is at 5.5 mol/kgw with an uncertainty of about ±0.5 mol/kgw. As expected, the data show that the crossing point shifts to lower H_2SO_4 concentrations with increasing temperature. All the data at temperatures higher than 42°C showed lower solubility for anhydrite than for gypsum in line with the results on the gypsum-anhydrite equilibrium in pure water.

Kruchenko and Beremzhanov, B. A. (1976) determined the solubility of gypsum and anhydrite in solutions of HCl at 25°C. From the plot (Figure 11) the solubility of both phases is equal between 3.8–4.0 mol/kgw HCl.

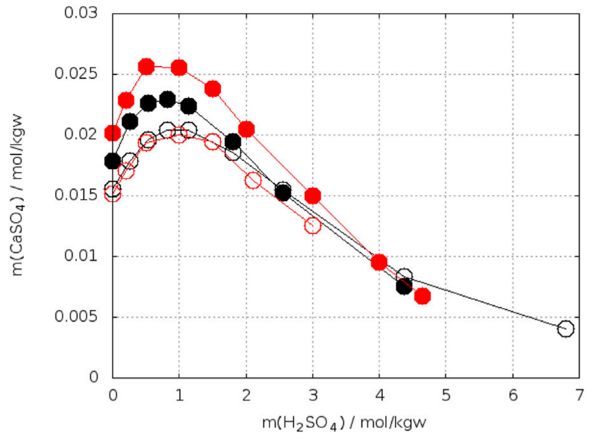

FIGURE 7
Solubility of gypsum (open circles) and anhydrite (close circles) in $H_2SO_4-H_2O$ at 25°C. Zdanovskii, A. B. and Vlasov, G. A. (1968) in black, Wang et al. (2013) in red.

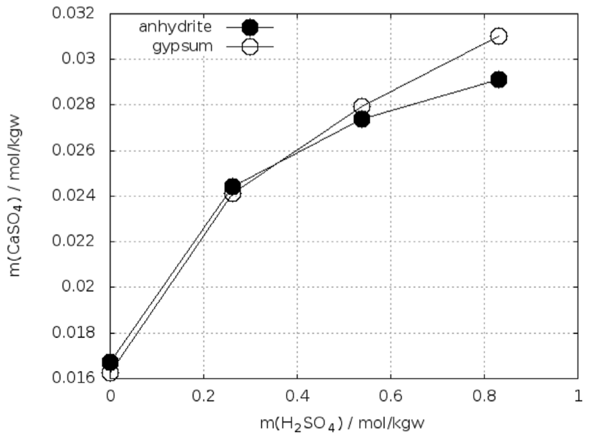

FIGURE 9
Solubility of gypsum and anhydrite in $H_2SO_4-H_2O$ at 42°C (Zdanovskii, A. B. and Vlasov, G. A., 1968).

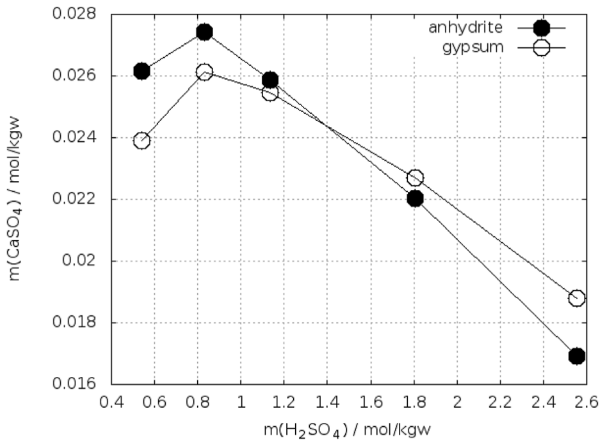

FIGURE 8
Solubility of gypsum and anhydrite in $H_2SO_4-H_2O$ at 35°C (Zdanovskii, A. B. and Vlasov, G. A., 1968).

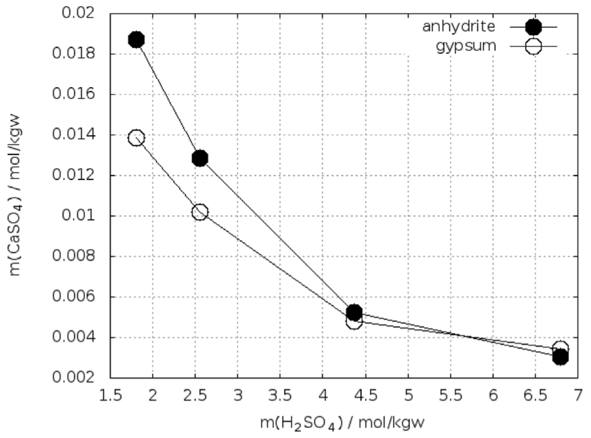

FIGURE 10
Solubility of gypsum and anhydrite in $H_2SO_4-H_2O$ at 10°C (Zdanovskii, A. B. and Vlasov, G. A., 1968).

Figure 12 shows the solubility of gypsum and anhydrite in $CaCl_2$-H_2O at 25°C according to Mel'nikova et al. (1971). From this diagram a crossing-point between 2.3–2.7 mol/kgw $CaCl_2$ can be estimated.

In sodium chloride solutions corresponding solubilities for gypsum and anhydrite were reported at different temperatures. Figure 13 shows plots for 25°C. In order to fix the crossing-point, data near this point were linearly fitted (see insert in Figure 13). Another plot is shown in Figure 14 for T = 40°C. The data for anhydrite are from Bock (1961), whereas for gypsum also other data have been added (Sborgi, 1926; Marshall, W. L. et al., 1964; Marshall and Slusher, 1966; Block and Waters, O. B., 1968). Up to 2 mol/kgw NaCl the results for gypsum agree, at higher concentrations the data diverge. The crossing-point with the anhydrite curve of Bock can be located between 1.1 and 1.8 mol/kgw NaCl. Data at 50°C gave higher solubilities for gypsum in the entire concentration range (Bock, 1961; Zen, 1965).

In Table 5 the data for the crossing-points in the electrolyte solutions mentioned above are summarized and complemented with the corresponding water activities. According to Eq. 4 and Eq. 4a all data should be located on a common curve T = f($\ln a_w$). In Figure 15 the data from Table 5 are plotted together with the theoretical curve (see Section 2.3). The latter is obtained when applying the caloric equation Eq. 21 from Robie et al. (1989). As can be seen from Figure 15, the transition temperatures determined from solubilities in different electrolyte solutions scatter around the theoretical curve. For every experimental datum the two symbols connected by a line reflect the uncertainty for that datum as can be read-off as m_{min} and m_{max} from Table 5. Thus, the transition temperatures determined from solubility curves in electrolyte solutions are in accordance with the calorimetric result (Section 2.3), but do not reduce the

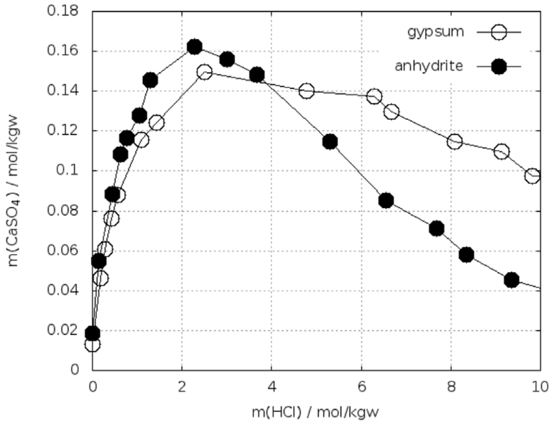

FIGURE 11
Solubility of gypsum and anhydrite in HCl-H_2O at 25°C (Kruchenko, V. P. and Beremzhanov, B. A., 1976).

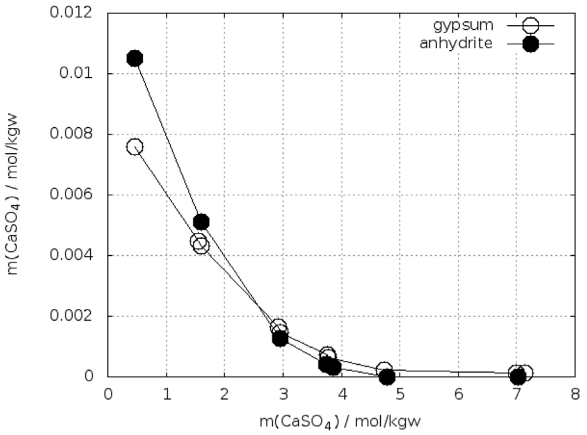

FIGURE 12
Solubility of gypsum and anhydrite in $CaCl_2$-H_2O at 25°C (Mel'nikova et al., 1971).

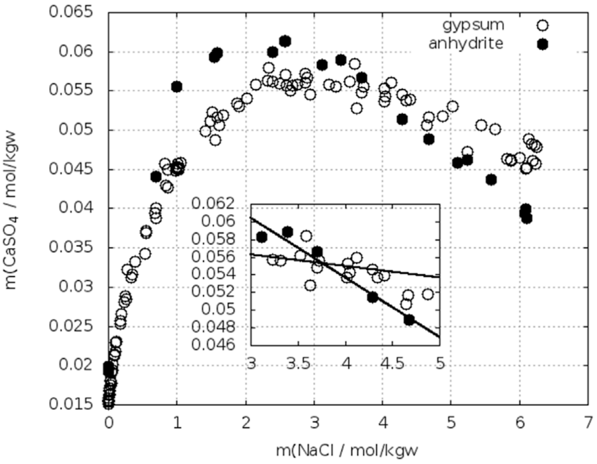

FIGURE 13
Solubility of gypsum (Cameron, 1901; Madgin and Swales, 1956; Bock, 1961; Denman, 1961; Marshall and Slusher, 1966; Power et al., 1966; Block and Waters, O. B., 1968) (Shchukarev 1939, 1950; Shternina 1949 cited in Pelsh (1973) and anhydrite (Madgin and Swales, 1956; Bock, 1961; Mel'nikova et al., 1971) cited in Pelsh (1973) in NaCl−H_2O at 25°C.

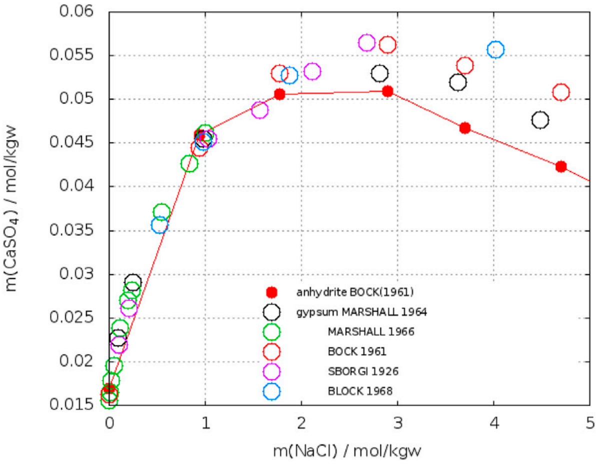

FIGURE 14
Solubility of gypsum (open circles) and anhydrite (closed red circles) in NaCl−H_2O at 40°C.

uncertainty. Although one could hope for improved crystallization and dissolution kinetics of anhydrite other factors like analytics at high electrolyte concentration obviously effect the precision of results.

2.3 Calorimetric determination of the transition temperature gypsum-anhydrite

The Gibbs energy of reaction in Eq. 1 is fixed through the quantities $\Delta_R S^\varnothing$ and $\Delta_R H^\varnothing$. The latter can be determined by purely calorimetric methods. These methods are not dependent on the crystallization or dissolution kinetics of the solids. $\Delta_R S^\varnothing$ can be calculated from absolute entropy determinations for gypsum and anhydrite by measuring the heat capacities Cp from 0 K (−273°C) to about 333 K (60°C) and integrating Cp over this temperature range (Eq. 12)

$$S^\varnothing = \int_0^T C_P \, dlnT \qquad (12)$$

$\Delta_R H^\varnothing$ can be determined from the difference of heat of dissolutions of gypsum and anhydrite at 298.15 (25°C).

Kelley et al. (1941) reported such results (Eq. 13–15) for the reaction (IV), which is the reverse of eq. (I).

TABLE 5 Concentrations and water activities at intersection of gypsum and anhydrite solubility curves in different electrolytes at different temperatures.

Electrolyte	T/°C	m_{min}	m_{max}	a_w-min^a	a_w-max	References
H_2SO_4	10.0	5.25	5.75	0.6748	0.6346	Zdanovskii, A. B. and Vlasov, G. A. (1968)
	25.0	2.4	2.6	0.8890	0.8767	Zdanovskii, A. B. and Vlasov, G. A. (1968)
		3.25	3.75	0.8338	0.7984	Wang et al. (2013)
	35.0	1.3	1.5	0.9485	0.9391	Zdanovskii, A. B. and Vlasov, G. A. (1968)
	42.0	0.25	0.45	0.9909	0.9836	Zdanovskii, A. B. and Vlasov, G. A. (1968)
NaCl	25.0	3.65	3.85	0.8634	0.8551	Bock (1961)
	40.0	1.2	1.8	0.9587	0.9370	Bock (1961)
HCl	25.0	3.8	4.0	0.8140	0.7999	Kruchenko, V. P. and Beremzhanov, B. A. (1976)
$CaCl_2$	25.0	2.3	2.7	0.8304	0.7859	Mel'nikova et al. (1971)

^{a}Belongs to m_{min}, a_w calculated the Pitzer model with parameters from THEREDA, database.

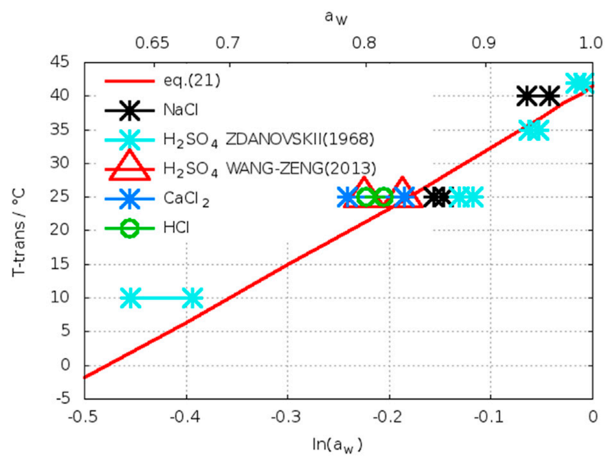

FIGURE 15
Relationship between water activity and transition temperature gypsum-anhydrite in different electrolytes (two symbols, some connected by a line, reflect the uncertainty as can be read-off as m_{min} and m_{max} from Table 5).

The thermochemical conversion factor 1 cal = 4.184 J/mol was applied.

$$CaSO_4 \cdot 2H_2O_{(s)} \rightarrow CaSO_{4(s)} + 2H_2O_{(l)} \quad \text{(IV)}$$

$$\Delta_R C_P = 28.3 - 0.043\,T \left\{\frac{cal}{mol \cdot K}\right\} = 118.4 - 0.1799\,T \left\{\frac{J}{mol \cdot K}\right\} \quad (13)$$

$$\Delta_R H^{\varnothing} = -2495 + 28.3\,T - 0.0215\,T^2 \left\{\frac{cal}{mol}\right\}$$
$$= -10439 + 118.4\,T - 0.08996\,T^2 \left\{\frac{J}{mol}\right\} \quad (14)$$

$$\Delta_R G^{\varnothing} = -2495 - 65.17\,T\,log_{10}T + 0.0215\,T^2 + 163.89\,T \left\{\frac{cal}{mol}\right\}$$
$$= -10439 - 272.67\,T\,log_{10}T + 0.08996\,T^2 + 685.72\,T \left\{\frac{J}{mol}\right\} \quad (15)$$

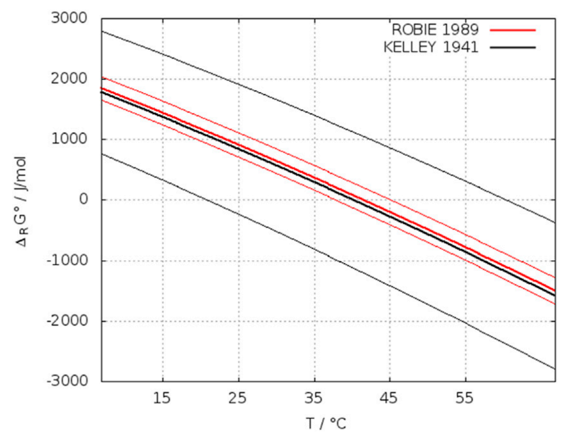

FIGURE 16
Temperature dependence of the standard Gibbs energy of reaction (IV). Thin lines: upper and lower limit of $\Delta_R G^{\varnothing}$.

For the limited temperature range 25°C–60°C the linear approximations Eqs 16, 17 were made and Cp(H_2O,liq.) was set to 18.02 cal/(mol K) by Kelley et al. (1941).

$$Cp\,(gypsum) = 21.84 + 0.076\,T \quad cal/(mol\,K) \quad (16)$$
$$Cp\,(anhydrite) = 14.10 + 0.033\,T \quad cal/(mol\,K) \quad (17)$$

Solving Eq. 15 for T yields a transition temperature of 313 K (=40°C) when $\Delta_R G^{\varnothing} = 0$. For the standard enthalpy of hydration ($\Delta_H H^{\varnothing} = \Delta_R H^{\varnothing}$) at 25°C Kelley listed in his Table 2 p. 15 the values given in Table 6.

For the entropies at 25°C Anderson in Kelley et al. (1941) listed the following values from his Cp measurements for anhydrite and gypsum (Table 7):

From the recommended data of Kelley et al. and Eqs 16, 17 one can write Eq. 18 including the uncertainties:

$$\Delta_R G^{\varnothing} = \Delta_R H^{\varnothing} - T \cdot \Delta_R S^{\varnothing}$$
$$= -16862 \pm 84 - T \cdot (\Delta_R S^{\varnothing} \pm 3.3) \left\{\frac{J}{mol}\right\} \quad (18)$$

TABLE 6 Listing of caloric quantities from Kelley (1941).

$\Delta_H H^{\varnothing}$/cal/mol	$\Delta_R H^{\varnothing}$/J/mol	Type of anhydrite	Authors
−4020	−16820	Natural	Newman and Wells (1938)
−4020	−16820	Gypsum heated to 900°C	Southard in Kelley et al. (1941)
−4040	−16903	Natural, acid wash and drying	Southard in Kelley et al. (1941)
−4030	−16862	Selenite heated to 870°C for 4 h	Southard in Kelley et al. (1941)
−4030 ± 20	**−16862 ± 84**	**Recommended**	Southard in Kelley et al. (1941)

TABLE 7 Absolute entropy data given in Kelley et al. and Latimer et al.

Solid	S^0(298.1)/cal/mol·K	S^0 (298.1)/J/mol·K	Author
Anhydrite	25.5 ± 0.4	106.7 ± 1.7	Anderson in Kelley et al. (1941)
Gypsum	46.4 ± 0.4	194.1 ± 1.7	Anderson in Kelley et al. (1941)
Gypsum	46.4 ± 0.2	194.1 ± 0.85	Latimer et al. (1933)

with

$$\Delta_R S^{\varnothing} = -\frac{(\Delta_R G^{\varnothing} - \Delta_R H^{\varnothing})}{T} = 567.32 - 272.67\, log_{10} T + 2.0{*}0.08996\, T \left\{\frac{J}{mol \cdot K}\right\} \quad (19)$$

The upper and lower limit of Eq. 18 yields a broad interval of uncertainty of ±25 K, which had been pointed out by Zen (1965). In Kelley's Gibbs energy function also the solid-gas decomposition pressure measurements gypsum-anhydrite were incorporated. Zen criticized this, modified the equation of Kelley by introducing more new entropy data of water and neglecting the decomposition data of gypsum. Zen also introduced a more new Cp function for anhydrite from Kelley (1960). However, this Cp function is linear for anhydrite up to 1,400 K, which cannot be an improvement for the application discussed here. Zen's revised equation (Eq. 20) shifts the transition temperature to 45°C but cannot be considered as an improvement. The large uncertainty remained.

$$\Delta_R G^{\circ}(T, 1\, atm) = -2890 + 179.40\, T + 0.026\, T^2 - 30.98\, TlnT,\ \text{T in K} \quad (20)$$

Robie, R. A. et al. (1989) repeated heat capacity measurements of anhydrite and gypsum and could reduce the uncertainty in the reaction entropy from 3.32 (Kelley et al., 1941) to 0.39 J/(mol K). Their Gibbs energy function (Eq. 21) for reaction (IV) crosses the zero value at 314.7 K (=41.5°C). Their estimated error of ±3.5 K is composed of ±1.4 K using the uncertainty of the hydration enthalpy of ±20 cal/mol (=± 84 J/mol/K) (Kelley et al., 1941) and ±2.1 K from their uncertainty in $\Delta_R S^{\varnothing}$. These uncertainty limits are shown in Figure 16.

$$\Delta_R G^{\varnothing} = -11216 + 0.099 \cdot T^2 - 123.69 \cdot TlnT + 715.9 \cdot T;\ \text{T in K} \quad (21)$$

However, in our opinion the uncertainty of the reaction enthalpy was set too high by Kelley. Considering the values given in Table 6, it should be half as large that is ±42 J/mol instead of 84. With the estimation described above this reduces the uncertainty to ±2.8 K.

More recent Cp measurements applying a DSC technique (Majzlan et al., 2002) show a larger scatter and thus could not improve the accuracy of Cp for anhydrite.

2.4 Thermodynamic modelling of $CaSO_4$-containing solutions

Precipitation of calcium sulfate from various aqueous solutions is of equal interest in geochemistry and hydrometallurgy. Therefore, several thermodynamic models had been established to describe precipitation processes in both fields of application at various conditions. Within the framework of such models also the transition temperature gypsum-anhydrite had been discussed. Sometimes the authors raised the hope to enhance the reliability of that value by thermodynamic modelling. However, it has to be emphasized that in case of calcium sulfate (compound with low solubility) a calculated transition temperature from a thermodynamic model is not an independent proof. The benefit of a thermodynamic model consists in combining different types of data (activity, caloric data, solubility), which support each other in a description of these properties as function of composition and temperature. If for a system only a few experimental solubility data are available the inclusion of a model for activity coefficients of unsaturated solutions and some caloric data (dissolution enthalpy, heat capacities) can enable a calculation of solubility curves, which could not be estimated with spare solubility data alone. However, for calcium sulfate this situation does not apply. There exists a plenty of solubility data in water within the interesting temperature range and it possess a low solubility.

Solubility and thermodynamic data are related through the solubility constant and the calculation of the latter requires the activity coefficient $\gamma_{\pm(CaSO4)}$ (Eq. 22). The concentration dependence of activity coefficients is described by models like extended Debye-Hückel equation, Pitzer ion interaction model and others. These activity coefficient models contain parameters, which are adjusted to experimental data. For unsaturated $CaSO_4$ solutions activity

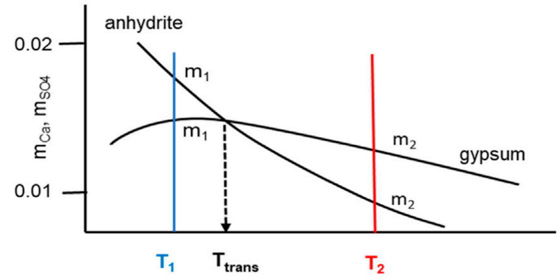

FIGURE 17
Scheme of solubility curves of gypsum and anhydrite in water demonstrating the small molality differences at selected temperatures T_1 and T_2.

coefficients had been measured only at 25°C (Lilley, T. H. and Briggs, 1976). As one can see from Eq. 22 for a given value of solubility (m_{Ca}, m_{SO4}) the value of $K_s^{\varnothing}$ will vary with the chosen $\Upsilon_{\pm}$. As long as there are no constraints for the solubility constant from caloric data (right-hand side Eq. 22) the solubility can be described with arbitrary corresponding pairs of $K_s^{\varnothing}$ and $\Upsilon_{\pm}$.

$$ln K_s^{\varnothing} = ln\, m_{Ca} + ln\, m_{SO4} + 2\, ln \gamma_{\pm(CaSO4)} = -\frac{\Delta_s G^{\varnothing}}{RT} = \frac{-\Delta_s H^{\varnothing} - \Delta_s S^{\varnothing}}{RT} \tag{22}$$

The solubility constants as well as the activity coefficients depend on temperature. From Eq. 2–4 follows Eq. 23

$$ln \frac{K_{gyp}^{\varnothing}}{K_{anh}^{\varnothing}} = \ln \frac{(m_{Ca} m_{SO4})_{gyp}}{(m_{Ca} m_{SO4})_{anh}} + 2\, ln \frac{(\gamma_{\pm})_{gyp}}{(\gamma_{\pm})_{anh}} + 2\, ln\, a_w \tag{23}$$

The schematic solubility diagram in Figure 17 illustrates the situation with Eq. 23. Below and above (T_1, T_2) the transition temperature T_{trans} the saturation molality for gypsum and anhydrite is different, but due to the low absolute value of solubility (differences are even smaller) the activity coefficient can be set equal for both molalities at the selected temperature T_1 or T_2. Thus, the second term on the right-hand side in Eq. 23 can be set to zero and the ratio of both equilibrium constants $K_{gyp}^{\varnothing}/K_{anh}^{\varnothing}$ is entirely independent on the model chosen to calculate $\Upsilon_{\pm}$. In water also $ln a_w$ is zero. This means, the transition temperature is obtained at equal values of the concentration products of gypsum and anhydrite, which is just another way to express solubilities. Therefore, calculating the transition temperature through a model is only a reflection of the quality of the assessment of experimentally determined solubility data and its smoothing through the models fit. By the way, this is also true, if the model includes a constant for the ion-pair formation $(CaSO_4)_{aq}$. For solutions of gypsum and anhydrite in presence of other electrolytes the $ln a_w$ will not be zero and has to be calculated by means of the model. However, this is not very critical, since the calculation of water activities is less sensitive on electrolyte concentration than the calcium sulfate solubility.

Table 1 contains some references where the transition temperature is calculated by means of thermodynamic models. Models based on a thorough assessment of solubility data in the system $CaSO_4$-H_2O obtain transition temperatures at (41 ± 2)°C (Altmaier et al., 2011; Marshall, W. L. et al., 1964; Marshall and Slusher, 1966; Corti and Fernandez-Prini, 1984; Azimi et al., 2007; Wang et al., 2013; Li et al., 2018; Shen et al., 2019). For the remaining models, which predict a much higher or lower temperature deficiencies in data evaluation can be detected. The origin of the low value of about 30°C in Messnaoui and Bounahmidi (2006) can be recognized from Figure 5 in their publication. The calculated solubility of gypsum is systematically above the experimental data and thus shifting the section point with the anhydrite line to a lower temperature. The same with the high value (49°C) from the model of Möller (1988a). Here also the calculated gypsum solubilities are located above the experimental data [see Figure 3 in Möller (1988a)]. The reason of the high value (59.9°C) from Raju and Atkinson (1990) cannot be figured out explicitly. The authors emphasized to trust first of all on solubility data, but also applied caloric data from NBS tables (Wagman et al., 1982) without giving details. This was also criticized by Shen et al. (2019). However, one word more should be in place here about the most recent model of Shen et al. Although their model gives a transition temperature of 42.8°C within the limit of our determination, the agreement is fortuitous. The model is based on an assessment of solubility data in the binary system $CaSO_4$–H_2O, where the authors accepted also a large number of data points in a table of D'Ans et al. (1955), which represent calculated (and not experimental!) solubilities from a thermodynamic model developed by D'Ans. The effect of the data selection is illustrated in Figures 18, 19, where our data selection and that of Shen et al. is compared. The calculated data of D'Ans et al. which we had excluded (see discussion Section 2.2.1) were included by Shen et al. (closed red circles in Figures 18, 19). These calculated data points dominate the course of the solubility isotherm of gypsum and anhydrite in the selection of Shen et al. Other, positively and negatively deviating data accepted by Shen et al. are compensating each other in respect to the course of the isotherm, only enhancing the scatter. The careful solubility determinations of Raupenstrauch (1885b), Raupenstrauch (1885a), and Hulett and Allen (1902) for gypsum had not been considered by Shen et al. Since D'Ans calculated data are in agreement with these data, the neglection had no effect on the data fit of Shen et al.

3 Conclusion

The temperature at which gypsum and anhydrite can co-exist in equilibrium with each other represents the upper limit for the long-term existence of gypsum in contact with solutions and the lower limit for anhydrite. When passing this temperature one phase should be converted or transferred into the other one as long as contact with solution exists. Therefore, the term transition or conversion temperature is in use. As a thermodynamically fixed quantity it does not make any statement on the time required for a transition for instance from gypsum to anhydrite. The extremely slow crystallization kinetics of anhydrite at temperatures below 90°C prevents to approach the solubility equilibrium from super- and undersaturation. In this work several methods to fix this temperature were discussed. The assessment of reported solubility data of gypsum and anhydrite in water represents the most important method to estimate the temperature of the gypsum-anhydrite equilibrium. Although a large pool of solubility data exists, particularly for gypsum, we demonstrated that statistical

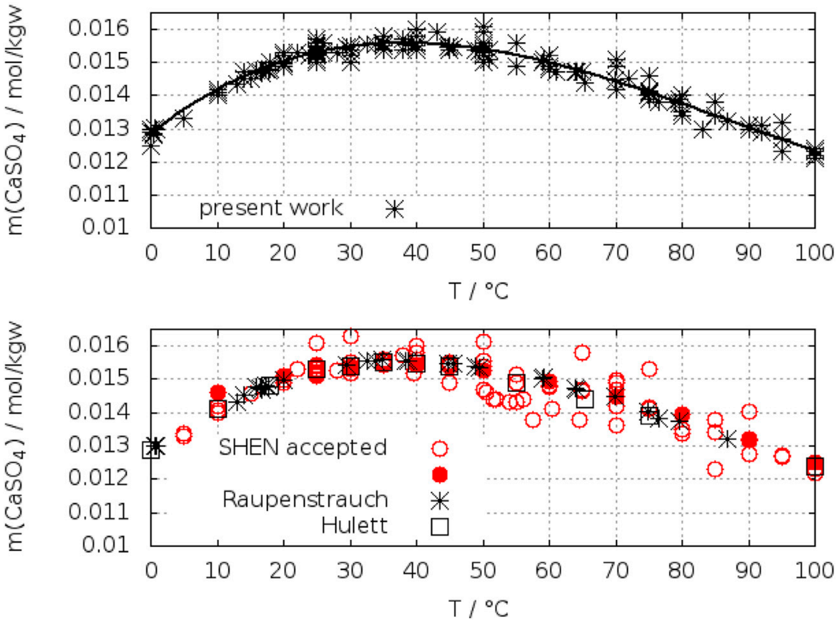

FIGURE 18
Comparison of the data selection of Shen et al. (2019) and in this work for gypsum. Black stars: accepted data of this work (top); red circles (open and closed) accepted by Shen et al. (2019), closed red circles are calculated data of D'Ans, which had been selected as "experimental" by Shen et al. In the lower figure the data of Raupenstrauch (1885a) (stars) and Hulett and Allen (1902) (squares) were added, which had not been considered by Shen et al. Line: fit in this work.

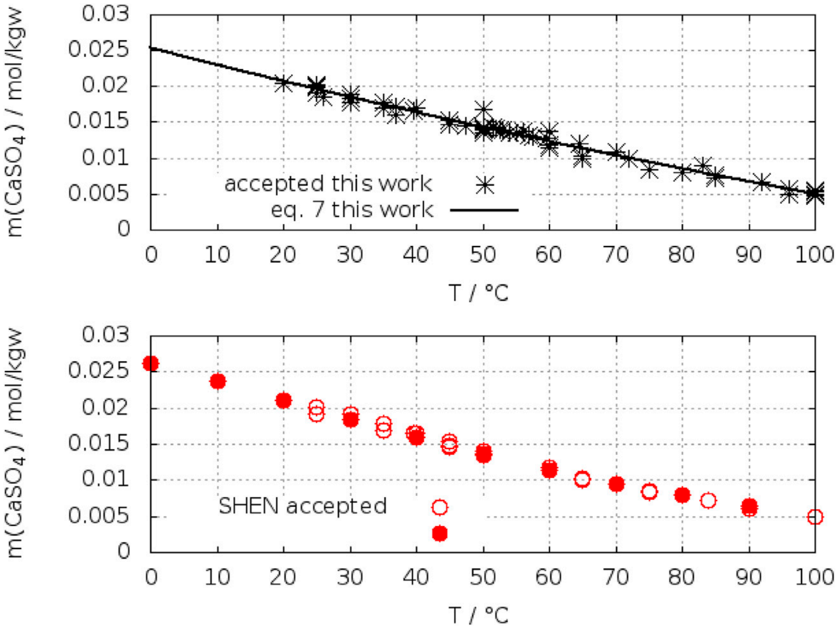

FIGURE 19
Comparison of the data selection of Shen et al. (2019) and in this work for anhydrite. Black stars: accepted data of this work (top); red circles (open and closed): accepted data of Shen et al. (2019) including the calculated data of D'Ans (closed red circles) (buttom). Line: fit this work.

criteria are not sufficient to achieve the required accuracy to narrow the temperature range for the transition temperature gypsum-anhydrite. Critical selection based on experimental details shifted the mean value given by Krumgalz from 45.6°C to 42.0°C. In addition, it was shown that solubility experiments near the crossing-point of the solubility polytherms of both phases with the same experimental technique yield T_{trans} = (42.0 ± 1)°C, which is considered as the best determination at ambient pressure. Independent evidence for this temperature is provided from calorimetric measurements yielding (42 ± 2.8)°C. The presence of electrolyte solutions decreases this temperature, however, the relationship with the water activity supports the value in water, but with a broader uncertainty. Furthermore, it was shown that thermodynamic modelling cannot be considered as an independent proof of the transition temperature, but when based on thorough assessment of solubility data of gypsum and anhydrite the results agree with 42°C. For deviating results we could figure out the deficiencies. The question of the thermodynamic transition temperature can now be considered as resolved. The value of (42 ± 1)°C represents a geochemical reference for the long-term stability of gypsum and anhydrite in water at 1 bar, which can be adapted to other pressures or solutions with lower water activity by applying the relevant thermodynamic equations including additional data as volume change in dissolution or water activities. This should be valuable in a geochemical characterization of host rocks for waste disposal.

Author contributions

WV: Performed the data re-assessments and draw the conclusion. DF: Checked the results based on her experience and knowledge of the system. All authors contributed to the article and approved the submitted version.

Funding

Open Access Funding by the Publication Fund of TU Bergakademie Freiberg.

Conflict of interest

The authors declare that the research was conducted in the absence of any commercial or financial relationships that could be construed as a potential conflict of interest.

Publisher's note

References

Altmaier, M., Bube, C., Neck, V., Marquardt, C., Richter, A., Scharge, T., et al. (2011). Thereda - thermodynamische referenz-datenbasis. *Hexäres Syst. ozeanischen Salze.*

Azimi, G., Papangelakis, V. G., and Dutrizac, J. E. (2007). Modelling of calcium sulphate solubility in concentrated multi-component sulphate solutions. *Fluid Phase Equilib.* 260, 300–315. doi:10.1016/j.fluid.2007.07.069

Bell, J. M., and Taber, W. C. (1906). The solubility of gypsum in solutions of ammonium sulphate. *J. Phys. Chem.* 10, 119–122. doi:10.1021/j150074a005

Berdugo, I., Romero, E., Saaltink, M., and Albis, M. (2008). On the behaviour of the CaSO4-H2O system. *Rev. Acad. Colomb. Cienc.* 32, 555.

Block, J., and Waters, O. B. (1968). Calcium sulfate-sodium sulfate-sodium chloride-water system at 25.deg. to 100.deg. *J. Chem. Eng. Data* 13, 336–344. doi:10.1021/je60038a011

Blount, C. W., and Dickson, F. W. (1973). Gypsum-Anhydrite equilibria in systems CaSO4 - H2O and CaSO4-NaCl-H2O. *Am. Mineral.* 58, 323–331.

Bock, E. (1961). ON the solubility of anhydrous calcium sulphate and of gypsum in concentrated solutions of sodium chloride at 25 °C, 30 °C, 40 °C, and 50 °C. *Can. J. Chem.* 29, 1746–1751. doi:10.1139/v61-228

Cameron, F. K. (1901). Solubility of gypsum in aqueous solutions by sodium chloride. *J. Phys. Chem.* 5, 556–576. doi:10.1021/j150035a002

Corti, H. R., and Fernandez-Prini, R. (1984). Thermodynamics of solution of gypsum and anhydrite in water over a wide temperature range. *Can. J. Chem.* 62, 484–488. doi:10.1139/v84-081

D'Ans, J., Bredtschneider, D., Eick, H., and Freund, H.-E. (1955). Untersuchungen über die Calciumsulfate. *Kali Steinsalz*, 17–38.

D'Ans, J. (1968). Der übergangspunkt gips-anhydrit. *Kali U. Steinsalz* 5, 109–111.

d'Anselme, M. A. (1903). Solubility of calcium sulfate hydrate in solutions of seawater. *Bull. Soc. Chim. Fr.* 29, 372–374.

Denman, W. (1961). Maximum Re-use of cooling water based on gypsum content and solubility. *Ind. Eng. Chem.* 53, 817–822. doi:10.1021/ie50622a026

Dickson, F. W., Blount, C. W., and Tunell, G. (1963). Use of hydrothermal solution euqipment to determine the solubility of anhydrite in water from 100 °C to 275 °C and from 1 bar to 1000 bars pressure. *Am. J. Sci.*

Freyer, D., and Voigt, W. (2003). Crystallization and phase stability of CaSO4 and CaSO 4 - based salts. *Monatsh. fur Chem.* 134, 693–719. doi:10.1007/s00706-003-0590-3

Fu, H., Guan, B., Jiang, G., Yates, M. Z., and Wu, Z. (2012). Effect of supersaturation on competitive nucleation of CaSO4 phases in a concentrated CaCl2 solution. *Cryst. Growth Des.* 12, 1388–1394. doi:10.1021/cg201493w

Grigor'Ev, A. P., and Shamaevp, P. P. (1976). Determination of gypsum-anhydrite equilibrium temperature. *Izv. Sib. Otd. Akad. Nauk. SSSR. Ser. Khim.*, 104.

Hardie, L. A. (1967). Gypsum-anhydrite equilibrium at one atmosphere pressure. *Amer. Mineral.* 52, 171–200.

Hill, A. E. (1934). Ternary systems. XIX. Calcium sulfate, potassium sulfate and water. *J. Am. Chem. Soc.* 56, 1071–1078. doi:10.1021/ja01320a019

Hill, A. E. (1937). The transition temperature of gypsum to anhydrite. *J. Am. Chem. Soc.* 59, 2242–2244. doi:10.1021/ja01290a039

Hulett, G. A., and Allen, L. E. (1902). The solubility of gypsum. *J. Am. Chem. Soc.* 24, 667–679. doi:10.1021/ja02021a007

Innorta, G., Rabbi, E., and Tomadin, L. (1980). The gypsum-anhydrite equilibrium by solubility measurements. *Geochim. Cosmochim. Acta* 44, 1931–1936. doi:10.1016/0016-7037(80)90192-1

Kelley, K. K. (1960). *Reference material: Bulletin 584-bureau of mines - contributions to the data on theoretical metallurgy, XIII. High-temperature heat-content, heat-capacity, and entropy data for the elements and inorganic compounds*. Denton, Texas, USA: UNT Digital Library.

Kelley, K. K., Southard, J. C., and Anderson, C. T. (1941). *Thermodynamic properties of gypsum and its dehydration products* Washington D. C.,USA: US Bur. Mines Tech Paper.

Knacke, O., and Gans, W. (1977). The thermodynamics of the system CaSO4 - H2O. *Z. Phys. Chem. N. F.* 104, 41–48. doi:10.1524/zpch.1977.104.1-3.041

Kontrec, J., Kralj, D., and Brečević, L. (2002). Transformation of anhydrous calcium sulphate into calcium sulphate dihydrate in aqueous solutions. *J. Cryst. Growth* 240, 203–211. doi:10.1016/S0022-0248(02)00858-8

Kruchenko, V. P., and Beremzhanov, B. A. (1976). Solubility of salts in the calcium sulfate-hydrochloric acid-water system at 25 °C. *Zh. Neorg. Khim.* 21, 281–282.

Krumgalz, B. S. (2018). Temperature dependence of mineral solubility in water. Part 3. Alkaline and alkaline earth sulfates. *J. Phys. Chem. Reference Data* 47, 23101. doi:10.1063/1.5031951

Kuznetsov, A. M. (1946). The solubility of CaSO4 in the system CaCl2-HCl-H2O. *Zh. Prikl. Khim.* 19, 1335–1339.

Lancia, A., Musmarra, D., and Prisciandaro, M. (1999). Measuring induction period for calcium sulfate dihydrate precipitation. *AIChE J.* 45, 390–397. doi:10.1002/aic.690450218

Latimer, W. M., Hicks, J. F. G., and Schutz, P. W. (1933). The heat capacities and entropies of calcium and barium sulfates from 15 to 300°K. The entropy and free energy of sulfate ion. *J. Chem. Phys.* 1, 620–624. doi:10.1063/1.1749337

Li, D., Zeng, D., Yin, X., and Gao, D. (2018). Phase diagrams and thermochemical modeling of salt lake brine systems. III. Li2SO4+H2O, Na2SO4+H2O, K2SO4+H2O, MgSO4+H2O and CaSO4+H2O systems. *Calphad* 60, 163–176. doi:10.1016/j.calphad.2018.01.002

Lilley, T. H., and Briggs, C. C. (1976). Activity coefficients of calcium sulphate in water at 25 °C. *Proc. R. Soc. Lond. A* 349, 355–368.

Li, Z., and Demopoulos, G. P. (2005). Solubility of CaSO4 phases in aqueous HCl + CaCl2 solutions from 283 K to 353 K. *J. Chem. Eng. Data* 50, 1971–1982. doi:10.1021/je050217e

Madgin, W. M., and Swales, D. A. (1956). Solubilities in the system CaSO4-NaCl-H2O at 25° and 35°. *J. Appl. Chem.* 6, 482–487. doi:10.1002/jctb.5010061102

Majzlan, J., Navrotsky, A., and Neil, J. M. (2002). Energetics of anhydrite, barite, celestine, and anglesite: A high-temperature and differential scanning calorimetry study. *Geochim. Cosmochim. Acta* 66, 1839–1850. doi:10.1016/S0016-7037(01)00881-X

Marshall, W. L., Slusher, R., and Iones, E. V. (1964). Aqueous systems at high temperatures XIV. Solubility and thermodynamic relationships for CaSO$_4$ in NaCl-H$_2$O solutions from 40° to 200° C., 0 to 4 molal NaCl. *J. Chem. Eng. Data* 9, 187–191. doi:10.1021/je60021a011

Marshall, W. L., and Slusher, R. (1966). Thermodynamics of calcium sulfate dihydrate in aqueous sodium chloride solutions, 0-110$^{\circ1,2}$. *J. Phys. Chem.* 70, 4015–4027. doi:10.1021/j100884a044

Mel'nikova, S. M., Moshkina, I. A., and Kolosov, A. S. (1971). *Izv. Sib. Otd. Atad. Nauk. SSSR, Ser. Khim. Nauk.* https://speciation.net/Database/Journals/Sib-Khim-ZhIzv-Sib-Otd-Akad-Nauk-SSR-Ser-Khim-Nauk-;i405.

Messnaoui, B., and Bounahmidi, T. (2006). On the modeling of calcium sulfate solubility in aqueous solutions. *Fluid Phase Equilib.* 244, 117–127. doi:10.1016/j.fluid.2006.03.022

Möller, N. (1988a). The prediction of mineral solubilities in natural waters: A chemical equilibrium model for the Na-Ca-Cl-SO4-H2O system, to high temperature and concentration. *Geochim. Cosmochim. Acta* 52, 821–837. doi:10.1016/0016-7037(88)90354-7

Möller, N. (1988b). The prediction of mineral solubilities in natural waters: A chemical equilibrium model for the Na-Ca-Cl-SO4-H2O system, to high temperature and concentration. *Geochim. Cosmochim. Acta* 52, 821–837. doi:10.1016/0016-7037(88)90354-7

Nakayama, F. S., and Rasnik, B. A. (1967). Calcium electrode method for measuring dissociation and solubility of calcium sulfate dihydrate. *Anal. Chem.* 39, 1022–1023. doi:10.1021/ac60252a010

Newman, E. S., and Wells, L. S. (1938). Heats of hydration and transition of calcium sulfate. *Nat. Bur. Stand. J. Res.* 20, 825. doi:10.6028/jres.020.004

Ossorio, M., van Driessche, A., Pérez, P., and García-Ruiz, J. M. (2014). The gypsum–anhydrite paradox revisited. *Chem. Geol.* 386, 16–21. doi:10.1016/j.chemgeo.2014.07.026

Otalora, F., and Garcia-Ruiz, J. (2014). Nucleation and growth of the Naica giant gypsum crystals. *Chem. Soc. Rev.* 43, 2013–2026. doi:10.1039/C3CS60320B

Partridge, E. P., and White, A. H. (1929). The solubility of calcium sulfate from 0 to 200°. *J. Am. Chem. Soc.* 51, 360–370. doi:10.1021/ja01377a003

Pelsh, A. D. (1973). *Handbook of experimental data on solubility in multi-component aqueous salt systems*. Leningrad: Khimiya: Water-Salt System Chemistry, Press.

Poggiale, M. (1843). Memoire sur la solubilite des sels dans L'eau. *Ann. de chimie de physique*, 463–478.

Posnjak, E. (1938). The system CaSO4 - H2O. *Am. J. Sci.*, 247–272.

Power, W. H., Fabuss, B. M., and Satterfield, C. N. (1966). Transient solubilities and phase changes of calcium sulfate in aqueous sodium chloride. *J. Chem. Eng. Data* 11, 149–154. doi:10.1021/je60029a005

Power, W. H., Fabuss, B. M., and Satterfield, C. N. (1964). Transient solubilities in the calcium sulfate - water system. *J. Chem. Eng. Data* 9, 437–442. doi:10.1021/je60022a046

Raju, Krishnam U. G., and Atkinson, G. (1990). The thermodynamics of "scale" mineral solubilities. 3. Calcium sulfate in aqueous sodium chloride. *J. Chem. Eng. Data* 35, 361–367. doi:10.1021/je00061a038

Raupenstrauch, G. A. (1885a). Über die Bestimmung der Löslichkeit einiger Salze in Wasser bei verschiedenen Temperaturen. *Monatsh Chem.* 6, 563–591. doi:10.1007/bf01554655

Raupenstrauch, G. A. (1885b). Über die Bestimmung der Löslichkeit einiger Salze in Wasser bei verschiedenen Temperaturen. Sitzb. kaiserl. Akad. Wissensch. *XCII*.

Robie, R. A., Russel-Robinson, S., and Hemingway, B. S. (1989). Heat capacities and entropies from 8 to 1000 K of langbeinite (K2Mg2(SO4)3), anhydrite (CaSO4) and of gypsum (CaSO4·2H2O). *Thermochim. Acta* 139, 67–81. doi:10.1016/0040-6031(89)87010-8

Sagaidachnyi, A. F., and Mordberg, L. K. (1933). *Tr. Vses. Inst. Galurgii*, 1–458.

Sborgi, U. (1926). Influenza degli elettroliti sulla velocita di presa del gesso. *Atti Soc. Toscana Mem.* 37, 179–195.

Shen, L., Sippola, H., Li, X., Lindberg, D., and Taskinen, P. (2019). Thermodynamic modeling of calcium sulfate hydrates in the CaSO4 –H2O system from 273.15 to 473.15 K with extension to 548.15 K. *J. Chem. Eng. Data* 64, 2697–2709. doi:10.1021/acs.jced.9b00112

Stolle, F. (1900). *Z. Ver. Rubenzucker-Ind.*, 321–341.

Van Driessche, A. E. S., García-Ruíz, J. M., Tsukamoto, K., Patiño-Lopez, L. D., and Satoh, H. (2011). Ultraslow growth rates of giant gypsum crystals. *Proc. Natl. Acad. Sci. U.S.A.* 108, 15721–15726. doi:10.1073/pnas.1105233108

van't Hoff, J. H. (1912). *Untersuchung über die Bildungsverhältnisse der ozeanischen Salzablagerungen insbesondere des Stassfurter Salzlagers* Leipzig: Akademische Verlagsges. mbH.

Wagman, D., Evans, W. H., Parker, V. B., Schumm, R. H., Halow, I., Bailey, S. M., et al. (1982). The NBS tables of chemical thermodynamic properties: selected values for inorganic and C1 and C2 organic substances in SI units. *J. Phys. Chem. Ref. Data* 11, 1–392.

Wang, W., Zeng, D., Yin, X., and Chen, Q. (2012). Prediction and measurement of gypsum solubility in the systems CaSO$_4$ + HMSO$_4$ + H$_2$SO$_4$ + H$_2$O (HM = Cu, Zn, Ni, Mn) at 298.15 K. *Ind. Eng. Chem. Res.* 51, 5124–5134. doi:10.1021/ie201721m

Wang, W., Zeng, D., Chen, Q., and Yin, X. (2013). Experimental determination and modeling of gypsum and insoluble anhydrite solubility in the system CaSO4–H2SO4–H2O. *Chem. Eng. Sci.* 101, 120–129. doi:10.1016/j.ces.2013.06.023

Zdanovskii, A. B., and Vlasov, G. A. (1968). Determination of the transition border CaSO4.2H2O and gamma-CaSO4 in solutions of H2SO4. *Zh. Neorg. Khim.* 13, 2552–2554.

Zen, (1965). Solubility measurements in the system CaSO4-NaCl-H2O at 35, 50, and 70 Cand one atmosphere pressure. *J. Petrololgy* 6, 124–164. doi:10.1093/petrology/6.1.124

Zeng, D., and Wang, W. (2011). Solubility phenomena involving CaSO4 in hydrometallurgical processes concerning heavy metals. *Pure Appl. Chem.* 83, 1045–1061. doi:10.1351/PAC-CON-10-09-11

frontiers | Frontiers in Nuclear Engineering

TYPE Original Research
PUBLISHED 27 September 2023
DOI 10.3389/fnuen.2023.1236544

OPEN ACCESS

EDITED BY
Taishi Kobayashi,
Kyoto University, Japan

REVIEWED BY
Jun-Yeop Lee,
Pusan National University, Republic of Korea
Arnault Lassin,
Bureau de Recherches Géologiques et Minières, France

*CORRESPONDENCE
Daniela Freyer,
✉ daniela.freyer@chemie.tu-freiberg.de

RECEIVED 07 June 2023
ACCEPTED 23 August 2023
PUBLISHED 27 September 2023

CITATION
Freyer D, Pannach M and Voigt W (2023), Solid–liquid equilibria of Sorel phases and $Mg(OH)_2$ in the system Na-Mg-Cl-OH-H_2O. Part II: Pitzer modeling.
Front. Nucl. Eng. 2:1236544.
doi: 10.3389/fnuen.2023.1236544

Solid–liquid equilibria of Sorel phases and $Mg(OH)_2$ in the system Na-Mg-Cl-OH-H_2O. Part II: Pitzer modeling

Daniela Freyer*, Melanie Pannach and Wolfgang Voigt

TU Bergakademie Freiberg, Institut für Anorganische Chemie, Freiberg, Germany

For geochemical calculations of solubility equilibria between Sorel phases, $Mg(OH)_2$, and oceanic salt solutions, the polythermal THEREDA dataset (based on the HMW model at 25°C) was extended. With both models, H^+ solution concentrations in equilibrium with $Mg(OH)_2$(s) and the 3-1-8 Sorel phase at 25°C can be calculated in good agreement. In contrast, calculated OH^- solution concentrations do not agree. Using the solubility constants (lg *K*s) determined up to 60°C in Part I of this work, together with available solubility isotherms up to 120°C, temperature functions for the 3-1-8 phase (25°C–100°C), 2-1-4 phase (60°C–120°C), and 9-1-4 phase (100°C–120°C) were derived. In order to accurately model the OH^- solution concentrations, it was necessary to implement the solution species $Mg_3(OH)_4{}^{2+}$ ($\Delta_R G_m{}^\circ$ temperature function) in addition to the $MgOH^+$ already contained in the previous model. Finally, fitting Pitzer mixing coefficients for both species now allow the calculation of the solubility equilibria of $Mg(OH)_2$(s) and the Sorel phases in agreement with the experimental data in the Mg-Cl-OH-H_2O and Na-Mg-Cl-OH-H_2O systems.

KEYWORDS

Pitzer modeling, system Na-Mg-Cl-OH-H_2O, system Mg-Cl-OH-H_2O, magnesium chloride hydroxides, Sorel phases, $Mg(OH)_2$

1 Introduction

Geochemical modeling is an integral tool in the safety assessment of radioactive waste repositories in deep geological formations. The long-term stability of geotechnical barriers and backfill materials must be confirmed under relevant geochemical conditions, such as a saline host rock in the presence of a complex salt solution. Sorel phases are the binder phases of MgO-based building material used for constructing geotechnical barriers (plugs and sealing systems) in the host of rock salt. With the experimentally determined solid–liquid equilibria of Sorel phases and $Mg(OH)_2$(s) in Part I of this work (Pannach et al., 2023), including the data of Altmaier et al. (2003) and Pannach et al. (2017), the long-term stability of magnesia building material (Sorel phases) in contact with solutions in a saline environment (NaCl saturated with already-minor concentrations of $MgCl_2$) has been proven. These data, together with those of $Mg(OH)_2$(s), allow an extension of the geochemical dataset of Pitzer's ion interaction model (Pitzer, 1991) to calculate the solubility equilibria of Sorel phases and $Mg(OH)_2$(s) in solutions of the oceanic salt system. They also allow the calculation of the pH_m values (-lg m (H^+) = pH_m) that evolve in the presence of Sorel phases or $Mg(OH)_2$. The weakly alkaline milieu generated offers favorable geochemical conditions (e.g., by buffering the pH and limiting carbonate concentration) to minimize radionuclide transport processes via potential salt solutions.

The first Pitzer dataset was developed by Harvie et al. (1984) (HMW model) for modeling mineral solubilities in the complex system of Na-K-Mg-Ca-H-Cl-SO_4-OH-HCO_3-CO_3-CO_2-H_2O at 25°C. The model contains ion interaction coefficients and standard Gibbs energies for aqueous solution species such as $MgOH^+$ and for solid phases like $Mg(OH)_2$ (brucite) and the 3-1-8 Sorel phase ($3Mg(OH)_2·MgCl_2·8H_2O$ = 2 $Mg_2Cl(OH)_3·4H_2O$, korshunovskite).

The HMW model valid for 25°C was used in 2006 as the basis for developing a polythermal THEREDA database of the system Na-K-Mg-Ca-H-Cl-SO_4-CO_3-OH-H_2O for a temperature range of 0°C–100°C (for certain subsystems, the range is extended to 200°C or 250°C). The main objective of THEREDA was to provide a comprehensive and internally consistent thermodynamic reference database for the geochemical modeling of near- and far-field processes in radioactive waste repositories in rock formations currently under discussion in Germany. For the host rock salt, THEREDA is the only database in the world that provides a polythermal model that covers the entire system of oceanic salts, including acids and bases (Voigt et al., 2007; www.thereda.de).

2 Previous data and model situation

The THEREDA model contains some improvements for the oceanic system to the underlying HMW model at 25°C. Examples are: the correct chemical formula of kainite is used ($4KCl·4MgSO_4·11H_2O$ instead of $KCl·MgSO_4·3H_2O$); the missing mineral goergeyite ($K_2SO_4·5CaSO_4·H_2O$) is included, which has a crystallization field at 298 K; the solubility of KCl is described more correctly; the water activity of gypsum/anhydrite transition at NaCl saturation is shifted to the more acceptable value of 0.84–0.85 (instead of 0.775 in the HMW model); two additional aqueous solution species ($KMgSO_4^+$ and $KCaSO_4^+$) have been implemented, which was necessary in order to describe solubilities at enhanced temperatures.

As the solubility of $Mg(OH)_2(s)$ in water is $m_{Mg(OH)2} < 2·10^{-5}$, experimental data such as activity and osmotic coefficients are not available to determine binary Pitzer coefficients. Since sufficient data from ternary systems containing magnesium and hydroxide were not available until 2017, no parameters could be derived from these systems either. The temperature-dependent parameters given in THEREDA had been derived from adjustments to the solubility data of the binary system $Mg(OH)_2$-H_2O. As per Harvie et al. (1984) for 25 °C, the solubility constant of $Mg(OH)_2(s)$ was adapted from the data of McGee and Hostetler (1977) (values up to 90°C) fitting the temperature function up to 250°C to the solubility data of the system $Mg(OH)_2$-H_2O (Travers, 1929; Lambert and Clever, 1992). Analogous to HMW, all binary interactions Mg^{2+}-OH^- were assigned to the complex species $MgOH^+$. Its temperature function was adapted according to the stability constants published by Palmer and Wesolowski (1997). Due to the lack of data before 2017 for the system $Mg(OH)_2$-$MgCl_2$-H_2O at higher temperatures, parameters and the solubility constant for the Sorel phase 3-1-8 could only be given for 25°C and were taken unchanged from Harvie et al. (1984).

In the comparing HMW and THEREDA, the deviation in the description of the solubility of $Mg(OH)_2$ and the 3-1-8 phase at 25°C in the ternary Mg-Cl-OH-H_2O system (Figure 1A) is mainly due to the deviating stability constant of the complex species $MgOH^+$, which originates from the re-determination of Palmer and Wesolowski (1997). Figure 1A shows the newer solubility data from Pannach et al. (2017); as discussed there, the experimental data determined by Robinson and Waggaman (1909) are generally too low. The calculated isotherms with both HMW and THEREDA for the ternary system Mg-Cl-OH-H_2O describe quite well the invariant point of $Mg(OH)_2$ and the 3-1-8 phase at 1.75 m_{MgCl2} but not the experimentally determined OH^- solution concentrations (Pannach et al., 2017) over the entire $MgCl_2$ concentration range. The model values in the presence of $Mg(OH)_2(s)$ and the 3-1-8 phase up to 3.5 m_{MgCl2} are too low, and above are too high. This is because Harvie et al. (1984) is fitted to the solubility data of D'Ans et al. (1955) (open symbols in Figure 1). However, these data do not belong to the ternary system but to the NaCl-containing Na-Mg-Cl-OH-H_2O due to the use of NaOH solution to precipitate the solids from the different $MgCl_2$ solutions.

In NaCl-saturated $MgCl_2$ solutions, the OH^- concentrations (given as $Mg(OH)_2$ molality in the diagrams, representative of half of the OH^- solution concentration) are generally calculated too high, as can be seen in Figure 1B, in comparison with the experimental data from Part I of this work (Pannach et al., 2023) and the data of D'Ans et al. (1955) at unknown NaCl concentrations.

Contrary to OH^-, the H^+ concentrations (as $-\lg m(H^+) = pH_m$) in equilibrium with $Mg(OH)_2(s)$ and 3-1-8 phase calculated by both models agree with the experimental data (Figure 2). The agreement between modeled and experimental results is clear in both logarithmic and non-logarithmic plots (the latter is not illustrated).

In summary, neither the HMW nor the THEREDA model sufficiently describes the OH^- concentrations in equilibrium with $Mg(OH)_2(s)$ and the Sorel phase. Hence, with the new experimental data, with OH^- equilibrium concentrations in the Mg-Cl-OH-H_2O system up to 120°C (Pannach et al., 2017), in the Na-Mg-Cl-OH-H_2O system up to 40°C, and the solubility constants of Sorel phases at 25°C, 40°C, and 60°C (Part I of this paper—Pannach et al., 2023), the model was adjusted and expanded; this included the Sorel phases 3-1-8, 9-1-4, and 2-1-4, and the metastable 5-1-8 phase.

3 Procedure for model adjustment

For fitting and extending the model, the solubility constants of the Sorel phases (Part I of this work) were first implemented in a test dataset. These K_S values were further constrained within their given uncertainty range by fitting them to the experimentally available invariant points (IP) at the corresponding $MgCl_2$ concentration (or the $MgCl_2$ concentration range in which they are expected) in the Mg-Cl-OH-H_2O (Pannach et al., 2017) and Na-Mg-Cl-OH-H_2O systems (Part I of this work). At first, the $\lg K_S$ of the 3-1-8 phase was constrained by the IP with $Mg(OH)_2(s)$, which is possible because the $\lg K_S$ of $Mg(OH)_2(s)$ is fixed in the THEREDA dataset. Using the $\lg K_S$ of the 3-1-8 phase thus fixed, $\lg K_S$ of the 2-1-4 was then refined using their common IPs (3-1-8 + 2-1-4). At higher temperatures of 100°C and 120°C, where $Mg(OH)_2(s)$ borders the 9-1-4 phase, their IPs were used to determine the $\lg K_S$ values of the 9-1-4 phase. At

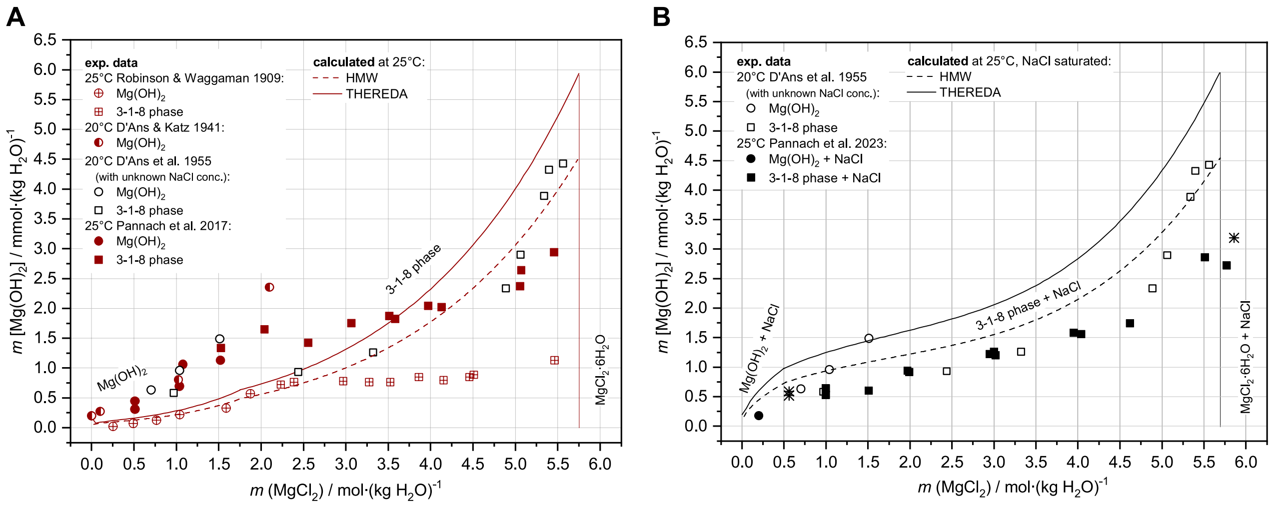

FIGURE 1
Solubility data for the Mg-Cl-OH-H_2O system **(A)** and the Na-Mg-Cl-OH-H_2O system **(B)** at 25 °C and the data from D'Ans et al. at 20 °C compared to the HMW and THEREDA models.

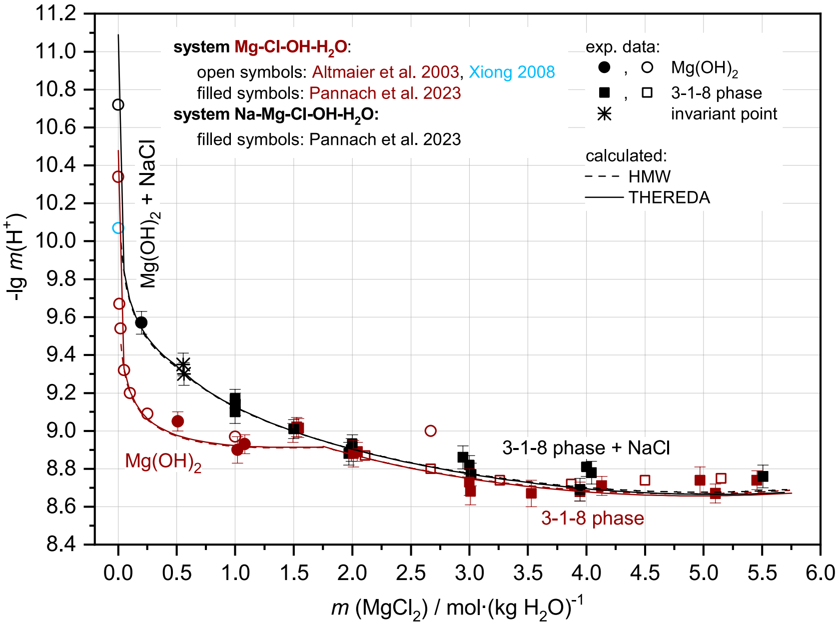

FIGURE 2
Comparison between H^+ equilibrium concentrations as -lg m (H^+) = pH_m from experimental data and HMW and THEREDA models for the Mg-Cl-OH-H_2O (brown symbols and line) and Na-Mg-Cl-OH-H_2O systems at NaCl saturation (black symbols and line) at 25°C.

these two temperatures, IPs of the 9-1-4 and 2-1-4 phases were then used to determine the lgK_S of the 2-1-4 phase at 100°C and 120°C. More precise K_S and $\Delta_R G_m$ values were thus obtained with significantly smaller corresponding errors. A temperature function was then derived from the single $\Delta_R G_m^\circ$ values of each Sorel phase and finally implemented in the THEREDA dataset (Section 4.1). The second step (Section 4.2) was to fit the Pitzer parameters in the presence of the fixed solubility constants, where it became apparent that an extension of the OH^- speciation model was also necessary (Section 4.2.2). Only then was it possible to successfully fit Pitzer parameters to reproduce the OH^- solution concentrations of both systems (Section 4.2.3).

All calculations were performed using the ChemSage (Eriksson and Hack, 1990) or ChemApp (Eriksson et al., 1997) codes. For adjustments, a specially written C-program was used, implemented in ChemApp, to calculate the smallest error sum of squares between the experimental and calculated values for up to three parameters to be changed, within the specified limits for all possible combinations.

TABLE 1 Overview of solid phases, solution species, and ion interactions already provided in THEREDA for the title system by molal standard Gibbs energies of reaction ($\Delta_R G_m^\circ$) and Pitzer coefficients. Note that, for all Primary Master species in THEREDA, $\Delta_R H^\circ_{i,T=T0}$, $\Delta_R S^\circ_{i,T=T0}$ = 0, and thus $\Delta_R G^\circ_{i,T=T0}$ = 0. Primary Master species of the title system are Na^+, Mg^{2+}, Cl^-, H^+, and H_2O (all further species and solids are formed from them by corresponding formation reactions).

$\Delta_R G_m^\circ$ for solids				
$NaCl$	Temperature function, 0°C–200°C			
$MgCl_2.6H_2O$	Temperature function, 0°C–120°C			
$Mg(OH)_2$	Temperature function, 0°C–250°C			
$Mg_2(OH)_3Cl\cdot4H_2O$	*At 25°C*			
$\Delta_R G_m^\circ$ for solution species				
OH^-	Temperature function, 0°C–250°C			
$MgOH^+$	Temperature function, 0°C–250°C			
Ion interaction coefficients				
i	**j**	$\beta^{(0)}_{ij}$	$\beta^{(1)}_{ij}$	C^{φ}_{ij}
H^+	Cl^-	Temperature functions, 0°C–120°C		
Na^+	Cl^-	Temperature functions, 0°C–200°C		
Mg^{2+}	Cl^-	Temperature functions, 0°C–120°C		
$MgOH^+$	*Cl^-*	*25 °C*	*25 °C*	-
Na^+	OH^-	Temperature functions, 0°C–120°C		
i	**j**	**k**	θ_{ij}	ψ_{ijk}
Na^+	Mg^{2+}	Cl^-	Temperature functions, 0°C–120°C	
H^+	Na^+	Cl^-	Temperature functions, 0°C–120°C	
H^+	Mg^{2+}	Cl^-	Temperature functions, 0°C–120°C	
$MgOH^+$	*Na^+*	*Cl^-*	-	-
$MgOH^+$	*Mg^{2+}*	*Cl^-*	-	*25°C*
OH^-	Cl^-	Na^+	Temperature functions, 0°C–120°C	

This was applied to determine the final Pitzer parameters, with subsequent fine-tuning performed on the optical trend of each isotherm.

4 THEREDA model adaption on Sorel phases

For the title system, the THEREDA model already contains molal standard Gibbs energies $\Delta_R G_m^\circ$, which correspond to the solubility constants K_s, (Eq. 1), as well as the Pitzer coefficients as summarized in Table 1.

$$\Delta_R G_m^\circ = -R\cdot T\cdot \ln K_S \quad \text{resp.} \quad \Delta_R G_m^\circ = -2.303\cdot R\cdot T\cdot \lg K_S. \quad (1)$$

Where the data in Table 1 are written in non-italics, no changes were made for the extension of THEREDA by the Sorel phases, as subsystems such as $NaCl$-H_2O, $MgCl_2$-H_2O, $Mg(OH)_2$-H_2O, $NaOH$-H_2O, and $NaCl$-$MgCl_2$-H_2O were already described well by the model.

4.1 Solubility constants and T-functions for Sorel phases

Solubility constants for the Sorel phases at different temperatures are available from Part I of this work (Pannach et al., 2023) and are shown in Table 2. The values in bold are used for model parameterization.

4.1.1 Sorel phase 3-1-8

The standard Gibbs energy proposed by the HMW model (Harvie et al., 1984) and the corresponding solubility constant for the reaction:

$$2\,Mg^{2+} + Cl^- + 7\,H_2O \rightleftharpoons Mg_2Cl(OH)_3\cdot 4\,H_2O_{(s)} + 3\,H^+ \qquad (2)$$

$$lgK^\circ_{S,3-1-8} = -26.03$$

is already contained in the THEREDA model and is within the error range, with the overall mean value lg $K_{S,3\text{-}1\text{-}8,25^\circ C} = -26.1 \pm 0.2$ at 25°C given in Table 2. From this value, $\Delta_R G_m^\circ = 149.0 \pm 1.1$ kJ mol^{-1} is calculated. To fix the value within the error range, the invariant point (IP) of $Mg(OH)_2(s)$ and 3-1-8 phase in the Na-Mg-Cl-OH-H_2O system (at NaCl saturation) experimentally determined in Part I was used (none is available from the ternary Mg-Cl-OH-H_2O system). To reproduce this IP at 0.56 ± 0.1 m_{MgCl2} by the model, $\Delta_R G_{m\ ,25^\circ C}^\circ$ narrows to 148.7 ± 0.1 kJ mol^{-1}, which corresponds to lg $Ks = -26.046 \pm 0.011$ (Figure 3).

No experimental IP of the $Mg(OH)_2(s)$ and 3-1-8 phase is available to refine the $\Delta_R G_{m\ ,40^\circ C}^\circ$ (148.7 ± 1.2 kJ mol^{-1}) calculated from the solubility constant at 40 °C (lg $K_{S,3\text{-}1\text{-}8,40^\circ C} = -24.8 \pm 0.2$). However, according to the solubility data for $Mg(OH)_2$ and the 3-1-8 phase, the IP is expected to be between 1.6 and 2.0–2.5 m_{MgCl2} in the Mg-Cl-OH-H_2O system and between 1.0 and 1.5 m_{MgCl2} in the NaCl-saturated solutions (Na-Mg-Cl-OH-H_2O system) at 40°C. To ensure that the model does not slip below 1.0 m_{MgCl2} at NaCl saturation and remains in the IP range for the Mg-Cl-OH-H_2O system, $\Delta_R G_{m\ ,40^\circ C}^\circ$ cannot exceed 147.7 kJ mol^{-1}, which corresponds to the lower error limit resulting from $K_{S,3\text{-}1\text{-}8,40^\circ C}$ (Figure 3).

At 60°C, only solubility data in the Mg-Cl-OH-H_2O system are available to fix $\Delta_R G_{m\ ,60^\circ C}^\circ$ calculated from the mean value of the solubility constant lg $K_{S,3\text{-}1\text{-}8,60^\circ C} = -23.04 \pm 0.11$ (Table 2) resulting in 147.0 ± 0.7 kJ mol^{-1}. The IP of $Mg(OH)_2(s)$ and the 3-1-8 phase is expected between 2.6 and 3.0 m_{MgCl2}, which limits $\Delta_R G_{m\ ,60^\circ C}^\circ$ to 146.3 ± 0.2 kJ mol^{-1}.

At 80 °C, no solubility constant is available, so the IP of $Mg(OH)_2(s)$ and the 3-1-8 phase in the Mg-Cl-OH-H_2O system is expected to be between 3.2 and 4.0. In addition, the experimentally determined IP of the 3-1-8 and 2-1-4 phases was found at 5.8 m_{MgCl2}. This concentration should be reproduced by the model with ±0.1 m_{MgCl2} alongside the expected IP range of the $Mg(OH)_2(s)$ and 3-1-8 phase, constraining $\Delta_R G_{m\ ,80^\circ C}^\circ$ to 144.5 ± 0.2 kJ mol^{-1} (re-calculating lg $K_{S,3\text{-}1\text{-}8,80^\circ C} = -21.369 \pm 0.011$).

Using all the determined values for $\Delta_R G_{m\ ,3\text{-}1\text{-}8}^\circ$ for the different temperatures (open squares in Figure 3), the THEREDA-conforming temperature function

TABLE 2 Solubility constants (lg K_S) for the Sorel phases 3-1-8, 5-1-8 and 2-1-4 determined in Part I of this work (Pannach et al., 2023) compared to available data from the literature. The values in bold are used for model fitting. No data are available for the 9-1-4 phase.

Sorel phase	T [°C]	System Mg-Cl-OH-H_2O		System Na-Mg-Cl-OH-H_2O		Overall mean value, lg K_S
		lg K_S ± σ	Ref	lg K_S ± σ	Ref	
3-1-8 phase	**25**	−26.15 ± 0.16	Altmaier et al. (2003)	−26.16 ± 0.13	*Part I of this work*	**−26.1 ± 0.2**
		−26.10 ± 0.13	*Part I of this work*			
	40	−24.72 ± 0.04	*Part I of this work*	−24.88 ± 0.16	*Part I of this work*	**−24.8 ± 0.2**
	60	**−23.04 ± 0.11**	*Part I of this work*	-		
5-1-8 phase	**25**	−43.39 ± 0.25	*Part I of this work*	−43.21 ± 0.33	Xiong et al. (2010)	**−43.3 ± 0.3**
2-1-4 phase	**60**	**−32.95 ± 0.20**	*Part I of this work*	-		

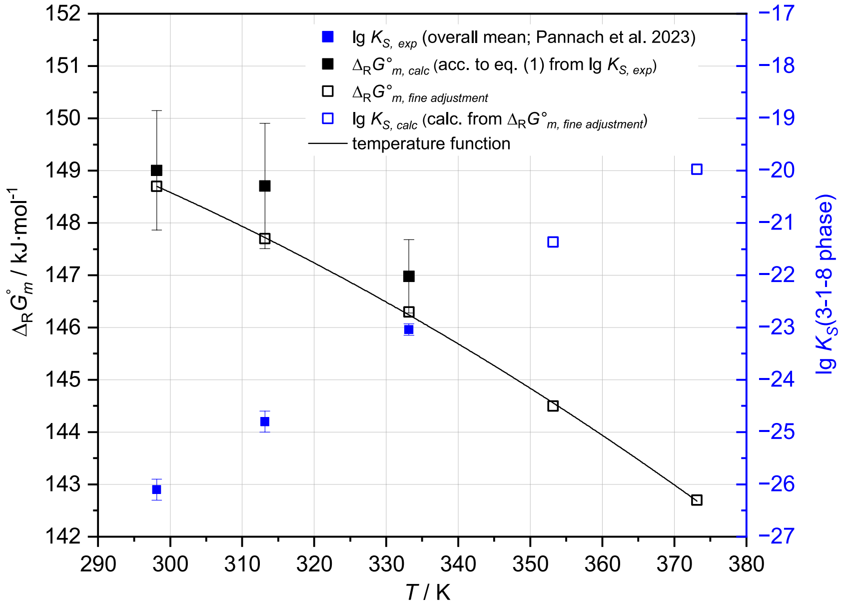

FIGURE 3
$\Delta_R G_m^\circ$ function of the 3-1-8 phase resulting from the single isotherm values of the experimentally determined lg $K_{S,3\text{-}1\text{-}8}$ at 25°C, 40°C, and 60°C, together with available solubility data, the positions of IP's with this phase up to 100°C in the Mg-Cl-OH-H_2O system, and at 25°C and 40°C in the Na-Mg-Cl-OH-H_2O system (Pannach et al., 2017; Pannach et al., 2023).

$$\Delta_R G_m^\circ = A + B \cdot T + C \cdot T \cdot \ln(T) + D \cdot T^2 + E \cdot T^3 + \frac{F}{T} \quad (3)$$

was fitted and extrapolated to 100°C. According to the experimental data at 100°C, the 3-1-8 phase is replaced by the 9-1-4 phase (Pannach et al., 2017). In order to model the metastable range, the $\Delta_R G_m^\circ$ obtained by extrapolation had to be slightly shifted to $\Delta_R G_{m}^{\circ}{}_{,100°C}$ = 142.8 kJ mol^{-1}. The finally fitted $\Delta_R G_{m}^{\circ}{}_{,3\text{-}1\text{-}8\ (T)}$ function (Table 3) calculates $\Delta_R G_{m}^{\circ}{}_{,100°C}$ = 142.59 kJ mol^{-1} and is shown in Figure 3 together with all single values at the different temperatures.

4.1.2 Sorel phase 2-1-4

The Sorel phase 2-1-4 is stable from 60 °C and was found in the Mg-Cl-OH-H_2O system at higher $MgCl_2$ solution concentrations during the investigations of Pannach et al. (2017). The solubility constant according to the formation reaction in Eq. 4 was determined in Part I of this work at 60 °C (Table 2).

$$3\,Mg^{2+} + 2\,Cl^- + 8\,H_2O \rightleftharpoons Mg_3Cl_2(OH)_4 \cdot 4\,H_2O_{(s)} + 4\,H^+ \quad (4)$$

Analogous to the evaluation of the $\Delta_R G_m^\circ$ function of the 3-1-8 phase, further values of $\Delta_R G_m^\circ$ for the 2-1-4 phase were derived from the available solubility data up to 120°C.

The solubility constant lg $K_{S,2\text{-}1\text{-}4,60°C}$ = −32.95 ± 0.20 (Table 2) corresponds to $\Delta_R G_{m}^{\circ}{}_{,2\text{-}1\text{-}4,60°C}$ = 210.2 ± 1.3 kJ mol^{-1}. From the solubility data at 60°C, the IP of the 3-1-8 and 2-1-4 phases is expected to be slightly above 5.4 m_{MgCl2} (between 5.4 and 5.7 m_{MgCl2}). To represent this by the model, the $\Delta_R G_{m}^{\circ}{}_{,2\text{-}1\text{-}4,60°C}$ needs to be constrained to 211.2 ± 0.1 kJ mol^{-1}. From the solubility data at 80°C, the experimentally determined IP of the 3-1-8 and 2-1-4 phases in 5.8 m_{MgCl2} is available. For a model reproducing the

TABLE 3 Temperature coefficients for the standard Gibbs energy $\Delta_R G_m^{\circ}$ for the formation of species or phases from ions and water for the title system Na-Mg-Cl-OH-H_2O and subsystem in THEREDA. The new data from this work are highlighted in bold.

$\Delta_R G_m^{\circ}(T) = A + B \cdot T + C \cdot T \cdot \ln(T) + D \cdot T^2 + E \cdot T^3 + F/T$							
Formula	**$T_{min-max}$/K**	**A**	**B**	**C**	**D**	**E**	**F**
H_2O	273.15–393.15	0	0	0	0	0	0
H^+	273.15–393.15	0	0	0	0	0	0
Na^+	273.15–393.15	0	0	0	0	0	0
Mg^{2+}	273.15–393.15	0	0	0	0	0	0
Cl^-	273.15–393.15	0	0	0	0	0	0
OH^-	273.15–523.15	977916.173	−24698.7262	4264.428838	−8.43137921	0.003231957	−34104000
$MgOH^+$	273.15–523.15	444044.0813	−5495.03903	798.7412063	0	−0.00052773	−24391000
$Mg_3(OH)_4^{2+}$	**298.15–393.15**	**380640.7744715**	**−1108.926598837**	**0**	**2.666840823399**	**−0.002366734203628**	**0**
$Mg(OH)_2(s)$ (brucite)	273.15–393.15	127348.8077	−99.3761865	0	0	0	0
NaCl	273.15–480.15	−1585611	37614.26246	−6327.712366	11.10781391	−0.003763213	71992993
$MgCl_2 \cdot 6H_2O$ (bischofite)	273.15–389.15	4095895.434	−195408.9322	36798.92745	−109.7047406	0.05399217544	0
3-1-8 phase (korshunovskite)	**298.15–373.15**	**144872.5390947**	**87.22354499983**	**0**	**−0.2494948491172**	**0**	**0**
5-1-8 phase	**298.15**	**247202.4585**	**0**	**0**	**0**	**0**	**0**
2-1-4 phase	**333.15–393.15**	**20577.93725001**	**1205.370**	**0**	**−1.90**	**0**	**0**
9-1-4 phase	**373.15–393.15**	**594712.0**	**−480.0**	**0**	**0**	**0**	**0**

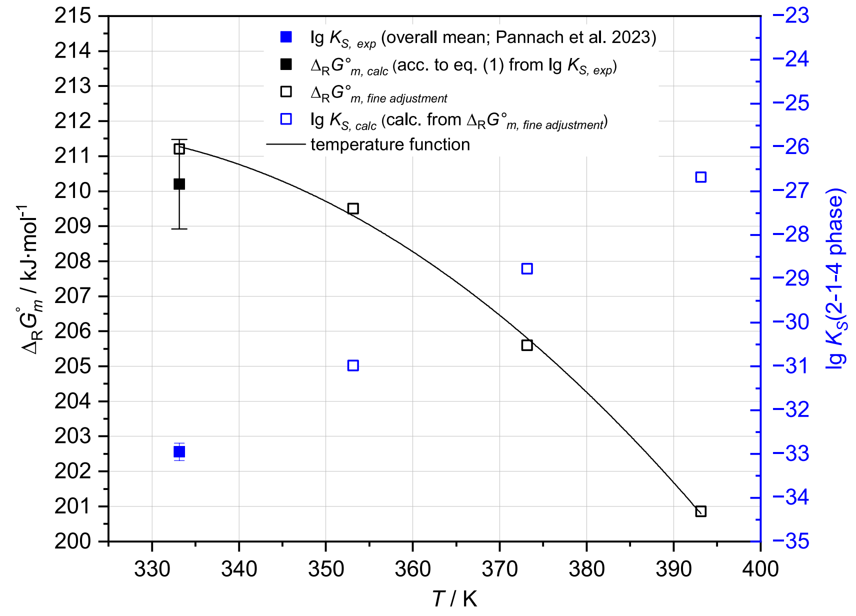

FIGURE 4
$\Delta_R G_m^{\circ}$ values of the 2-1-4 phase, derived from lg $K_{S,2\text{-}1\text{-}4,60^{\circ}C}$ at 60°C, and available solubility data at 60°C, 80°C, 100°C, and 120°C in the Mg-Cl-OH-H_2O system (Pannach et al., 2017; Pannach et al., 2023).

IP with ±0.1 m_{MgCl2}, $\Delta_R G_{m}^{\circ}{}_{,2\text{-}1\text{-}4,80^{\circ}C}$ needs to be 209.5 ± 0.1 kJ mol^{-1}.

At 100°C, in addition to the 2-1-4 phase, the 9-1-4 phase occurs as a stable Sorel phase in the Mg-Cl-OH-H_2O system (Pannach et al., 2017). The estimation of the crossing point from the trend of the solubility data of the 9-1-4 and 2-1-4 phases at 100°C suggests the IP at 5.4 ± 0.2 m_{MgCl2}. To represent it by the model, a value of $\Delta_R G_{m}^{\circ}{}_{,2\text{-}1\text{-}4,100^{\circ}C}$ = 205.6 ± 0.1 kJ mol^{-1} needs to be applied.

At 120°C, the IP of the 9-1-4 and 2-1-4 phases was determined at 5.8 m_{MgCl2} (Pannach et al., 2017) and adjusts $\Delta_R G_m{}^{\circ}{}_{,2\text{-}1\text{-}4,120°C}$ = 200.86 ± 0.1 kJ mol^{-1}.

Using all the values determined at different temperatures, a $\Delta_R G_m{}^{\circ}{}_{,2\text{-}1\text{-}4}$ temperature function according to Eq. 3 was generated (Figure 4; Table 3).

4.1.3 Sorel phase 9-1-4

The 9-1-4 phase ($9Mg(OH)_2 \cdot MgCl_2 \cdot 4H_2O = 2\ Mg_5Cl(OH)_9 \cdot 2H_2O$) occurs above 80°C. Solubility data for the 9-1-4 phase are available at 100°C and 120°C, including IPs with $Mg(OH)_2(s)$ for both temperatures, as well as with the 2-1-4 phase at 120°C. However, unlike the 3-1-8 or 2-1-4 phases, there are no solubility constants available. For an initial estimation of lg $K_{S,9\text{-}1\text{-}4}$ values, the IPs with $Mg(OH)_2(s)$ were used, as the 9-1-4 phase formation according to reaction (5) is in equilibrium with $Mg(OH)_2(s)$ at the same $MgCl_2$ concentration (at 100°C: 4.04 m_{MgCl2} and 120°C: 4.00 m_{MgCl2} (Pannach et al., 2017)). The solubility constants were calculated according to Eq. 6 using the activity coefficients γ_i of Mg^{2+} and Cl^- and the activities for water (a_W), and H^+ ($a_{H+} = m_{H+} \cdot \gamma_{H+}$) calculated by THEREDA for these $MgCl_2$ concentrations at 100°C and 120°C. This results in lg $K_{S,9\text{-}1\text{-}4,100°C} = -58.2$ and lg $K_{S,9\text{-}1\text{-}4,120°C} = -53.9$, which correspond to $\Delta_R G_m{}^{\circ}{}_{,9\text{-}1\text{-}4,100°}$ = 415.5 kJ/mol and $\Delta_R G_m{}^{\circ}{}_{,9\text{-}1\text{-}4,120°}$ = 405.9 kJ/mol according to Eq. 1.

$$5\,Mg^{2+} + Cl^- + 11\,H_2O \rightleftharpoons Mg_5Cl(OH)_9 \cdot 2H_2O_{(s)} + 9\,H^+ \tag{5}$$

$$lgK^{\circ}_{S,9-1-4} = lg\left(\frac{m^9_{H^+}}{m^5_{Mg^{2+}} \cdot m_{Cl^-}} \cdot \frac{\gamma^9_{H^+}}{\gamma^5_{Mg^{2+}} \cdot \gamma_{Cl^-}} \cdot \frac{1}{a^{11}_W}\right). \tag{6}$$

Both “initial values” were adjusted to the position of the IPs of $Mg(OH)_2(s)$ and the 9-1-4 phase in 4.0 molal $MgCl_2$ solution at 100°C and 120°C respectively, and to the IP of 9-1-4 and 2-1-4 phase at 120°C in 5.8 m_{MgCl2} (Pannach et al., 2017). The final Gibbs energies are $\Delta_R G_m{}^{\circ}{}_{,9\text{-}1\text{-}4,100°C}$ = 415.60 kJ mol^{-1} and $\Delta_R G_m{}^{\circ}{}_{,9\text{-}1\text{-}4,120°C}$ = 406.00 kJ mol^{-1}, respectively, and agree well with the previously calculated values. A linear temperature function was generated for the small temperature range of 100°C–120°C (Table 3).

4.1.4 Metastable Sorel phase 5-1-8

The 5-1-8 phase forms from OH^- supersaturated $MgCl_2$ or NaCl-$MgCl_2$ solutions before the stable 3-1-8 phase crystallizes (Pannach et al., 2017; 2023). Within the time window of metastable existence, the lg $K_{S,5\text{-}1\text{-}8}$ according to Eq. 7 could be determined at 25°C from pH_m measurements in the Na-Mg-Cl-OH-H_2O system by Xiong et al. (2010) and in the Mg-Cl-OH-H_2O system in Part I of this work (Pannach et al., 2023). The mean values of both, which agree within the error range (see Table 2), were implemented in the THEREDA model as $\Delta_R G_m{}^{\circ}{}_{,5\text{-}1\text{-}8,25°C}$ calculated according to Eq. 1; (Table 3).

$$3\,Mg^{2+} + Cl^- + 9\,H_2O \rightleftharpoons Mg_3Cl(OH)_5 \cdot 4\,H_2O_{(s)} + 5\,H^+ \tag{7}$$

4.2 Adaptation of the model to reproduce the experimental OH⁻ solution concentrations

As described in Chapter 2, the current model dataset (HMW as well as THEREDA) cannot reproduce the experimentally determined OH^- solution concentrations in the presence of $Mg(OH)_2(s)$ or the Sorel phases (up to the order of 100% deviation) at 25°C, and also not at higher temperatures after implementation of the $\Delta_R G_m{}^{\circ}$ temperature functions of the Sorel phases as observed in initial test calculations. All the calculated OH^- solution concentrations were significantly too low.

However, the calculated H^+ equilibrium concentrations are in excellent agreement with the experimental values, which are available up to 60°C for the Mg-Cl-OH-H_2O system and at 25°C and 40°C for the Na-Mg-Cl-OH-H_2O system, as shown in Figures 8, 9 respectively (see Section 5.1).

4.2.1 Attempts to adjust already existing Pitzer coefficients

To improve the model, attempts were made to adjust Pitzer coefficients that affect the OH^- solution concentrations in $MgCl_2$ and NaCl-$MgCl_2$ solutions. According to the HMW model, THEREDA already contains the binary coefficients $\beta^{(0)}$ and $\beta^{(1)}$ between $MgOH^+$ and Cl^-, and the mixing coefficient ψ, between $MgOH^+$, Mg^{2+}, and Cl^- at 25°C (Table 1). Only these act in the two systems Mg-Cl-OH-H_2O and Na-Mg-Cl-OH-H_2O and are not relevant for the well-described binary $Mg(OH)_2$-H_2O system; also there are no other complex Mg, Cl, and OH-containing systems for which experimental data are available, so adjustments were made. Based on the solubility data in the Mg-Cl-OH-H_2O system at 25°C (Pannach et al., 2017), systematic fit tests were performed. Both $\beta^{(0)}$ alone and with $\beta^{(1)}$, as well as with and without $\psi_{MgOH^+\text{-}Mg^{2+}\text{-}Cl^-}$ (and also ψ alone), were fitted. Furthermore, the parameters $C^{\phi}{}_{MgOH^+\text{-}Cl^-}$ and $\psi_{MgOH^+\text{-}OH^-\text{-}Cl^-}$ not included in the dataset were also tested. However, no results could be obtained that sufficiently described the analyzed total OH^- concentrations. When fitting the data at higher temperatures (available up to 120°C for the Mg-Cl-OH-H_2O system), the deviation was even greater than at 25°C.

4.2.2 Further complex Mg-OH solution species

Since the modeling of OH^- concentrations is not improved by Pitzer coefficients, it is assumed that, besides $MgOH^+$, further Mg-OH species that influence OH^- concentration must exist in the solution.

As known from other aqueous metal oxide or hydroxide salt systems, such as Be, Cu, Ni, and Zn (Feitknecht and Schindler, 1963; Mesmer and Baes, 1990; Plyasunova et al., 1997; 1998; Zhang and Muhammed, 2001), the existence of complex Mg-OH species containing more than one cation $Mg_x(OH)_y{}^{(2x\text{-}y)+}$ has been already discussed (D’Ans and Katz, 1941; Ved et al., 1976; Mesmer and Baes, 1990). Stability constants (Lewis, 1963; Einaga, 1977) alongside $MgOH^+$ (McGee and Hostetler, 1977; Palmer and Wesolowski, 1997) have also been proposed. Einaga (1977) derives the species $Mg_2(OH)_2{}^{2+}$ and $Mg_3(OH)_4{}^{2+}$ from emf measurements in nitrate solutions at 25°C with the stability constants log $\beta = -22.0$ and log $\beta = -39.0$, respectively. However, the determination of complex Mg-OH solution species lacks sufficient resolution to precisely determine the formulas, especially when more than one species coexists over a range of solution compositions. As Mg^{2+} is exclusively octahedrally coordinated by OH^- (partly together with OH_2) in these solids ($Mg(OH)_2$, Sorel phases 3-1-8, 5-1-8, and 9-1-4 (De Wolf and Walter-Lévy, 1953; Sugimoto et al., 2007; Dinnebier et al., 2010)),

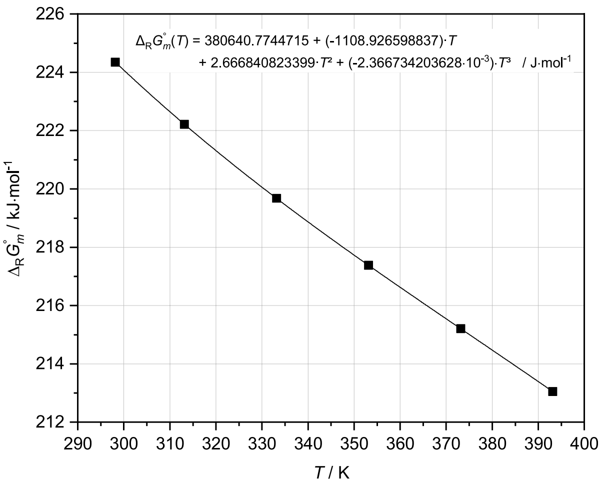

FIGURE 5
$\Delta_R G_m^\circ$ values for the solution species $Mg_3(OH)_4^{2+}$ derived from adjustments to the solubility data available at different temperatures in the Mg-Cl-OH-H_2O system, with the temperature function (black curve) fitted to these values (see also Table 3).

multiple OH^- coordinated Mg ions, in addition to $MgOH^+$ = $[Mg(H_2O)_5OH]^+$, could be expected to exist in appropriate equilibrium solutions.

Therefore, additional species were postulated based on the following considerations. In contrast to the solid structures with up to six OH^- ions in the octahedral coordination sphere of Mg^{2+}, the OH^- concentration in the equilibrium solution is relatively very low compared to the Mg^{2+} (and Cl^-) concentration. Thus, besides $MgOH^+$, additional solution-Mg^{2+} should be only slightly more highly coordinated with OH^-. Hence, species with a systematically increasing ratio of OH^- to Mg^{2+} up to a maximum of two were taken into account—$Mg_3(OH)_4^{2+}$ (ratio = 1.33), $Mg_2(OH)_3^+$ (ratio = 1.5), and $Mg(OH)_2^{\pm 0}$ (ratio = 2)—and were tested for their effect. Estimated $\Delta_R G_m^\circ$ values were used, in orientation to the value of $MgOH^+$ and the stability constant for $Mg_3(OH)_4^{2+}$ given by Einaga (1977), to first see the general effects. $Mg_2(OH)_2^{2+}$ was not taken into account because the Mg:OH ratio is the same as in $MgOH^+$ (tests have shown that the different charge does not have an effect). Calculations with the current THEREDA model show that $MgOH^+$ determines the total OH^- concentration, so the fraction of free OH^- is negligible. Fitting studies with the additional three postulated species were performed both singularly and in combinations.

Finally, the fitting tests to the 25°C isotherm in the Mg-Cl-OH-H_2O system (Pannach et al., 2017) showed that the total OH^- concentrations can be reproduced when including additional Mg-OH species. It was found that the species $Mg_3(OH)_4^{2+}$ alone was sufficient. The other species, alone or in combination, worsened the agreement with experimental results. Therefore, the final fits to all isotherms in the system Mg-Cl-OH-H_2O were performed with $Mg_3(OH)_4^{2+}$ additionally in the THEREDA dataset, turning off all ion interactions for $MgOH^+$ (see Table 1). $\Delta_R G_{m}^\circ{}_{,Mg_3(OH)_4^{2+}}$ (according to the formation reaction: $3Mg^{2+} + 4H_2O \leftrightarrow Mg_3(OH)_4^{2+} + 4H^+$) was adjusted so that the isothermal branch of $Mg(OH)_2(s)$ up to the invariant point with the 3-1-8 phase will be reproduced in agreement with the experimental data. With increasing $MgCl_2$ concentration, the total OH^- concentration in the presence of the 3-1-8 phase is calculated to be increasingly too high until $MgCl_2$ saturation is reached. This overestimation was subsequently adjusted with the final Pitzer coefficients (Section 4.2.3). The resulting values of $\Delta_R G_m^\circ{}_{, Mg_3(OH)_4^{2+}}$ for each temperature are shown in Figure 5, together with the fitted temperature function (Table 3).

4.2.3 Final Pitzer coefficients

To remove the over-calculated total OH^- concentrations following the IP of $Mg(OH)_2(s)$ and the 3-1-8 phase caused by the implementation of $Mg_3(OH)_4^{2+}$, ion interactions for that species were introduced. Fitting tests were carried out with binary as well as mixing Pitzer coefficients. Finally, the mixing parameter $\psi_{\text{Mg-Mg}_3(\text{OH})_4\text{-Cl}}$ was

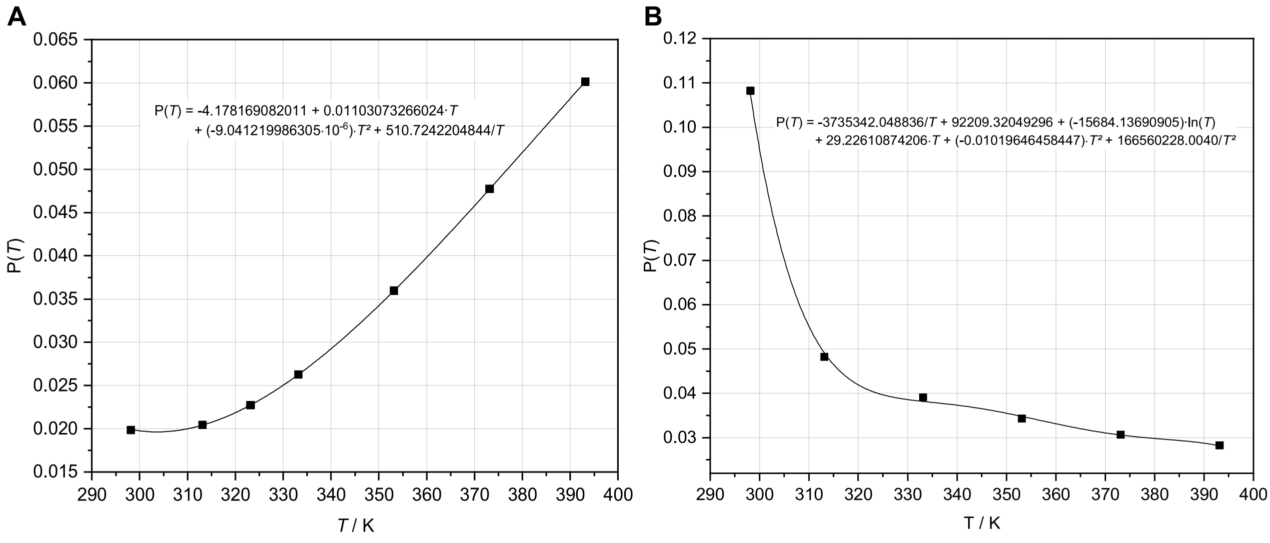

FIGURE 6
Pitzer coefficients $\psi_{\text{Mg-MgOH-Cl}}$ **(A)** and $\psi_{\text{Mg-Mg3(OH)4-Cl}}$ **(B)** resulting from fits to the isotherms in the Mg-Cl-OH-H_2O system (Pannach et al., 2017) and fitted temperature functions (Eq. 8).

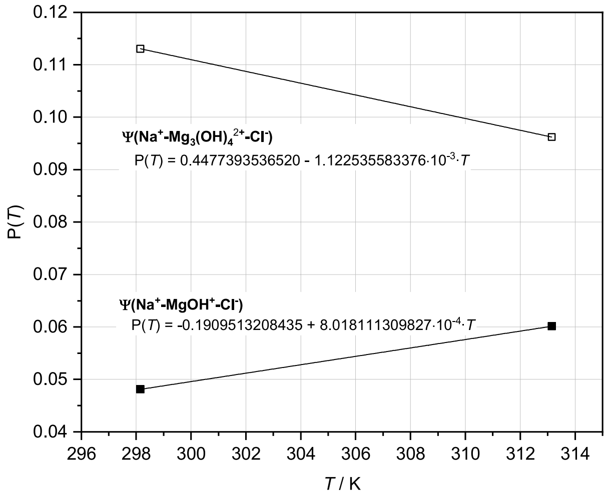

FIGURE 7
Pitzer coefficients $\psi_{\text{Na-MgOH-Cl}}$ and $\psi_{\text{Na-Mg3(OH)4-Cl}}$ resulting from adjustments to both the isotherms in the Na-Mg-Cl-OH-H_2O system (Part I = Pannach et al., 2023) and fitted temperature functions (Eq. 7).

adjusted together with $\psi_{\text{Mg-MgOH-Cl}}$. The binary coefficients $\beta^{(0)}$ and $\beta^{(1)}$ between $MgOH^+$ and Cl^- previously included beside the mixing $\psi_{\text{Mg-MgOH-Cl}}$ proved unnecessary; they were removed from the dataset. The parameterization was again performed separately on each isotherm. The obtained values for $\psi_{\text{Mg-Mg}_3\text{(OH)}_4\text{-Cl}}$ and $\psi_{\text{Mg-MgOH-Cl}}$ are shown in Figures 6A, B. The THEREDA conformal temperature function (Eq. 8) was fitted to the systematic variation of the parameters with T obtained from the isothermal fits (Figure 6).

$$P = \frac{a}{T} + b + c \cdot \ln(T) + d \cdot T + e \cdot T^2 + \frac{f}{T^2}. \tag{8}$$

Due to the polynomial type of the function (Eq. 8), the course for $\psi_{\text{Mg-Mg3(OH)4-Cl}}$ with the strong decrease from the 25°C value to the only slightly decreasing values up to 120°C can only be adjusted with turning points (Figure 6B). However, this does not show any noticeable effects on the model results within the experimental data trend and reproduction (Section 4.2).

For the modeling of the two solubility isotherms in the system Na-Mg-Cl-OH-H_2O at 25°C and 40°C, the implementation and adjustment of the mixing parameters $\psi_{\text{Na-MgOH-Cl}}$ and $\psi_{\text{Na-Mg}_3\text{(OH)}_4\text{-Cl}}$ were still necessary. The fitted values with linear progression over the two temperatures are shown in Figure 7.

All Pitzer coefficients with their temperature functions are listed in Table 4.

5 Calculation results with the extended THEREDA model

5.1 Modeling of H^+ equilibrium concentrations

With the addition of the $\Delta_R G_m^\circ$ temperature functions for the Sorel phases 3-1-8, 2-1-4, and 9-1-4 and for the metastable 5-1-8 phase at 25°C to the THEREDA dataset, the H^+ equilibrium concentrations can be calculated in good agreement with the experimental data. Figure 8 shows the comparison for the Mg-Cl-OH-H_2O system and Figure 9 for the Na-Mg-Cl-OH-H_2O system at NaCl saturation. Calculation results between and just outside the temperatures of the experimental data are still included, showing that the model reliably calculates the occurring solids depending on $MgCl_2$ solution concentration and the $pH_m = -\lg m(H^+)$, evolving in their presence over the entire and somewhat extended temperature field.

5.2 Modeling of OH^- equilibrium concentrations

The implementation of a second Mg-OH solution species, $Mg_3(OH)_4^{2+}$, was the key to the accurate calculation of the OH^- solution concentrations in equilibrium with $Mg(OH)_2(s)$ or the Sorel phases. Still requiring mixing Pitzer coefficients, $\psi_{\text{Mg-Mg3(OH)4-Cl}}$ and $\psi_{\text{Na-Mg3(OH)4-Cl}}$, were introduced and fitted together with $\psi_{\text{Mg-MgOH-Cl}}$ or $\psi_{\text{Na-MgOH-Cl}}$ for final adjustment to the solubility isotherms in the Mg-Cl-OH-H_2O (Nakayama, 1959; Nakayama, 1960; Pannach et al., 2017) and Na-Mg-Cl-OH-H_2O systems (Part I of this work—Pannach et al., 2023), respectively.

Finally, the solubilities can be calculated in agreement with all experimental data. As Figure 10A shows for the Mg-Cl-OH-H_2O system at 25°C, the total OH^- concentration is mainly a result of the $MgOH^+$ solution species over the entire concentration range but in addition from lesser proportions of $Mg_3(OH)_4^{2+}$ with the highest contribution at the $MgCl_2$ concentration of the IP $Mg(OH)_2(s)$ and 3-1-8 phase. This now leads to a correct representation of the total OH^- concentration. With increasing temperature, $Mg_3(OH)_4^{2+}$ becomes increasingly predominant over $MgOH^+$, as shown in Figure 10B for the 60°C isotherms as an example in comparison to 25°C (Figure 10A). The contribution of free OH^- in the order of 10^{-9} molal at 60°C (10^{-5} molal at 25°C) is insignificant: its proportion is unaffected by the implementation of the second Mg-OH species since it is calculated together with H^+ from Kw (Eq. 9), which is already included in the model (Figure 11 shows Kw, H^+, and OH^- as a function of the $MgCl_2$ solution concentration according to the HMW and THEREDA model at 25°C). This also justifies the already-correct calculation of the H^+ solution concentrations in the presence of $Mg(OH)_2(s)$ or the Sorel phases with the previous model; it also confirms that the earlier poor model description of the total OH^- solution concentrations is due to missing further Mg-OH speciation.

$$K_W^0 = \frac{[H^+] \cdot [OH^-] \cdot \gamma_\pm^2}{a_W} = \frac{K_W \cdot \gamma_\pm^2}{a_W}. \tag{9}$$

The calculation results for the Mg-Cl-OH-H_2O system compared to all reliable experimental datasets are shown in Figure 12. Within their experimental scatter range, the calculated $Mg(OH)_2(s)$ isotherms overlie each other, with ranges extending toward higher $MgCl_2$ concentrations up to the positions of the IPs with the Sorel phases. The subsequent isotherms for the 3-1-8 phase (stable phase up to 80°C) or the 9-1-4 phase (from 100 °C) effectively describe the course of the experimental values. For the 9-1-4 phase, the IPs with brucite and the isotherms at 100°C and 120°C are

TABLE 4 Temperature coefficients of Pitzer parameters for the title system Na-Mg-Cl-OH-H_2O and subsystem in THEREDA. The new data from this work are highlighted in bold.

$P(T) = a/T + b + c\cdot\ln(T) + d\cdot T + e\cdot T^2 + f/T^2$								
			a	b	c	d	e	f
H^+	Cl^-	Beta (0)	9901.2219784713	−285.6473091587	50.067215202357	−0.10902829201997	4.2832131817909E-5	−351026.15442901
		Beta (1)	189788.67075591	−4588.8079271153	776.48444741115	−1.3963936941488	4.6718218052799E-4	−8599260.9958506
		Cphi	0	0	0	0	0	0
Na^+	Cl^-	Beta (0)	9931.0954	−223.8321	37.468729	−0.063524	2.0008E-5	−508663.3
		Beta (1)	27034.783	−611.8806	102.2781	−0.171355	5.4624E-5	−1335514
		Cphi	−4635.055	107.86756	−18.11616	0.0311444	−9.9052E-6	221646.78
Mg^{2+}	Cl^-	Beta (0)	−9.5949075987732	0.52058075085694	0	−4.5632571158819E-4	0	0
		Beta (1)	1239.2880942931	−7.3631696542185	0	0.016394622815563	0	0
		Cphi	12.528229322268	−0.045346523422936	0	2.8564736424319E-5	0	0
Na^+	OH^-	beta (0)	−98.888405195742	0.74845113296049	0	−0.0010478515797703	0	0
		Beta (1)	−206.11199903783	1.2022295299777	0	−0.0012958058812917	0	0
		Cphi	17.300056299236	−0.091131605628721	0	1.1826675205965E-4	0	0
Na^+	H^+	Theta	−4.0542575885501	0.048135767274039	0	0	0	0
Na^+	Mg^{2+}	Theta	0	−0.063343456551807	0	4.4723332094534E-4	0	0
Mg^{2+}	H^+	Theta	0	0.51653862168501	0	−0.0031309680558061	5.8285013290036E-6	0
OH^-	Cl^-	Theta	−49.361345504841	0.11048570304889	0	0	0	0
psi								
Na^+	Cl^-	OH^-	0	−3.61342282638764	0.828412891695231	−0.00473162879186962	3.37394750135306E-6	0
Na^+	Mg^{2+}	Cl^-	0	−2.67633662036202	0.618873156654038	−0.00367854306693126	2.64366820374045E-6	0
Na^+	H^+	Cl^-	3.59304603523964	−0.0145621583979794	0	0	0	0
Mg^{2+}	H^+	Cl^-	−1357.291354862	61.244574321968	−11.309231470323	0.029270572012749	−1.1173505755006E-5	−33.683663900415
Na^+	**$MgOH^+$**	**Cl^-**	**0**	**−0.1909513208435**	**0**	**0.008018111309827**	**0**	**0**
Na^+	**$Mg_3(OH)_4^{2+}$**	**Cl^-**	**0**	**0.4477393536520**	**0**	**−0.001122535583376**	**0**	**0**
Mg^{2+}	**$MgOH^+$**	**Cl^-**	**510.7242204844**	**−4.178169082011**	**0**	**0.01103073266024**	**−9.041219986305E-6**	**0**
Mg^{2+}	**$Mg_3(OH)_4^{2+}$**	**Cl^-**	**−3735342.048836**	**92209.32049296**	**−15684.13690905**	**29.22610874206**	**−0.01019646458447**	**166560228.0040**

alpha (1) = 2 and alpha (2) = 0 for all binary ion interactions.

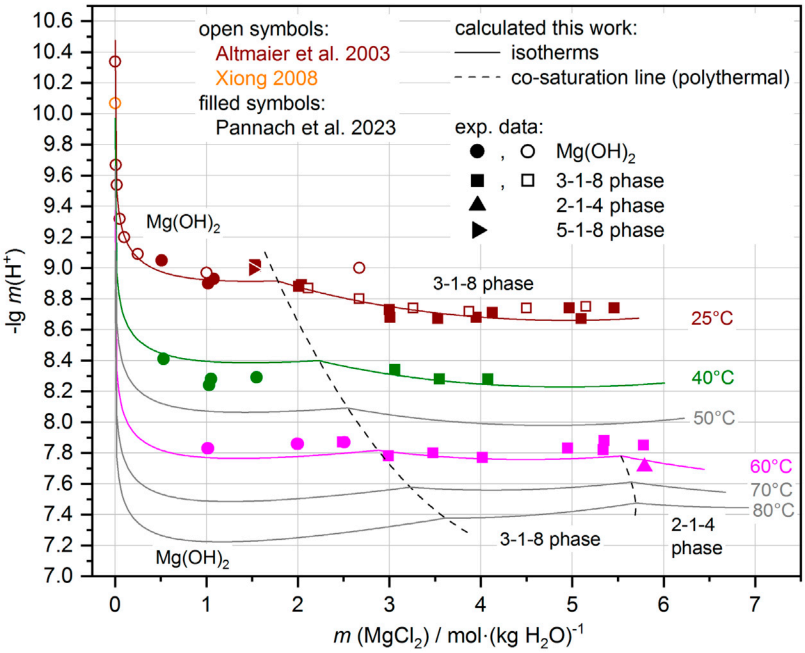

FIGURE 8
Comparison of experimental and calculated pH$_m$ = -lg *m* (H$^+$) in the Mg-Cl-OH-H$_2$O system. Experimental data available at 25°C, 40°C, and 60°C (see also Pannach et al., 2023). Away from these temperatures, the model shows systematic trends (gray lines calculations at 50°C, 70°C, and 80°C, and the dashed co-saturation lines of the Mg(OH)$_2$(s) and 3-1-8 phase, and the 3-1-8 and 2-1-4 phases respectively) that follow the experimental data.

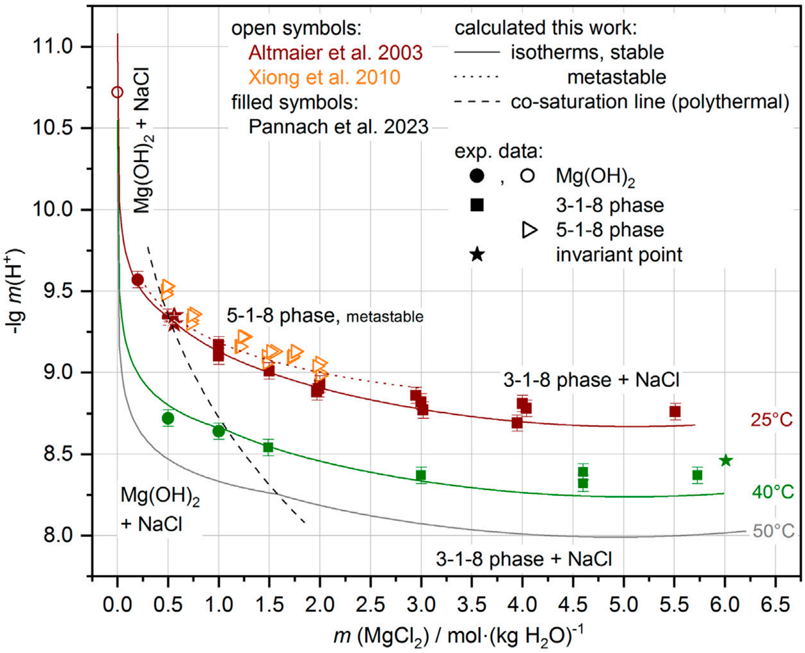

FIGURE 9
Comparison of experimental and calculated pH$_m$ in almost NaCl-saturated MgCl$_2$ solutions (system Na-Mg-Cl-OH-H$_2$O). Experimental data available at 25°C and 40°C (see also Pannach et al., 2023). Away from these temperatures, the model shows systematic trends (gray lines for 50 C and dashed co-saturation line of Mg(OH)$_2$(s) and 3-1-8 phase) that follow the experimental data.

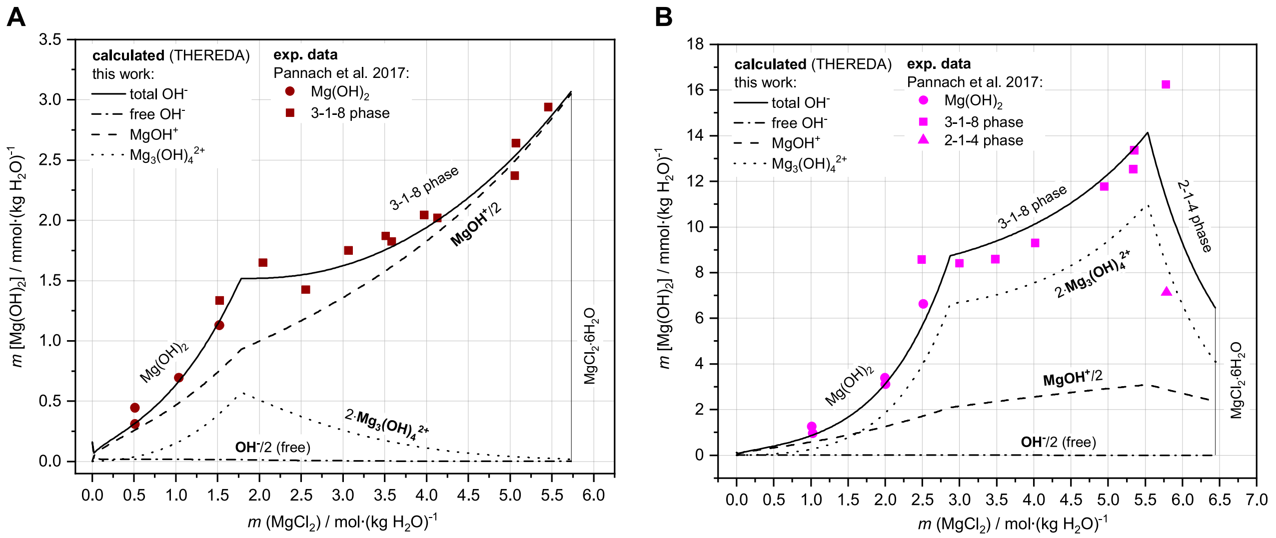

FIGURE 10
Comparison of experimental and calculated (with OH-species distribution) solubility data of $Mg(OH)_2$(s) and 3-1-8 phase in the Mg-Cl-OH-H_2O system at 25°C **(A)** and 60°C **(B)**.

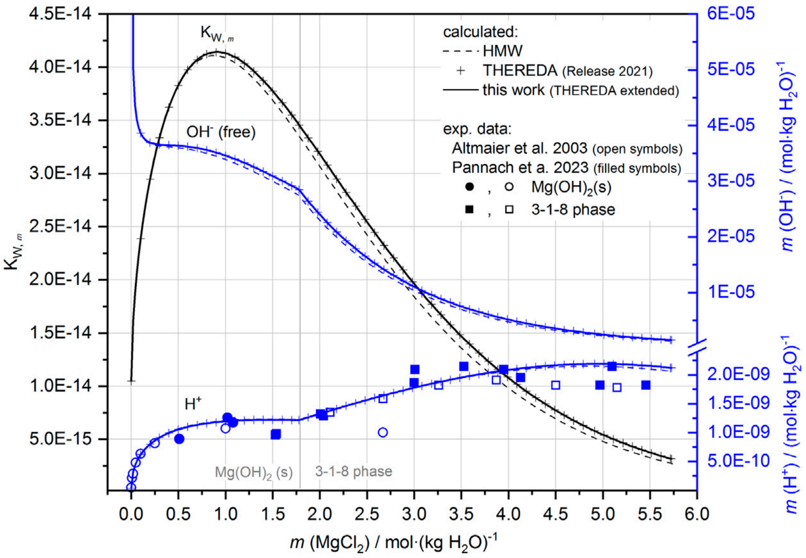

FIGURE 11
$K_{W,m}$, H^+ (comparison with experimental data, cf. Figure 8) and OH^- as a function of the $MgCl_2$ solution concentration (system Mg-Cl-OH-H_2O) according to the HMW and THEREDA models at 25°C.

calculated nearly exactly in line with the experimental data. The calculated isotherm for the metastable 3-1-8 phase at 100°C is slightly below the experimental values but on trend; it is above the 9-1-4 phase 100°C isotherm.

The 2-1-4 phase, occurring above 60°C at high $MgCl_2$ concentrations with its strongly decreasing solubility behavior up to the $MgCl_2$ saturation concentrations, is calculated in conformity with the experimental (more scattering) values. The calculated isotherm, especially at 100°C, is shifted to slightly higher values compared with the trend of the experimental dataset. When using the isothermally determined $\Delta_R G_m^\circ$ value of the 2-1-4 phase (see Section 4.1.2), a somewhat better agreement with the experimental data would result. However, since the temperature function does not reproduce the individually determined $\Delta_R G_m^\circ$ value to 100% ($\Delta_R G_{m}^\circ{}_{,2\text{-}1\text{-}4,100^\circ C}$ = 205.6 kJ mol^{-1} is calculated by the temperature function with 205.8 kJ mol^{-1}), the model result via temperature function deviates somewhat. Furthermore, with increasing temperature and $MgCl_2$ concentration, the possible existence of further Mg-OH solution species must be assumed, also affecting solubility. However, without experimental evidence and data, the

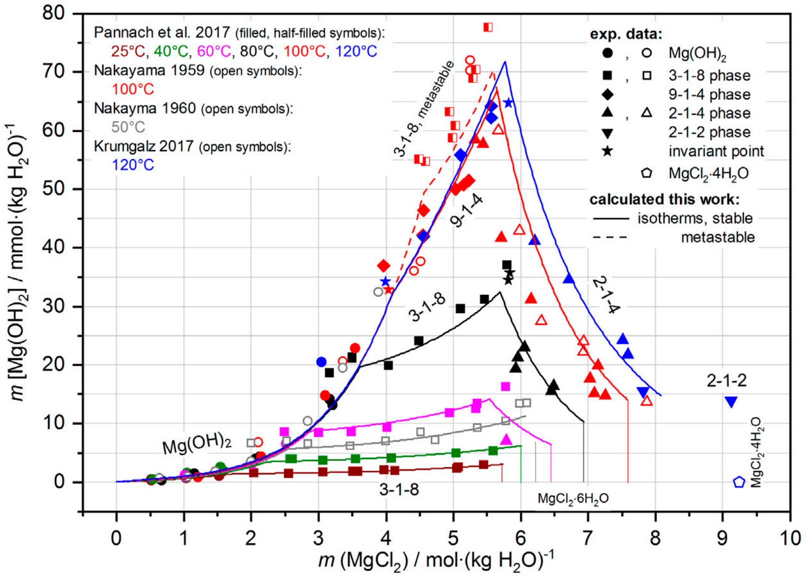

FIGURE 12
Solubility data of the Mg-Cl-OH-H_2O system from 25°C to 120°C; comparison of the experimental data with the calculated isotherms.

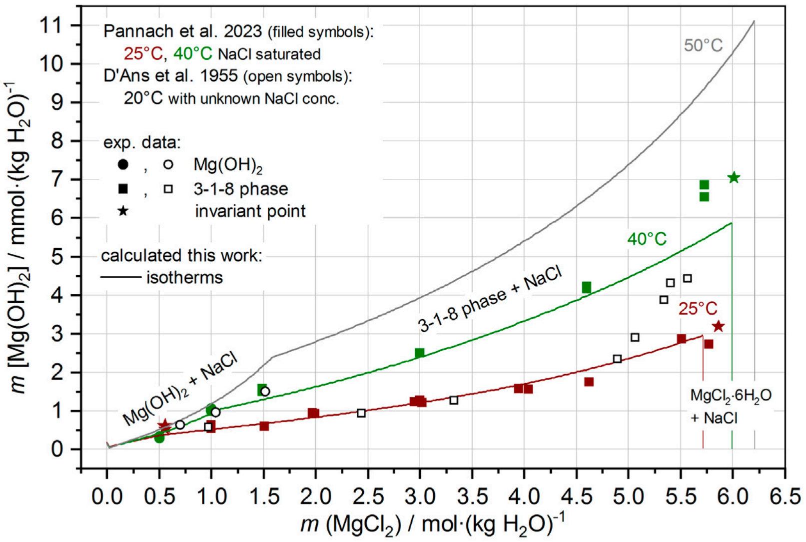

FIGURE 13
Solubility data of the Na-Mg-Cl-OH-H_2O system with NaCl saturation at 20°C–50°C; comparison of the experimental data with the calculated isotherms.

model cannot be further modified. With the present model (THEREDA extended), the solubility behavior of $Mg(OH)_2$(s) and the Sorel phases can be described quite well up to 120°C. This is also true in the presence of NaCl saturation in the Na-Mg-Cl-OH-H_2O system, as shown by the comparison of the experimental datasets at 25°C and 40°C and the calculated isotherms in Figure 13. The additional calculated isotherms for 50°C indicate a reasonable trend with the IP of the $Mg(OH)_2$(s) and 3-1-8 phase in an approximately 1.6 molal solution of $MgCl_2$ (at 25°C and 40°C in 0.5 and ca. 1 molal solution, respectively).

The 2-1-2 phase, with only two solubility data points at 120°C in the Mg-Cl-OH-H_2O system (Figure 12), was not included in the model.

6 Summary

With this work, the Pitzer model dataset of THEREDA was extended and adjusted for the calculation of the solubility equilibria of the Sorel phases and of $Mg(OH)_2$(s) in salt solutions of the system Na-Mg-Cl-OH-H_2O.

Previously, calculations were possible only with strong deviations from the now available experimental OH^- solution concentrations of the 25°C isotherms of $Mg(OH)_2(s)$ as well as the Sorel phase 3-1-8, although the H^+ concentrations could be calculated in agreement. The Pitzer dataset, corresponding to the HMW model and implemented in THEREDA, was valid only for 25°C; due to the lack of experimental data, no sufficient adjustments were possible.

With the data now available for the Mg-Cl-OH-H_2O system up to 120°C and in NaCl-saturated solutions (Na-Mg-Cl-OH-H_2O system) at 25°C and 40°C within Part I of this work, a new adjustment of the model and polytherm was possible. In addition to the implementation of the solubility constants for the Sorel phases as temperature functions of molal standard Gibbs energies of formation, a model extension for the OH^- solution speciation (the implementation of $Mg_3(OH)_4^{2+}$ in addition to $MgOH^+$ and OH^-) was necessary to reproduce the experimentally determined OH^- solution concentrations. Thus, the solubility equilibria of the Sorel phases and $Mg(OH)_2(s)$ can now be calculated in agreement with the experimental data.

THEREDA now provides a reliable database for the long-term safety assessment of geotechnical barriers made of Sorel cement/concrete for a repository in host rock salt. It also allows the calculation of the evolving pH_m values (caused by the pH buffer material MgO which reacts to Sorel phases or $Mg(OH)_2$ in the presence of salt solutions), which is particularly important for predictions regarding the retention capacity of radionuclides in the near field of a repository.

Data availability statement

The raw data supporting the conclusion of this article will be made available by the authors, without undue reservation.

Author contributions

DF: procedure for the extension of the Pitzer model dataset and writer of the paper. MP: calculation tests, adjustments, preparation of figures and tables, and co-writer. WV: Pitzer model expert, discussions and contributions to dataset development, and co-writer. All authors contributed to the article and approved the submitted version.

Funding

This research was supported by the Open Access Funding by the Publication Fund of the TU Bergakademie Freiberg.

Conflict of interest

The authors declare that the research was conducted in the absence of any commercial or financial relationships that could be construed as a potential conflict of interest.

Publisher's note

References

Altmaier, M., Metz, V., Neck, V., Müller, R., and Fanghänel, T. (2003). Solid-liquid equilibria of $Mg(OH)_2(cr)$ and $Mg_2(OH)_3Cl·4H_2O(cr)$ in the system Mg-Na-H-OH-Cl-H_2O at 25°C. *Geochim. Cosmochim. Acta* 67 (19), 3595–3601. doi:10.1016/s0016-7037(03)00165-0

D'Ans, J., Busse, W., and Freund, H. E. (1955). Basic magnesium chloride. *Kali Steinsalz* 8, 3–7.

D'Ans, J., and Katz, W. (1941). The solubility of magnesium hydroxide, the pH value and buffering in the system H2O-MgCl2-Mg(OH)2. *Kali Steinsalz* 35, 37–41.

De Wolf, P. M., and Walter-Lévy, L. (1953). The crystal structure of $Mg_2(OH)_3(Cl, Br)·4H_2O$. *Acta Cryst.* 6, 40–44. doi:10.1107/s0365110x53000089

Dinnebier, R. E., Freyer, D., Bette, S., and Oestreich, M. (2010). $9Mg(OH)_2·MgCl_2·4H_2O$, a high temperature phase of the magnesia binder system. *Inorg. Chem.* 49, 9770–9776. doi:10.1021/ic1004566

Einaga, H. (1977). Hydrolysis of magnesium(II) in 1.0 mol dm^{-3} aqueous $(Na,H)NO_2$ solution. *J. Chem. Soc. Dalton Trans. Inorg. Chem.* 9, 912–914. doi:10.1039/DT9770000912

Eriksson, G., and Hack, K. (1990). ChemSage - a computer program for the calculation of complex chemical equilibria. *Metall. Trans.* B21 (6), 1013–1023. doi:10.1007/bf02670272

Eriksson, G., Hack, K., and Petersen, S. (1997). "ChemApp - a programable thermodynamic calculation interface," in Werstoffwoche '96, Symposium 8: Simulation, Modellierung, Informationssysteme (Deutschland: DGM Informationsgesellschaft mbH).

Feitknecht, W., and Schindler, P. (1963). Solubility constants of metal oxides, metal hydroxides, and metal hydroxide salts in aqueous solution. *Pure Appl. Chem.* 6, 125–206. doi:10.1351/pac196306020125

Harvie, C. E., Møller, N., and Weare, J. H. (1984). The prediction of mineral solubilities in natural waters: na-K-Mg-Ca-H-Cl-SO_4-OH-HCO_3-CO_3-CO_2-H_2O system to high ionic strengths at 25°C. *Geochim. Cosmochim. Acta* 48, 723–751. doi:10.1016/0016-7037(84)90098-x

Krumgalz, B. S. (2017). Temperature dependence of mineral solubility in water. Part I. Alkaline and alkaline earth chlorides. *J. Phys. Chem. Ref. Data* 46 (4). AIP Publishing. doi:10.1063/1.5006028

Lambert, I., and Clever, H. L. (1992). "Alkaline earth hydroxides in water and aqueous solutions," in *IUPAC solubility data series* (Oxford, UK: Pergamon Press), 52.

Lewis, D., Lund, A., Vänngård, T., Håkansson, R., and Munch-Petersen, J. (1963). Studies on the hydrolysis of metal ions. 45. The hydrolysis of magnesium in chloride self-medium. *Acta Chem. Scand.* 17 (7), 1891–1901. doi:10.3891/acta.chem.scand.17-1891

McGee, K. A., and Hostetler, P. B. (1977). Activity-product constants of brucite from 10° to 90°C. *J. Res. U.S. Geol. Surv.* 5 (2), 227–233.

Mesmer, R. E., and Baes, C. F. (1990). Review of hydrolysis behavior of ions in aqueous solutions. *Mat. Res. Soc. Symp. Proc.* 180, 85–96. doi:10.1557/proc-180-85

Nakayama, M. (1959). A new basic triple salt containing magnesium hydroxide Part II. The quaternary system KCl-$MgCl_2$-$Mg(OH)_2$-H_2O at 100°. *Bull. Agr. Chem. Soc. Jpn.* 23(1), 46–48. doi:10.1080/03758397.1959.10857524

Nakayama, M. (1960). A new basic triple salt containing magnesium hydroxide Part IV. The quinary system KCl-K_2SO_4-$MgCl_2$-$MgSO_4$-$Mg(OH)_2$-H_2O at 50°. *Bull. Agr. Chem. Soc. Jpn.* 24(4), 362–371. doi:10.1080/03758397.1960.10857688

Palmer, D. A., and Wesolowski, D. J. (1997). Potentiometric measurements of the first hydrolysis quotient of magnesium(II) to 250°C and 5 molal ionic strength (NaCl). *J. Solut. Chem.* 26 (2), 217–232. doi:10.1007/bf02767923

Pannach, M., Bette, S., and Freyer, D. (2017). Solubility equilibria in the system $Mg(OH)_2$-$MgCl_2$-H_2O from 298 to 393 K. *J. Chem. Eng. Data* 62 (4), 1384–1396. doi:10.1021/acs.jced.6b00928

Pannach, M., Paschke, I., Metz, V., Altmaier, M., Voigt, W., and Freyer, D. (2023). Solid-liquid equilibria of Sorel phases and $Mg(OH)_2$ in the system Na-Mg-Cl-OH-H_2O. Part I: experimental determination of OH^- and H^+ equilibrium concentrations and solubility constants at 25°C, 40°C and 60°C. *Front. Nuc. Eng.* 2. doi:10.3389/fnuen.2023.1188789

Pitzer, K. S. (1991). *Activity coefficients in electrolyte solutions*. 2. Edition. Boca Raton: CRC Press.

Plyasunova, N. V., Wang, M., Zhang, Y., and Muhammed, M. (1997). Critical evaluation of thermodynamics of complex formation of metal ions in aqueous solutions II. Hydrolysis and hydroxo-complexes of Cu^{2+} at 298.15 K. *Hydrometallurgy* 45 (1-2), 37–51. doi:10.1016/s0304-386x(96)00073-4

Plyasunova, N. V., Zhang, Y., and Muhammed, M. (1998). Critical evaluation of thermodynamics of complex formation of metal ions in aqueous solutions. IV. Hydrolysis and hydroxo-complexes of Ni^{2+} at 298.15 K. *Hydrometallurgy* 48 (1), 43–63. doi:10.1016/s0304-386x(97)00070-4

Robinson, W. O., and Waggaman, W. H. (1909). Basic magnesium chlorides. *J. Phys. Chem.* 13, 673–678. doi:10.1021/j150108a002

Sugimoto, K., Dinnebier, R. E., and Schlecht, T. (2007). Structure determination of $Mg_3(OH)_5Cl{\cdot}4H_2O$ (F5 phase) from laboratory powder diffraction data and its impact on the analysis of problematic magnesia floors. Acta Cryst. *B* 63, 805–811. doi:10.1107/S0108768107046654

THEREDA (2021). *Thermodynamic reference database*. Release (2021). Available at: www.thereda.de.

Travers, A. (1929). The solubility of magnesium hydroxide at elevated temperatures. *C. R. Acad. Sci.* 188, 499–501.

Ved, E. I., Zharov, E. F., and Hoang, V. P. (1976). Mechanism of magnesium oxychloride formation during the hardening of magnesia cements. *Zh. Prikl. Khim.* 49, 2154–2158.

Voigt, W., Brendler, V., Marsh, K., Rarey, R., Wanner, H., Gaune-Escard, M., et al. (2007). Quality assurance in thermodynamic databases for performance assessment studies in waste disposal. *Pure Appl. Chem.* 79 (5), 883–894. doi:10.1351/pac200779050883

Xiong, Y., Deng, H., Nemer, M., and Johnsen, S. (2010). Experimental determination of the solubility constant for magnesium chloride hydroxide hydrate ($Mg_3Cl(OH)_5{\cdot}4H_2O$, phase 5) at room temperature, and its importance to nuclear waste isolation in geological repositories in salt formations. *Geochim. Cosmochim. Acta* 74, 4605–4611. doi:10.1016/j.gca.2010.05.029

Xiong, Y. (2008). Thermodynamic properties of brucite determined by solubility studies and their significance to nuclear waste isolation. *Aquat. Geochem.* 14 (3), 223–238. doi:10.1007/s10498-008-9034-3

Zhang, Y., and Muhammed, M. (2001). Critical evaluation of thermodynamics of complex formation of metal ions in aqueous solutions VI. Hydrolysis and hydroxo-complexes of Zn^{2+} at 298.15 K. *Hydrometallurgy* 60 (3), 215–236. doi:10.1016/s0304-386x(01)00148-7

frontiers | Frontiers in Nuclear Engineering

TYPE Original Research
PUBLISHED 17 October 2023
DOI 10.3389/fnuen.2023.1192463

EDITED BY
Johan Andersson,
JABIA AB, Sweden

REVIEWED BY
Vladimir Petrov,
Lomonosov Moscow State University, Russia
Andrey G. Kalinichev,
IMT Atlantique Bretagne-Pays de la Loire, France

*CORRESPONDENCE
Nese Çevirim-Papaioannou,
✉ nese.cevirim@kit.edu
Xavier Gaona,
✉ xavier.gaona@kit.edu

RECEIVED 23 March 2023
ACCEPTED 26 September 2023
PUBLISHED 17 October 2023

CITATION
Çevirim-Papaioannou N, Androniuk I, Miron GD, Altmaier M and Gaona X (2023), Beryllium solubility and hydrolysis in dilute to concentrated $CaCl_2$ solutions: thermodynamic description in cementitious systems.
Front. Nucl. Eng. 2:1192463.
doi: 10.3389/fnuen.2023.1192463

Beryllium solubility and hydrolysis in dilute to concentrated $CaCl_2$ solutions: thermodynamic description in cementitious systems

Nese Çevirim-Papaioannou[1]*, Iuliia Androniuk[1], George Dan Miron[2], Marcus Altmaier[1] and Xavier Gaona[1]*

[1]Institute for Nuclear Waste Disposal, Karlsruhe Institute of Technology, Karlsruhe, Germany, [2]Laboratory for Waste Management, Paul Scherrer Institute, Villigen PSI, Switzerland

The solubility and hydrolysis of Be(II) was investigated from undersaturation conditions in alkaline, dilute to concentrated $CaCl_2$ solutions (0.05–3.5 M). Experiments were performed with α-$Be(OH)_2$(cr) under Ar atmosphere at T = (22 ± 2)°C. Aqueous Be speciation was further investigated by means of molecular dynamics (MD) calculations. For the most diluted $CaCl_2$ systems (0.05 and 0.25 M), a solubility minimum is observed at $pH_m \approx 9.5$ {with $[Be(II)] \approx 10^{-7}$ M}, consistent with solubility data previously reported in NaCl and KCl solutions. Above this pH_m, and at higher $CaCl_2$ concentrations, a steep increase in the solubility with a slope of ~ +2 is observed, hinting towards the predominance of the moiety $[Be(OH)_4{}^{2-}]$ in the aqueous phase. In NaCl and KCl systems, this hydrolysis species prevails only above pH_m ~ 13, thus supporting the formation of ternary complex/es Ca–Be(II)–OH(aq) in $CaCl_2$ solutions. The analysis of solubility data in combination with MD calculations underpin the key role of the complex $Ca_2[Be(OH)_4]^{2+}$ in alkaline to hyperalkaline systems containing Ca. In combination with our previous work in NaCl–NaOH and KCl–KOH systems, complete chemical, thermodynamic and (SIT) activity models are derived for the first time for the system $Be^{2+}-Ca^{2+}-Na^{+}-K^{+}-H^{+}-Cl^{-}-OH^{-}-H_2O(l)$. This model provides an accurate and robust tool for the evaluation of Be(II) solubility and speciation in a diversity of geochemical conditions, including source term calculations of beryllium in the context of repositories for nuclear waste disposal with a high cement inventory.

KEYWORDS

beryllium, calcium, solubility, hydrolysis, thermodynamics, SIT, cement

1 Introduction

Beryllium is a widely used metal in test and research fission reactors as neutron reflector/moderator. It is characterized by a relatively low thermal neutron absorption cross section and unique chemical and structural properties (Beeston, 1970; Chandler et al., 2009). During the reactor operation, ^{9}Be undergoes (n, 2n) and (n, α) nuclear reactions resulting in the generation of large quantities of ^{4}He, ^{3}He and ^{3}H. This leads to the swelling of beryllium components with the corresponding alteration of their mechanical properties. The disposal of these components results in specific streams of nuclear waste containing a significant inventory of chemotoxic beryllium (Beeston, 1970; Longhurst et al., 2003; Chandler et al., 2009).

In contrast to the rest of the alkali-earth element series and due to its very small ionic radii ($r_{Be^{2+}}$ = 0.27 Å, for a coordination number (CN) of 4) (Shannon, 1976; Alderighi et al., 2000), beryllium is characterized by very strong hydrolysis. This results in an amphoteric behaviour involving the formation of positively- and negatively-charged hydrolysis species. Several solubility and potentiometric studies previously investigated the solubility and hydrolysis of beryllium in acidic to near-neutral pH conditions, deriving thermodynamic data for the hydrolysis species $Be_n(OH)_m^{2n-m}$, with (*n*,*m*) = (1,1), (1,2), (2,1), (3,3), (5,6) and (6,8) (Mattock, 1954; Gilbert and Garrett, 1956; Kakihana and Sillen, 1956; Schindler and Garett, 1960; Carell and Olin, 1961; Schwarzenbach, 1962; Hietanen and Sillen, 1964; Bertin et al., 1967; Mesmer and Baes, 1967; Ohtaki, 1967; Ohtaki and Kato, 1967; Lanza and Carpéni, 1968; Pâris and Gregoire, 1968; Schwarzenbach and Wenger, 1969; Kakihana and Maeda, 1970; Tsukuda et al., 1975; Vanni et al., 1975; Baes and Mesmer, 1976; Bruno et al., 1987b; Bruno, 1987; Chinea et al., 1997; Brown and Ekberg, 2016). A significantly scarcer number of studies investigated the hydrolysis of Be(II) in alkaline to hyperalkaline conditions (Gilbert and Garrett, 1956; Green and Alexander, 1965; Bruno et al., 1987a), where the hydrolysis species $Be(OH)_3^-$ and $Be(OH)_4^{2-}$ are expected to prevail. In our recent solubility and ^{9}Be-NMR study, we systematically investigated the solubility and hydrolysis of Be(II) in dilute to concentrated NaCl–NaOH and KCl–KOH systems. Experiments were conducted with a well-defined solid phase, α-$Be(OH)_2$(cr), and extended from acidic to hyperalkaline conditions (Çevirim-Papaioannou et al., 2020). In combination with previous studies available in the literature, chemical, thermodynamic and (SIT) activity models for the system Be^{2+}–Na^+–K^+–H^+–Cl^-–OH^-–H_2O(l) were derived.

Cementitious materials are widely used in underground repositories for nuclear waste disposal for the stabilization of the waste and for construction purposes. Upon contact with groundwater, cement materials undergo degradation through a sequence of dissolution reactions. In the degradation stage I, the dissolution of K- and Na-oxides/hydroxides imposes hyperalkaline conditions (pH ≈ 13.3) and high alkali content in the pore water. The degradation stage II is characterized by a pore water composition buffered by portlandite at pH ≈ 12.5 and $[Ca]_{tot} \approx 2 \cdot 10^{-2}$ M. After the complete dissolution of portlandite, the degradation stage III is dominated by the incongruent dissolution of calcium silicate hydrate (C-S-H) phases, with Ca:Si ratios of ≈1.6 to ≈0.6 and 12.5 ≤ pH ≤ 10. In the context of waste disposal in rock salt formations, the corrosion of cementitious waste forms has been reported to potentially generate $CaCl_2$-rich brines (up to 4 M) in combination with very high pH values ($pH_m \approx 12$, with $pH_m = -\log [H^+]$ in molal units) (Neck et al., 2009; Bube et al., 2013). Intermediate ionic strength conditions (*I* = 2–3 M) are also found in Cretaceous argillites in Northern Germany (Brewitz, 1980), with pore waters mostly dominated by NaCl and $CaCl_2$.

Previous studies investigating the solubility and hydrolysis of transition metals, lanthanides and actinides in alkaline, concentrated $CaCl_2$ systems have shown the formation and predominance of highly hydrolysed moieties stabilized by the coordination with Ca^{2+} ions. Using a combination of solubility and TRLFS studies, Neck and co-workers reported the formation of the ternary complexes $Ca[M(III)(OH)_3]^{2+}$, $Ca_2[M(III)(OH)_4]^{3+}$ and $Ca_3[M(III)(OH)_6]^{3+}$ (with M = Nd, Am, Cm and Pu) in concentrated $CaCl_2$ solutions (Rabung et al., 2008; Neck et al., 2009). The formation of analogous ternary complexes of tetravalent metal ions, *e.g.*, $Ca_4[An(IV)(OH)_8]^{4+}$ (An(IV) = Th(IV), Pu(IV) and Np(IV)), $Ca_3[Zr(IV)(OH)_6]^{4+}$ and $Ca_3[Tc(IV)O(OH)_5]^{3+}$, has been reported to increase the solubility of the corresponding hydrous oxides by several orders of magnitude in alkaline $CaCl_2$ solutions (Brendebach et al., 2007; Altmaier et al., 2008; Fellhauer et al., 2010; Fellhauer, 2013; Yalcintas et al., 2016). In spite of the weaker hydrolysis of the pentavalent actinides, Fellhauer and co-workers observed the formation of the ternary complexes $Ca[Np(V)O_2(OH)_2]^+$ and $Ca_3[Np(V)O_2(OH)_5]^{2+}$ in alkaline, concentrated $CaCl_2$ solutions (Fellhauer et al., 2016a; Fellhauer et al., 2016b). Spectroscopic evidence for the participation of Ca^{2+} in the formation of inner-sphere complexes was provided for Cm(III), Zr(IV), Th(IV) and Np(V), whereas DFT calculations underpin the stability of such complexes in the case of Tc(IV). All investigations above emphasize the key role of Ca^{2+} in the stabilization of highly hydrolyzed metal ions in concentrated $CaCl_2$ systems with high pH, regardless of the oxidation state of the metal ion. In the case of Zr(IV) and possibly due to the stronger hydrolysis of this metal ion, the ternary complex/es Ca–Zr(IV)–OH become predominant at $[CaCl_2] > 10^{-2}$ M, which emphasizes their relevance also in dilute cementitious systems.

The behaviour of beryllium in aqueous solutions at the molecular level has been investigated in a number of computational studies. Beryllium preferentially coordinates ligands in tetrahedral geometry, has strong hydrolysing and polarising abilities, and shows complex pH-dependent solution chemistry (Marx et al., 1997; Alderighi et al., 2000; Jin et al., 2015; Perera et al., 2017). In our previous studies, it was shown that in cementitious environment Ca^{2+} ions play a key role in the uptake of Be(II) by C-S-H phases (Çevirim-Papaioannou et al., 2021a; Çevirim-Papaioannou et al., 2021b). Together with evidences gained for M(III), M(IV) and M(V) systems, this anticipates the possible formation of previously unreported ternary complexes Ca–Be(II)–OH in alkaline $CaCl_2$ solutions. Through a combination of experimental solubility studies, molecular dynamics calculations and thermodynamic modelling, this work aims at providing a comprehensive understanding of the solution chemistry of beryllium in Ca-containing alkaline systems representative of cementitious environments with low to elevated ionic strength conditions.

2 Experimental

2.1 Chemicals

All samples were prepared, stored and handled in an Ar-glove box (O_2 < 1 ppm) at *T* = (22 ± 2)°C. All solutions were prepared with purified water (Milli-Q academic, Millipore, 18.2 MΩ) purged with Ar for at least 1 h to remove CO_2(g). Beryllium sulfate tetrahydrate ($BeSO_4 \cdot H_2O$, 99.99% purity) and calcium chloride ($CaCl_2 \cdot H_2O$) EMSURE® were purchased from Merck. Calcium hydroxide ($Ca(OH)_2$) was purchased from Sigma-Aldrich.

2.2 pH measurements

A combination pH electrode (ROSS Orion with 3.0 M KCl as filling solution) was used to determine the proton concentration ($[H^+]$ in mol·kg^{-1}, with $pH_m = -\log [H^+]$). The pH electrode was calibrated using commercial pH buffers (pH = 1–12, Merck). In salt solutions of ionic strength $I \geq 0.1$ mol kg^{-1}, the measured pH value (pH_{exp}) is an operational apparent value related to $[H^+]$ by $pH_m = pH_{exp} + A_m$. The values A_m entail both the activity coefficient of H^+ and the liquid junction potential of the electrode at a given background electrolyte concentration and temperature. A_m values reported by Altmaier and co-workers for $CaCl_2$ systems were used for the determination of pH_m (Altmaier et al., 2008).

2.3 Solid phase preparation and characterization. Solubility experiments with α-Be(OH)$_2$(cr)

The solid phase used for undersaturation solubility experiments, α-Be(OH)$_2$(cr), was precipitated by slow addition of a 0.35 M $BeSO_4$ solution to a 2.0 M carbonate-free NaOH solution with a final pH ≈ 10.5. After an ageing time of ≈2 months, the solid phase was washed thoroughly with slightly alkaline water (pH ≈ 9.5) to remove the residues of the matrix solution (Na_2SO_4 and NaOH), and characterized by X-ray diffraction (XRD). Details on the preparation and characterization of the solid phase used in this work were provided in our previous study (Çevirim-Papaioannou et al., 2020).

A total of 30 independent batch samples were prepared by contacting 0.5–5 mg of α-Be(OH)$_2$(cr) to alkaline $CaCl_2$ solutions (0.05, 0.25, 1.0 and 3.5 M) with $8.9 \leq pH_m \leq 11.8$. Be(II) concentrations and pH_m values were monitored regularly from 7 to 337 days. In each sampling, aliquots (100–500 µL) of the supernatant of each sample were pipetted into 10 kD filters (2–3 nm cut-off Nanosep®, Pall Life Sciences), centrifuged for 10 min at 6000 g, and diluted (1:100 and 1:4000) with 2% ultrapure HNO_3 before the quantification by inductively coupled plasma mass spectrometry (ICP-MS, PerkinElmer ELAN 610). The detection limit of the technique ranged between $10^{-6.5}$ and 10^{-8} M, depending upon the dilution factors applied at different $CaCl_2$ concentrations. Equilibrium conditions were assumed after repeated measurements over time with constant [Be] and pH_m values, typically after 372 days. After attaining equilibrium conditions, the solid phase of a selected sample (1.0 M $CaCl_2$, $pH_m = 11.1$) was characterized by XRD. For this purpose, an aliquot of the solid phase (≈1–2 mg) was washed 7 times with ethanol (0.5–1 mL) under Ar atmosphere in order to remove the background electrolyte, *i.e.*, $CaCl_2$. After the last cleaning step, the washed solid phase was re-suspended in ethanol, deposited on the XRD sample holder and left drying for a few minutes inside the glovebox. The XRD diffractogram was collected using a Bruker D8 Advance X-Ray powder diffractometer (Cu anode) within the range $2\theta = 2–80^o$, incremental steps of 0.02 and a measurement time of 0.4 s per step.

2.4 Computational methods

The simulation model was built in a box with dimensions of 43 Å × 43 Å × 49 Å, which contained 3,120 water molecules with 3 $Be(OH)_4^{2-}$, 50 Ca^{2+}, and 84 Cl^-randomly distributed ions. This approximately corresponds to 1 M $CaCl_2$ and 0.05 M beryllium ion concentration. The high concentration of Be(II) is required in the simulations for better statistical sampling, and is in line with experimental observations in concentrated $CaCl_2$ solutions. The total electroneutrality of the simulation cell was ensured by balancing the number of counterions. Periodic boundary conditions were applied in three dimensions. Water was described using the extended simple point charge (SPC/E) model (Berendsen et al., 1987). The 12-6-4 Lennard-Jones-type nonbonded parameters for Ca^{2+} and Be^{2+} for SPC/E water, which include the contribution from the ion-induced dipole interaction, were taken from Li and Merz (Li and Merz, 2014; Li et al., 2020). Standard Lorenz-Berthelot mixing rules (Allen and Tildesley, 2017) were applied to calculate short-range Lennard-Jones interactions between the unlike atoms (with a cut-off distance of 1.4 nm). Long-range electrostatic forces were evaluated using the Ewald summation method. All molecular dynamics (MD) simulations were performed using the LAMMPS software package (3 March 2020 version) (Plimpton, 1995). Model equilibration was carefully monitored by assessing the temperature, pressure, kinetic and potential energy of the system, and dimensions of the simulation box, in order to confirm that these parameters reach their equilibrium steady state values on average (Braun et al., 2019). The Newtonian equations of the atomic motions were numerically integrated with a time step of 1 fs, and the model systems were initially equilibrated for 5 ns in the isobaric–isothermal statistical ensemble (*NPT*), then for 5 ns in the canonical ensemble (*NVT*). Temperature and pressure were constrained using the Nose-Hoover thermostat and barostat (Braun et al., 2019) at ambient conditions (T = 295 K, p = 0.1 MPa). The production run was performed in the *NVT* ensemble for 5 ns, and the trajectory was recorded every 500 fs. To describe local structural properties, radial distribution functions for pairs of atoms, and running coordination numbers were calculated from the recorded trajectory. The VMD software package (version 1.9.3) has been used for visualisation (Humphrey et al., 1996).

3 Results and discussion

3.1 Solid phase characterization

XRD patterns collected for the beryllium solid phase equilibrated in 1.0 M $CaCl_2$ at $pH_m = 11.1$ and 3.5 M $CaCl_2$ at $pH_m = 10.6$ are shown in Figure 1, together with the diffractograms previously reported for α-Be(OH)$_2$(cr) in Bear and Turnbull (1965) and in our previous study (Çevirim-Papaioannou et al., 2020). The main features of this sample are in excellent agreement with the patterns previously reported for α-Be(OH)$_2$(cr). This observation confirms that the starting material used in the experiments, α-Be(OH)$_2$(cr), is the solid phase controlling the solubility of beryllium also in $CaCl_2$ systems.

3.2 Solubility experiments

Figure 2 shows the experimental solubility data determined in alkaline $CaCl_2$ solutions with $8.9 \leq pH_m \leq 11.8$, together with the solubility curve of α-Be(OH)$_2$(cr) at $I = 0$ calculated using the

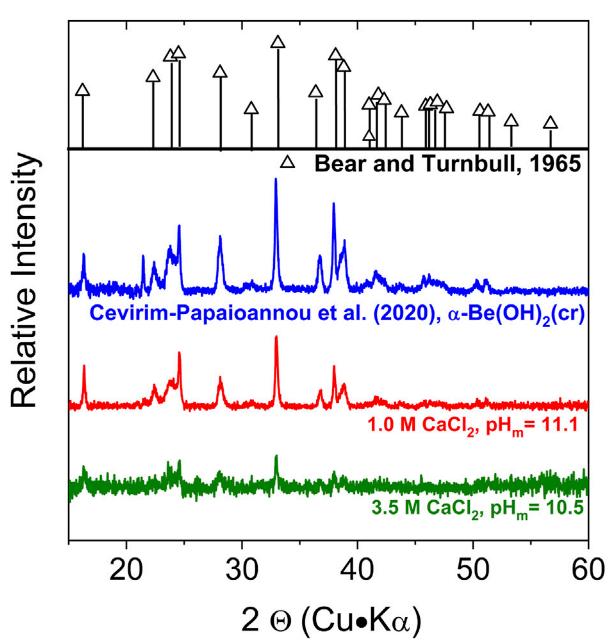

FIGURE 1
X-Ray diffraction patterns of the solid phase recovered from the solubility sample equilibrated in 1.0 M $CaCl_2$ at pH_m = 11.1, together with reference patterns reported for α-$Be(OH)_2$(cr) (Bear and Turnbull, 1965) and patterns obtained in our previous study (Çevirim-Papaioannou et al., 2020).

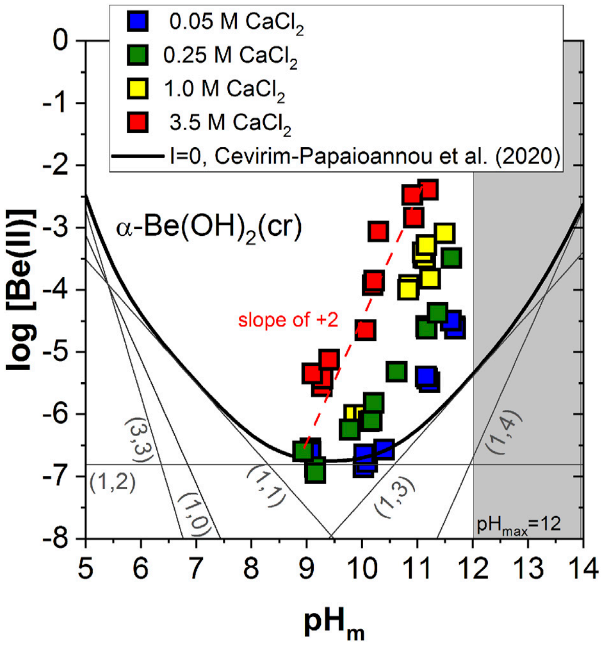

FIGURE 2
Experimental Be(II) solubility data obtained in the present work in 0.05, 0.25, 1.0 and 3.5 M $CaCl_2$ solutions with 8.9 ≤ pH_m ≤ 11.8. Solid thick line corresponds to the solubility curve of α-$Be(OH)_2$(cr) at I = 0 calculated with thermodynamic data reported in Çevirim-Papaioannou et al. (2020). Dashed red line indicates the slope analysis performed in this study. Shadowed area represents the precipitation of $Ca(OH)_2$(s) [at ($CaCl_2$) ≤ 2 M] or Ca–OH–Cl(s) solid phases. Uncertainties of individual measurements are within the size of the symbols.

thermodynamic model reported in (Çevirim-Papaioannou et al., 2020) (see Supplementary Tables SI-S1, S2 in the Supplementary Material). The solubility of Be(II) in 0.05 M $CaCl_2$ shows a pH-independent behaviour within 9 ≤ pH_m ≤ 10.5, which is in good agreement with the calculated solubility line and can be assigned to the solubility reaction α-$Be(OH)_2$(cr) ⇔ $Be(OH)_2$(aq). Above pH ≈ 10.5, the solubility in 0.05 M $CaCl_2$ increases steadily with a slope of ≈ +2 (as log [Be(II] vs. pH_m), in disagreement with the slope of +1 observed for NaCl/KCl systems within the same pH-range and also predicted by the calculated solubility line. This observation reflects that in $CaCl_2$ solutions the solubility of the α-$Be(OH)_2$(cr) phase is dominated by an equilibrium reaction involving the release of 2 H^+. A well-defined slope of ≈ +2 is also observed for all other $CaCl_2$ systems investigated in this work, with the highest solubility being achieved in 3.5 M $CaCl_2$ solutions. Our experimental observations in $CaCl_2$ systems and the direct comparison with solubility data in NaCl/KCl solutions support the earlier predominance of the $[Be(OH)_4]^{2-}$ moiety in the former systems, expectedly as a result of its stabilization by Ca^{2+} ions. This is in line with previous observations reported in the literature for strongly hydrolyzing metal ions, *e.g.*, M(III), M(IV) and M(V) (Altmaier et al., 2008; Neck et al., 2009; Fellhauer et al., 2010; Fellhauer, 2013; Yalcintas et al., 2016).

3.3 MD calculations of the system $Ca^{2+}–Be(OH)_4{}^{2-}–Cl^-–H_2O(l)$

The local structure of a solution can be described by means of the radial distribution functions of the ion-ion and ion-water pairs. The RDF shows the probability of finding atoms at curtain distance during simulation time, and allows to calculate time-averaged coordination numbers. Figure 3 presents calculation results for Be^{2+} ions in $CaCl_2$ aqueous solution.

Figures 3A, B shows that the interaction of Be^{2+} with hydroxyl ions is strong and was stable during all the simulation time. There are 4 oxygen atoms of the aqueous hydroxyl ions in the first coordination sphere of Be^{2+} at $r \approx 1.7$ Å. This result agrees well with the reported distances between Be^{2+} and hydroxyl ions calculated by DFT (Jin et al., 2015). The oxygen atoms of the first shell are coordinated with other solution molecules through hydrogen bonding (Hw peak at distances around 2–3 Å) to the second solvation shell (small Ow peak at $r \approx 3–4$ Å). As it can be seen from Figures 3A, B, there is a low probability of binding between Be^{2+} and Cl^- ions: no distinct peak of chloride ions was recorded, and Cl^- presence was only found at r > 5 Å.

Three peaks for Ca^{2+} are found in the outer coordination sphere of Be^{2+}: a high-intensity peak at $r \approx 3.1$ Å, a small peak between 3 Å and 4 Å, and very broad peak of very low intensity around 5 Å. The first peak corresponds to binding of two calcium cations with oxygens of the hydroxyl ions in bidentate coordination, as can be seen in the snapshot from simulations (Figure 3C). The peak between 3 and 4 Å is the coordination of Ca^{2+} with a single hydroxyl group. The broad peak after 5 Å stands for Ca^{2+} ions in the solution that are not bound to the complex. We have previously shown that Ca^{2+} plays a crucial role in the sorption of Be(II) in

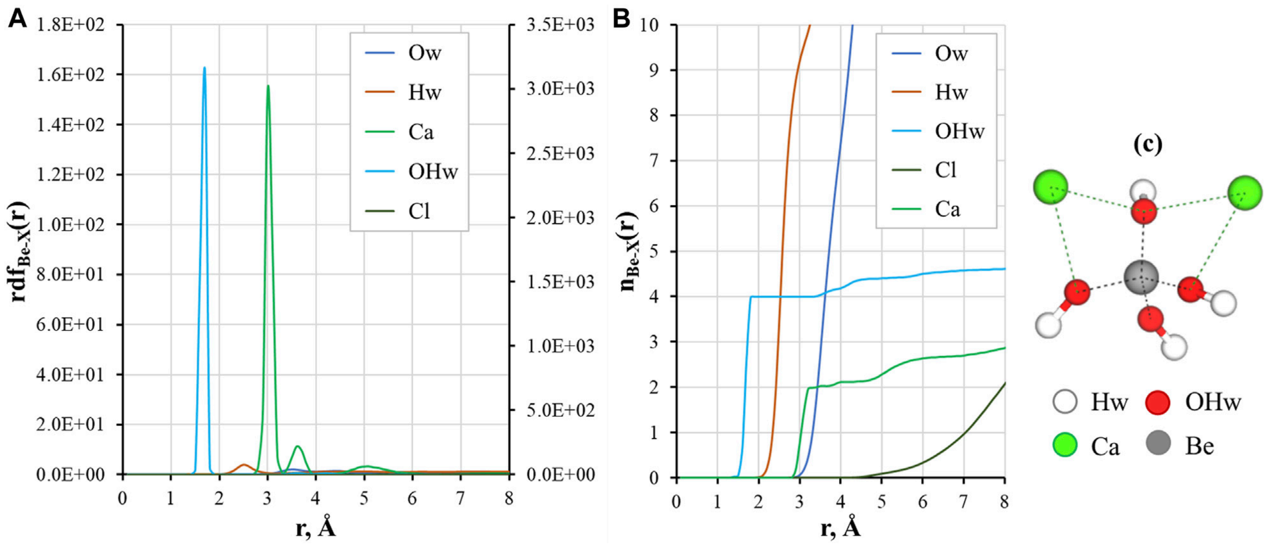

FIGURE 3
Local structural properties of $Be(OH)_4^{2-}$ in a $CaCl_2$ solution: **(A)** radial distribution functions (the secondary axes show rdf(r) for the Be-OHw pair); **(B)** running coordination numbers for Be-X atom pairs, where X is O, H, Cl, and Ca; **(C)** Simulation snapshot of the complex, water molecules omitted for clarity.

cementitious systems (Çevirim-Papaioannou et al., 2021a; Çevirim-Papaioannou et al., 2021b). The surface of C-S-H provides a more structured environment, where both ions and water molecules are coordinated with the surface in the sorption layer increasing the probability for Be hydroxyl species to form complex with multiple Ca^{2+} ions (up to three). From the results of this study, it can be concluded that in the solution complexes of $Be(OH)_4^{2-}$ with two Ca^{2+} are dominant, while binding of the third calcium cation remains possible, which is reflected in the slightly higher value of running coordination for the Be-Ca pair (n ≈ 2.2 at a distance of 4 Å).

3.4 Chemical, thermodynamic and SIT activity models

The specific ion interaction theory (SIT) (Ciavatta, 1980) based on the Brønsted-Guggenheim-Scatchard model is used in this study to account for ion interactions in systems at $I > 0$. This is also the method adopted for ion strength corrections within the NEA-TDB project (Grenthe et al., 2020). In SIT, the activity coefficient of a given ion j (γ_j) is calculated according to:

$$\log\gamma_j = -z_j^2 D + \sum_k \varepsilon(j,k,I_m)m_k \tag{1}$$

where z_j is the charge of the ion j, D is the Debye-Hückel term ($D = \frac{0.509\sqrt{I_m}}{1+1.5\sqrt{I_m}}$), m_k is the molality of the oppositely charged ion k, and $\varepsilon(j, k, I_m)$ is the specific ion interaction parameter. The Debye Hückel term in Equation 1 accounts for the electrostatic, non-specific long-range interactions prevailing in dilute systems, whereas the term $\sum_k \varepsilon(j,k,I_m)m_k$ accounts for short-range, non-electrostatic interactions that become relevant at higher ionic strength conditions. The SIT coefficient $\varepsilon(j, k, I_m)$ reflects also differences between ions of the same charge but different size. The applicability of the SIT approach is often considered limited to $I_m \leq 3.5$ mol kg^{-1}, although previous studies have reported reliable results for 1:1 and 1:2 electrolytes (including $CaCl_2$ systems) up to $I_m \approx 13.5$ mol kg^{-1} (Neck et al., 2009; Fellhauer et al., 2010; Yalcintas et al., 2016; Altmaier et al., 2017).

Based on the slope analysis discussed in Section 3.1 and considering that α-$Be(OH)_2$(cr) is the solid phase controlling the solubility in all investigated systems, the equilibrium reaction (2) is proposed to describe the solubility of Be(II) in $CaCl_2$ solutions above $pH_m \approx 9$–10 (depending upon salt concentration). As reflected in reaction (2), the number of Ca-atoms participating in the complexation reaction (n) is unknown and must be included in the optimization process.

$$\alpha - Be(OH)_2(cr) + nCa^{2+} + 2H_2O(l) \Leftrightarrow Ca_nBe(OH)_4^{(2n-2)} + 2H^+ \tag{2}$$

with

$$\log{}^* K'_{s,Ca_nBe(OH)_4^{(2n-2)}} = \log[Ca_nBe(OH)_4^{2n-2}] + 2\log[H^+] - n\log[Ca^{2+}] \tag{3}$$

$$log^* K^\circ_{s,Ca_nBe(OH)_4^{(2n-2)}} = log^* K'_{s,Ca_nBe(OH)_4^{(2n-2)}} + log\gamma_{Ca_nBe(OH)_4^{(2n-2)}} + 2log\gamma_{H^+} - nlog\gamma_{Ca^{2+}} - 2loga_w \tag{4}$$

$$log^* K'_{s,Ca_nBe(OH)_4^{(2n-2)}} - \Delta z^2 D - 2loga_w = log^* K^\circ_{s,Ca_nBe(OH)_4^{(2n-2)}} - \Delta\varepsilon m_{Cl^-} \tag{5}$$

Conditional solubility constants, $\log {}^*K'_{s,Ca_nBe(OH)_4^{(2n-2)}}$, were determined from the experimental solubility data obtained in 0.05, 0.25, 1.0 and 3.5 M $CaCl_2$ using the minimization function

TABLE 1 Values of log $*K'_{s,Ca_nBe(OH)_4^{(2n-2)}}$ determined from solubility data of Be(II) in 0.05–3.5 M $CaCl_2$ solutions for the chemical models assuming the formation of the ternary complexes $Ca[Be(OH)_4](aq)$, $Ca_2[Be(OH)_4]^{2+}$ or $Ca_3[Be(OH)_4]^{4+}$. Equilibrium constants in the reference state, log $*K'_{s,CanBe(OH)4(2n-2)}$ and SIT coefficients as determined from the corresponding SIT-plots (see Supplementary Figures SI-S1 in the Supporting Information). Quality parameter (Δ) calculated for each chemical model as described in the text.

	log $*K'_{s,Ca_nBe(OH)_4^{(2n-2)}}$				Results of the SIT plot			
Species (*i*)	0.05 M	0.25 M	1.0 M	3.5 M	log $*K°$	*j*	ε(*i*, *j*)	Qual. par. (*Δ*)
$CaBe(OH)_4(aq)$	−26.72	−26.06	−25.80	−25.14	−(25.97 ± 0.46)	Ca^{2+}/Cl^-	−(0.35 ± 0.15)	0.72
$Ca_2Be(OH)_4^{2+}$	−25.37	−25.43	−25.73	−25.73	−(25.13 ± 0.46)	Cl^-	(0.00 ± 0.15)	0.03
$Ca_3Be(OH)_4^{4+}$	−24.07	−24.83	−25.74	−26.32	−(25.74 ± 0.46)	Cl^-	(0.48 ± 0.15)	3.36

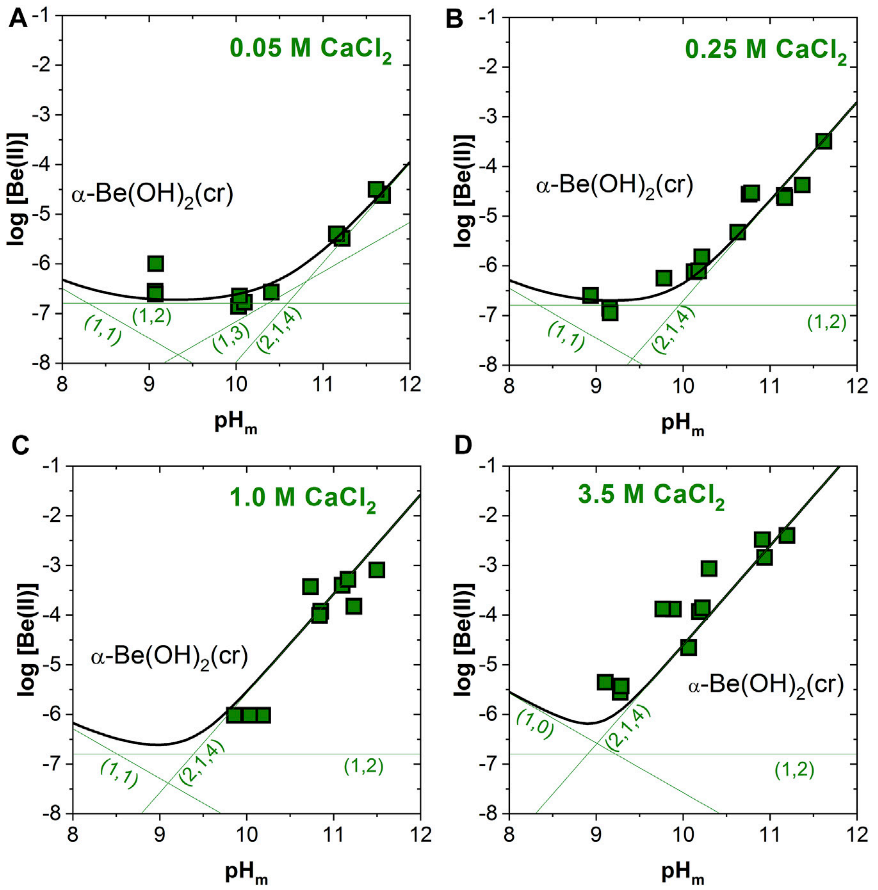

FIGURE 4
Experimental and calculated solubility of α-$Be(OH)_2$(cr) in **(A)** 0.05, **(B)** 0.25, **(C)** 1.0 and **(D)** 3.5 M $CaCl_2$ solutions. Calculations conducted using the thermodynamic and activity models derived in Çevirim-Papaioannou et al. (2020) and extended in this work. Uncertainties of individual measurements are within the size of the symbols.

$\sum((\log\,[Be]_{exp} - \log\,[Be]_{calc})^2)^{1/2}$. Three different chemical models were considered in the calculations, assuming the predominance of the ternary complexes $Ca_nBe(OH)_4^{(2n-2)}$ with n = 1–3 in the aqueous phase. The SIT-plot was used to derive the solubility constant at the reference state, log $*K°_{s,Ca_nBe(OH)_4^{(2n-2)}}$, and corresponding SIT ion interaction coefficient/s based on the linear regression (log $*K'_{s,Ca_nBe(OH)_4^{(2n-2)}} + \Delta z^2 D - 2\log a_w$) vs. $[Cl^-]$ (in molal units). The SIT ion interaction coefficients of the ternary complexes $Ca_nBe(OH)_4^{(2n-2)}$ were calculated from the slope of the linear regression (−Δε) in combination with $\varepsilon(H^+, Cl^-) = (0.12 \pm 0.01)$ kg·mol^{-1}, $\varepsilon(Ca^{2+}, Cl^-) = (0.14 \pm 0.01)$ kg·mol^{-1} and a_w values as reported in the NEA-TDB (Grenthe et al., 2020). The criteria considered for the selection of the chemical model describing the solubility of Be(II) in $CaCl_2$ was based on:

(i) minimization of the quality parameter (Δ) calculated as $\sum |log^{*} K'^{\,\exp}_{s,Ca_nBe(OH)_4^{(2n-2)}} - logK'^{\,calc}_{s,Ca_nBe(OH)_4^{(2n-2)}}|$ (Fellhauer et al., 2010; Fellhauer, 2013; Yalcintas et al., 2016),

(ii) reasonable values of the SIT interaction coefficients, considering charge analogies described in Hummel (2009), and

(iii) smooth shape of the plot log $^{*}K'_{s,Ca_nBe(OH)_4^{(2n-2)}}$ vs. $[Cl^-]$

Table 1 shows the conditional solubility constants, log $^{*}K'_{s,Ca_nBe(OH)_4^{(2n-2)}}$, determined for each chemical model and background electrolyte concentration, together with log $^{*}K^{\circ}_{s,Ca_nBe(OH)_4^{(2n-2)}}$, $\varepsilon(Ca_nBe(OH)_4^{(2n-2)}, Ca^{2+}/Cl^-)$ and the quality parameter (Δ). The SIT-plot as well as the representation of log $^{*}K'_{s,Ca_nBe(OH)_4^{(2n-2)}}$ vs. $[Cl^-]$ for the three chemical models evaluated in this work are shown in Supplementary Figures SI-S1, S2 of the Supporting Information.

Table 1 shows very large values of the quality parameter (Δ) for the chemical models including the aqueous complexes $CaBe(OH)_4(aq)$ and $Ca_3Be(OH)_4^{4+}$, which reflect the significant deviations between experimental and calculated log $^{*}K'_{s,Ca_nBe(OH)_4^{(2n-2)}}$ for these systems (see also Supplementary Figures SI-S1 in the Supplementary Material). Note that although values of $\varepsilon(i, j) = 0$ for neutral species are considered per definition in SIT, a number of neutral species with $\varepsilon(i, j) \neq 0$ are reported in the NEA-TDB books (see for instance Grenthe et al., 2020), and this cannot be considered as criteria to reject a specific chemical model. The chemical model including the complex $Ca_2[Be(OH)_4]^{2+}$ shows the lowest value of Δ, a reasonable SIT coefficient, as well as a smooth shape of the plot log $^{*}K'_{s,Ca_nBe(OH)_4^{(2n-2)}}$ vs. $[Cl^-]$ (see Supplementary Figures SI-S2). This outcome is in agreement with the MD calculations summarized in Section 3.3, which predict the predominance of an aqueous complex with two Ca-atoms. The same model calculations described above but excluding solubility data in 3.5 M $CaCl_2$ were also performed in order to remain within the range of ionic strength normally considered for SIT. The best fit was obtained again for the chemical model including the complex $Ca_2[Be(OH)_4]^{2+}$ (see Supplementary Figures SI-S3; Supplementary Tables SI-S4). Consistent values of log $^{*}K^{\circ}_{s,Ca_2[Be(OH)_4]^{2+}}$ and $\varepsilon(Ca_2[Be(OH)_4]^{2+}, Cl^-)$ were obtained using both datasets, and thus the model derived including also solubility data in 3.5 M $CaCl_2$ was finally favored.

The chemical reaction (6) and corresponding thermodynamic functions are thus considered for the extension of the thermodynamic and activity models reported in Çevirim-Papaioannou et al. (2020) to the system $Be^{2+}–Ca^{2+}–Na^{+}–K^{+}–H^{+}–Cl^{-}–OH^{-}–H_2O(l)$.

$$\alpha - Be(OH)_2(cr) + 2Ca^{2+} + 2H_2O(l) \Leftrightarrow Ca_2Be(OH)_4^{2+} + 2H^{+} \quad (6)$$

$$\log {}^{*}K^{\circ}_{s,Ca_nBe(OH)_4^{(2n-2)}} = -(25.13 \pm 0.27)$$

$$\varepsilon\left(Ca_2[Be(OH)_4]^{2+}, Cl^{-}\right) = (0.00 \pm 0.15)\,kg \cdot mol^{-1}$$

Figures 4A–D shows the excellent agreement between the experimental solubility data determined in 0.05–3.5 M $CaCl_2$ solutions with solubility calculations conducted using the thermodynamic and activity models derived in Çevirim-Papaioannou et al. (2020) and extended in this work. Future work will target the development of a Pitzer activity model for this system, which is clearly favored for the description of brine systems.

3.5 Speciation of beryllium in cementitious systems

C-S-H phases of various compositions determine the most relevant properties of cement pastes in ordinary Portland and blended systems. The non-ideal multisite CASH + solid solution model (Miron et al., 2022a; Miron et al., 2022b; Kulik et al., 2022) can accurately model the C-S-H solubility, water content and elemental uptake accounting for the continuous change of solid and pore solution compositions as a function of pH, alkali concentration, and Ca/Si ratio in the system. In the present work, the CASH + model is used to compute the evolution of a pore solution composition assuming the degradation of a Portland cement in a repository setting defined by low ionic strength conditions. This is done by removing alkalis and of Ca from the system (Ca-Si-Na-K-H_2O) in equilibrium with C-S-H to produce the change of the pore solution composition (Figures 5A, B) as a function of $[H^+]$, present at different cement degradation stages. At the starting point the pore solution composition in equilibrium with a hydrated Portland cement is taken from (Vollpracht et al., 2016) and has a pH = 13.40 and [NaOH + KOH] = 0.555 M (with K/Na = 2). Alkalis are then removed and the pH decreases to a value of 12.4, when the system is in equilibrium with high Ca/Si C-S-H and portlandite. In natural systems, the pore solution composition is buffered at this condition until all portlandite is dissolved. By removing Ca from the system, after the full dissolution of portlandite, the composition of C-S-H goes towards lower Ca/Si ratios and the pH of the solution decreases to 9.8 at which point the system is in equilibrium with low Ca/Si C-S-H and amorphous silica. The evolution of the pore water composition obtained from calculations with the CASH + solid solution model in combination with the thermodynamic and activity models derived in this work and reported in Çevirim-Papaioannou et al. (2020) have been used to calculate the aqueous speciation of beryllium throughout the complete degradation process of cement (see Figure 5C).

Figure 5C shows that the hydrolysis species $Be(OH)_{3}^{-}$ and (to less extent) $Be(OH)_4^{2-}$ prevail within the degradation stage I of cement, characterized by very high pH and low Ca concentration. Due to the enhanced Ca concentration defined by the equilibrium with portlandite, the ternary complex $Ca_2[Be(OH)_4]^{2+}$ dominates the aqueous speciation of Be(II) within the degradation stage II, as well as in the early steps of the degradation stage III at pH > 12.1. With the decrease in Ca concentration, the hydrolysis species $Be(OH)_{3}^{-}$ becomes predominant again at $10.6 \leq pH \leq 12.1$, in systems controlled by C-S-H phases with Ca:Si = 0.80–1.27. Below pH ≈ 10.6, the neutral species $Be(OH)_2(aq)$ becomes predominant until the full degradation of cement.

Note that CASH + has not been yet verified for calculating systems with concentrated $CaCl_2$ solutions. In particular, the evolution of C-S-H and other cement phases at high Ca concentrations remains ill-defined. Although this contribution has focused on the SIT activity model, the development of the corresponding Pitzer activity model for the system $Be^{2+}–Ca^{2+}–Na^{+}–K^{+}–H^{+}–Cl^{-}–OH^{-}–H_2O(l)$ is foreseen in the next phase of this study. Pitzer formalism is clearly favored for the description of high-saline systems. Efforts dedicated to the thermodynamic modelling of cementitious systems in high saline conditions are also on-going in the context of the THEREDA Reference Database project (Moog et al., 2015).

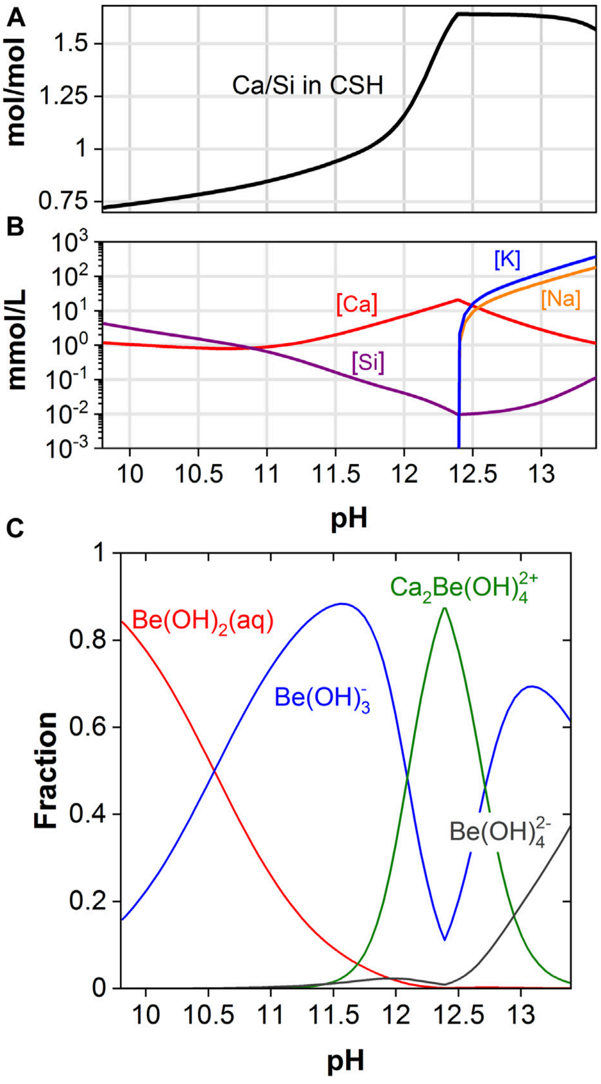

FIGURE 5
(A) Evolution of the Ca/Si ratio in C-S-H phases and **(B)** simulated pore solution composition as a function of pH during the process of cement degradation. **(C)** Fraction diagram of Be(II) within 9.8 ≤ pH_m ≤ 13.5 for the pore water composition shown in **(B)**, as calculated using the thermodynamic and activity models derived in Çevirim-Papaioannou et al. (2020) and extended in this work.

4 Summary and conclusion

The solubility and hydrolysis of Be(II) in dilute to concentrated $CaCl_2$ solutions (0.05–3.5 M) was investigated using a combination of undersaturation solubility experiments with α-$Be(OH)_2$(cr) and molecular dynamics (MD) calculations. The solubility of Be(II) in 0.05 M $CaCl_2$ shows a pH-independent behaviour in weakly alkaline systems (9 ≤ pH_m ≤ 10.5), which corresponds to the solubility equilibrium α-$Be(OH)_2$(cr) ⇔ $Be(OH)_2$(aq). These observations are in excellent agreement with previous solubility experiments in NaCl and KCl solutions. A steep increase of the solubility with a slope of ≈ +2 (as log [Be(II)] vs. pH_m) is observed above pH_m ≈ 10.5 and at higher $CaCl_2$ concentrations. At pH_m ≈ 12, this results in solubility values significantly higher (1–4 orders of magnitude, depending upon $CaCl_2$ concentration) than those reported previously for analogous NaCl and KCl systems (Çevirim-Papaioannou et al., 2020). In line with previous studies in the literature on M(III), M(IV) and M(V) metal ions in $CaCl_2$ systems, these observations unequivocally point towards the formation and predominance of ternary complexes of the type $Ca_nBe(OH)_4^{(2n-2)}$ in alkaline to hyperalkaline systems containing Ca. MD calculations show the coordination of two Ca-ions in the second coordination sphere of Be^{2+} at $r \approx 3.1$ Å. These Ca-ions are coordinated in bi-dentate mode to the hydroxyl groups of the $[Be(OH)_4]^{2-}$ moiety. Consistently with MD calculations, the fit of solubility data indicates the predominance of the complex $Ca_2[Be(OH)_4]^{2+}$ in the investigated $CaCl_2$ systems.

In combination with data previously reported in (Çevirim-Papaioannou et al., 2020), chemical, thermodynamic and (SIT) activity models are derived in this work for the system $Be^{2+}–Ca^{2+}–Na^+–K^+–H^+–Cl^-–OH^-–H_2O(l)$. These new Be(II) models allow the precise characterization of the solubility and speciation of beryllium throughout all degradation stages of cement, as analysed in this paper for low ionic strengths systems. This can be used for source term estimations of beryllium in the context of nuclear waste disposal, as well as input parameter for advanced surface complexation or solid-solution sublattice models for the retention of beryllium in cementitious systems.

Data availability statement

The original contributions presented in the study are included in the article/Supplementary Material, further inquiries can be directed to the corresponding authors.

Author contributions

NÇ-P: Methodology, Investigation, Writing–Original Draft. IA: Simulation, Investigation, Writing–Original Draft. GM: Investigation, Writing–Original Draft. XG: Conceptualization, Writing–Review and Editing, Supervision, Project administration. MA: Writing–Review and Editing, Project administration, Funding acquisition. All authors contributed to the article and approved the submitted version.

Funding

The research leading to these results has received funding from the European Union's European Atomic Energy Community's (Euratom) Horizon 2020 Programme (NFRP-2014/2015) under grant agreement, 662147—Cebama.

Acknowledgments

Frank Geyer, Annika Fried and Cornelia Beiser (all KIT–INE) are gratefully acknowledged for the ICP–MS and ICP–OES measurements. We thank Bianca Schacherl for her support on sample preparation. We acknowledge support by the KIT-

Publication Fund of the Karlsruhe Institute of Technology. The authors acknowledge support by the state of Baden-Wurttemberg through bwHPC and the German Research Foundation (DFG) through grant no INST 40/575-1 FUGG (JUSTUS 2 cluster).

Conflict of interest

The author XG declared that they were an editorial board member of Frontiers at the time of submission. This had no impact on the peer review process and the final decision.

The remaining authors declare that the research was conducted in the absence of any commercial or financial relationships that could be construed as a potential conflict of interest.

Publisher's note

Supplementary material

The Supplementary Material for this article can be found online at: https://www.frontiersin.org/articles/10.3389/fnuen.2023.1192463/full#supplementary-material

References

Alderighi, L., Gans, P., Midollini, S., and Vacca, A. (2000). "Aqueous solution chemistry of beryllium," in *Main chemistry group, advances in inorganic chemistry, vol 50*. Editors A. G. Sykes and A. Cowley (San Diego: Academic Press), 110–172.

Allen, R., and Tildesley, D. J. (2017). *Computer simulation of liquids*. 2nd edition. New York: Oxford University Press, 626.

Altmaier, M., Neck, V., and Fanghanel, T. (2008). Solubility of Zr(IV), Th(IV) and Pu(IV) hydrous oxides in $CaCl_2$ solutions and the formation of ternary Ca-M(IV)-OH complexes. *Radiochim. Acta* 96, 541–550. doi:10.1524/ract.2008.1535

Altmaier, M., Yalcintas, E., Gaona, X., Neck, V., Müller, R., Schlieker, M., et al. (2017). Solubility of U(VI) in chloride solutions. I. The stable oxides/hydroxides in NaCl systems, solubility products, hydrolysis constants and SIT coefficients. *J. Chem. Thermodyn.* 114, 2–13. doi:10.1016/j.jct.2017.05.039

Baes, C. F., and Mesmer, R. E. (1976). *The hydrolysis of cations*. New York: John Wiley and Sons.

Bear, I. J., and Turnbull, A. G. (1965). The heats of formation of beryllium compounds. I. Beryllium hydroxides. *J. Phys. Chem.* 69, 2828–2833. doi:10.1021/j100893a004

Beeston, J. M. (1970). Beryllium metal as a neutron moderator and reflector material. *Nucl. Eng. Des.* 14, 445–474. doi:10.1016/0029-5493(70)90161-5

Berendsen, H. J. C., Grigera, J. R., and Straatsma, T. P. (1987). The missing term in effective pair potentials. *J. Phys. Chem.* 91, 6269–6271. doi:10.1021/j100308a038

Bertin, F., Thomas, G., and Merlin, J. C. (1967). Studies on beryllium complexes. I. Solvolysis of Be^{2+} ions in aqueous media. *J. C. Bull. Soc. Chim. Fr.* 2393.

Braun, E., Gilmer, J., Mayes, H. B., Mobley, D. L., Monroe, J. I., Prasad, S., et al. (2019). Best practices for foundations in molecular simulations [article v1.0]. *Living J. Comp. Mol. Sci.* 1, 5957. doi:10.33011/livecoms.1.1.5957

Brendebach, B., Altmaier, M., Rothe, J., Neck, V., and Denecke, M. A. (2007). EXAFS study of aqueous Zr^{IV} and Th^{IV} complexes in alkaline $CaCl_2$ solutions: $ca_3[Zr(OH)_6]^{4+}$ and $Ca_4[Th(OH)_8]^{4+}$. *Inorg. Chem.* 46, 6804–6810. doi:10.1021/ic070318t

Brewitz, W. (1980). *Zusammenfassender zwischenbericht, GSF T 114*. Braunschweig: Ges. f. Strahlen-und Umweltforschung.

Brown, P. L., and Ekberg, C. (2016). *Hydrolysis of metal ions*. Weinheim: Wiley-VCH Verlag GmbH.

Bruno, J. (1987). Beryllium(II) hydrolysis in 3.0 mol·dm^{-3} perchlorate. *J. Chem. Soc. Dalton Trans.* 1987, 2431–2437. doi:10.1039/dt9870002431

Bruno, J., Grenthe, I., and Munoz, M. (1987a). Studies of metal carbonate equilibria. Part 16. The beryllium(II) - water-carbon dioxide(g) system in neutral-to-alkaline 3.0 mol dm^{-3} perchlorate media at 25°C. *J. Chem. Soc. Dalton Trans.* 1987, 2445–2449. doi:10.1039/dt9870002445

Bruno, J., Grenthe, I., Sandstrom, M., and Ferri, D. (1987b). Studies of metal carbonate equilibria. 15. The beryllium(II)- water-carbon dioxide(g) system in acidic 3.0 mol dm^{-3} perchlorate media. *J. Chem. Soc. Dalton Trans.* 1987, 2439–2444. doi:10.1039/dt9870002439

Bube, C., Metz, V., Bohnert, E., Garbev, K., Schild, D., and Kienzler, B. (2013). Long-term cement corrosion in chloride-rich solutions relevant to radioactive waste disposal in rock salt - leaching experiments and thermodynamic simulations. *Phys. Chem. Earth* 64, 87–94. doi:10.1016/j.pce.2012.11.001

Carell, B., Olin, A., and Valen, K. (1961). Studies on the hydrolysis of metal ions. 37. Application of the self-medium method to the hydrolysis of beryllium perchlorate. *Acta Chem. Scand.* 15, 1875–1884. doi:10.3891/acta.chem.scand.15-1875

Çevirim-Papaioannou, N., Androniuk, I., Han, S., Mouheb, N. A., Gaboreau, S., Um, W., et al. (2021a). Sorption of beryllium in cementitious systems relevant for nuclear waste disposal: quantitative description and mechanistic understanding. *Chemosphere* 282, 131094. doi:10.1016/j.chemosphere.2021.131094

Çevirim-Papaioannou, N., Gaona, X., Böttle, M., Bethune Yalcintas, E., Schild, D., Adam, C., et al. (2020). Thermodynamic description of Be(II) solubility and hydrolysis in acidic to hyperalkaline NaCl and KCl solutions. *Appl. Geochem.* 117, 104601–104613. doi:10.1016/j.apgeochem.2020.104601

Çevirim-Papaioannou, N., Han, S., Androniuk, I., Um, W., Altmaier, M., and Gaona, X. (2021b). Uptake of Be(II) by cement in degradation stage I: wet-chemistry and molecular dynamics studies. *Minerals* 11, 1149. doi:10.3390/min11101149

Chandler, D., Primm, R. T., and Maldonado, G. I. (2009). *Reactivity accountability attributed to beryllium reflector poisons in the high flux isotope reactor*. Oak Ridge, USA: ORNL Report. TM-2009/188.

Chinea, E., Dominguez, S., Mederos, A., Brito, F., Sanchez, A., Ienco, A., et al. (1997). Hydrolysis of beryllium(II) in DMSO:H_2O. *Main. Group Mater. Chem.* 20, 11–17. doi:10.1515/mgmc.1997.20.1.11

Ciavatta, L. (1980). The specific interaction theory in evaluating ionic equilibria. *Ann. Chim-Rome* 70, 551–567.

Fellhauer, D., Altmaier, M., Gaona, X., Lutzenkirchen, J., and Fanghanel, T. (2016a). Np(V) solubility, speciation and solid phase formation in alkaline $CaCl_2$ solutions. Part II: thermodynamics and implications for source term estimations of nuclear waste disposal. *Radiochim. Acta* 104, 381–397. doi:10.1515/ract-2015-2490

Fellhauer, D., Neck, V., Altmaier, M., Lutzenkirchen, J., and Fanghanel, T. (2010). Solubility of tetravalent actinides in alkaline $CaCl_2$ solutions and formation of $Ca_4[an(OH)_8]^{4+}$ complexes: A study of Np(IV) and Pu(IV) under reducing conditions and the systematic trend in the an(IV) series. *Radiochim. Acta* 98, 541–548. doi:10.1524/ract.2010.1751

Fellhauer, D., Rothe, J., Altmaier, M., Neck, V., Runke, J., Wiss, T., et al. (2016b). Np(V) solubility, speciation and solid phase formation in alkaline $CaCl_2$ solutions. Part I: experimental results. *Radiochim. Acta* 104, 355–379. doi:10.1515/ract-2015-2489

Fellhauer, D. (2013). *Untersuchungen zur Redoxchemie und Löslichkeit von Neptunium und Plutonium*. PhD thesis. Germany: University of Heidelberg.

Gilbert, R. A., and Garrett, A. B. (1956). The equilibria of the metastable crystalline form of beryllium hydroxide - $Be(OH)_2$ in hydrochloric acid, perchloric acid and sodium hydroxide solutions at 25°C. *J. Am. Chem. Soc.* 78, 5501–5505. doi:10.1021/ja01602a012

Green, R. W., and Alexander, P. W. (1965). Schiff base equilibria .2. Beryllium complexes of N-N-butylsalicylideneimine and hydrolysis of Be^{2+} ion. *Aust. J. Chem.* 18, 651–659. doi:10.1071/ch9650651

Grenthe, I., Gaona, X., Plyasunov, A. V., Rao, L., Run-de, W. H., Grambow, B., et al. (2020). *Second update on the chemical thermodynamics of uranium, neptunium, plutonium, americium and technetium*. Paris, France 2020: OECD Publications. OECD Nuclear Energy Agency Paris.

Hietanen, S., Sillen, L. G., Toplin, I., Melera, A., and Nilsson, L. (1964). Studies on the hydrolysis of metal ions. 52. A recalculation of emf data on beryllium hydrolysis. *Acta Chem. Scand.* 18, 1015–1016. doi:10.3891/acta.chem.scand.18-1015

Humphrey, W., Dalke, A., and Schulten, K. (1996). VMD: visual molecular dynamics. *J. Mol. Graph.* 14, 33–38. doi:10.1016/0263-7855(96)00018-5

Jin, X. Y., Liao, R. B., Wu, H., Huang, Z. J., and Zhang, H. (2015). Structures and formation mechanisms of aquo/hydroxo oligomeric beryllium in aqueous solution: A density functional theory study. *J. Mol. Model.* 21, 232. doi:10.1007/s00894-015-2779-x

Kakihana, H., and Maeda, M. (1970). The hydrolysis of the beryllium ion in heavy water. *Bull. Chem. Soc. Jpn.* 43, 109–113. doi:10.1246/bcsj.43.109

Kakihana, H., Sillen, L. G., Ormerod, J. G., Stenhagen, E., and Thorell, B. (1956). Studies on the hydrolysis of metal ions. XVI. The hydrolysis of the beryllium ion, Be2+. *Acta Chem. Scand.* 10, 985–1005. doi:10.3891/acta.chem.scand.10-0985

Kulik, D. A., Miron, G. D., and Lothenbach, B. (2022). A structurally-consistent CASH+ sublattice solid solution model for fully hydrated C-S-H phases: thermodynamic basis, methods, and Ca-Si-H_2O core sub-model. *Cem. Conc. Res.* 151, 106585. doi:10.1016/j.cemconres.2021.106585

Lanza, E., and Carpéni, G. (1968). Recherches sur le point isohydruque et les equilibres de condensation ou association-XXV. Etude electromerique de l'hydroxoxomplexation du cation $(Be. aq)^{2+}$ Electrochim. *Acta* 13, 519–533. doi:10.1016/0013-4686(68)87023-9

Li, P. F., and Merz, K. M. (2014). Taking into account the ion-induced dipole interaction in the nonbonded model of ions. *J. Chem. Theory Comput.* 10, 289–297. doi:10.1021/ct400751u

Li, Z., Song, L. F., Li, P. F., and Merz, K. M. (2020). Systematic parametrization of divalent metal ions for the OPC3, OPC, TIP3P-FB, and TIP4P-FB water models. *J. Chem. Theory Comput.* 16, 4429–4442. doi:10.1021/acs.jctc.0c00194

Longhurst, G. R., Carboneau, M. I., and Mullen, C. K. (2003). "Challenges for disposal of irradiated beryllium," in Proceedings of the 6th IEA Workshop on Beryllium Technology, Mizayaki, Japan, Dec. 2-5.

Marx, D., Sprik, M., and Parrinello, M. (1997). *Ab initio* molecular dynamics of ion solvation. The case of Be^{2+} in water. *Chem. Phys. Lett.* 273, 360–366. doi:10.1016/s0009-2614(97)00618-0

Mattock, G. (1954). The hydrolysis and aggregation of the beryllium ion. *J. Am. Chem. Soc.* 76, 4835–4838. doi:10.1021/ja01648a019

Mesmer, R. E., and Baes, C. F. (1967). *Hydrolysis of beryllium(II) in 1 m NaCl*. Chem: Inorganic Chemistry Inorg.

Miron, G. D., Kulik, D. A., and Lothenbach, B. (2022a). Porewater compositions of Portland cement with and without silica fume calculated using the fine-tuned CASH+NK solid solution model. *Mat. Struct.* 55, 212. doi:10.1617/s11527-022-02045-0

Miron, G. D., Kulik, D. A., Yan, Y., Tits, J., and Lothenbach, B. (2022b). Extensions of CASH+ thermodynamic solid solution model for the uptake of alkali metals and alkaline earth metals in C-S-H. *Cem. Conc. Res.* 152, 106667. doi:10.1016/j.cemconres.2021.106667

Moog, H. C., Bok, F., Marquardt, C. M., and Brendler, V. (2015). Disposal of nuclear waste in host rock formations featuring high-saline solutions - implementation of a thermodynamic reference database (THEREDA). *Appl. Geochem.* 55, 72–84. doi:10.1016/j.apgeochem.2014.12.016

Neck, V., Altmaier, M., Rabung, T., Lutzenkirchen, J., and Fanghanel, T. (2009). Thermodynamics of trivalent actinides and neodymium in NaCl, $MgCl_2$, and $CaCl_2$ solutions: solubility, hydrolysis, and ternary Ca-M(III)-OH complexes. *Pure Appl. Chem.* 81, 1555–1568. doi:10.1351/pac-con-08-09-05

Ohtaki, H. (1967). Ionic equilibria in mixed solvents. I. Hydrolysis of beryllium ion in a 0.2 mole fraction dioxane-water mixture containing 3 M $LiClO_4$ as an ionic medium. *Inorg. Chem.* 6, 808–813. doi:10.1021/ic50050a033

Ohtaki, H., and Kato, H. (1967). Ionic equilibria in mixed solvents. 2. Hydrolysis of beryllium ion in a 0.1 mole fraction dioxane-water mixture and in aqueous solution containing 3 M $LiClO_4$ as an ionic medium. *Inorg. Chem.* 6, 1935–1937. doi:10.1021/ic50056a045

Pâris, M. R., and Gregoire, C. (1968). Application de la coulometrie à l'etude des complexes. I. Appareillage et application à l'hydrolyse de l'ion beryllium(II). *Anal. Chim. Acta* 42, 431–437. doi:10.1016/s0003-2670(01)80335-4

Perera, L. C., Raymond, O., Henderson, W., Brothers, P. J., and Plieger, P. G. (2017). Advances in beryllium coordination chemistry. *Coord. Chem. Rev.* 352, 264–290. doi:10.1016/j.ccr.2017.09.009

Plimpton, S. (1995). Fast parallel algorithms for short-range molecular-dynamics. *J. Comput. Phys.* 117, 1–19. doi:10.1006/jcph.1995.1039

Rabung, T., Altmaier, M., Neck, V., and Fanghanel, T. (2008). A TRLFS study of Cm(III) hydroxide complexes in alkaline $CaCl_2$ solutions. *Radiochim. Acta* 96, 551–560. doi:10.1524/ract.2008.1536

Schwarzenbach, G. (1962). Metastabile Protonierungs-und Deprotonierungsprodukte anorganischer Molekeln und Ionen. *Pure Appl. Chem.* 5, 377–402. doi:10.1351/pac196205030377

Schindler, P., and Garett, A. B. (1960). Löslichkeitsprodukte Von Metalloxiden Und -Hydroxiden .5. Die Loslichkeit von -$Be(OH)_2$ in Verdunnten Säuren. *Helv. Chim. Acta* 43, 2176–2178. doi:10.1002/hlca.19600430740

Schwarzenbach, G., and Wenger, H. (1969). Die protonierung von metall-aquaionen I.: be·aq^{2+} solvatations-isomerie. *Helv. Chim. Acta* 52, 644–665. doi:10.1002/hlca.19690520313

Shannon, R. D. (1976). Revised effective ionic radii and systematic studies of interatomic distances in halides and chalcogenides. *Acta Cryst.* A32, 751–767. doi:10.1107/s0567739476001551

Tsukuda, H., Kawai, T., Maeda, M., and Ohtaki, H. (1975). Ionic equilibria in mixed solvents. XI. A critical survey of hydroxo complexes of beryllium in aqueous and aqueous mixed solvents. *Bull. Chem. Soc. Jpn.* 48, 691–695. doi:10.1246/bcsj.48.691

Vanni, A., Gennaro, M. C., and Ostacoli, G. (1975). Equilibrium studies of beryllium complexes. *J. Inorg. Nucl. Chem.* 37, 1443–1451. doi:10.1016/0022-1902(75)80788-3

Vollpracht, A., Lothenbach, B., Snellings, R., and Haufe, J. (2016). The pore solution of blended cements: A review. *Mater. Struct.* 49, 3341–3367. doi:10.1617/s11527-015-0724-1

Yalcintas, E., Gaona, X., Altmaier, M., Dardenne, K., Polly, R., and Geckeis, H. (2016). Thermodynamic description of Tc(IV) solubility and hydrolysis in dilute to concentrated NaCl, $MgCl_2$ and $CaCl_2$ solutions. *Dalton Trans.* 45, 8916–8936. doi:10.1039/c6dt00973e

frontiers | Frontiers in Nuclear Engineering

TYPE Original Research
PUBLISHED 27 November 2023
DOI 10.3389/fnuen.2023.1308064

OPEN ACCESS

EDITED BY
Tara Beattie,
TB Environmental Services Ltd.,
United Kingdom

REVIEWED BY
Mavrik Zavarin,
Lawrence Livermore National Laboratory
(DOE), United States
Nathalie Wall,
University of Florida, United States

*CORRESPONDENCE
B. Grambow,
✉ grambow@subatech.in2p3.fr

RECEIVED 05 October 2023
ACCEPTED 08 November 2023
PUBLISHED 27 November 2023

CITATION
Grambow B, Müller R, Schild D and
Gaona X (2023), Solids, colloids, and the
hydrolysis of tetravalent uranium in
chloride media.
Front. Nucl. Eng. 2:1308064.
doi: 10.3389/fnuen.2023.1308064

Solids, colloids, and the hydrolysis of tetravalent uranium in chloride media

B. Grambow[1,2]*, R. Müller[1], D. Schild[1] and X. Gaona[1]

[1]Karlsruhe Institute for Technology, Institut für Nukleare Entsorgung, Karlsruhe, Germany, [2]SUBATECH, CNRS-IN2P3, Nantes University, IMT Atlantique, Nantes, France

Understanding of the properties of dissolution and precipitation of Uranium under reducing geochemical conditions is important in radioactive waste management and assessments of natural uranium deposits. The mechanism of forming UO_{2+y} from U(VI) and U(IV) containing aqueous solution (1 M NaCl) and the solubilities of the precipitates were studied under well-controlled reducing conditions as a function of pH, particle size, and supersaturation. The results show that tetramer and colloid formation are critical initial steps. Precipitation is not growth-controlled but appears to be nucleation-controlled, with critical nuclei dimensions of one unit cell of UO_2. The precipitates were always crystalline, and amorphous UO_2 was not observed.

KEYWORDS

solubility, uranium, redox, colloids, precipitation

1 Introduction

The geochemical cycle of uranium, the stability of ore deposits, and its general distribution among mobile and immobile phases strongly depends on phase and species oxidation states and corresponding redox reactions. In natural geochemical environments, uranium exists almost entirely as U(IV) or U(VI). The low mobility of uranium is associated with the tetravalent state, with uraninite being the most abundant solid phase. Uraninite ore deposits are often stable for billions of years, provided that reducing conditions are maintained. By analogy, as a nuclear waste form for deep geological disposal, uranium dioxide is expected to be highly stable if reducing conditions are maintained. Under oxidizing conditions, uranium is soluble as a uranyl(VI) ion; in particular, carbonate complexation further increases uranium(VI) mobility, even under fairly strong reducing conditions ($pe + pH < 5$).

However, due to colloid formation, the tetravalent state of uranium also shows some mobility.

Well-performed experimental studies have established the thermodynamics of UO_2 solubility with respect to dissolved tetravalent uranium species in the pH range 0–12 (Parks and et Pohl, 1988; Bruno et al., 1987; Rai et al., 1997; Cevirim-Papaioannou, N. 2018; Fujiwara et al., 2003). Uncertainty in thermodynamic solubility data remains, particularly under low-temperature (25 °C) conditions (Yajima and Kawamura, 1995). At ambient temperatures, solubility data under carbonate-free reducing conditions vary by as much as five orders of magnitudes for a given pH (Yajima and Kawamura, 1995). This difference was interpreted as resulting from different crystallinity (Bruno et al., 1987) or insufficient control of low redox conditions (Rai et al., 1990; Yajima and Kawamura, 1995). A further source of uncertainty is the oxidation state of uraninite. Pure $UO_{2.00}$ can be oxidized rather easily to phases such as UO_{2+x}, U_4O_9, or U_3O_7. All these phases have essentially the same crystal structure (fluorite), but their solubility as well as their dissolution rates can deviate by orders of magnitude.

The aim of this research was to study the transition from dissolved U(IV) to the formation of polymer and colloidal species and then to solid precipitates to study the properties of these precipitates, including the effect of particle size on solubility.

2 Experimental

2.1 Description of test procedures

Four types of solid/liquid interaction experiments were performed under reducing hydrogen saturated conditions, approaching solubility equilibria either from supersaturated or undersaturated conditions: 1) electrochemical reduction of an aqueous U(VI) solution to an U(IV) solution, followed or not by formation of a U(IV) precipitate; 2) solubility tests with U(IV) precipitates from test (1); 3) precipitation of U(IV) solid phases by alkaline titration of an initially acid U(IV) solution; 4) solubility tests with large UO_2 particles. pH values and reducing conditions were always controlled by the counteraction of acidometric and coulometric titration. No precautions were taken to fix the pH at constant values if the reaction drove the pH in an acidic direction, such as due to precipitation or polymerization.

(1) Reduction experiments with UO_2Cl_2 in 1 M NaCl solutions were performed in the pH range 1–4. A new experiment was performed at each pH. The pH was held constant at ±0.05 pH units. In most reduction tests, the current being passed through the coulometric bridge was held at 1 mA, with a starting concentration of U(VI) of 0.005 m. Supersaturated conditions were slowly achieved by this coulometric reduction. In order to study the effect of U(IV) generation rates on the formation of U(IV) precipitates, the current in a few tests was varied between 0.05 and 1 mA (error ±0.1%). In order to study the effect of colloid growth or crystal growth on final U(IV) concentrations, starting concentrations of 0.01 and 0.001 m were also used in certain experiments. Experiments typically lasted a few days.

(2) In order to investigate whether the measured ultrafiltered U(IV) concentrations reflect thermodynamic equilibrium with respect to stable or metastable precipitates, solubility experiments were performed in the same reaction vessels after terminating the reduction reaction. The precipitate of a reduction experiment performed at pH 2.56 was therefore allowed to settle, and unsaturated conditions were established by replacing the supernatant solution with the help of an Ar-filled syringe by fresh deoxygenated 1 M NaCl solution without allowing the precipitate to dry or come in contact with oxygen. The procedure was repeated twice. The solubility test was then started under conditions of coulometric/acidometric control of reducing conditions and of pH. The uranium concentration increased in the fresh NaCl solution by dissolution of the precipitate. The increase of uranium concentration in the new solution was studied as a function of time until constant concentrations were obtained (3 days). Thereafter, the pH was varied stepwise to study the solubility as a function of pH.

(3) In another experiment, supersaturated conditions were achieved by alkali added to a 0.005 M UCl_4/1 M NaCl solution (pH 0.2) until a selected pH was achieved. This experiment avoids the drawback of experiment (1), where some U(VI) may have been incorporated into the U(IV) precipitate. The entire experiment lasted 60 days, including the shift to pH 12 and, thereafter, the return to pH 0.

(4) For comparison, solubility tests were performed for 60 days with high bulk purity $UO_{2.00}$ of 100–200 µm size using depleted uranium. This material had been stored as pellets for some years in air, which may have caused surface oxidation of a few monolayers. The powder was cleaned in an ultrasonic bath in acetone to remove adhering fines and was placed under Ar into the reaction vessel. Based on the geometric surface area of the powder (0.04 m^2/g), a ratio of surface area to solution volume of $S/V = 40\ m^{-1}$ was adjusted. The experiment was commenced at pH 2.5, and the pH was varied both in acid and alkaline directions. The supernatant solution was replaced twice by fresh solution to test the equilibrium state of the solid/liquid system and to dissolve potentially remaining U_3O_7 surface layers. The whole experiment lasted 60 days.

2.2 Description of equipment

All experiments were performed in 50–100 mL of 1 M NaCl solution placed in a double-walled reaction vessel made from borosilicate glass. A scheme of the reaction vessel is given in Supplementary Figure S1.

The vessel was equipped with five ground glass neck joints for introducing Teflon capillary tubing (inner diameter 0.3 mm) for acidometric titration, a pH-electrode, a salt bridge, a platinized Pt-counter electrode combined with an Ar-gas inlet, and a sampling port for solution samples. The temperature was held constant at 25.0 °C±0.1 °C using a K20/DC1thermostat (Fa. Haake). Coulometric titrations were performed using a mercury electrode connected to the reaction vessel via a 1 M $NaClO_4$-filled salt bridge. The salt bridge was filled with 1 M $NaClO_4$. After passing $5{\cdot}10^{-3}$ F through the bridge, the Hg had to be regenerated (alternate washing with 10% NaOH and 10% HCl); due to the formation of white crystals, the $NaClO_4$ of the bridge had to be replaced. The counter electrode consisted of Pt–Rh mesh enclosing the Ar-gas inlet. Finally, the sampling port consisted of a stopcock connected to a pipe tee with ends closed by septa.

The coulometric titration was controlled either by a constant current source type 6402 (Fa. Burster) with a maximum error of 0.1% or using a DIGISTAN® Typ 6705 (Fa. Burster) calibration source with an error of 0.2% at 1 mA and 2% at 0.1 mA. Coulometric titration leads to both reduction and alkalization of the solution. In order to perform reductive titration at a fixed pH or at a sequence of preselected pH-values, alkalization was counterbalanced by acidimetric pH-stat titration using a Titroprocessor 686 with a Dosimat 665 (both Fa. Metrohm).

2.3 Stability of reducing media

Even traces of oxidants will cause oxidation of dissolved U(IV) to U(VI), so experiments with U(IV) species must be performed under conditions which exclude all oxygen access. This is ensured in the present work by performing the experiments in nearly closed reaction vessels under a permanent stream of 4 L/h of 99.999% pure Ar. Prior to passing into the reaction vessel, the Ar was passed through three washing bottles: the first contained a blue solution of ammonium vanadate in HCl over Zn-amalgam to remove traces of oxygen in the gas. V(V) was regenerated if the vanadate had been oxidized to green V(VII). The second and third wash bottles contained 1 M NaCl to ensure that the relative humidity of the Ar-stream was in equilibrium with the water activity in the reaction vessel to avoid water evaporation or condensation during Ar-bubbling. Since this bubbling may not have been sufficient to remove all leaking oxygen, the solutions were permanently titrated coulometrically using a current of 0.05–1 mA. This should ensure the immediate reduction of any leaking oxygen.

Special precautions were taken to maintain reducing conditions during the introduction of solid and liquid phases into the reaction vessel, as well as during sampling, transfer, and the use of samples in the various analytical procedures.

- Oxygen-free NaCl solutions, U(VI) containing NaCl solutions, and HCl solutions for acidometric titration were prepared by boiling 1) nanopure water for 3 h in an Ar stream in a quartz vessel and 2) passing the oxygen-free water by Ar pressure via liquid transfer lines into an Ar-containing stopcock-sealed storage flask. Oxygen-free conditions in the flask were ensured prior to introducing oxygen-free water by alternating evacuation and flushing by Ar gas. From the storage flask, oxygen-free water was transferred by Ar pressure via liquid transfer tubes into similarly prepared flasks previously filled with either a weighted aliquot of solid NaCl (p.a. quality) with an aliquot of a uranyl chloride solution, or with HCl. The flask was located on a balance to allow the accurate adjustment of target concentrations. The resulting solutions were analyzed for U (ICP-AES). Errors in the starting concentrations were below 0.5%. Finally, the oxygen-free uranyl ion containing NaCl solutions were transferred by Ar pressure via liquid transfer lines through a septum into the reaction vessel (sampling port).
- Solution and solid sampling during the experiment or at test termination was also performed under inert conditions. This is true for non-filtered samples, for solutions filtered by 0.45 μm membranes, and for ultrafiltered solution samples. Solution sampling was facilitated via an Ar-filled syringe attached to an inline membrane filter (pore size 0.45 μm), a two directional stopcock, and a Teflon capillary that intersected the septum of the sampling port. An aliquot of the 0.45 μm filtrate was transferred by this system directly under Ar into the ultrafilter unit (Centrisart cut-off 20.000, Fa. Sartorius) prior to being centrifuged for 5 min.
- In case of precipitation, suspended samples of the solid phase were collected on the 0.45 μm filter membrane. The precipitate was washed twice with 10 mL water to remove NaCl contents. No precautions were taken to avoid oxygen access during the washing of the solid precipitates, but, after few minutes, the filters with the solid samples were dried and stored in a desiccator over $CaCl_2$ in an Ar atmosphere. However, this precaution may not have been sufficient to prevent surface oxidation of the precipitates detectable by XPS analyses (see chapter 3.6.4). Therefore, in the case of solubility experiments with large UO_2 particles, the reaction vessel was opened in an inert gas box (impurities of 15 ppm of O_2) to prevent oxidation of the UO_2 surfaces. After washing off the adhering NaCl solution, the samples were pressed in their wet state into a foil of indium and were transferred under inert gas conditions into the vacuum chamber of the XPS.

2.4 Analytical procedures

2.4.1 Solution analyses

Online pH measurements were performed during the experiments. A combination electrode System Ross (SC 8162) was used, filled with 1 M NaCl solution. This electrode is highly stable in saline solutions and small time drifts. Electrode calibration was performed using NIST-standard solutions. For pH levels close to 0, a 1 M HCl solution was used as reference. A pH of 0.24 with respect to the NBS-pH convention was calculated with the geochemical code EQ3/6 (Wolery, 1983; Scherbaum and Knopp, 1996). The electrode calibration procedures were adapted to the experimental setup. In case of the reduction of a U(VI) solution at a fixed pH, two-point calibration within one pH unit was performed, whereas if the pH varied between 0 and 12, calibration was performed using seven pH buffers. The deviation of a single buffer from a straight-line calibration curve was always less than 0.03 pH units. If an experiment lasted up to 5 days, only one calibration at the beginning of the test was sufficient. In experiments with pH variations between 0 and 12, the duration of the test was up to 2 months. In this case, the calibration was checked at test termination, using the same buffer solutions as before. An average drift of +0.18±0.05 pH units was observed after 2 months. Drift correction was made assuming a linear drift increase with time at a rate of 0.003/d. All pH values measured were corrected for liquid junction and were referred to the pH convention $pH \equiv \log m_{H+} — \log \gamma_{H+} \equiv 1$. Correction was made by the equation $pH_{corr} = pH_{meas} + \Delta pH$ with a ΔpH value of 0.06 determined using the NIST-buffer calibrated electrodes in 1 M NaCl solutions with a known molality of H^+.

Solution samples for determining total U-concentrations were acidified prior to analysis. Solution concentrations of uranium $>10^{-4}$ m were analyzed by ICP-OES (ARL 3580), and lower concentrations by ICP-MS (PerkinElmer Elan 6000). The introduction of highly saline solutions into the ICP-mass spectrometer will cause mechanical blocking of the sampler and skimmer cones. The analysis of uranium in saline solutions, therefore, is made by flow injection. Only 100 μL of a 1:5 diluted sample was injected into the ICP-MS. Physical and chemical interferences generated by the salt matrix were corrected by using Lu-175 as an internal standard.

To determine solution speciation and to check the completeness of the reduction process and the efficiency of inert solution handling procedures, U(IV)-containing solutions in the pH range 0–2 were analyzed by UV-VIS spectroscopy in a glove box with 100% Ar atmosphere and an oxygen content lower than 10 ppm. A sample holder with a 1 cm quartz cuvette was therefore placed in the glove box and connected to a CARY-5E spectrometer (Varian) outside the box via an optical fiber system. The spectra were taken in the wavelength range 300–750 nm and evaluated using GRAMS software (Galactic). In certain cases, the evolution with time of solution speciation was followed over more than 14 days.

2.4.2 Colloid analyses

Colloids formed during the reduction of U(VI) solutions were analyzed using both ultrafiltration and laser breakdown detection (LIBD). By focusing a laser beam with sufficient power on or into the probe, a plasma can be generated. The critical power density to produce a plasma—the breakdown threshold—is much lower for solids than for liquids (Radziemski and et Cremers, 1989; Bettis, 1992). Thus, if the laser pulse power density does not exceed the breakdown threshold of the aqueous phase, the plasma is generated almost exclusively on the colloids. As shown in the literature, the breakdown probability under constant experimental conditions depends on the number, density, size, and material of the colloids (Kitamori et al., 1989; Fujimori et al., 1992; Scherbaum and Knopp, 1996). Colloid sizes as low as a few nm can be detected (Bundschuh et al., 2001).

The experimental setup of the LIBD system is shown in Supplementary Figure S2. A pulsed Nd-YAG laser (Continuum; Surelite I) frequency doubled at $\lambda_{em.}$ = 532 nm with a pulse length of 12 ns and a repetition rate of 20 Hz was used. The energy of the laser pulse is adjusted by a variable attenuator. A breakdown-induced acoustic wave is measured by a piezoelectric detector (PZT) directly attached to the cuvette wall. The spatial distribution of the plasma light emission is monitored by a CCD camera system triggered by the laser pulse using a macro-microscope. This yields, in addition to the acoustic signal of the pressure wave, information about the size distribution of the particles in solution. Colloid sizes as low as 10 nm can be detected.

The LIBD-analyses were performed on U(IV)-containing solutions formed by the reduction of U(VI) solutions at pH values between 1.66 and 1.76 (experiment type 1). The same Ar-filled cuvettes from UV-VIS spectroscopy were also used for LIBD analyses to allow comparison. Colloid formation was followed in the cuvette as a function of time.

2.4.3 Solid-state analyses

The morphology and composition of solid precipitates were determined by SEM/EDX analysis. To obtain the required high resolution of 10 nm, an SEM (CAMSCAN FE-44) with a Schottky emitter source was used.

XRD analyses were performed to determine the crystal structure of the precipitate and estimate the particle size of the precipitates. The powder samples for X-ray diffraction analyses were prepared either by spreading the fine-grained uranium powder over a flat sample holder or by analyzing the precipitate-containing filters directly. By using a theta–theta powder diffractometer Seifert XRD 5000 with a graphite secondary monochromator and Ni-filtered Cu K_α (λ = 1.5406 Å) radiation, the sample remained in a horizontal position during measurement. X-ray investigations were performed in step-scan mode over the range $2\theta = 10^\circ$–65° in steps of 0.02°, with a counting time of 2 s/step. The voltage applied was 40 kV and the current was 30 mA (fixed divergency, scatter slits of 1°, receiving slit of 0.2 mm). To improve particle statistics, the sample was rotated using a sample spinner.

The broadening of the diffracted line profiles can be used to estimate mean crystallite dimensions. The width β of a line profile at half maximum (FWHM) is given by the Scherrer relationship

$$\beta = \frac{K \cdot \lambda}{D \cdot \cos \theta},$$

where K is the crystal shape factor (~1), λ is the wavelength, β is the line broadening (radian) derived from the measured width and corrected for instrumental broadening, θ is the diffraction angle (radian), and D is the average particle dimension.

From the equation, it follows that, for particle sizes approximately below 50 nm, the broadening of the diffraction lines increases strongly and, conversely, the method is very sensitive for small particles <500 Å. Particle size determination by X-ray diffraction does not necessarily agree with the real or microscopic size. Only the coherent diffracting domains are determined by X-ray diffraction. The line broadening can also be increased by lattice strains, which result from displacements of the unit cells and by crystal defects, such as stacking disorder in montmorillonite. In the case of the sample material studied, such broadening effects can be excluded.

In order to determine uranium oxidation states and water/hydroxide contents of the solid phases and their surfaces, analysis by XPS (PHI Model 5600ci) was performed using the monochromatized X-ray radiation Al K_α (1486.7 eV). Transfer of solid UO_2 particles (experiment type 4) was performed for all steps in an Ar atmosphere. The diameter of the sampling areas was 0.4 or 0.8 mm. No charging of the sample during measurement was observed. To identify and quantify the elements, survey scans were determined at high pass energy of the analyzer (187.85 eV). Atomic concentration was determined with 10%–20% of relative uncertainty. In order to determine binding energies, the energy resolution of the analyzer was increased by reducing the pass energy to 11.75 eV. The full width half maximum (FWHM) of the Ag $3d_{5/2}$ elemental line of pure silver was then 0.62 eV. The binding energy scale was calibrated by reference lines of Cu $2p_{3/2}$, Ag $3d_{5/2}$, and Au $4f_{7/2}$ of the pure metals determined with the same measurement parameters.

Transmission electron microscopy analyses (TEM) were performed with two devices: the TEM EM 400 (Philips) was used with HV = 120 kV, and HRTEM analyses were performed using the CM12 (Philips) with a Super Twin Objective Lens, HV = 120 kV, a point resolution of 3 Å, and a line resolution of 1.4 Å.

Solid samples were analyzed by TEM without precautions against surface oxidation. They were stored under Ar but were exposed to air during shipment and sample preparation for approximately 3 days. The precipitated powder was removed from the filter membrane by cutting an area of 2 mm × 2 mm from the membrane, dissolving it in 1 mL p.a. acetone in an ultrasonic bath for 4 min, centrifuging it for 5 min at 6000 U/min in a Eppendorf centrifuge 5415C, and washing four times with 1 mL acetone (4 min ultrasonic bath, 5 min centrifugation); then, after decanting the acetone, the wet residue was homogenized in an ultrasonic bath and a drop of it was placed onto a carbon-coated Cu-grid (200 mesh) for analysis.

3 Results

3.1 Reduction of water and oxygen in the reaction vessel

The coulometric reductive decomposition of water molecules leads to an alkalization of the solution, which is balanced by

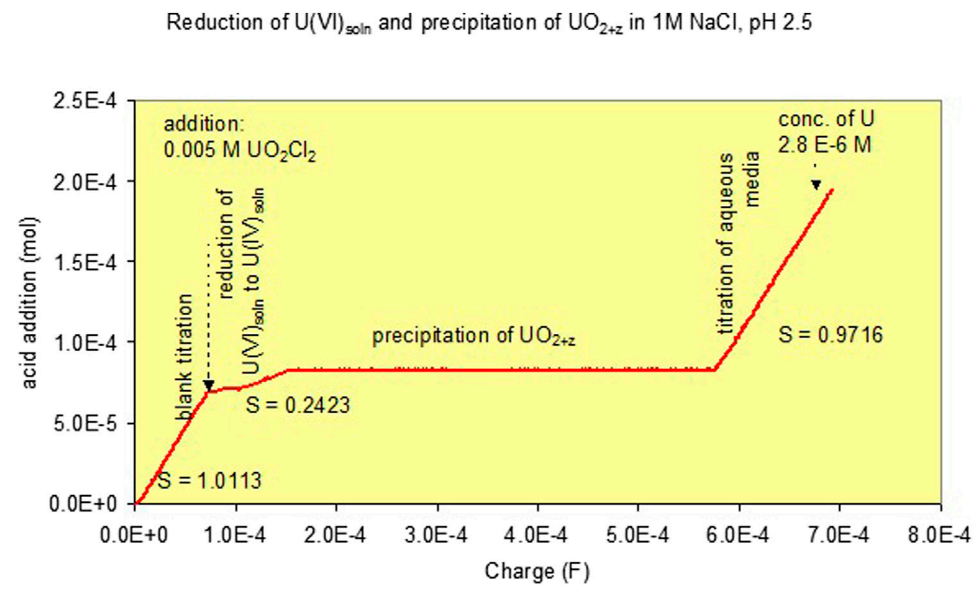

FIGURE 1
Curve for combined volumetric pH stat and coulometric titrations to a 1 M NaCl solution at pH 2.5. Effect of the addition of 0.005 m U(VI) and its reduction and precipitation as UO_{2+z} [Experiment (1)].

acidimetric titration. In the absence of uranyl ions or after completely terminating the reduction of uranyl ions, slopes m = Δ(equivalents added acid)/ΔFaraday close to unity were determined between pH 2 and 11 with correlation coefficients between coulometric and acidometric additions between 0.99 and 0.9999 (Supplementary Figure S3).

There are two reactions in the absence of uranyl ions, both of which require one equivalent of acid added per mole of electron transfer for pH stat conditions; the reduction of water according to the reaction was

$$2e^- + 2H_2O + 2Na^+_{Bridge} \rightarrow H_2(g) + 2Na^+ + 2OH^-$$

and the reduction of possibly remaining traces of dissolved oxygen was according to

$$2e^- + \frac{1}{2}O_2(aq) + H_2O + 2Na^+_{Bridge} \rightarrow 2Na^+ + 2OH^-$$

3.2 Reduction of U(VI)-containing solutions (experiment type 1)

In the presence of uranyl ions, slopes m between 2 and 0 were observed. The results for various pH levels are given in Supplementary Figure S4. Slopes m of 0 were observed once precipitation was encountered. A typical titration curve for precipitation at pH 2.5 is given in Figure 1. Initially, a 1 M NaCl blank solution was reduced to remove potentially remaining oxygen. After adding $7.2\cdot10^{-5}$ F, an aliquot of deoxygenated UO_2Cl_2 solution was added to achieve a U concentration of 0.005 m. Further addition of up to $7.8\cdot10^{-5}$ F led to a reduction of U(VI) to U(IV) in the solution phase. The slope m was 0.24. Addition of a further charge led to precipitation of black U(IV) containing phases and a slope of zero. Finally, after all U(VI) was again reduced, a slope of unity was achieved. It can be seen that the onset of precipitation can be monitored by the changes of slopes m = Δ(equivalent added acid)/ΔFaraday.

The heterogeneous reduction leads to U(IV) oxide precipitation principally according to the following reaction:

$$UO_2^{2+} + 2e^- + 2Na^+_{Bridge} \rightarrow UO_2(S) + 2Na^+$$

which would not lead to any change in pH. Considering mass balance, 2 Faradays would have to be used for 1 mole of $UO_2(s)$ formation. Alternatively, U_3O_7, or U_4O_9, or UO_{2+y} in general may have been formed with y being 0.33 for U_3O_7 and 0.25 for U_4O_9:

$$UO_2^{2+} + 2(1-y)e^- + yH_2O + 2(1-y)Na^+_{Bridge} \rightarrow UO_{2+y}(S) + 2(1-y)Na^+ + 2yH^+$$

This reaction would lead to an acidification of the solution. However, no precautions were taken for alkalimetric titration to fix the pH. Consequently, the pH would decrease until the reduction was completed. In the plot Δ(equivalent added acid) versus ΔFaraday, this would result also in a slope m of 0.

A variety of reactions are possible for homogeneous reduction in solution phase, which lead either to U(V) or U(IV). The reduction to U(V) is only possible in the acid range because, under alkaline conditions, U(V) is not stable. Under acidic conditions, only the free non-hydrolyzed uranyl(V) ion is stable (UO_2^+) as intermediate species and reduction may thus be described by a single reaction:

$$UO_2^{2+} + e^- + Na^+_{Bridge} \rightarrow UO_2^+ + 2Na^+$$

This process does not require the addition of acid to keep the pH constant. The reduction of an intermediate U(V) to U(IV) would require 4 moles of acid addition per mole of electron transfer:

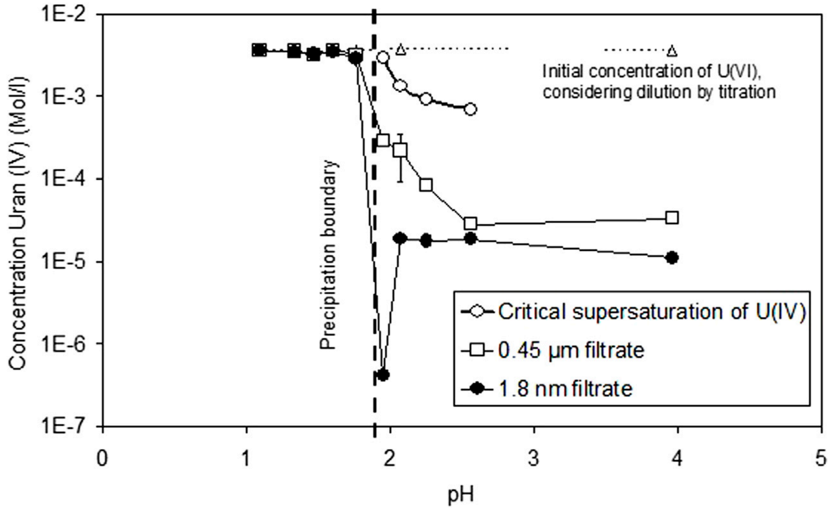

FIGURE 2
Solution concentrations of dissolved U(IV) as a function of pH, comparing both filtered, ultrafiltered, and non-filtered solutions. Critical supersaturation concentrations of U(IV) before precipitation are observed.

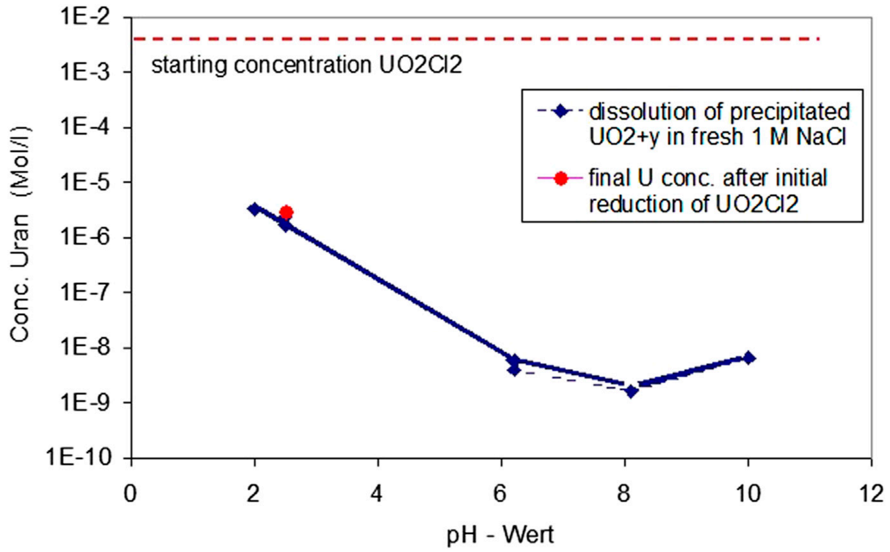

FIGURE 3
Study of the reversibility of the solubility equilibrium of the precipitates by redissolution at the same pH and solution composition of precipitates formed 1 M NaCl solution at pH 2.56, continuing coulometric titration and counterbalancing acidometric titration.

$$UO_2^+ + e^- + 2H_2O + Na^+_{Bridge} \rightarrow U^{4+} + Na^+ + 4OH^-$$

In contrast, the direct reduction of U(VI) to U(IV) under strongly acid conditions leads to U^{4+} and requires two equivalent additions of a strong acid per mole of electron transfer.

$$UO_2^{2+} + 2e^- + 2H_2O + 2Na^+_{Bridge} \rightarrow U^{4+} + 2Na^+ 4OH^-$$

More generally, considering hydrolysis of U(IV), the general direct reduction from U(VI) to U(IV) can be written as

$$UO_2^{2+} + 2e^- + 2H_2O + 2Na^+_{Bridge} \rightarrow U(OH)_n^{(4-n)} + 2Na^+ + (4-n)OH^-$$

(4−n)/2 moles of strong acid are required to keep the pH constant during the reduction process, whereas the reduction of an intermediate U(V) species would require 4−n moles of strong acid. In this equation, $U(OH)_n^{(4-n)+}$ may be a real species or may represent the species distribution $U(OH)_n^{(4-n)+} \equiv \sum fi \cdot U(OH)_{n_i}^{(4-n_i)}$, with f_i being the fraction of the species i ($\sum_i^i f_i = 1$) and $n = \sum_i f_i \cdot n_i$. Consequently, in the

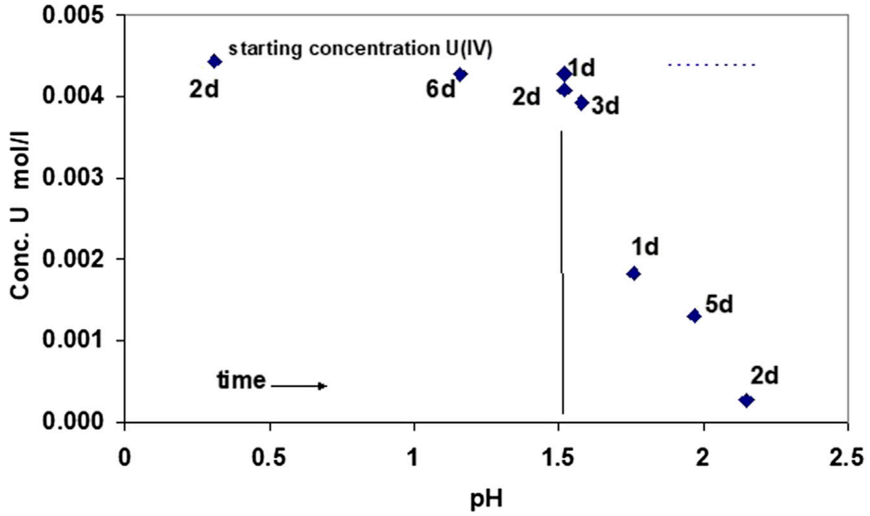

FIGURE 4
Evolution of U(IV) concentrations as a function of time and pH, adding a NaOH solution to a solution of U(IV) at an initial pH of 0.31. Precipitation starts at pH 1.5, as measured by decreasing U(IV) concentration in solution.

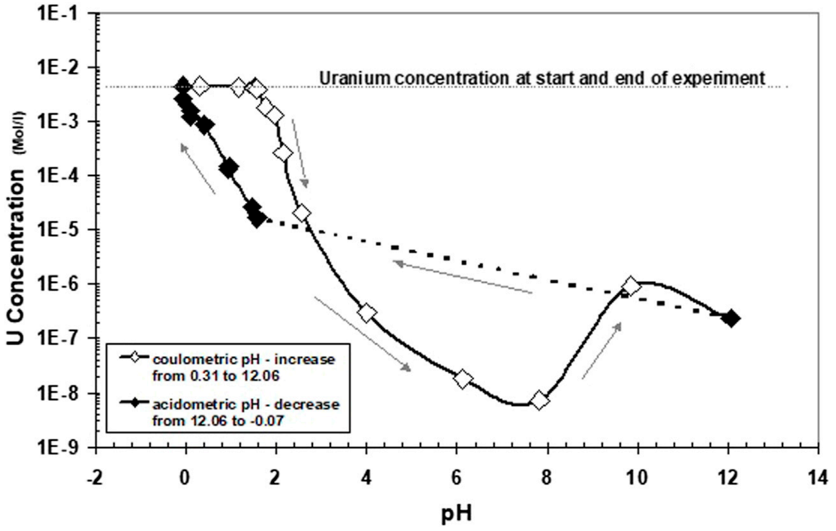

FIGURE 5
Same experiment as described in Figure 4, showing solution concentrations at higher pH values. Arrows denote the direction of pH change.

absence of precipitation and with negligible U(V) intermediates, one may determine n and, with it, an important constraint on the distribution of species from the slope m of the curves of acid consumption during the reduction process $n = 4 - 2 \cdot m$. Supplementary Figure S4 shows the dependency of the slope on pH. In the case of precipitation, only the initial slope until the onset of precipitation is plotted. The data clearly indicate increasing hydrolysis with increasing pH. After completing the reduction of dissolved U(VI), the slope always returned to values close to unity.

The corresponding solution concentrations of dissolved U(IV) are shown in Figure 2 as a function of pH, comparing both filtered, ultrafiltered, and non-filtered solutions. Included in the diagram are the critical supersaturation concentrations C_{cr} of U(IV) necessary to be achieved before precipitation of U(IV) is observed. C_{cr} values are determined by half of the charge added (in Faraday) before slope m turns to 0. Precipitation was observed only at pH values >1.95. At lower pH, the critical supersaturation concentrations were higher than the initial U concentration. This means that, even if all U(VI) is reduced, there is still insufficient U(IV) to allow precipitation in 1–2 days. For pH values higher than 1.95, the C_{cr} values decrease with increasing pH, and, at pH 3.96, precipitation occurred almost instantaneously with the start of the reduction reaction. At pH > 2.1, constant concentrations were observed in the ultrafiltrate samples. The low value at pH 1.95 appears to be an artifact, but repeated

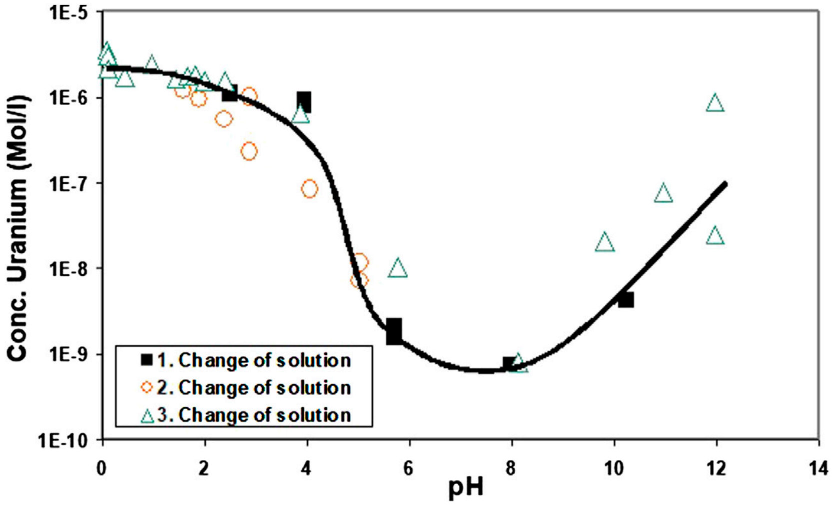

FIGURE 6
Ultrafiltered solution samples resulting from solubility tests with pure 100–200 μm UO_2 particles. The tests were performed under similar conditions as those with the precipitates formed by coulometric reduction.

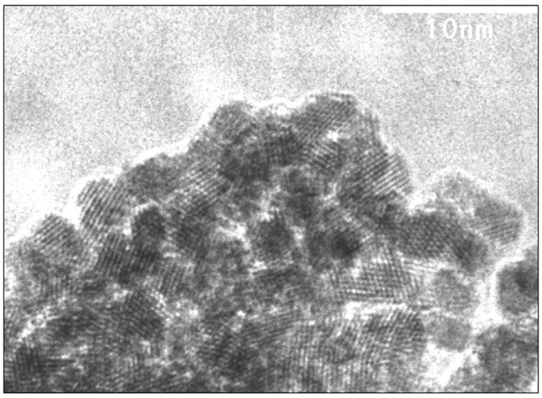

FIGURE 7
HRTEM analyses of precipitate formed after reduction under acidic conditions and subsequent coulometric alkalization of the solution (experiment type 3). Precipitation started at approximately pH 2, and the sample was taken after pH excursion to a value of 12, showing a particle size of approximately 4 nm. The 111 direction is visible with d-spacings between 3.06 and 3.18 Å, corresponding to unit cell parameters between 5.38 and 5.50 Å.

TABLE 1 pH dependence of the color of the solution in the reaction vessel after terminating the reduction process.

pH	Color
0	Weakly rose
1.06	Weakly green
1.33–1.54	Weakly turquoise
1.76	Clear
1.95	Initially clear, then weakly green, and then yellow with traces of gray
2.25–4	Black-gray suspension at the bottom

analyses gave the same results. Based on sequential filtration comparison, the quantity of colloids (difference between 0.45 μm and 1.8 nm filtrate) decreases with pH, potentially indicating pH-dependent coagulation phenomena.

An important parameter in the precipitation process is the rate by which the C_{cr} values are exceeded. This rate was changed by changing the current passing through the coulometric bridge. Supplementary Figure S5 shows the effect of the coulometric current on final U concentrations after terminating the reduction process at pH 2.56 with a starting concentration of U(VI) of 0.005 m.

Increasing currents led to slightly higher supersaturation (pH 2.6: $6.9{\cdot}10^{-4}$ M at 1 mA versus 6.0–$6.3{\cdot}10^{-4}$ M at 0.05–0.1 mA) due to the faster formation of U(IV). They also led to in an increase in the final U-concentration (at pH 2.6 $1.8{\cdot}10^{-5}$ M at 1 mA instead of $5(\pm 2.5){\cdot}10^{-6}$ M at 0.05–0.1 mA) associated with smaller particle sizes and larger solubility (see discussion of the effect of particle size on solubility in chapters 3.4 and 3.5 and in Figure 12). In an attempt to increase particle size (and decrease solubility equilibrium concentrations), the starting concentration of U(VI) was varied. This had no effect on final U-concentrations (data not shown). Consequently, final U(IV) concentrations are controlled by the degree of supersaturation prior to precipitation (nucleation control) and not by the quantity of U available for particle growth (growth control).

3.3 Solubility of precipitates formed by U(VI) reduction (experiment type 2)

In order to check whether final U concentrations from Experiment 1 represent equilibrium concentrations, fresh precipitates formed at pH 2.56 were dissolved at the same pH in fresh 1 M NaCl solution continuing coulometric titration and counterbalancing acidometric titration to study the solubility of the precipitates (Figure 3). After 2 h, U concentrations of $2.3{\cdot}10^{-6}$ m were already achieved, returning almost to the value of $2.8{\cdot}10^{-6}$ m

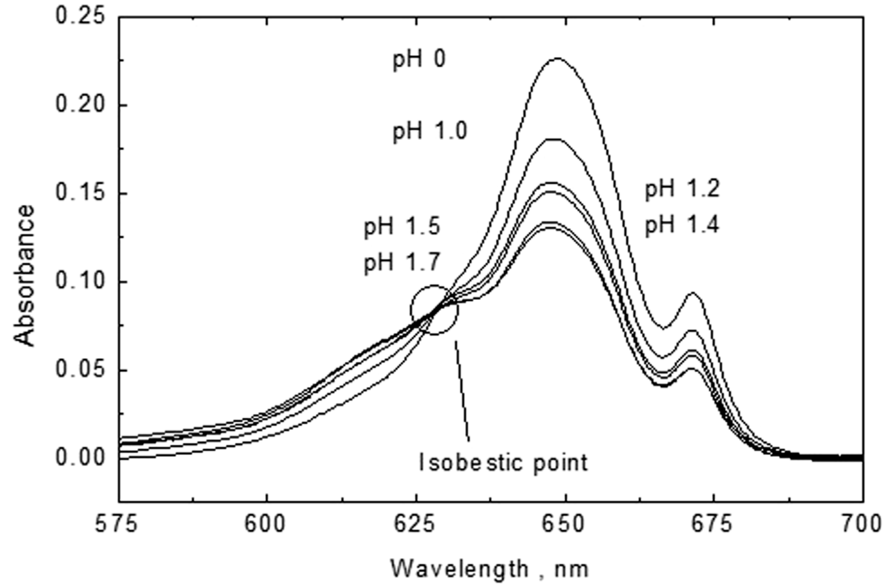

FIGURE 8
An enlargement of the absorption peaks showing an isosbestic point at 623 nm indicative for the presence of only two U(IV) species: U^{+4} and UOH^{+3}.

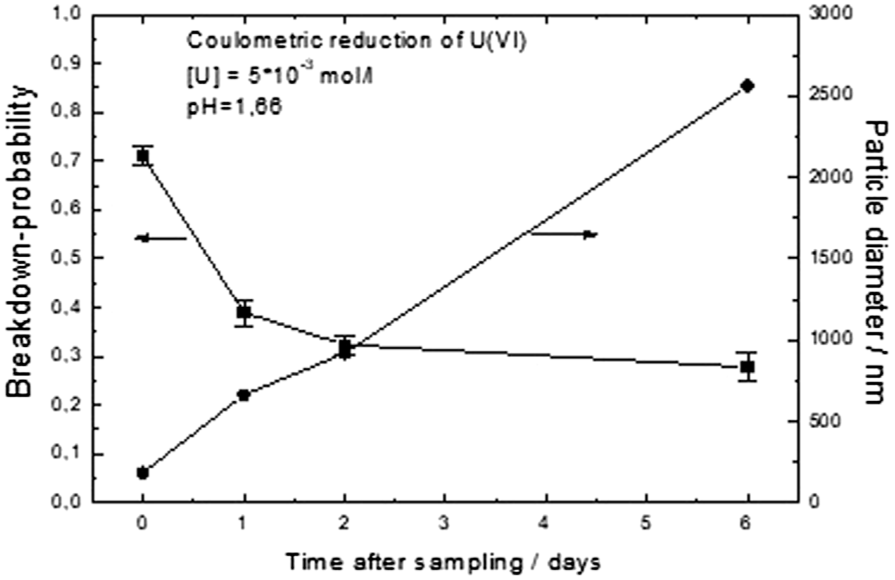

FIGURE 9
Colloid formation studied by laser-induced breakdown detection (LIBD) in a sample resulting from the complete reduction of initially U(VI)-containing solutions at a constant pH of 1.66. The evolution of colloid formation was followed as a function of time for up to 15 days.

achieved in the initial reduction experiment. This indicates equilibrium with respect to the precipitated phases. After three more days, the solution concentration decreased slightly to a value of $1.7{\cdot}10^{-6}$, probably caused by the precipitate's ripening. Thereafter, the pH was first decreased to a value of 2.05 and then stepwise increased to pH 10, leading in the neutral to slightly alkaline pH range to U concentrations well below 10^{-8} m. The experiment lasted 20 days.

3.4 Precipitation from acid U(IV) solutions and solubility of precipitates (experiment type 3)

A characteristic of the reduction experiments (type 1) is that the reaction path often passes the stability field of higher oxidation states first, such as U_4O_9 and U_3O_7, prior to entering the stability field of UO_2. This is shown in Supplementary Figure S6 for the

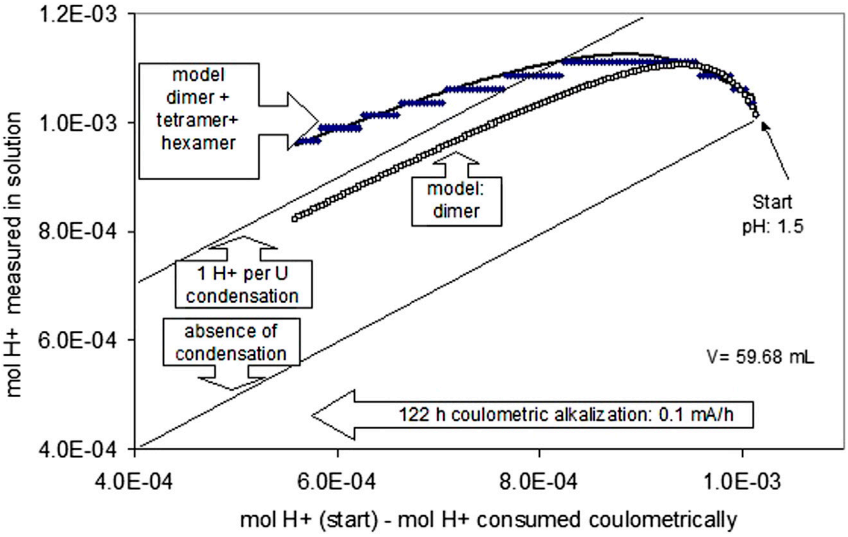

FIGURE 10
Polymerization of U(IV) hydrolysis species at pH 1.5. The lower straight line indicates the expected evolution of the quantity of H^+ in solution in case of the absence of polymerization.

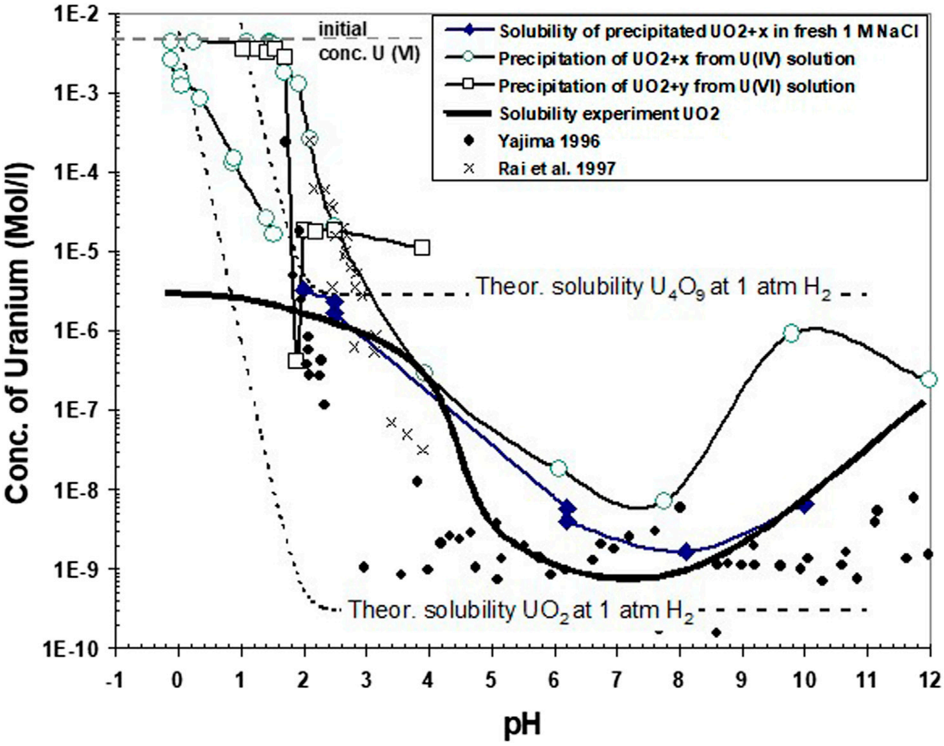

FIGURE 11
Comparison of solubility data obtained in the present study with calculated solubilities (see text) of stoichiometric crystalline and nanocrystalline UO_2 and of crystalline U_4O_9 for aqueous solutions of 1 M NaCl at 1 atm H_2. Additionally, the data are compared with the solubility of crystalline UO_2 in the presence of traces (1E-8 atm) of dissolved O_2, which might have existed in the experimental device.

coulometric reduction/precipitation at pH 2.56, using an Eh/pH diagram calculated for the starting concentration of dissolved U(VI) of 0.005 m. Thus, the path of the coulometric reduction reaction at pH 2.56 will not go directly from the uranyl ion to uraninite, but the first stable phase is U_4O_9. However, the calculation in Supplementary Figure S6 is for well-crystalline

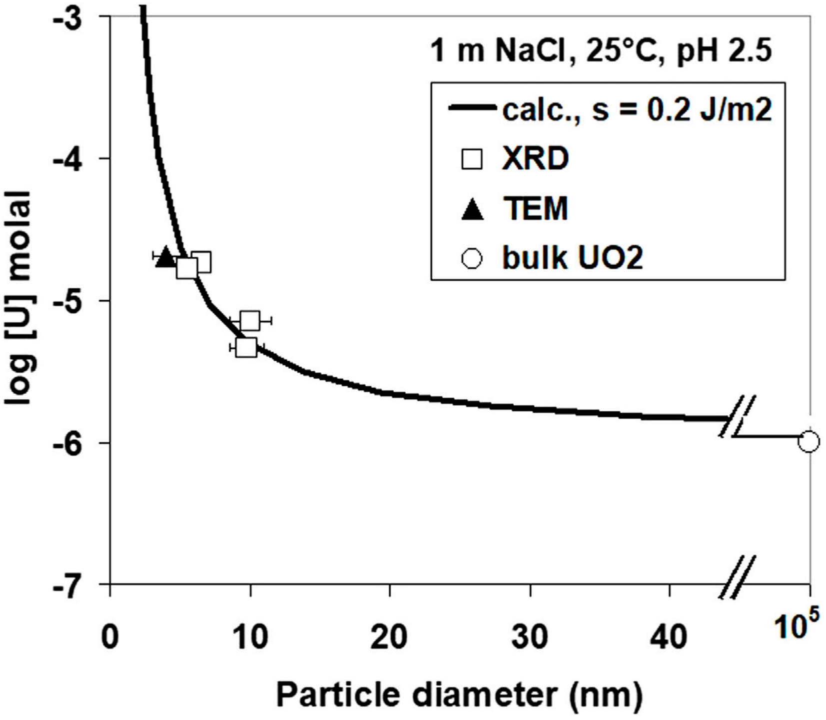

FIGURE 12
Theoretical solubility calculations for UO_2 as a function of particle size.

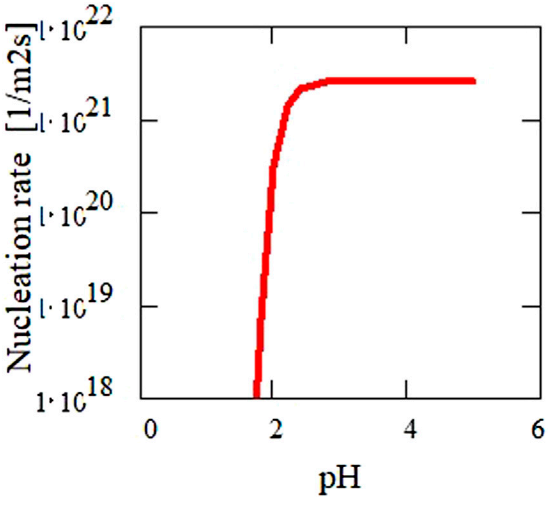

FIGURE 13
Calculated nucleation rate as a function of pH for the determined surface energy (Figure 12) of 0.2 $J \cdot m^{-2}$. The diameter of the critical nuclei is approximately 5 Å.

phases. The exact position of phase boundaries will vary with crystallinity/particle size.

In order to minimize the presence of U(VI) in the formed solid phases, the solubility of precipitates was studied, formed by stepwise alkali added to initially acid U(IV) solutions (starting pH 0.3). Precipitation here occurs only after all U(VI) has been transformed into U(IV). Using this procedure, the evolution of U concentrations at the start of the precipitation process is shown in Figure 4. At pH 1.5, the U concentrations started to decrease with time. Hence, the first signs of precipitation occurred at approximately 0.4 pH units earlier than in case of direct coulometric U(VI) reduction (experiment 1).

The kinetics of this growth process were also studied by monitoring the pH evolution in the reaction vessel. The solutions became slightly more acid. Acidimetric titration did not work to fix the pH. The maximum deviation in pH was 0.1 pH units. This pH evolution is assessed further as the initial steps of the precipitation process.

At pH 1.7, precipitation started to become more pronounced. Solution concentrations at higher pH values are shown in Figure 5. Arrows denote the direction of pH change. As in Experiment 1, strong precipitation occurred at approximately pH 2. Apparent equilibrium solution concentrations of U at pH 2.56 remained higher than in direct reduction of U(VI). A minimum solution concentration of U is attained at a pH of approximately 6–8. The subsequent increase of U concentrations at higher pH values cannot be explained by known data of U(IV) hydrolysis and may be attributed to oxygen contamination of the precipitates or of the aqueous solution (discussed chapter 3.5). The return to lower pH values leads to U concentrations much lower than those initially observed when the pH was changed in an alkaline direction. U concentrations increased with a slope of −1.3 with decreasing pH. These data do not reflect an equilibrium of stoichiometric UO_2, neither with U^{4+} nor with $U(OH)^{3+}$. At pH 0, the whole precipitate became dissolved again. In the pH range 2–3, the data are very similar to the data for 1 M

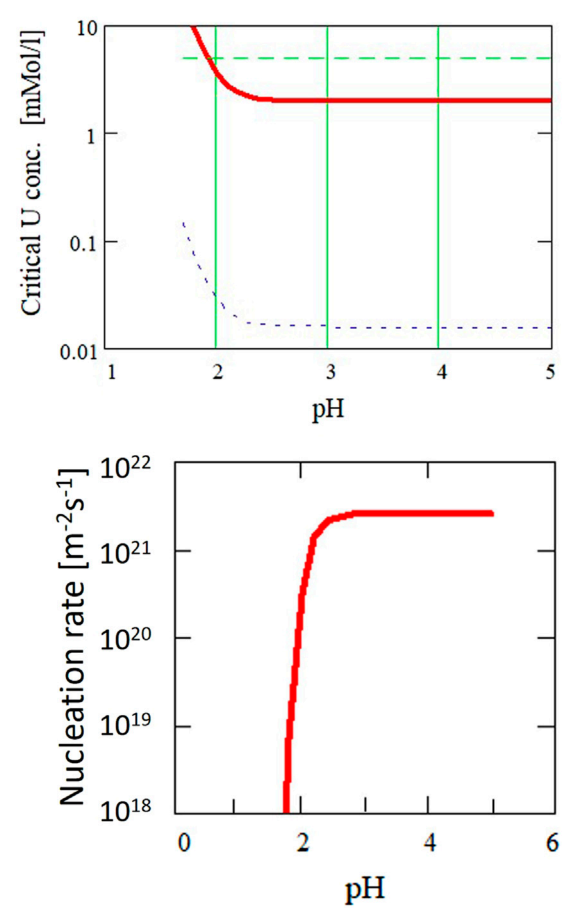

FIGURE 14
Critical supersaturation concentration for the formation of UO_{2+y} from aqueous solutions with nucleation rates of 10^{20} $m^{-3}s^{-1}$ (upper curve) and 10^{6} $m^{-3}s^{-1}$ (lower curve).

NaCl solution in Rai et al. (1997), who derived from these data the thermodynamic solubility of so-called hydrous UO_2(am).

3.5 Solubility of 100–200 µm UO_2 particles (experiment type 4)

For comparison and as reference for particle size effects, solubility tests with crystalline UO_2 were performed under the same conditions as the solubility tests with the precipitates formed by coulometric reduction. The results of ultrafiltered solution samples are given in Figure 6. A minimum solubility was observed in the pH range 6–10. The increase in solution concentration at higher pH can be explained by the formation of a surface oxidation film (see below). Almost constant concentrations were achieved between pH 0 and 2. This is caused by the slow dissolution rates of UO_2 at pH 2. The duration of acidometric titration was too short for some weeks and the surface area of particles (approximately 0.001 m^2/L of solution) too small to allow the dissolution of sufficient U(IV) to approach the solubility limit of UO_{2+y}.

After the third change of the supernatant solution, the experiment started again with fresh solution and permanent coulometric reduction at pH 0. It was expected that this would effectively remove any potential oxidized surface layer still adhering on the UO_2 powder. However, at pH 0, the solution concentrations decreased with time (for 3 days). This was surprising since, at this pH, the solution was expected to be undersaturated with respect to pure UO_2 and even more with respect to more oxidized surface layers. Under alkaline conditions, the solution concentration from the pH excursion after the third exchange of supernatant solutions was higher than during the first cycle. A possible explanation would be the fresh solution containing traces of oxygen introduced into the reaction vessel to cause U(VI) formation.

3.6 Results from solid-phase characterization

3.6.1 X-ray diffraction

X-ray diffraction patterns were obtained from three precipitates formed during the reduction of U(VI) at pH 2.56 (Supplementary Figure S7). The broadest lines were observed under conditions of high coulometric currents of 0.5 mA (high rates of U(IV) formation), and the finest lines were observed in experiments with slow reduction rates using 0.05 mA. A comparison was made with the powder pattern of pure $UO_{2.00}$ used in the solubility tests. This pattern closely matched the values reported in the literature for $UO_{2.03}$ (JCPDS-ICDD No. 13-0225, 1996). The precipitates show strong line broadening, yet the major peaks of uraninite remain clearly visible, indicating that crystalline rather than amorphous UO_2 had formed. Note that we considered here the UO_2 crystalline, even if the coherence length was only a few nm.

The oxidation of stoichiometric uraninite results in a decreased unit cell dimension of 5.47 Å for $UO_{2.00}$ to 5.44 Å for U_4O_9. The line broadening does not allow the accurate determination of the structure of the precipitates, but peak analyses of the 111 peak (peak at $2\theta = 28–29$) indicates a cell dimension of 5.43 Å, closely resembling the U_4O_9 unit cell. U_4O_9 has a small reflection at $2\theta = 58.8$. No indications for U_3O_7 formation were found (absence of a peak shoulder at $2\theta = 55.1$). The formation of U_4O_9 is consistent with the thermodynamic calculations given in Supplementary Figure S6: at pH 2.56, the reaction path for reduction of U(VI) intersected only the stability field of U_4O_9 and not of U_3O_7. The average particle size of the precipitate was estimated from the line broadening. Particle sizes were found in the range of 6–13 nm at pH 2.56 (see discussion chapter 4.4 on the effect of particle size on solubility). It is important to note that the particle size of the UO_2 precipitates was significantly smaller than that of crystalline (pure) UO_2 of 100–200 µm.

3.6.2 SEM analyses

Precipitates formed during coulometric reduction were analyzed under SEM to obtain a first image of the morphology. Spherical particles were typically observed. An example is precipitates collected on a filter membrane, given in Supplementary Figure S8 for precipitates formed at pH 2.25. At pH 2–2.5, the average particle sized was 30–60 nm, whereas it was close to 100 nm at higher pH values. The SEM images were not sufficiently clear to rule out agglomerates of smaller particles being formed and thus explaining the difference with the X-ray-determined particle sizes.

3.6.3 HRTEM analyses

Two samples of solid precipitate were selected for TEM and HRTEM analyses. The first precipitate was formed during coulometric reduction of 0.005 m U(VI)-containing solution at a constant pH of 2.5; the second was formed after reduction under acidic conditions and subsequent coulometric alkalization of the solution (experiment type 3). In the latter case, the precipitate was formed at approximately pH 2 (Figure 4) and the sample was taken after pH excursion to a value of 12. The results are given in Figure 7 and Supplementary Figure S9. Clearly, crystalline phases are formed in both cases: in the first, with a size of approximately 30 nm, in the second case, only 4 nm. The reasons for this difference will be further discussed below. Using TEM analyses (diagrams not shown), attempts were made to determine whether the observed particles from the coulometric reduction experiment are representative or were only arbitrarily encountered. It appears that a large fraction of particles were 30 nm in size; however, there were also many more larger particles of approximately 100 nm, similar to those encountered during SEM analyses. This is important for studying the dependency of solubility on the particle size of the precipitated material: if two size fractions coexist in the precipitate, the smallest particles will determine the overall solubility as long as the precipitate has not completely dissolved.

The lattice fringes of the precipitated crystals most closely match those of UO_2 or similar fluorite type phases like U_4O_9 or U_3O_7. In Figure 7, the 111 direction is visible with d-spacings between 3.06 and 3.18 Å, corresponding to unit cell parameters between 5.38 and 5.50 Å. The accuracy of the electron diffraction data is not sufficient to determine the oxidation state of the precipitate.

There is obviously no slow transition from initially formed amorphous phases to more crystalline phases, but crystalline phases are very quickly formed almost directly by precipitation. With these data, one may question whether phases denoted in the literature as UO_2(am) or U(IV)-hydrous oxides really exist. Many solubility studies use so-called precipitated amorphous UO_2 (e.g. Bruno et al., 1987; Rai et al., 1997) as characterized by almost structureless X-ray diffraction patterns. The present study suggests that the X-ray amorphous phases used in those studies may have really been very small crystalline phases similar than those of Supplementary Figure S9. An average particle size of 4 nm will essentially give the appearance of an amorphous X-ray diffraction pattern. This particle size corresponds to a molar surface area of UO_2 of approximately 36,000 m^2/mol, much higher than the value of 7,954 m^2/mol reported by Bruno (1989) for "amorphous" UO_2. Consequently, one must study the effect on solubility of particle size and not of crystallinity vs. amorphous behavior.

3.6.4 XPS

High resolution XPS investigations of the U $4f_{7/2}$ elemental line of precipitates from reduction experiments at pH 2.56 (current 0.05 mA) show slight asymmetry at the high-binding energy side (Supplementary Figure S10) compared to the U $4f_{7/2}$ elemental line of certified UO_2 (IRMM No. CBNM106) fractured under UHV inside the XPS as reference. This slight asymmetry can be assigned to less crystallinity of the fine precipitate compared to UO_2 bulk. No additional satellite is observed which may indicate presence of U(V) or U(VI). The O1s spectrum indicates the presence of hydroxide and water.

An UOx precipitate formed at pH 2.5 was collected on a filter and imprinted onto indium foil (as substrate for XPS). The sample showed very low oxidation, if any, compared to the fractured UO_2 sample; some H_2O/OH was present at the O 1s spectrum. An anhydrous oxide appears to have been precipitated from the solution covered with only few monolayers of hydroxide surface groups. Samples from solubility testing with crushed UO_2 pellets clearly show some oxidation. It is well known that even short contact to air will cause $UO_{2.0}$ oxidation to UO_{2+x}.

3.7 Results from a spectrophotometric study

It is already apparent that pH-dependent changes in the color of the solution in the reaction vessel were observed in the acid range after terminating the reduction process. The observations are summarized in Table 1.

UV/VIS absorption spectra were taken from U(IV)-containing solutions immediately after completing the reduction reaction (experiment type 1) in the pH range 0–1.7 (Supplementary Figure S11). The spectra could be interpreted as being composed of two monomer species: U^{+4} and UOH^{+3}. With increasing pH, the spectra show a decrease in the U^{+4}-peaks at 671, 649, 549, 495, and 430 nm, an increase in the minimum between the peaks, and the growth of a new shoulder at approximately 614 nm associated to UOH^{+3} formation. The spectra in Supplementary Figure S11 are very similar to those reported between pH 0.7 and pH 2.2 in perchlorate media with identically positioned peaks (according to Table 2 and Figure 1B in Cha et al., 2020). Comparing at the peak of 649 (or 648 nm in the literature) the reported $\varepsilon(cm^{-1}\cdot M^{-1}) = 66.5 \pm 1.8$ (Table 2 of the authors) in the perchlorate medium with a value of $\varepsilon(cm^{-1}\cdot M^{-1}) = 45 \pm 2$ obtained in the present work for chloride media, we can explain the decreased absorption by the coexistence of U(IV) chloride complexation. Indeed, by using the stability constants reported in Grenthe et al. (2020), UCl^{+3} complexes should be dominant (65% when applying PHREEQC with SIT coefficients—see details of calculations chapter 4.1) in this system. It is notable that no increase of absorption at wavelengths <400 nm is observed, indicating the absence of polymerization. The degree of contamination by remaining or regenerated U(VI) is difficult to assess because the extinction coefficients are very small. The extinction at 404 nm between 0.001 and 0.005 indicates U(VI) concentrations between 1×10^{-4} and 1.4×10^{-3} M.

An enlargement of the absorption peaks shows an isosbestic point at 623 nm (Figure 8) which is indicative of the presence of only two U(IV) species of U^{+4} and UOH^{+3} (Cha et al., 2020). Indeed, the spectra and isosbestic point are similar to those reported for perchlorate media (Figure 2B in Cha et al., 2020). The similarity of our spectra with the literature data in perchlorate media indicates that ours are not influenced by chloride complexation. By peak deconvolution at the various pH values and ignorance of potential U(VI) contributions, concentrations of UOH^{+3} were determined which resulted in a conditional formation constant of UOH^{+3} of log $^*ß_1$(1 M NaCl) = −1.44 ± 0.06. If potential U(VI) contamination is corrected for, a log $^*ß_1$ value of −1.58 ± 0.15 is obtained. The latter value agrees well with the first hydrolysis constant determined by Kraus and Nelson (1950) under analogous experimental conditions: log *ß$_1$(1.03 M Na/HCl) = −1.73. Note that this reference was considered in the NEA-TDB review by Grenthe et al. (1992) for the extrapolation to I = 0 and selection of log *ß$_{.1}$ = −0.54 ± 0.06.

3.8 Polymer formation with time

The evolution of U(IV) absorption spectra with time was studied for 15 days at pH 1.66. As indicated by increased absorption in the range 300–700 nm (diagram not shown), strong polymerization was observed after 14 days. “Polymerization” is used here in a generic form starting from dimerization, as no detailed polymer analyses were performed. A decrease in the U(IV) concentration from 3.1×10^{-3} M to 2.2×10^{-3} M probably resulted from the reaction.

$$U^{+4} + H_2O \overset{\text{fast}}{\leftrightarrow} UOH^{+3} + H^{+} \overset{\text{slow}}{\rightarrow} \text{Polymer}$$

No intermediate species between the monomer UOH^{+3} and the polymer could be identified spectrophotometrically, neither in the wavelength range 400–700 nm nor in the range 900–1300 nm.

Polymer formation occurs almost instantaneously at pH 2. The time dependency of its formation could be identified by studying the increase in the polymer signal. After mathematical subtraction of this polymer background, the residual spectrum only shows peaks for UOH^{+3} with a maximum of approximately 625 nm (Supplementary Figure S12). No higher hydrolysis species (e.g., $U(OH)_2^{+2}$, etc.) were observed. With increasing time, the UOH^{+3} concentration decreased, as expected for continuing polymerization. After adding acid to this solution (pH = 0), UOH^{+3} peaks only remain as small shoulders of a dominant U^{+4} peak at 649 nm (Supplementary Figure S13). The kinetics of redissolution of the polymer are slow, in contrast to the fast transformation of UOH^{+3} to U^{+4}.

3.9 Laser-induced breakdown detection of colloid formation

Colloid formation was studied by laser-induced breakdown detection (LIBD) in two duplicate samples which resulted from the complete reduction of initial solutions containing U(VI). One experiment was performed at a constant pH of 1.66 (Figure 9) and the other at a pH of 1.76 (Supplementary Figure S14). After reduction to U(IV), both solutions were supersaturated. The evolution of colloid formation was followed as a function of time for up to 15 days. The same solutions were also analyzed by UV-VIS absorption spectroscopy (see chapter 3.7).

In both cases, the growth of colloids was clearly observed. However, the behavior at the two pH values was reproducibly quite different. At pH 1.76 within 14 h, small colloids were grown with an average dimension of approximately 30 nm (Supplementary Figure S14). Prior to colloid growth, there were also some preexisting larger colloids; later, however, the dominant colloid form was the newly formed small ones. This size range is similar to the particle size of the precipitates of coulometric reduction experiments observed at pH values > 1.9 (see chapter 3.6). Thus, it is likely that UO_{2+y} colloids were formed.

At pH 1.66, the colloid growth process had a different character: much larger colloids were formed (Figure 9). It appears as if the preexisting colloids simply grew with time, whereas the concentration of colloids decreased (decreasing breakdown probability). Final sizes (after few days) were larger than a micrometer. The character of this colloid growth process is thus that of coagulation, probably caused by the action of U(IV) ions in solution.

4 Discussion

4.1 First step of reaction: hydrolysis

The stability ranges of dominant uranium (IV) hydrolysis species were estimated using the standard state stability constants from a recent review (Grenthe et al., 2020). Only two hydrolysis species of U(IV) appear to be important: UOH^{+3} and $U(OH)_4$(aq). For UOH^{+3}, a standard state formation constant log *ß$^{a}_{1}$ of −0.54 and for $U(OH)_4$(aq) of log *ß$^{a}_{4}$ of −10.0 were reported. Additionally, UCl^{3+} formation in 1 M NaCl must be accounted for, with a log *β$^{°}_{1}$ = 1.72 ± 0.13 reported in the aforementioned review. To calculate the corresponding activity coefficients, the SIT theory was used. We first used the interaction coefficients $\varepsilon = 0.76 \pm 0.06$ kg·mol^{-1} and $\varepsilon = 0.48 \pm 0.08$ kg·mol^{-1} given in the aforementioned work for the interaction of U^{4+} and of UOH^{3+} in perchlorate media. We then considered the difference of these species between perchlorate and chloride media being the same difference Δ as for Th^{4+} and $ThOH^{3+}$ in both media of Δ = 0.45 and Δ = 0.29. This led to ion interaction coefficients in chloride media of $\varepsilon(U^{4+},Cl^{-}) = 0.31$ kg·mol^{-1} and $\varepsilon(UOH^{3+},Cl^{-}) = 0.19$ kg·mol^{-1}. The activity coefficient for the neutral $U(OH)_4$(aq) was assumed to be unity in 1 M NaCl solution. Using these data, a conditional formation constant log *ß$_1$(1 M NaCl) of −1.80 was calculated for the reaction $U^{+4} + H_2O \Rightarrow UOH^{+3} + H^{+}$ in 1 M NaCl solution. This is slightly lower than the average value (average of values obtained with and without considering U(VI) contamination) of log *ß$_1$(1 M NaCl) = −1.51 ± 0.15 obtained by our spectrophotometric study; it is close to the spectrophotometrically determined value of log *ß$_1$ = −1.73 reported by Kraus and Nelson (1950) for 1.01 M Na/HCl solutions.

Hydrolysis of tetravalent uranium [U(IV)] and U(IV) nanoparticle formation kinetics were examined by Cha et al. (2020) in aqueous $NaClO_4$ over a wide range of temperatures using spectrophotometric reaction modeling analysis. As in our work, no further hydrolysis equilibrium beyond the formation of $U(OH)^{3+}$ was identified for pH < 2.2. The UV and Vis spectra observed by these authors are quite similar to ours. These authors obtained, at room temperature, a log *ß$_1$(1.05 m $NaClO_4$) = −1.48 ± 0.03 rather than the value of −1.51 ± 0.15 for NaCl at the same molality and temperature in our study.

4.2 Second step of reaction: formation of polymers

The spectrophotometric data show for the pH range 0–1.8 that monomer solution species (mainly U^{+4} and UOH^{+3}) dominate aqueous speciation during the first day after completion of coulometric reduction at constant pH. However, at pH 1.76, for example, the first signs of colloidal UO_{2+y} formation become obvious. Consequently, polymer transition species between monomer and colloid species are expected to form under certain conditions.

The polymerization reaction became observable at pH 1.5 in the coulometric alkalization experiment of acid U(IV) solutions. At this pH, despite coulometric alkalization, the pH became more acidic for a certain period, and further alkalization was retarded (Figure 10). Figure 10 shows a straight line, indicating the expected evolution of the quantity of H^+ in solution in the absence of polymerization. Retardation of alkalization may be explained by polymerization reactions. This may be illustrated, for example, by a hypothetical binarization reaction of the general type

$$U(OH)_n^{4-n}(H_2O)_x U(OH)_m^{4-m}(H_2O)_y \leftrightarrow \left[(H_2O)_{x-1}(OH)_{n-1}U_O^O U(OH)_{m-1}(H_2O)_{y-1}\right]^{\beta-m-n-2}$$

$$+2H^+ + 2\mathrm{H_2O}\,(0 \leq m, n \leq 4)$$

In this example, the binary species is formed by a dehydration reaction of two monomers bound together by two adjacent oxo-bonds. This speculative mechanism is deliberately selected, as the lattice of the fluorite structure of UO_2 can be constructed entirely by infinite condensation of these units. There is no proof that such species also exist in aqueous solution, but if anhydrous crystalline UO_{2+y} forms directly from aqueous solution, dehydrative polymerization is probably an initial step.

More than one H^+-ion per monomer uranium species is not released if a binary species with two oxo-bonds is formed, and even less H^+ ions are produced if only one oxo-bond is formed. The respective theoretical straight line is included in Figure 10. The observed retardation of the coulometric alkalization is stronger than expected for forming binary species. Consequently, higher polymerized species must be invoked, such as trimers and tetramers. The formation of tetramers ($U_4(OH)_{12}^{4+}$) was also inferred from potentiometric titrations in 1 M $NaClO_4$ (Ekberg et al., 2001). In the simplest, yet speculative, way, two binary species may condense to form tetramers, then hexamers, and finally uraninite.

The experimental curve for the evolution of the quantity of H^+-ions in solution was fitted by rate equations for binary, tetramer, and hexamer formation. Attempts failed to use only binary species (Supplementary Figure S15). Coupled general rate equations of the form

$$\frac{d[binary]}{dt} = \mathrm{K}_1\,[\mathrm{momomer}]^2,$$

$$\frac{d[tetramer]}{dt} = K_2\,[binary]^2,$$

$$\frac{d[hexary]}{dt} = K_3\,[tetramer]\cdot[binary],$$

were used to describe the experimental data. The monohydroxo species UOH^{+3} was considered as a monomer since it is the dominant species at this pH and no polymerization was observed at more acidic pH values with U^{+4} as the dominant species. The initial concentration of the monohydroxo species was calculated with the hydrolysis stability constant, derived previously. The following constants were obtained: $k_1 = k_2 = 70{\cdot}s^{-1}$ and $k_3 = 13{\cdot}s^{-1}$.

The corresponding species distribution as a function of time is given in Supplementary Figure S15. The fitting exercise was mainly performed for illustrative purposes. More accurate experiments would be necessary to study the details of the polymerization kinetics in depth. If this mechanism for the initial polymerization stages of uraninite formation is correct, polymer species such as dimers, tetramers, or hexamers would merely be transitory, leading finally to the nucleation and growth of uraninite.

4.3 Third step of reaction: formation of colloids

Colloid formation is a key mechanism that increases the mobility of tetravalent uranium in natural water systems. According to Supplementary Figure S14, small colloids, probably UO_2, were formed at pH 1.76; according to Figure 9, large colloids at only a 0.1 pH unit less. The different behavior at the two pH values was reproducible and may be explained by the rate at which supersaturated conditions are achieved. Although the rate of U(IV) formation was the same at the two pH values (controlled by coulometric reduction with 1 mA), this is not true for the rate for achieving supersaturated conditions. For a given solution concentration of U(IV) to supersede the thermodynamic solubility of UO_{2+y}, solutions at pH 1.76 are supersaturated to a higher degree than at pH 1.66 because the thermodynamic solubility decreases in this pH range with increasing pH.

The relationship between the rate of achieving supersaturation and the mechanism of colloid formation is illustrated schematically in Supplementary Figure S16. With high supersaturation rates, homogeneous nucleation of colloids may be achieved, whereas, at lower rates, the uptake of U(IV) by sorption on preexisting colloids is faster than the production rate of U(IV), and the critical nucleation boundary cannot be achieved. Using this reasoning, one may conclude that the critical nucleation boundary in our experiments lies between pH 1.66 and 1.76 for a critical U(IV) concentration of $5{\cdot}10^{-5}$ M. However, this boundary may shift to higher pH values in natural systems because there are much more heterogeneous nucleation sites available than in the laboratory. Consequently, adherence of U(IV) to natural colloids is expected.

4.4 Fourth step of reaction: solid-phase formation

The results of solid-state characterization indicate the formation of uraninite of different degrees of oxidation probably most closely matching a stoichiometry between UO_2 and U_4O_9 under all conditions. The results are consistent with observations on natural uraninite, in that pure UO_2 is not formed directly from aqueous solutions. The observed particle size of the precipitates is similar to those of the "true" colloids observed at pH 1.76, indicating that precipitation also has the character of a coagulation process. The changes in the slopes Δ acid addition/Δ added charge, however, show a clear difference between the colloid forming conditions at pH 1.76 and the precipitation regime (Supplementary Figure S3).

In order to assess the formation conditions of "uraninite," both the nucleation and growth processes must be quantified. According to classical nucleation and growth theories, the degree of supersaturation is a key parameter. This requires an assessment of the solubility of the precipitates as a function of pH, particle size, and oxidation state—both of the solid and aqueous media. The saturation state is difficult to assess for redox sensitive phases because it depends both on solid and solution oxidation states.

A comparison of solubility data obtained in the present study with calculated solubilities of stoichiometric UO_2 and of U_4O_9 with well-known thermodynamic properties and with some experimental data from the present work and from literature is given in Figure 11. The thermodynamic solubilities were calculated for aqueous solutions of 1 M NaCl at 1 atm H_2 using the thermodynamic data described previously, with solid-phase stability constants for well-crystalline UO_2 and U_40_9 taken from Grenthe et al. (2020). As particle size and associated surface energy might have influenced our solubility data, a curve for nanocrystalline UO_2 has also been calculated using the surface energy obtained in Figure 12 (see further this chapter below). After terminating the reduction process in all our experiments, the slopes (Δ acid addition/Δ current) indicate the electrolytic decomposition of water, so the assumption is made that equilibrium is established between the aqueous solution and 1 atm H_2(g). Under these conditions, only U(IV) aqueous species are dominant. Under these conditions, the difference in solubility between U_4O_9 and UO_2 is four orders of magnitude. The importance of solid-state oxidation states on controlling aqueous solubility under reducing conditions is well recognized (Parks and et Pohl, 1988; Bruno, 1989) for solubility studies with well-crystalline UO_2. Parks and et Pohl (1988) reported a solid-phase stoichiometry close to $UO_{2.006}$ after terminating their solubility experiment. However, probably due to difficulties in the characterization of solids and their surfaces, many studies with so-called amorphous UO_2 reported in the literature do not discuss the implication of solid phase oxidation states on solubility under reducing conditions (Rai et al., 1997; Yajima and Kawamura, 1995; Bruno et al., 1987). In particular, reported amorphous to crypto-crystalline XRD data do not allow distinguishing between UO_2 and U_4O_9. Hence, it may well be that the observed difference in the reported solubility of “UO_2(am)” (e.g., discussion in Yajima and Kawamura, 1995) may be attributed to differences in surface or bulk solid oxidation states rather than to differences in maintaining reductive environments, as proposed by Rai et al. (1990).

However, above pH 4, all experimental solubility values are higher than any of the three model curves, showing that neither oxidation of the solid (U_4O_9) nor particle size can explain the results. Therefore, the hypothesis is tested, with another calculated curve, that traces of O_2 (1E-8 atm) might have persisted in the experimental device, despite permanent purging by hydrogen. The calculated curve matches exact average experimental data. Indeed, all experimental data could be “explained” with different, rather small quantities of remaining dissolved oxygen.

Nevertheless, it cannot be excluded that different oxidation states of uraninite coexisted in our experiment. This was clearly observed in our experiments with “pure UO_2”, but coulometric reduction may also have led to coexistence of different oxidation states. The initial precipitates remain in contact with not-yet reduced U(VI) in solution, whereas the final precipitate is formed in the absence of U(VI). Consequently, the initial products are expected to be more oxidized than the later ones.

The reaction path from higher to lower Eh values is illustrated in Supplementary Figure S6. If two uraninite phases of different degree of oxidation coexist, they may establish equilibrium conditions, implying that the Eh is fixed by the phase equilibrium and that U-solubility would have to be assessed at this phase boundary redox potential. The solubility at this boundary is calculated, for example, for the boundary UO_2/U_4O_9 with an equilibrium oxygen fugacity log $O_2(g) = -51.85$. Such conditions may exist at the solid’s surface even under conditions of aqueous solutions saturated with H_2. U(VI) and not U(VI) species are dominant solution species at this “surface redox potential.” Hence, the solubility and the pH dependency of solubility are quite different from those calculated given in Figure 11 for the case of Eh values at the lower stability field boundary of water. If this situation had occurred in our tests, a non-equilibrium system would have been established: any U(VI) generated by dissolution of U_4O_9 would be reduced coulometrically, and, subsequently, new U(VI) would be dissolved. The steady state between coulometric reduction and the dissolution of U(VI) may have resulted in some of the variability of solubility data in Figure 11. The results of all our tests show the lowest concentrations in the pH range 6–8, which is a range of high significance for many natural water systems. In this pH range, our data are similar to those of Yajama (1996) for “amorphous” UO_2. When comparing the results of our different experiments with the data from solubility tests with large particles, stoichiometric UO_2 show the lowest solubility as expected. Compared with the thermodynamic solubility of pure UO_2, much lower solution concentrations are experimentally encountered below pH 1. This is interpreted as resulting from the slow dissolution rates of the large UO_2 particles and does not reflect solubility but control by slow dissolution rates which do not allow dissolved U concentrations to achieve equilibrium. The data for precipitation by coulometric alkalization from initially acid U(IV) solutions require special attention: precipitation does not initially occur to a large extent until a pH of approximately 2. Thereafter, up to pH 8, the solution concentrations decrease rapidly with increasing pH. In the pH range of 2–3, the data are very similar to those of Rai et al. (1997), also obtained in 1 M NaCl solution with an initial acid solution of U(IV). Rai et al. (1997) used these solubility values, with other similar data, to obtain thermodynamic parameters for describing the solubility of so called hydrous UO_2(am). However, the acidometric return of our curve to low pH values (0–2) also shows a hysteresis, with lower solubilities than previously encountered. Solution concentrations of precipitate with a particle size of only 4 nm (HRTEM analyses, Figure 7) are also much lower than those of Rai et al. (1997). TEM images of crystalline primary particles of only 2–3 nm with uraninite-like structure and their clusters (20–30 nm) were also recently reported by Cha et al. (2020), which could also have resulted in an aging of the initial precipitate. However, the aging time of 60 days was lower than in Rai et al. (1997). Another explanation could be a control of U-concentrations by dissolution kinetics of the precipitate, similar to the experiment with large particles of UO_2. However, the particle size is rather small, and the specific surface area is much higher than in the experiment with large particles of UO_2. Consequently, equilibrium should be reached much more easily. Moreover, in the acidic range, solution concentrations remained essentially constant with time, provided the pH was kept constant. This would suggest that the pH data would reflect solubility data rather than kinetically controlled values. If this were true, there would be a transition from solubility values close to theoretical U_4O_9 solubility at the end of coulometric alkalization (pH 10–12) to theoretical solubility values close to theoretical UO_2 solubility at the end of acidometric titration at pH values close to zero. This transition may be caused by the dissolution of U_4O_9, which is thermodynamically unstable at very low pH values.

The observed difference in the solubility data may not only reflect different oxidation states but also different particle sizes. The effect of particle size on solubility was studied by compiling various experiments performed at pH 2.56. The results are shown in Figure 12. A theoretical curve for the solubility S of small cubic particles of diameter d can be determined from the eqution

$$\log S = \log S_o + \frac{4 \cdot \sigma \cdot V_m}{2.303 \cdot R \cdot T \cdot d},$$

if the solubility S_o of large particles and the surface energy σ is known. In this equation, V_m is the molecular volume of UO_2, R is the gas constant, and T is the absolute temperature. A surface energy of 0.4 J/m^2 is obtained using the measured solubility for large particles of 10^{-6} m for a uraninite phase of the surface stoichiometry UO_{2+y}. This is approximately a factor of 5 lower than the value calculated from solubility data by Bruno (1989) for UO_2. If the reported surface energy value was correct, 4-nm particles would not be stable in solution.

Using our surface energy value, the conditions for solid phase nucleation can now be established. According to classical theory, for a given solution concentration $C_{U(IV)}$, the nucleation rate J is given by the following equation.

with the pre-exponential factor A being 10^{33} $m^{-3}s^{-1}$, the shape factor ß with a value of 32 for cubic

$$J = A \cdot \exp\left[\frac{\beta \cdot V_m^2 \cdot \sigma^3}{K^3 \cdot T^3 \cdot \left[n \cdot \mathrm{in}\left(\frac{C_{U(IV)}}{S_o}\right)\right]^2}\right]$$

crystal morphology, the Boltzmann constant k, and the number of atoms *n* in molecule.

Using this equation together with the theoretical solubility calculations for UO_2 as a function of particle size (Figure 12), the nucleation rate is calculated as function of pH (Figure 13). The diameter of the critical nuclei is approximately 5 Å. Based on this relation, critical U concentrations for precipitation were calculated as a function of pH (Figure 14) for both a nucleation rate of 10^{20}/(m^3s) (upper curve) and for 1/(cm^3s)—the so-called "critical supersaturation condition." This diagram may help explain our experimental results: precipitation (high nucleation rate) starts at pH 1.9, whereas true colloid formation (slow nucleation rate) already commences at a lower pH of approximately 1.7. The calculations also qualitatively describe the observed (experiment type 1, Figure 2) decrease in the critical concentration for precipitation with pH.

5 Conclusion

Reduction of U(VI) solutions leads to uraninite solid phases with oxidation states between UO_2 and U_4O_9. Observed solubilities at pH > 4 were much higher than those predicted in pure H_2 saturated systems. Discrepancies can be explained by a combination of three effects: oxidation of the solid to U_4O_9, effect of particle size, and/or oxygen traces as low as 1E-8 atm in gas contacting the aqueous solution. The effect of particle size/crystallinity and solid oxidation alone cannot explain the observation. Crystalline phases are always precipitated, and amorphous phases are never formed. Precipitation rates are controlled by nucleation kinetics, not by growth. Surface energies were approximately 0.2 J/m^2. Homogeneous nucleation led to colloid formation at pH > 1.7. At lower pH, pseudocolloids were observed. The homogeneous nucleation of uraninite is not expected under natural conditions, unless the total U(IV) concentration is higher than 10^{-5} m. Such concentrations are seldom encountered.

Data availability statement

The raw data supporting the conclusion of this article will be made available by the authors, upon request without undue reservation.

Author contributions

BG: conceptualization, formal analysis, investigation, methodology, supervision, validation, writing–original draft, and writing–review and editing. RM: data curation, formal analysis, investigation, methodology, and writing–original draft. DS: investigation, validation, and writing–original draft. XG: supervision, validation, and writing–review and editing.

Funding

The authors declare that no financial support was received for the research, authorship, and/or publication of this article.

Acknowledgments

The experimental work of this paper was conducted at INE between 1997 and 1998. It has never been published but was quoted in the research work of INE as "BG, RM, to be published," as in Neck et Kim (2001).

Conflict of interest

The authors declare that the research was conducted in the absence of any commercial or financial relationships that could be construed as a potential conflict of interest.

The BG and XG declared that they were an editorial board member of Frontiers, at the time of submission. This had no impact on the peer review process and the final decision.

Publisher's note

Supplementary material

The Supplementary Material for this article can be found online at: https://www.frontiersin.org/articles/10.3389/fnuen.2023.1308064/full#supplementary-material

References

Bettis, J. R. (1992). Correlation among the laser-induced breakdown thresholds in solids, liquids, and gases. *Appl. Spectrosc.* 31, 3448. doi:10.1364/ao.31.003448

Bruno, J., Casas, I., Lagerman, B., and et Munoz, M. (1987). "The determination of the solubility of amorphous UO2(s) and the mononuclear hydrolysis constants of uranium(IV) at 25°C," in Materials Research Society Symposium Proceedings. Editors J. K. édité par and W. B. Bates et (Pittsburgh, PA USA: Materials Research Society), 153–160. Seefeldt, Scientific Basis for nuclear waste management X.

Bruno, J., Turpeinen, U., Lehmann, M. S., Sjöström, M., Wold, S., Colacio, E., et al. (1989). A reinterpretation of the solubility product of solid uranium(IV) dioxide. *Acta Chem. Scand.* 43 (1), 99–100. doi:10.3891/acta.chem.scand.43-0099

Bundschuh, T., Knopp, R., and et Kim, J. I. (2001). Laser-induced breakdown detection (LIBD) of aquatic colloids with different laser systems. *Colloids Surfaces A Physicochem. Eng. Aspects* 177 (1), 47–55. doi:10.1016/s0927-7757(99)00497-5

Cevirim-Papaioannou, N. (2018). *Redox chemistry, solubility and hydrolysis of uranium in dilute to concentrated salt systems*. PhD Thesis. Karlsruhe, Germany: Karlsruhe Institute of Technology.

Cha, W., Kim, H.-K., Cho, H., Cho, H.-R., Jung, E. C., and et Lee, S. Y. (2020). Studies of aqueous U(IV) equilibrium and nanoparticle formation kinetics using spectrophotometric reaction modeling analysis. *RSC Adv.* 10, 36723–36733. doi:10.1039/d0ra05352j

Ekberg, C., Brown, P., Comarmond, J., and et Albinsson, Y. (2001). "On the hydrolysis of tetravalent metal ions," in Materials Reseach Society Symposia Proceedings. Editors K. édité par, P. Hart et, and G. R. Lumpkin (Warrendale, PA, USA: Materials Research Society), Scientific Basis for nuclear waste management XXIV, 1091–1099.

Fujimori, H., Matsui, T., Ajiro, T., Yokose, K., Hsueh, Y. M., and et Izumi, S. (1992). Detection of fine particles in liquids by laser breakdown method. *Jpn. J. Appl. Phys.* 31, 1514. doi:10.1143/jjap.31.1514

Fujiwara, K., Yamana, H., Fujii, T., and et Hirotake, M. (2003). Determination of uranium(IV) hydrolysis constants and solubility product of $UO_2 \cdot xH_2O$. *Radiochim. Acta* 91 (6), 345–350. doi:10.1524/ract.91.6.345.20023

Grenthe, I., Fuger, J., Konings, R. J. M., Lemire, R. J., Muller, A. B., Nguyeng-Trung, C., et al. (1992). *Chemical thermodynamics of uranium* in *Chemical thermodynamics series* (Amsterdam, Netherlands: North-Holland), 1.

Grenthe, I., Gaona, X., Plyasunov, A. V., Rao, L., Runde, W., Grambow, B., et al. (2020). *Second update on the chemical thermodynamics of uranium, neptunium, plutonium, americium and technetium*, 14. Paris: NEA/OECD. Chemical Thermodynamics https://www.oecd-ilibrary.org/fr/nuclear-energy/second-update-on-the-chemical-thermodynamics-of-uranium-neptunium-plutonium-americium-and-technetium-volume-14_bf86a907-en.

Kitamori, T., Yokose, K., Sakagami, M., and et Sawada, T. (1989). Detection and counting of ultrafine particles in ultrapure water using laser breakdown acoustic method. *Jpn. J. Appl. Phys.* 28, 1195. doi:10.1143/jjap.28.1195

Kraus, K. A., and et Nelson, F. (1950). Hydrolytic behavior of metal ions. I. The acid constants of uranium(IV) and plutonium(IV). *J. Am. Chem. Soc.* 72 (9), 3901–3906. doi:10.1021/ja01165a020

Neck, V., and et Kim, J. I. (2001). Solubility and hydrolysis of tetravalent actinides. *Radiochim. Acta* 89 (1), 1–16. doi:10.1524/ract.2001.89.1.001

Parks, G. A., and et Pohl, D. C. (1988). Hydrothermal solubility of uraninite. *Geochimica Cosmochimica Acta* 52 (4), 863–875. doi:10.1016/0016-7037(88)90357-2

Radziemski, L. J., and et Cremers, D. A. (1989). *Laser-induced plasmas and applications*. New York·Basel: Marcel Dekker.

Rai, D., Felmy, A. R., and et Ryan, J. L. (1990). Uranium(IV) hydrolysis constants and solubility product of $UO_2.xH_2O(am)$. *Inorg. Chem.* 29, 260–264. doi:10.1021/ic00327a022

Rai, D., Felmy, A. R., Sterner, S. M., Moore, D. A., Mason, M. J., and et Novak, C. F. (1997). The solubility of Th(IV) and U(IV) hydrous oxides in concentrated NaCl and $MgCl_2$ solutions. *Radiochim. Acta* 79 (4), 239–247. doi:10.1524/ract.1997.79.4.239

Scherbaum, F. J., Knopp, R., and et Kim, J. I. (1996). Counting of particles in aqueous solutions by laser-induced photoacoustic breakdown detection. *Appl. Phys. B Lasers Opt.* 63 (3), 299–306. doi:10.1007/s003400050087

Wolery, T. J. (1983). *EQ3/6 modifications for geochemical modeling of brines*. Livermore, CA USA: Lawrence Livermore National Laboratory.

Yajima, T., Kawamura, Y., and et Ueta, S. (1995). "Uranium(IV) solubility and hydrolysis constants under reduced conditions," in Materials Research Society Symposia Proceedings. Editors T. édité par and R. C. Murakami et (Pittsburgh, PA, USA: Materials Research Society), 1137–1142. Ewing, Scientific Basis for nuclear waste management XVIII.

Frontiers in
Nuclear Engineering

Advances and applications in nuclear science, technology, and engineering

A forum for the nuclear research community working across fission and fusion physics, power generation, safety and waste management, materials and modelling to find new applications.

Discover the latest Research Topics

See more →

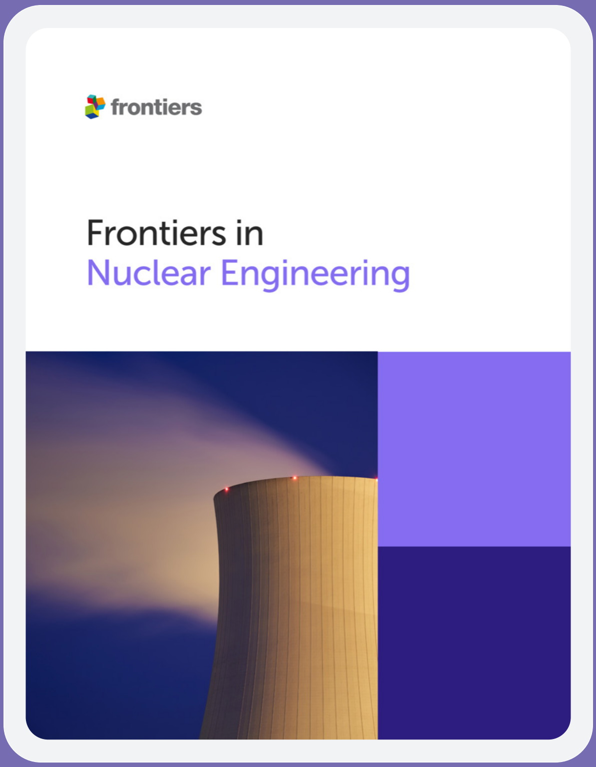

frontiers

Frontiers in
Nuclear Engineering

Frontiers

Avenue du Tribunal-Fédéral 34
1005 Lausanne, Switzerland
frontiersin.org

Contact us

+41 (0)21 510 17 00
frontiersin.org/about/contact